Numerical modelling of the absolute stress state in the Marmara Sea region

– a contribution to seismic hazard assessment

Zur Erlangung des akademischen Grades eines
DOKTORS DER NATURWISSENSCHAFTEN
von der Fakultät für Physik
der Universität Karlsruhe (TH)

genehmigte

DISSERTATION

von
Dipl.-Geophys. Tobias Hergert
aus Heidenheim a. d. Brenz

Tag der mündlichen Prüfung:	6. Februar 2009
Referent:	Prof. Dr. Friedemann Wenzel
Korreferent:	Prof. Dr. Karl Fuchs

Contents

Summary

During the last century a westward propagating sequence of major earthquakes occurred along the North Anatolian Fault (NAF), Turkey. The last event in 1999 occurred at the eastern end of the Marmara Sea and increased Coulomb Failure Stress on the NAF to the west, thus enhancing the probability of the next event to occur beneath the Sea of Marmara. This submarine section of the NAF had been previously identified as a seismic gap as it had not ruptured since 1766. This circumstance gravely concerns the city of Istanbul due to its proximity to the fault. With regard to potential damage, location and coseismic slip during a future event is of importance as well as the question whether the seismic gap will yield in one large earthquake or in several smaller ones.

The standard approach for time-dependent seismic hazard assessment is based on a statistical analysis of the mean recurrence rate of characteristic earthquakes. The recurrence rate is either inferred from catalogues of historical earthquakes or from the slip rate on the fault segment under consideration and typical coseismic slip. In the Sea of Marmara, both directly inferred mean recurrence rates and fault slip rates represent an uncertainty.

This thesis addresses size and location of a future large earthquake by accounting for its basic physical causes. These are the stress accumulation up to a critical level on a locked fault due to the relative motion of two plates. The kinematics and absolute stress is modelled simultaneously, both their secular steady-state evolution as well as during the interseismic and coseismic phases of the seismic cycle. Based on that, potential coseismic slip on a fault and associated seismic moment can be quantified dependent on time, while rough constraints on occurrence times of earthquakes can be made, though at a precision in the order of a few decades. No *a priori* information on mean interevent times of earthquakes or fault slip rates is required.

In order to model the absolute stress, the major sources of stress are integrated into the model. Topography/bathymetry, the basement-topography and Moho are considered as transitions in density and elastic properties, the 3D fault system of the NAF obeying the Coulomb friction law is included as well as gravity, the load of the overlying water column, the regional plate motion and an initial stress field that ensures equilibrium of gravitational forces and a ratio of horizontal to vertical stress that keeps to global measurements of stress magnitudes.

The resulting velocity and stress field of the model is found in agreement with available direct and indirect observations and constraints of the ongoing kinematics and dynamics. Modelled vertical motion reproduces a characteristic pattern of subsidence in the basins of the Marmara Trough and other areas under extension while uplift is found in areas of compression, in wide agreement to model-independent data.

The inferred slip rate on the main branch of the NAF is found to be 12.5-20 mm/yr, depending on location and rock properties, which is smaller by up to 40 % in comparison to earlier works. Right-lateral slip is partitioned on several strands of the NAF and also permanent strain and rotation in the rock volume between the faults contribute in accommodating relative plate motion. A consequence of lower fault slip rates is that reported seismic hazard based on fault slip rates is lower.

A high variability in slip rate along strike of the main branch is revealed. Since this implies variable loading conditions, consequences for recurrence rates of earthquakes should arise so that in this respect smaller earthquakes are more likely. The same conclusion can be drawn from the inferred fault-normal stress that exhibits strong variations along strike of the main branch.

The modelled stress field is in a strike-slip regime that is close to extension. Modelled orientations of the three principle stresses are in good agreement with reported orientations from inversions of earthquake focal mechanisms and thereby indicate that the modelled 3D stress field agrees with

independent data. The observed pattern of micro-seismicity in the Marmara Sea can be widely explained in terms of a steady release of critical differential stresses that evolve in the rock volume adjacent to faults in response to the interaction between plate motion and local fault geometry.

Since both, the modelled velocity field and absolute stress state are in agreement with observations the model is used to simulate the co-seismic slip of earthquakes in a forward approach. For this purpose, time-dependency is introduced by modelling the strain accumulation in the neighbourhood of a locked fault during the interseismic period and slip by release of stress at the times of historical earthquakes, according to elastic rebound theory. Unlocking the Izmit fault segment in 1999 results in a co-seismic surface slip that deviates even in the near field by only 6 % in amount and 9° in direction from the slip deduced from GPS observations, while modelled seismic moment at depth largely agrees with slip inversions from seismological and InSAR data. This result gives confidence that the approach is capable of predicting seismic moments of future earthquakes at other segments of the fault. To infer the potential slip and seismic moment of earthquakes on the main Marmara fault, several testing earthquakes for the year 2010 were simulated. A worst case scenario filling the whole gap between the Tuzla and Ganos Bends would yield a M=7.6 event at present. However, earthquakes involving only one fault segment are more likely and would produce M=7.3 and 7.1 events on the Central and Western segments, respectively, at present. Since both segments are late in their seismic cycle, dynamic stress triggering could cause a rupture extending on both segments, which would result in a M=7.5 event. Inferred seismic moments are upper bounds since partially unbroken fault portions are not considered. The thick sedimentary sequence in the Marmara Sea reduces seismic moments by 10-20 %.

The presented approach of modelling the absolute stress state is suited for getting insight into the interconnections between plate motion and a fault system and how the driving stresses are related to kinematics. This contributes to a qualitative understanding of recurrence rates of earthquakes. Importantly, obtained fault slip rates can be used in quantitative estimates of seismic hazard. As far as one may deduce from independent constraints, the absolute stress state is attained, with all the valuable consequences, the most important of which is that potential slip on a fault can be provided at any arbitrary time.

Chapter 1

Introduction

1.1 Istanbul expecting an earthquake

On August 17th 1999 the eastern Marmara region, northwest Anatolia, was hit by a $M_w = 7.4$ earthquake (BSSA vol. 92). Over 18,000 people lost their lives and total economic, building and infrastructural losses amounted to $ 15-20 billion (Bendimerad et al., 2000; Erdik, 2000). Also, from a scientific point of view this 1999 Izmit earthquake received much attention, in particular due to the fact that its location was predicted being the next event in a west migrating earthquake sequence along the North Anatolian Fault (NAF) (Stein et al., 1997). Fig. 1.1 illustrates the sequence of major earthquakes that occurred during the last century along the NAF commencing in 1939 with the $M_w = 7.9$ Erzincan earthquake and reaching the eastern Sea of Marmara during the 1999 Izmit earthquake. A number of Coulomb Failure Stress analyses yielded that ten out of eleven earthquakes of this sequence were promoted by the previous earthquakes (e.g. Stein et al., 1997).

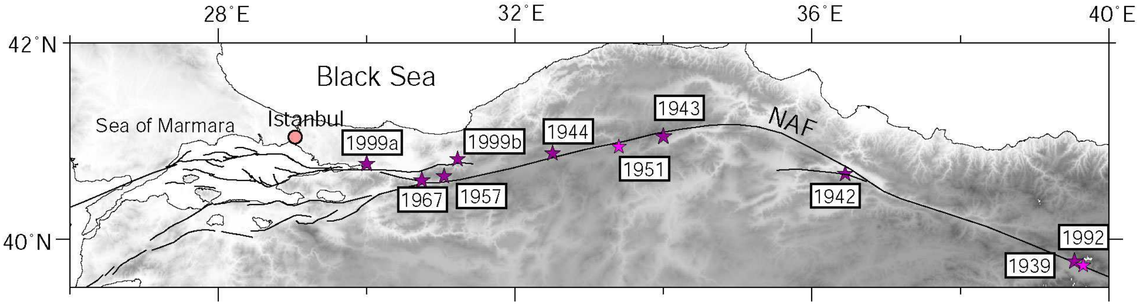

Fig. 1.1: Epicentres of major earthquakes ($M_w > 6.5$) along the North Anatolian Fault between 1939 and 1999 (Engdahl and Villasenor, 2002).

A continuation of this sequence further to the west is expectable and would result in an earthquake beneath the Sea of Marmara (Hubert-Ferrari et al., 2000; Parsons, 2004; Lorenzo-Martin et al., 2006). The central part of the NAF beneath the Marmara Sea was identified as a seismic gap with no major earthquake either since 1766 (Parsons, 2004; Pondard et al., 2007) or since 1509 (Ambraseys, 2001b). The possibility of a strong earthquake in the Sea of Marmara places a severe threat to the city of Istanbul which is located only ~ 20 km north of the main strand of the NAF (Fig. 1.1). Since mid of the 20th century Istanbul experiences enormous growth rates in population with to date 12.6 Mio.[1] registered inhabitants. Apart from that, Istanbul is Turkey’s leading industrial province where almost half of the gross national product is achieved. An earthquake of similar magnitude as the Izmit earthquake would therefore strongly affect Turkey as a whole (Bendimerad et al., 2000).

While there is agreement on that a major earthquake will occur beneath the Marmara Sea, expectations on location, coseismic slip, moment magnitude and probabilities of the next earthquake are non-uniform or vague (Le Pichon et al., 2003). The goal of this thesis is to

---

[1] TUIK. Address-based population registration system: City-Village Population By Province And Sex And Population Density (Turkish).

provide answers on these issues and to contribute to seismic hazard assessment in the Sea of Marmara by means of a deterministic 4D (space and time) geomechanical numerical model that describes the absolute stress and strain field. This is a novel approach since the probabilistic standard approach to assess seismic hazard is based on earthquake catalogues and/or fault slip rates and in some cases additionally accounts for coseismic stress changes. The absolute stress and strain field approach pursued here is not reliant on *a priori* knowledge of earthquake recurrence rates and fault slip rates. In contrast, it implicitly permits quantification of fault slip rates and allows estimation of potential coseismic slip, moment magnitude and at a lower precision time of a future earthquake, by means of forward modelled testing earthquakes that result from the release of accumulated stress. In addition it provides insight into the interconnections of motion and stress within the submarine fault system and thus pertains to a better understanding of the physical background of earthquakes in the Sea of Marmara.

In the following subchapter 1.2, the study area is introduced in more detail and the geodynamic frame of the Marmara region is explained. Subchapter 1.3.1 states to which part of a seismic hazard assessment and risk analysis this new approach pertains, 1.3.2 provides a brief overview on hitherto conducted approaches for seismic hazard assessment in the Marmara region and in 1.3.3 some critical aspects therein are identified that are to be challenged in this thesis.

1.2 Study area

Within this subsection a brief introduction into the geodynamics of the study area is given. Additionally, terms for areas, faults, etc. on which will be referred to later on are introduced.

1.2.1 Anatolia

The North Anatolian Fault (NAF) is a right-lateral strike-slip fault forming the boundary between the Anatolian and Eurasian Plates (Fig. 1.2; Barka, 1992; Şengör et al., 2005). Since historical times there is evidence for surface faulting due to earthquakes along the NAF (Ambraseys and Jackson, 1998). The occurrence of earthquakes along the NAF involves the interaction of different lithospheric plates in the eastern Mediterranean. The Arabian and African Plates move northward with respect to Eurasia (McClusky et al., 2003) at rates of 15.6 mm/yr (at 40°E) and 5.5 mm/yr (Fig. 1.3; Reilinger et al., 2006), respectively, separated by the sinistral Dead Sea Fault. The plate boundary between the African and Anatolian Plates is formed by the Hellenic–Cyprean trenches where the African Plate is subducted to the north beneath the Anatolian Plate (Papazachos et al., 2000). Convergence between the Arabian and Anatolian Plates occurs as continental collision (Allen et al., 2004). The Anatolian Plate escapes bounded by the NAF and the East Anatolian Fault, which is ascribed to the indentation of the Arabian Plate (McKenzie, 1972). The westward motion of Anatolia is permitted and accelerated by the slab retreat in the Hellenic subduction zone leading to NS-oriented back-arc extension in Greece and western Anatolia (Heidbach and Drewes, 2003; Flerit et al., 2004). The relative motion between the Anatolian and Eurasian Plate occurs along the NAF with a GPS derived slip rate of 24±1 mm/yr (McClusky et al., 2000) and Holocene geologic slip rates of ~ 18-20 mm/yr (Hubert-Ferrari et al., 2002; Kozacı et al., 2007). Deformation was observed to be quite localised at the NAF (Hubert-Ferrari et al., 2002) which lead to the interpretation that the Anatolian Plate behaves effectively as a rigid plate (Jiménez-Munt and Sabadini, 2002). In response to the pushing Arabian Plate and the pulling Hellenic subduction zone the Anatolian Plate fulfils a counter-clockwise rotation around an Eulerpole located in the Nile Delta (McClusky et al., 2000; Le Pichon et al., 2003; Reilinger et al., 2006).

The westward motion of Anatolia was also interpreted as gravitational collapse of an overthickened crust (Seyitoglu and Scott, 1996; Dhont et al., 2006). Crustal thickness decreases considerably from ~ 40-50 km in east Anatolia (Zor et al., 2003; Gök et al., 2007) to less than

30 km in the Aegean (Tirel et al., 2004; Sodoudi et al., 2006; Zhu et al., 2006). An argument against this hypothesis as dominant mechanism is the increase of south components of GPS velocity vectors from north to south in the Aegean region, which is better explained by back-arc extension. The westward movement of the Anatolian Plate was also attributed to varying rates of convergence along the subduction zone between the African and Anatolian Plates leading to rapid south-westward movement of Greece relative to Anatolia (Doglioni et al., 2002).

Seismicity is concentrated at the Hellenic subduction zone with dominant thrust-faulting focal mechanisms and at major strike-slip faults such as the NAF and East Anatolian Fault (Fig. 1.4, Jackson, 1994; Türkelli et al., 2003; Taymaz et al., 2004). Increased seismicity also characterises the extensional provinces in western Anatolia and Greece, where normal faulting earthquakes prevail in a number of grabens in response to the Hellenic back-arc extension (Zanchi and Angelier, 1993; Hatzfeld et al., 1999; Kiratzi, 2002) and where high heat flow (Pfister et al., 1998) and pronounced dilation rates were inferred (Kahle et al., 2000; Allmendinger et al., 2007). Seismicity in the northern Aegean marks the continuation of the NAF in the Aegean with predominantly strike-slip faulting earthquakes (Taymaz et al., 1991). Seismicity in the southern part of the Aegean is comparably low consistent with geodetic observations that suggest that this region is not much deforming and can be regarded as a rigid plate of its own (Papazachos, 1999; Kreemer and Chamot-Rooke, 2004; Nyst and Thatcher, 2004). In central Anatolia seismicity is relatively low, which is also reflected by the largely rigid plate behaviour inferred from geodetic observations.

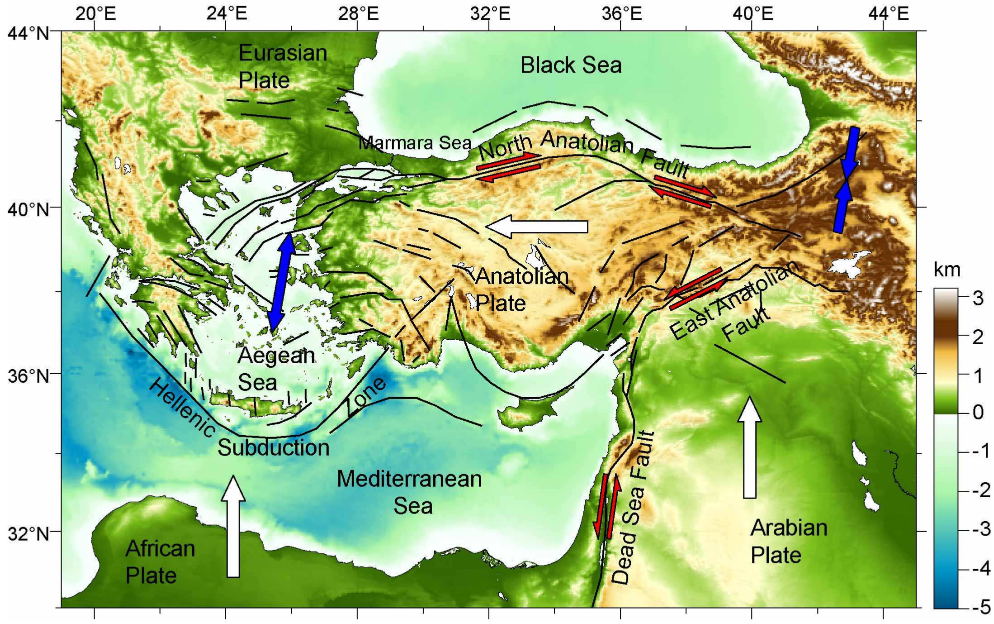

Fig. 1.2: Interaction between the plates in the eastern Mediterranean region indicated by plate motion directions relative to Eurasia (white arrows), deformation (blue double arrows) and sense of slip along major faults (red arrows). Faults are marked by black lines (Barka, 1992), colour contours indicate topography (GTOPO30) and bathymetry (ETOPO2).

The geological history of Anatolia is characterised by repeated collisions of continents and closure of ancient oceans (Şengör and Yılmaz, 1981; Bozkurt and Mittwede, 2001; Dilek and Pavlides, 2006; Robertson and Mountrakis, 2006). The remnants of the former oceanic basins are marked by several suture zones traversing Anatolia with exposed ophiolites (Robertson and Ustaömer, 2004). The NAF in northwest Anatolia follows the Intra-Pontide suture, which separates the Istanbul zone in the north from the Sakarya zone in the south (Elmas and Yiğitbaş, 2001; Okay et al., 2001b).

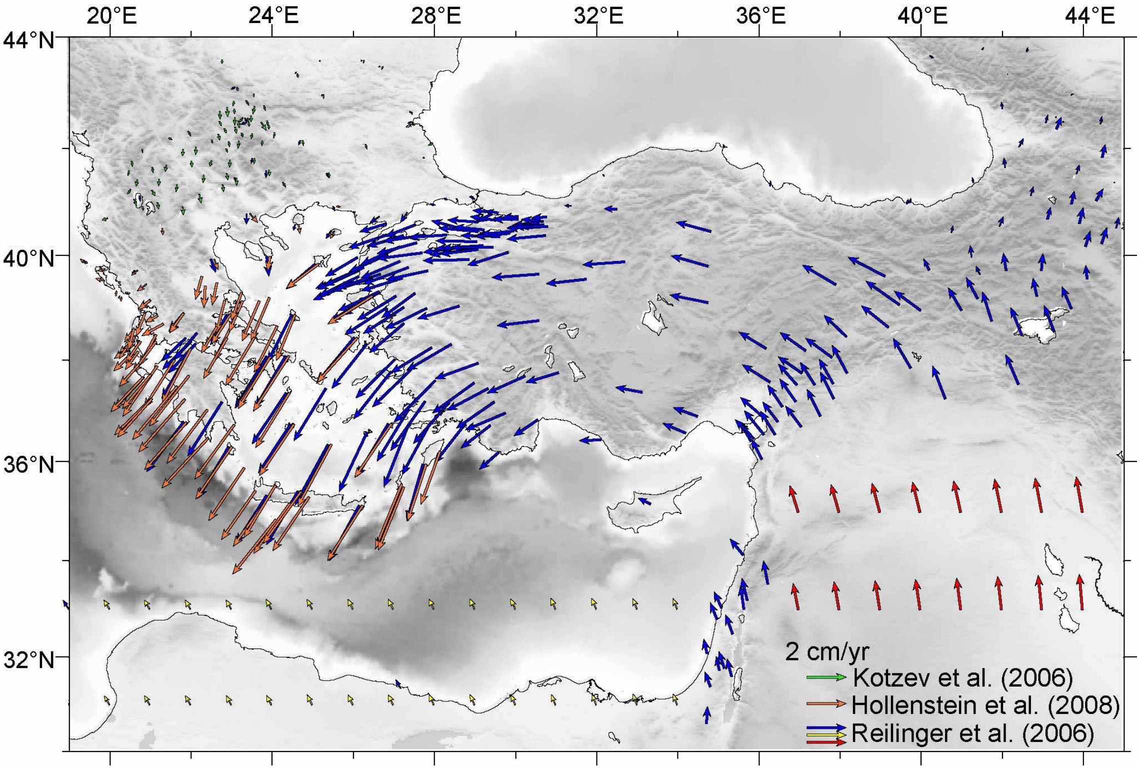

Fig. 1.3: GPS observations in the eastern Mediterranean region in a fixed European reference frame. Velocities of the Arabian and African Plates are from rotation rates around the Euler poles of the plates.

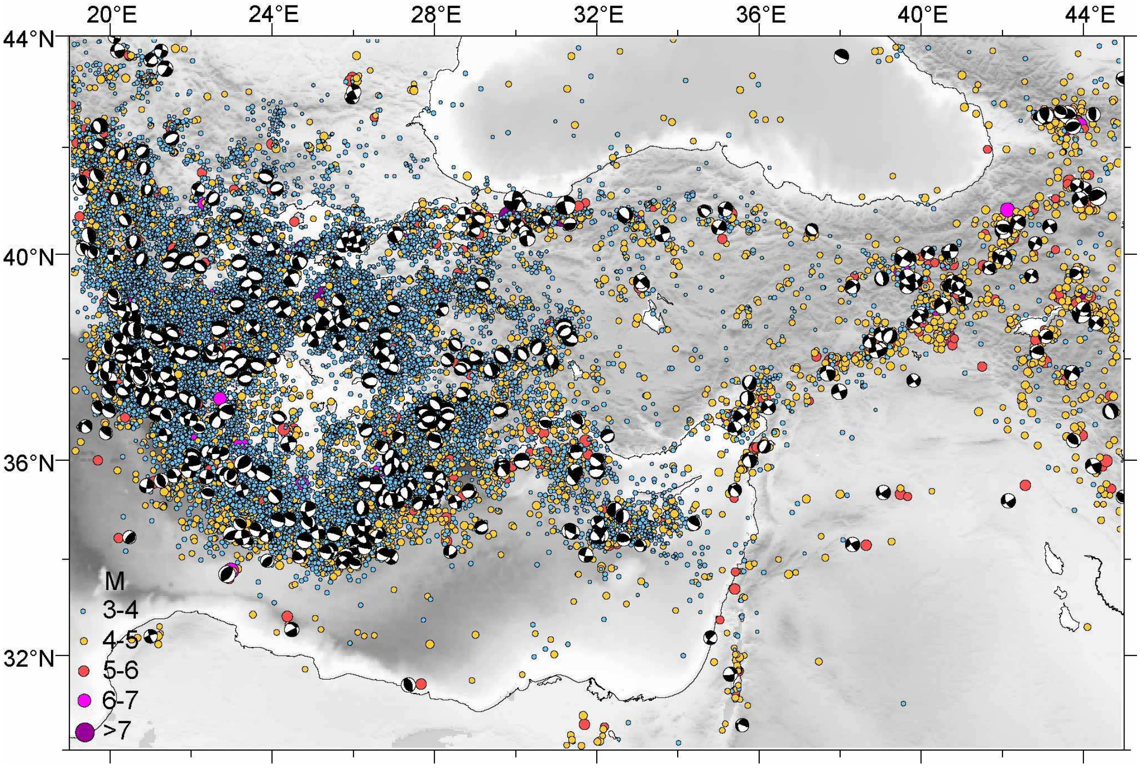

Fig. 1.4: Seismicity (M>3) between 1973 and 2007 (USGS-NEIC) and earthquake focal mechanisms from 1976-2007 (Harvard CMT) in the eastern Mediterranean region.

1.2.2 Marmara region

In northwest Anatolia the NAF splays into several branches (Barka and Kadinsky-Cade, 1988; Armijo et al., 1999) (Fig. 1.1; 1.5). The northern branch enters the Sea of Marmara at Izmit, runs beneath Izmit Bay (Alpar and Yaltırak, 2002; Cormier et al., 2006; Dolu et al., 2007) and passes the Sea of Marmara, therefore termed as the Main Marmara Fault (MMF). Further to the west it crosses Gelibolu Peninsula as Ganos Fault, enters the Gulf of Saros (Yaltırak et al., 1998; 2000) and traverses the Aegean Sea to Greece (Taymaz et al., 1991). The middle branch passes Iznik Lake, follows the southern shore of the Marmara Sea from Gemlik Bay to Kapıdağ Peninsula (Yaltırak and Alpar, 2002; Kurtuluş and Canbay, 2007), where it turns to SW. The southern branch forms the southern rim of the Bursa Graben and enters the Aegean south of Biga Peninsula. This branching was attributed to the influence of the extension associated with the Hellenic subduction zone and to the fact that the NAF increasingly deviates to the west from a small circle around the Euler Pole of the Anatolian Plate (Le Pichon et al., 2003), requiring extension. As a consequence, in northwest Anatolia deformation is distributed across a broader zone compared to central Anatolia. About 80% of the relative plate motion between the Anatolian and Eurasia Plates are commonly ascribed to the northern branch (Meade et al., 2002), which means a slip rate of ~20 mm/yr in case of total 24 mm/yr relative plate motion (McClusky et al., 2000).

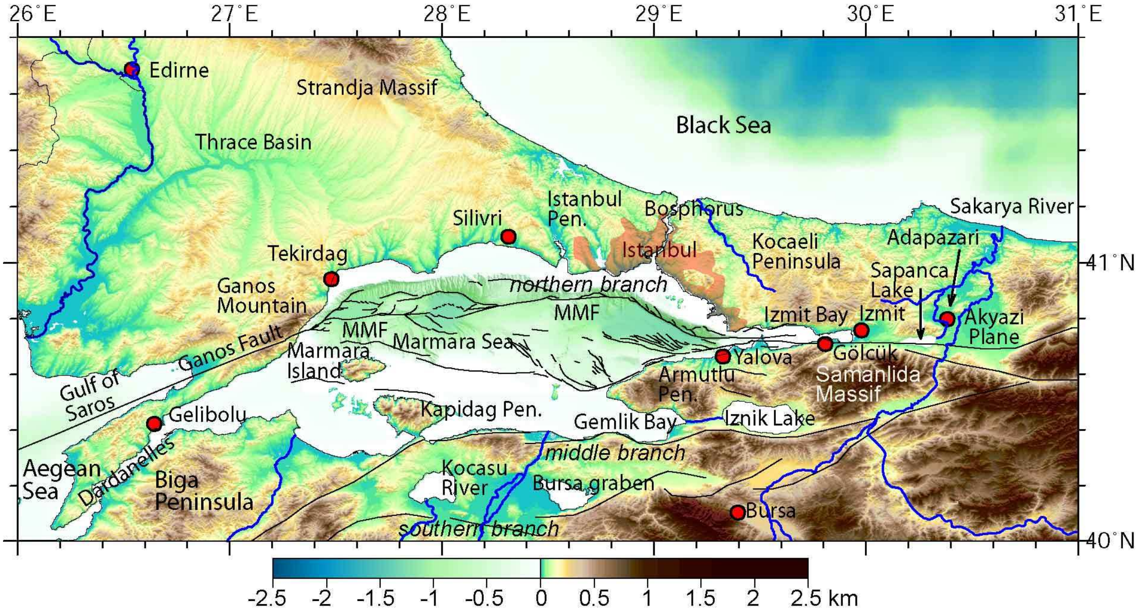

Fig. 1.5: Topography (GTOPO30), bathymetry (ETOPO2 and Ifremer), faults (Armijo et al., 2002), cities and names which will be referred to.

Following the 1999 Izmit earthquake numerous geophysical experiments were conducted to reveal the morphology of the Sea floor and the fault traces (Le Pichon et al., 2001; 2003; Armijo et al., 2002; Gökaşan et al., 2003), the subsurface structures using seismics (Wong et al., 1995; Okay et al., 1999; 2000; Aksu et al., 2000; İmren et al., 2001; Gökaşan et al., 2002; Parke et al., 2002; Demirbağ et al., 2003; Rangin et al., 2004; Carton et al., 2007; Kanbur et al., 2007; Laigle et al., 2008; Bécel et al., 2009), and the seismotectonics beneath in the Marmara Sea from microseismicity (Eyidoğan, 1988; Gurbuz et al., 2000; Örgülü and Aktar, 2001; Barış et al., 2002; Ito et al., 2002; Karabulut et al., 2002; Özalaybey et al., 2002; Polat et al., 2002a; Pınar et al., 2003; Aktar et al., 2004; Sato et al., 2004; Bohnhoff et al., 2006; Bulut and Aktar, 2007; Bulut et al., 2007).

The northern branch exhibits three major bends in the Marmara Sea. (1) The releasing bend at the western end of Izmit Bay (Tuzla Bend), (2) the bend SW of Istanbul (Istanbul Bend), and (3) the restraining bend at the western Tekirdağ Basin (Ganos Bend) (Fig. 1.6). The Prince’s Islands

Segment between the Tuzla Bend and the Istanbul Bend dips slightly to SW and follows the base of a major bathymetric scarp at the northern rim of the Çınarcık Basin that exceeds one kilometre in height. The Central Segment between Istanbul Bend and the Central Basin is rather straight and vertical. The Central Basin is bounded at its rims by outer and inner faults, which steeply dip towards the main branch. At the Ganos Bend the fault dips to the NW.

The North Marmara Trough is a distinct bathymetric depression along the northern branch of the NAF (Fig. 1.6) that comprises three major basins: (1) the Çınarcık Basin in the east, (2) the Central Basin in the middle and (3) the Tekirdağ Basin in the west. These are bounded or transected by the NAF and are up to ~1200 bsl. The basins are separated by the Central High and the Western High, respectively. Smaller basins are the Kumburgaz Basin at a minor stepover or restraining bend of the Central Segment and the Imralı Basin that is associated to a north dipping normal fault in the south of the Marmara Sea and almost filled by sediments. The basins are not only bathymetric depressions but are even more expressed in the basement topography since sediment thickness was inferred to exceed 5 km in the Çınarcık and Central Basins (Carton et al., 2007; Laigle et al., 2008). The shelf areas in the northern and southern Marmara Sea are of shallow water depths < 100 m (Ergin et al., 1997).

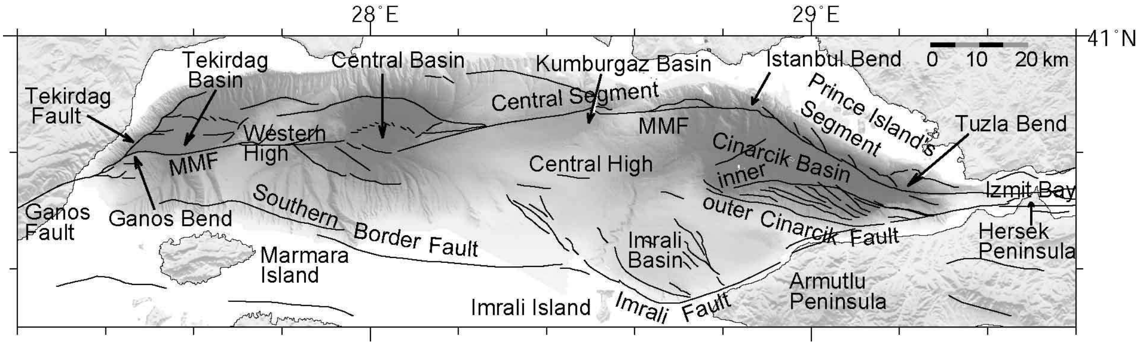

Fig. 1.6: Map of the North Marmara Trough with bathymetry (Ifremer) and faults (Armijo et al., 2002; Carton et al., 2007).

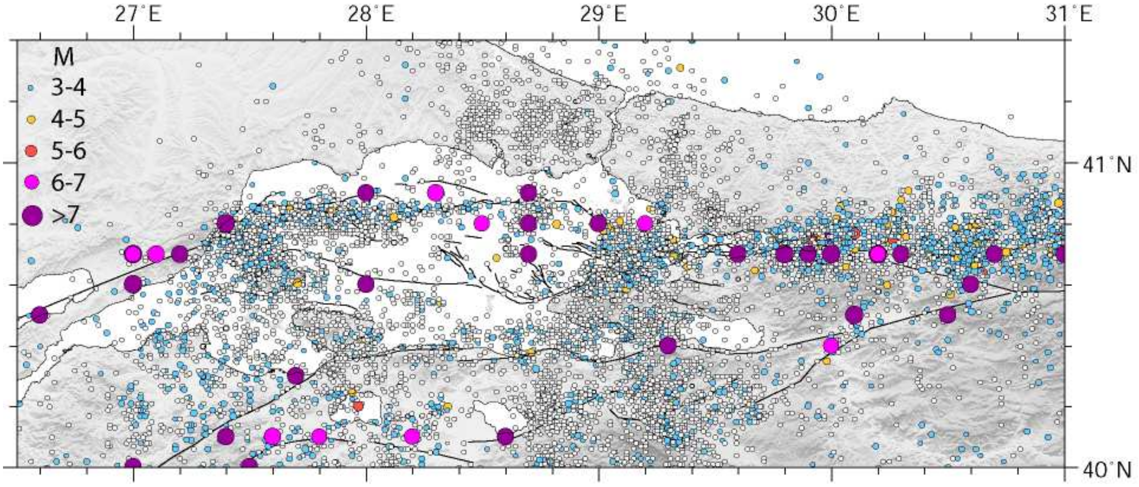

Fig. 1.7: Seismicity between 1990 and 2007 (Kandilli catalogue) and historical M>6.8 earthquakes during the last 2000 years (Ambraseys, 2002).

Seismicity is concentrated beneath the Central Basin, the Western High and to the south of the Tekirdağ Basin as well as in the area around Bursa and the easternmost Çınarcık Basin and on Armutlu Peninsula (Fig. 1.7). In contrast, the Central Segment, the Central High and the southern part of the North Marmara Trough are remarkably quiet. Epicentres of large historical earthquakes cumulate predominantly at the northern branch, suggesting that this is the more active branch as also indicated by geodetic observations (Straub et al., 1997). From a number of these also tsunamis are reported (Yalçıner et al., 2002).

Several tectonic models have been proposed for the Marmara Sea. It was interpreted as a system of pull-apart basins (Armijo et al., 2002), whereas others pointed out there was a pull-apart system, which is inactive now (Rangin et al., 2004). The view of a single through going pure strike-slip fault was contended based on the observation that focal mechanisms along the MMF show predominantly strike-slip faulting and that it comes close to a small circle around the Euler pole of a Marmara block, while extension is taken up in the eastern Çınarcık Basin by slip partitioning and by the southern strand of the NAF (Le Pichon et al., 2003). More recent interpretations assume the basins as asymmetric half grabens (McHugh et al., 2006) and the whole fault system of the Marmara region including the middle branch of the NAF as a large scale negative flower structure (Aksu et al., 2000; Koral, 2007; Laigle et al., 2008).

1.3 Seismic hazard assessment

This section briefly outlines the general workflow of seismic risk assessment and defines the role of seismic hazard assessment therein. Furthermore, it is explained how this work contributes to seismic hazard assessment (1.3.1). The commonly applied methodologies for assessing seismic hazard are summarised in 1.3.2, with emphasis on the Marmara region. Possible sources of uncertainty therein are identified in 1.3.3.

1.3.1 From seismic hazard to seismic risk

“In the framework of hazard and/or risk assessment studies, the hazard describes the probability of occurrence of a potentially destructive natural phenomenon in a defined area within a defined time period.” (Grünthal, 1984). Whereas seismic hazard addresses the occurrence of an earthquake, seismic risk describes the impact of a potential earthquake on human lives, buildings, infrastructure and economy.

Seismic risk assessment is of importance in earthquake-endangered megacities that experience rapid growth in population and take in a key role in the country’s economy. Favourably, knowledge of expectable damage could lead to mitigation of losses by planning of disaster management, preparedness programs for population and institutions, introduction of building codes and responsible city planning. For the city of Istanbul an earthquake master plan has been worked out with this purpose (IEMP, 2003). The quantification of loss potential is also important for both insurers and reinsurers.

The architecture of a seismic risk assessment typically consists of four inter-connected modules: the Hazard Module, the Exposure Module, the Vulnerability Module and the Financial Module (e.g. Bendimerad, 2001; Fig. 1.8). The Hazard Module provides information on the occurrence of earthquakes in space and time and their magnitude and associated expectable ground motions. The Exposure Module is a compilation of location, type, occupancy and value of properties. The Vulnerability Module consists of databases and algorithms for calculating damage quantities given a ground motion for the exposure (e.g. buildings, business interruption). Eventually, the Financial Module translates damage obtained in the Vulnerability Module into loss. An example for a seismic risk study is the CEDIM Megacities project focussing on the city of Istanbul, which was conducted by GeoForschungsZentrum Potsdam and University of Karlsruhe (http://www.cedim.de).

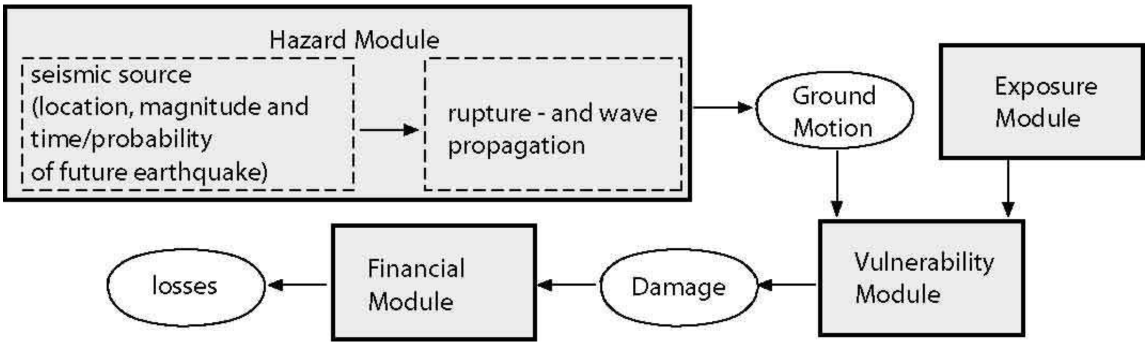

Fig. 1.8: Workflow for seismic risk assessment.

Within this framework this thesis deals with the Hazard Module (e.g. Frankel, 1995), that can be subdivided into two main parts (Fig. 1.8). The first one aims at estimation of magnitude and probability or time of a future earthquake in a given area. The second part provides a ground motion intensity parameter, mostly peak ground acceleration (PGA), at each site in the area of interest for a given earthquake. This can be done by using attenuation relations, which rely on data recorded during past earthquakes and relate ground motion to distance from the source for a given magnitude and can also account for site effects and potential liquefaction (Sadigh et al., 1997; Akinci et al., 2006; Bindi et al., 2006; 2007). Alternatively, rupture and wave propagation are modelled while taking spatial variations of seismic velocities, density and wave attenuation into account (Pulido et al., 2004; Goto et al., 2005; Sorensen et al., 2006). This thesis deals exclusively with the first part of the Hazard Module, i.e. up to the point of earthquake occurrence, and not with the subsequent effects of an earthquake on ground motion, damage and loss. Thus, if the term ´seismic hazard´ is used, only the first part is addressed.

1.3.2 Methods of seismic hazard assessment

In the following a summary is given on how the occurrence of earthquakes in space, time and their magnitude is commonly estimated. Most approaches in this respect rely on statistical evaluation of seismic catalogues. The simplest earthquake occurrence model is the Poisson Model, which assumes that earthquakes are temporally and spatially independent (Cornell, 1968). For the Poisson model commonly the Gutenberg-Richter magnitude-frequency relation (Richter, 1958) is used to define the recurrence time of an earthquake with specified magnitude. Preferably, the region of interest is subdivided in several areas of similar seismicity (Erdik et al., 1985; 1999; Koravos et al., 2003; Öncel and Wilson, 2006; Sayil and Osmansahin, 2008).

As large earthquakes are mostly confined to faults rather than being distributed over areas the concept of characteristic earthquakes was introduced (Schwartz and Coppersmith, 1984; Youngs and Coppersmith, 1985). It is assumed that a fault segment is repeatedly ruptured by a characteristic earthquake with certain magnitude and interevent time. Since conditional probability of a characteristic earthquake increases with elapsed time since the last event, this kind of earthquake occurrence is described by a time-dependent renewal model (McGuire, 1993) in narrow seismic zones that represent individual fault segments (Atakan et al., 2002; Erdik et al., 2004). Among the renewal models are the lognormal (Nishenko and Buland, 1987) and Brownian passage time (Matthews et al., 2002) probability density functions that distribute around some mean interevent time and account for variability on earthquake recurrence. The mean interevent time and its variability are either directly inferred by exploiting seismic catalogues (Parsons, 2004) or they are determined based on fault slip rates. One possibility is to divide coseismic slip of past earthquakes by the slip rate on a fault (Parsons et al., 2000; Erdik et al., 2004). Another possibility is to replace the recurrence rate by an annual activity rate of characteristic earthquakes that is defined by the ratio of the annual seismic moment to the seismic moment of a characteristic earthquake, where the annual seismic moment is determined by the fault slip rate (Kalkan et al., 2008). The pertaining data for the magnitude of characteristic earthquakes, coseismic slip, fault slip rates, mean interevent times and elapsed time since the last earthquake in the Marmara Sea region come from earthquake catalogues (Ambraseys, 2002; Öncel and Wilson, 2006), surface rupture measurements (Barka, 1996; Altunel et al., 2004), paleoseismological analyses (Rockwell et al., 2001; Klinger et al., 2003), geodetic observations (Straub et al., 1997; Ayhan et al., 2002; Le Pichon and Kreemer, 2005; Reilinger et al., 2006), geological investigations (Armijo et al., 1999), dating of soil specimens marking fault-related offsets or originating from earthquake-interrupted sedimentary layers (Polonia et al., 2004; McHugh et al., 2006), and considerations on fault segmentation (Barka and Kadinsky-Cade, 1988; Pondard et al., 2007). As expectable, the results of a renewal model significantly differ from those of the Poisson model (Parsons et al., 2000; Atakan et al., 2002; Erdik et al., 2004).

The pattern of the recent earthquakes along the NAF in space and time gave rise to consider a possible correlation between them. However, earthquake triggering and fault interactions are not considered in standard probabilistic descriptions of earthquake occurrence. During the last decade quantification of static stress changes on a fault due to a nearby earthquake became established with the concept of Coulomb Failure Stress (CFS) changes introduced by King et al. (1994). It is based on the Coulomb failure criterion that relates the shear stress τ necessary to overcome the resistive forces determined by the normal stress σ_n on the fault, its friction coefficient μ and cohesion C_0 (Jaeger and Cook, 1969):

$$\tau = \mu(\sigma_n - P_f) + C_0 \qquad (1.1)$$

The pore fluid pressure P_f reduces the normal stress on the fault. CFS changes due to a nearby earthquake and tectonic loading are calculated on fault segments as

$$\Delta CFS = \Delta\tau + \mu' \Delta\sigma_n \qquad (1.2)$$

where $\Delta\tau$ and $\Delta\sigma_n$ are the changes of shear stress and normal stress on a fault, respectively. In ΔCFS studies mostly an effective coefficient of friction μ' is used, which accounts for pore fluid pressure (eq. 3.1; e.g. Lorenzo-Martin et al., 2006). Positive values of ΔCFS indicate that the considered fault is brought closer towards failure, negative the contrary. Hence, the ΔCFS concept is a valuable tool to state increased or decreased hazard on a fault due to a near earthquake. A range of ΔCFS analyses were performed focussing on the NAF (Stein et al., 1997; Muller et al., 2003; Lorenzo-Martin et al., 2006), including the Marmara Sea region (Nalbant et al., 1998; Hubert-Ferrari et al., 2000; Parsons et al., 2000; Çakir et al., 2003a; Pondard et al., 2007), which brought about that almost all earthquakes of the sequence occurred on fault segments, that previously experienced an increase in CFS due to the earthquakes before and that the 1999 Izmit earthquake increased CFS on faults beneath the Marmara Sea.

The principle problem with the concept of CFS changes is that it provides no direct information on what stress changes mean in terms of probability changes of future earthquakes, unless additional information on earthquake recurrence rates and fault slip rates is available. This is illustrated in Fig. 1.9. Yet a small stress change would be sufficient to trigger an earthquake, if the respective fault is close to failure, whereas even a large stress change will not cause an earthquake if the fault is far from the critical stress state. In order to incorporate stress changes into probability calculations either a temporal advance or delay in the seismic cycle (‘clock change’) is performed or an adjustment of the recurrence interval by adding the clock change to it (Parsons, 2005). For calculation of the time shift corresponding to a stress change, knowledge of annual stressing rates on a fault are required. The stressing rates are mostly modelled by imposing slip on the faults below the locking depth at rates deduced from geodetic observations. Additionally, recurrence rates of earthquakes are required in order to establish a link between change in time till the next earthquake and probability change. When considering stress transfer, Parsons (2004) found an increase of earthquake probability in the Marmara Sea by 10 % and more (Parsons, 2005). The probability of a M>7 earthquake in the Sea of Marmara within the next 30 years was reported as 62 % (Parsons, 2004).

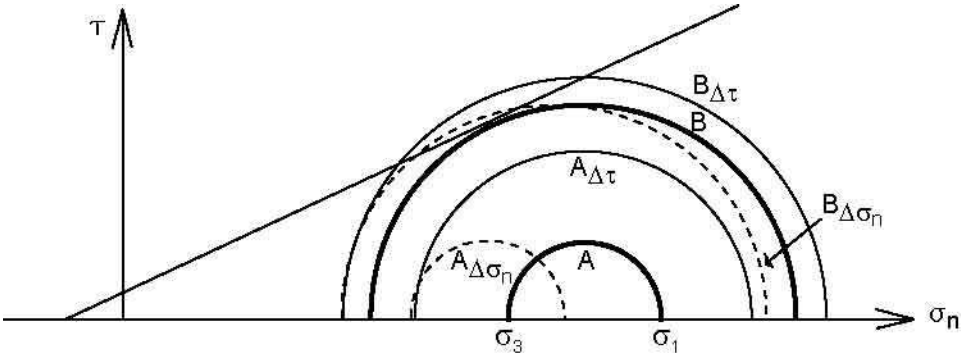

Fig. 1.9: Mohr cycles indicating the state of stress on a fault prior to an earthquake (bold lines A and B), and after an earthquake with increase in shear stress (thin lines) or decrease in normal stress (dashed lines). Note, that in case A even a large coseismic stress change does not lead to failure, whereas in case B a small stress change causes slip on the fault.

These are the most widely used methods to estimate seismic hazard. Apart from these there were other methods applied in the Marmara region, that mainly differ by their way on how to deduce information from seismic catalogues, e.g. by computing cumulative seismic moment (Cisternas et al., 2004), cumulative Benioff strain (Karakaisis et al., 2004) or multifractal dimensions in predefined areas (Öncel and Wilson, 2004; 2006).

Estimation of earthquake size

A first order approximation of the size of an earthquake on a given fault segment (characteristic earthquake) can be made using the analytical solution that exists for simple fault geometries (Kanamori and Andersen, 1975). The stress drop $\Delta\sigma$ is related to mean slip u by

$$\Delta\sigma = C\mu \frac{u}{L'}, \tag{1.3}$$

which is essentially Hooke's Law, where L' is a characteristic rupture dimension, u/L' the strain change, μ shear modulus and C a geometry factor. In case of a circular fault, L' is the radius of the fault and $C = 7\pi/16$. For a "rectangular" strike-slip fault of infinite length, L' = W, where W is fault width, and $C = 2/\pi$. Assuming a value for $\Delta\sigma$, which is typically about 3 MPa for interplate earthquakes (Kanamori and Andersen, 1975), and taking μ ~ 30 GPa, the mean slip can be calculated, that in turn can be used to find the corresponding seismic moment

$$M_0 = \mu\ A\ u, \tag{1.4}$$

where A is the fault area. The moment magnitude M_w (Hanks and Kanamori, 1979) is given by

$$M_w = \frac{2}{3}\log(M_0) - 6.0\,. \tag{1.5}$$

The expectable size of an earthquake can be also estimated from intensities of historical earthquakes using attenuation relations (e.g. Parsons, 2004) or from empirical scaling relations linking source dimensions to slip and seismic moment based on compilations of observed earthquakes (e.g., Wells and Coppersmith, 1994).

1.3.3 Sources of uncertainty in current seismic hazard assessment

Of course, the probabilistic standard approach for seismic hazard assessment following the concept of temporally and spatially equally distributed small to intermediate seismicity and characteristic high-magnitude earthquakes on particular fault segments, as described in 1.3.2, is a well established methodology for several good reasons. It allows mapping of expectable ground motion over arbitrary large areas and for any time period and is principally possible with moderate effort, provided a seismic catalogue is available (Kagan and Jackson, 1994; Giardini, 1999). In particular, the long-term behaviour of seismicity should be well reflected by this kind of approach. With the incorporation of CFS changes also short-term effects and part of the physical background of earthquakes become represented in earthquake probability calculations.

While methodology itself is approved, results depend on the data behind. In other words, “a probabilistic hazard analysis is no better than the earthquake catalogue on which it is based.” (Parsons et al., 2000). This concerns in particular the basis and starting point of probability calculations of earthquake occurrence, which is the mean recurrence rate of characteristic earthquakes (e.g. Atakan et al., 2002; Parsons, 2004) or fault slip rates (e.g., Kalkan et al., 2008; in press) or both (e.g., Parsons et al., 2000; Erdik et al., 2004). Another issue are adopted fault segmentation and geometry that affect estimations of earthquake occurrence.

(1) Recurrence rates of characteristic earthquakes

The variability of the mean interevent time that defines the width of the probability density function, strongly influences and reduces precision of resulting probabilities (Parsons, 2004). Although for the Marmara region a wealth of seismicity data is available including probably all major earthquakes during the last 2000 years (Ambraseys, 2002), it is nevertheless difficult to assign mean recurrence rates to individual fault segments with appropriate precision. This lead Parsons et al. (2000) to the statement that “No catalogue is adequate to estimate the coefficient of variation of the interevent time”, despite the long and detailed seismic record that is available for the Marmara Sea region.

One reason for the difficulty to determine mean recurrence rates of characteristic earthquakes in the Marmara Sea is related to the localisation of historical earthquakes that is hampered by several factors. The offshore origin of earthquakes complicates their localisation that is generally based on intensity distributions onshore which in turn is dependend on the distribution of settlements. There is reason to assume that ground motion in the Marmara Sea does not exclusively depend on distance to the source but that there is laterally anisotropic wave propagation and that site effects obliterate a clear localisation. Therefore, even systematic mislocations of historical earthquakes are possible that will be discussed in more detail in 5.2.1.

Another issue in the context of earthquake recurrence rates is the complexity of the fault system of the NAF beneath the Sea of Marmara that is characterised by several fault strands that exhibit bends, various dips and are oriented in both a releasing or restraining sense with respect to plate motion. Due to the various interconnections within a complex structural setting, patterns of high-magnitude seismicity in time and space must not necessarily repeat in a similar manner in the next seismic cycle compared to the previous ones.

The consequence of uncertainties in localisation and interconnections within a deforming fault system is that one cannot discern what recurrence rates and what aperiodicities are, in particular, if only a few earthquakes are used. Parsons (2005) showed that “an earthquake history that is well characterised by paleoseismic and historical observation can be fit with a broad range of interevent time and aperiodicity models, all with about equal choice of being correct.”

Resulting probabilities not only depend on the available data base but also on conceptual assumptions related to recurrence rates. Sornette and Knopoff (1997) found “statistical estimates of recurrence times … to be very sensitive to assumptions about statistical distributions" i.e. choice of the probability density function (Parsons, 2005). Resulting probabilities also depend on whether coseismic stress changes are incorporated into probability calculations by time shift or change in mean interevent time (1.3.2; Parsons, 2005).

(2) Fault slip rates

A crucial issue for seismic hazard assessment are fault slip rates, that become relevant, i) if used to estimate earthquake recurrence rates by assuming typical coseismic slip (Parsons et al., 2000; Erdik et al., 2004), ii) if used to quantify annual occurrence rates of characteristic earthquakes for a given fault segment and magnitude (Kalkan et al., 2008), iii) if used to infer annual stressing rates on a fault in order to transfer coseismic stress changes into probability changes (1.3.2) (Parsons et al., 2000), which is commonly done by imposing slip at that rate on the fault in numerical models (Hubert-Ferrari et al., 2000; Lorentzo-Martin et al., 2006) or iv) if used to estimate potential coseismic slip and hence magnitude of an earthquake, based on the elapsed time since the last earthquake (Hubert-Ferrari et al., 2000; Pınar et al., 2003; Armijo et al., 2005). For these purposes mostly reported geodetic slip rates are employed. At this point two issues have to be put forward. i) It is not straightforward to deduce fault slip rates from geodetic observations. Assumptions such as fault geometry, coefficient of friction, stiffness of the blocks moving relative to each other and locking depth are required that can significantly influence the result. ii) It is largely unknown how exactly total relative plate motion is partitioned on the respective fault strands in the Marmara Sea due to the inaccessibility of the sea by geodetic observations.

(3) Fault geometry and segmentation

Accounting for the renewal of characteristic earthquakes requires definition of narrow zones representing the respective fault segments of characteristic earthquakes. Atakan et al. (2002) found that their inferred probabilities for earthquake occurrence and ground motion are sensitive to and considerably affected by their anticipated fault geometry and fault segmentation. Kalkan et al. (2008) explained that e.g. assuming several smaller segments instead of a few large ones will result at a given fault slip rate in smaller but more frequent earthquakes. Concerning ΔCFS studies, there are numerous examples showing that resulting stress changes are strongly influenced by the geometry of both the fault experiencing an earthquake and the receiver fault (e.g., Muller and Aydin, 2004; Cianetti et al., 2005). For instance, Parsons (2005) found variations of 40-50% in ΔCFS when varying the dip of the receiver fault within reasonable ranges. Mostly, only the first-order features of the fault geometry were considered. Apart from Parsons (2004) faults were generally implemented as plane segments without any curvatures. Apart from Muller et al. (2006) faults were implemented uniformly vertically. Accuracy of the fault geometry is also important for proper annual stressing rates on the faults.

It is necessary to point out that the issue of finding precise recurrence rates or fault slip rates as well as the question of how to implement the fault geometry or where to adopt the terminations of characteristic earthquakes is not a shortcoming of the methodology but merely a practical matter involving assumptions. It is here, where this thesis starts. It contributes to a comprehension of the seismotectonic framework and recurrence rates in the Marmara region, provides fault slip rates and gives indications for likely rupture lengths. Moreover, the seismic moment of a future potential earthquake on a given fault segment of the MMF is quantified dependent on time by modelling coseismic slip from the accumulated stress at that time.

In chapter 2 a concept for a numerical model of the crustal strain and *in situ* stress state will be presented. This concept is dedicated to avoid the previously identified sources of uncertainty and opens new possibilities in quantitative estimation of future earthquake source parameters.

Chapter 2

Model concept

Within this chapter a conceptual framework is presented that permits simultaneous modelling of both the velocity and absolute stress field. As will be explained, this can be used as a basis for estimation of the size of a future earthquake as well as for framing its time of occurrence. At first, it is explained how to address the sources of uncertainty in common analyses of seismic hazard (2.1). In 2.2 the equations to be solved are given and 2.3 lists a number of simplifying assumptions. Finally, 2.4 gives an outline of this thesis by explaining what is done in the respective chapters.

2.1 Innovations

Resuming the sources of uncertainty in seismic hazard assessment in the Marmara region, as identified in 1.3.3, a concept is proposed in this chapter, that is intended to account for these uncertainties or to bypass them. The approach employs elaborate initial stress conditions and the sub-modelling technique that are briefly introduced. After outlining the concept, it will be briefly discussed.

(1) As concluded in 1.3.3 the mean recurrence time of characteristic earthquakes on single fault segments and its variability is a major cause of uncertainty in earthquake probabilities. Therefore, it should be aspired to become independent of both the mean recurrence time and its variability.

Within this thesis, a way of estimating size and time of a future earthquake is proposed. It does neither require *a priori* information on earthquake recurrence rates nor on fault slip rates. It is based on the absolute stress state whose time-dependency on a locked fault is modelled during the interseismic period. The size of a potential earthquake on a fault segment at some time is estimated by modelling a testing earthquake at that time on the fault segment under consideration, by releasing the accumulated shear stress according to elastic rebound theory. The state of the fault segment within its seismic cycle at that time is estimated by the ratio of modelled seismic moment to seismic moment from scaling relations for the same rupture length. Expected earthquake occurrence is estimated by extrapolation using the elapsed time since the last event or better by modelling testing earthquakes at different times until the ratio approaches one.

Though the occurrence time can be estimated only at a limited precision due to the standard deviations of empirical scaling relations, the absolute stress state may provide further possibilities for framing the time of earthquake occurrence, e.g. by employing the stress state on the fault directly. With absolute stress, the Mohr cycle indicative of the differential stresses is no longer unknown as in common ΔCFS studies (Fig. 1.9). Given rock strength parameters within a failure criterion are available, that may be deducible from laboratory measurements, the temporal evolution of absolute stress can be controlled with respect to this critical stress state. Or monitoring of the increase of shear stress during the interseismic period with respect to residual stress may reveal when a stress increase corresponding to a typical coseismic stress drop is reached.

(2) A thorough assessment of strain partitioning across the Marmara Sea is required in order to unravel how interseismic strain is accumulated across the fault system. This task is related to quantification of fault slip rates in the steady-state case. Slip rates have to be inferred not by

geometrically interpolating geodetic observations, but instead by a physical interpolation that considers the discontinuities in the velocity field due to the various faults as well as deformation of the material in between. The common technique with numerical models is to impose secular slip in-plane on the faults at depth. Instead, in this thesis secular fault slip evolves freely in response to stress exerted by the plate tectonic stresses. This is ensured by applying remote regional velocity boundary conditions exterior of the Marmara Sea using the sub-modelling technique. Through this, the faults experience releasing or restraining influence dependent on their orientation with respect to plate motion. Therefore, resulting slip rates reflect the prevalent dynamics.

(3) For the reasons discussed in 1.3.3, emphasis has to be put on the fault geometry that will be used to model the evolution of stress and strain in the Marmara region. In particular, the fault geometry is important since it affects the stress and strain around a fault, and also the resolved stress on a fault is dependent on its geometry. Therefore, thorough study of fault maps and seismic sections is necessary to obtain a sophisticated 3D representation of the fault system beneath the Marmara Sea.

The approach of simultaneously modelling the velocity and absolute stress field relies on two basic components, the sub-modelling technique and initial stress conditions, that are briefly described below.

Sub-modelling technique

The model representing a volume of the Earth's crust is driven laterally at its sides by applying velocity boundary conditions. Sub-modelling means, that the boundary conditions prescribed for the model of interest come from a larger model that encompasses the smaller one. This technique ensures that velocities at the boundaries of the inner model are physically meaningful since they account for local inhomogeneities, faults, etc. in the surrounding. For the larger model rather simple boundary conditions can be found, e.g. the Euler rotations of the involved plates. More details on that are explained in 3.6.

There are two valuable advantages of driving the model from outside. First, it enables an independent evolution of fault slip, consistent with stress as aspired in (4). Second, unlike imposing slip in plane on a fault, driving the model externally permits that resulting shear and normal stresses on the fault reflect local deviations between fault strike and plate motion. Therefore, interaction between driving stresses and fault slip, that in turn generates perturbations in the stress field, is allowed as desired in (1).

Initial stress conditions

Gravity and application of displacement boundary conditions in a geomechanical model require an initial stress field within the volume under consideration in order to ensure a meaningful stress state. This will be explained in more detail in 3.5. Whereas vertical stress can be approximated by the load of the overlying rock mass, horizontal stress is difficult to determine. Here, a theoretical stress path proposed by Sheorey (1994) was adopted that is widely confirmed by stress magnitude measurements. As will be shown, appropriate initial stress conditions are of key importance in any attempt to model absolute stresses (4.2.4).

Brief discussion of the concept

The approach applied in this thesis prefers and attempts to consider the physical background of earthquakes, which is basically the elastic rebound of crustal blocks after exceeding a critical level of stress on a previously tectonically loaded fault.

With regard to the future and with regard to an increase of precision and reliability of seismic hazard assessment there will be no alternative to integrating more physics (or physics at all) in calculations than to date. This is more and more recognised as statements such as the following show. Knopoff (1999) noted: "’What is an earthquake? What determines its size, and why is it likely to occur where and when it does?’ These are physics questions; they are not likely to be solved by statistically unsubstantiable means. We have so far been unsuccessful at prediction because laboratory and theoretical studies of the physics of deformation and fracture have been largely unsupported. The problem is not simple; however, that does not mean it is insoluble.” He further pointed out that “Powerful high-speed computers are needed for high resolution 3D models of stress and deformation patterns in complex communicating fault systems for improved hazard and risk simulation" (Fuchs, 2009). In an outlook for future efforts to be undertaken in earthquake research in Turkey Inan et al. (2007) stated that “realistic countrywide estimates of earthquake risk require mapping active faults, determining the strain accumulation and stress build-up as a function of space and time on these faults … and better understanding the interaction between adjacent active fault segments.”

Speaking with the words of Burdick (1964) (in Fuchs, 2009): “Of course, things are complicated - But in the end every situation can be reduced to a simple question: Do we act or not?” This thesis is dedicated to quantitatively contribute to and qualitatively gain insight into the seismic hazard of the Marmara region on a physical basis. This does, however, not imply that the presented approach for assessing size and time of a future earthquake will yield better results than the probabilities for earthquake occurrence from the standard approach. In some sense, one uncertainty is replaced by another uncertainty, since empirical scaling relations and fault strength parameters are afflicted with uncertainties as earthquake recurrence rates are. Therefore, precision of inferred occurrence times of future earthquakes will be only in the order of decades. Nevertheless, it is an alternative concept that may be valuable in particular in regions like the Marmara Sea, that are characterised by a complicated fault system in a submarine environment, where both recurrence rates and fault slip rates are not easily inferable. Importantly, fault slip rates can be quantified consistent with stress, while accounting for deformation in a 3D fault system including second order faults. Though the time of earthquake occurrence remains uncertain within decades, the approach is nevertheless capable of quantifying time-dependent potential coseismic slip and seismic moment in the Sea of Marmara based on the accumulated stress at the considered time. Furthermore, focussing on the evolution of stress and strain and the interplay of faults and motion within the complex tectonic setting of the Marmara Sea broadens comprehension of the governing processes acting across this plate boundary zone and helps to interpret many observations. Not at last, it enables qualitative insights into earthquake related issues, e.g. type of faulting or variations of earthquake recurrence rates along a fault.

There is room to integrate probabilistic components into this approach in view of the variability of input parameters by performing parameter studies or by applying statistical techniques in assessing the reliability of presumptions concerning failure on a fault (Uribe-Carvajal and Nyland, 1985; Haldar and Mahadevan, 2000). Of course, parts of the results can be also integrated into the probabilistic standard approach, e.g. by applying the deduced fault slip rates in the framework of Erdik et al. (2004) or Kalkan et al. (2008).

A requirement for modelling the absolute stress and strain field is that the region of interest is amply investigated by various geoscientific methods to build upon this input data and to control the model results with respect to their reasonableness. The various campaigns and surveys for imaging structures and measuring kinematic and dynamic constraints at the surface and subsurface during the last decade provide information for both model input and model validation.

2.2 Conservation of moment and moment of momentum

Within this section the governing equations of the performed stress-displacement analysis are given.

Consider a volume V (Fig. 2.1) of arbitrary shape within a larger volume under consideration. Conservation of moment requires that the traction forces $\vec{t}$ (force per unit area) acting on every point on its surface S and the body forces $\vec{f}$ (force per unit volume) within V sum to zero:

$$\int_S t_i dS + \int_V f_i dV = 0 \tag{2.1}$$

From conservation of moment also the definition of the Cauchy stress vector follows that states that the internal stresses are given by the surface tractions on S

$$t_i = \sigma_{ij} \cdot n_j , \tag{2.2}$$

where $\vec{n}$ is the outer normal unit vector on S at that point and

$$\sigma_{ij} = \begin{pmatrix} \sigma_{11} & \sigma_{12} & \sigma_{13} \\ \sigma_{21} & \sigma_{22} & \sigma_{23} \\ \sigma_{31} & \sigma_{32} & \sigma_{33} \end{pmatrix}$$

the Cauchy stress tensor. Applying eq. (2.2) and Gauss's theorem for the surface integral in eq. (2.1) yields

$$\int_S \sigma_{ij} \cdot n_j dS = \int_V \frac{\partial}{\partial x_j} \sigma_{ij} dV . \tag{2.3}$$

Comparison of equations (2.1) and (2.3) gives

$$\frac{\partial}{\partial x_j} \sigma_{ij} + f_i = 0 , \tag{2.4}$$

which are the three partial differential equations of moment conservation in a continuum in the static case.

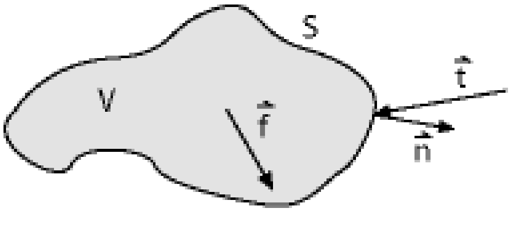

Fig. 2.1: Volume V that experiences traction forces $\vec{t}$ *at its surface S and body forces* $\vec{f}$ *in its interior.*

Conservation of moment of momentum requires that the summation of moments of momentum with respect to an arbitrary point is zero, in case of the origin:

$$\overrightarrow{M_0} = \int_S (\vec{r} \times \vec{t}) dS + \int_V (\vec{r} \times \vec{f}) dV = 0,$$

which leads to the conclusion that the stress tensor is symmetric, i.e.

$$\sigma_{ij} = \sigma_{ji}.$$

This means that the stress tensor has only six independent components. In turn, assumption of the stress tensor being symmetric implies that conservation of moment of momentum is automatically fulfilled.

The equations of conservation of moment (2.4) can be expressed in terms of displacements using the stress-strain and strain-displacement relations (Jaeger and Cook, 1969, p.111). The displacements u_i are determined by the strain-displacement relations

$$\varepsilon_{ij} = \frac{1}{2}\left(\frac{\partial u_j}{\partial x_i} + \frac{\partial u_i}{\partial x_j} \right) \tag{2.5}$$

where ε_{ij} is the strain tensor with six independent components.

Stress is related to strain by the constitutive equations. Via the constitutive relations the properties of the material come into the equations of conservation (2.4). In the linear elastic case Hooke's law

$$\sigma_{ij} = C_{ijkl}\varepsilon_{kl}, \tag{2.6}$$

describes the stress-strain relations, where C_{ijkl} is the elasticity tensor. In the isotropic and homogeneous case, the elasticity tensor is defined by two independent parameters

$$C_{ijkl} = \lambda\delta_{ij}\delta_{kl} + \mu\left(\delta_{ik}\delta_{jl} + \delta_{il}\delta_{jk}\right) \tag{2.7}$$

where λ is Lamé's constant and μ shear modulus, so that eq. (2.6) becomes

$$\sigma_{ij} = \lambda\delta_{ij}\varepsilon_{kk} + 2\mu\varepsilon_{ij} \tag{2.8}$$

Alternatively, eq. (2.8) can be written in terms of Young's modulus E and Poisson's ratio ν that are linked to λ and μ by the relations

$$\lambda = \frac{\nu E}{(1+\nu)(1-2\nu)} \quad \text{and} \tag{2.9}$$

$$\mu = \frac{E}{2(1+\nu)}. \tag{2.10}$$

The conservation equations together with the constitutive equations and strain-displacement relations fully describe the way, in which stresses and displacements vary in the interior of the volume. Therefore, an elasto-static boundary value problem for an isotropic homogeneous medium is a system of 15 independent equations and equal number of unknowns (three conservations equations, six constitutive equations and six strain-displacement equations).

Depending on whether the boundary conditions of the boundary value problem are prescribed in terms of stresses or displacements, the problem is written as stress formulation or displacement formulation. With prescribed displacement boundary conditions the conservation equations are formulated in terms of displacements. In the isotropic homogeneous case, the stresses are given and eliminated by the constitutive relations (2.8). Replacing the strains by displacements using eq. (2.5) gives

$$\sigma_{ij} = \lambda\delta_{ij}\frac{\partial u_k}{\partial x_k} + \mu\left(\frac{\partial u_j}{\partial x_i} + \frac{\partial u_i}{\partial x_j}\right) \tag{2.11}$$

Differentiating eq. (2.11) yields

$$\frac{\partial\sigma_{ij}}{\partial x_j} = \lambda\frac{\partial^2 u_k}{\partial x_k \partial x_i} + \mu\left(\frac{\partial^2 u_j}{\partial x_i \partial x_j} + \frac{\partial^2 u_i}{\partial x_j{}^2}\right) \tag{2.12}$$

Inserting eq. (2.12) into eq. (2.4) and regrouping gives

$$(\lambda+\mu)\nabla\left(\nabla\cdot\vec{u}\right) + \mu\nabla^2\vec{u} + \vec{f} = 0 \tag{2.13}$$

which are the Navier-Cauchy equations that give the conservation equations in terms of displacements. Once the displacement field is calculated, the strains are given by eq. (2.5) and these can be inserted into the constitutive equations to solve for stresses.

Besides linear elasticity expressed by Hooke’s law there are other constitutive relations that describe e.g. plastic or viscous material behaviour. These stress-strain relations involve further material parameters and non-linearities can appear, e.g. in case of temperature driven dislocation creep that is described by

$$\dot{\varepsilon} = A\sigma^n e^{-Q/RT}$$

where $\dot{\varepsilon}$ and σ denote the second invariants of the deviatoric stress and strain-rate tensors, respectively, A, n and Q (activation enthalpy) are material parameters, R is gas constant and T is temperature (e.g., Tsenn and Carter, 1987).

Equations (2.4) describe the static case which is a special case of the time-dependent equations of motion

$$\frac{\partial}{\partial x_j}\sigma_{ij} + f_i = \rho\frac{\partial^2 u_i}{\partial t^2}, \tag{2.14}$$

where t is time and ρ density.

In case of a tectonic system, the following types of mechanical forces can be found that control its dynamic evolution (e.g. Ramberg, 1981). The first term on the left hand side of eq. 2.14 can be associated with

i) Stresses that act at the boundaries of the considered volume. These stresses are transmitted through the interior of the volume in a manner controlled by the geometric pattern within the volume, by the mechanical properties of the rock and by the acting body forces.

ii) Internal stresses within the volume due to elastic strain and viscous drag. These stresses can be understood as response of the volume to external stresses. Local imbalance between the surface stresses and the body force of gravity causes relative motions within the volume, that act to readjust the unstable mass distribution in the field of gravity.

iii) other internal stresses as stresses due to volume change (e.g. by phase change, melting, thermal expansion) or fracturing.

The second term on the left hand side of eq. (2.14) denotes the body force of gravity that acts on every material particle in the volume. The term on the right hand side in (2.14) denotes inertial forces of accelerated masses.

Provided, the boundary conditions are specified, the boundary value problem is completely defined and theoretically, an exact analytical solution for the set of conservation equations in the whole volume can be found. However, practically this is not feasible due to the complexity of the problem, which primarily arises from the geometry. Therefore, the exact continuum conservation equations are approximated at a finite number of points within the volume and averaged between them. For this purpose, equations (2.4) are rewritten as the virtual work statement, which is the basis for application of the finite element method (App. 1). The numerical problem was solved using the commercial finite element software package ABAQUS^{TM}.

2.3 Assumptions

In the course of modelling the geodynamics of the Marmara Sea region a number of assumptions are made that are either brought about by lacking knowledge of actual material and state properties at depth or because they can be assumed to be negligible compared to uncertainties in other sources of stress.

The sources of stress mentioned under iii) in 2.2. as stresses due phase changes and thermal stresses due to temperature changes are not considered.

Negligence of inertial forces

Since the secular movements in the Earth’s crust are very slow, the inertial term in eq. (2.5) is neglected. In case of earthquakes this term influences rupture propagation and has to be considered. However, in this thesis only the static stress drop is addressed and neither the propagation process of rupture nor the radiation of energy by seismic waves.

Constant gravity

Gravitational acceleration is assumed to be constant ($g = 9.81 \text{ m/s}^2$), depth-independent (the models extend at most down to 42 km depth) and downward directed.

Rectangular box instead of spherical shell

The considered volume of the Earth’s crust is assumed as a rectangular box, which is an adequate approximation of the Earth’s spherical shape due to the limited dimensions of the area.

No pore fluid pressure

Pore fluid pressure P_f is not included explicitly. This is a strong assumption, since effective stresses in the Earth’s crust may strongly depend on P_f (e.g. Engelder and Fischer, 1994). The effect of P_f on stress in rock is mainly twofold. First, P_f increases horizontal stresses within the rock as will be shown in 3.5.1. However, the established prestress in the model accounts for this increase in horizontal stress by P_f. Second, P_f reduces the normal stress on faults right about the magnitude of P_f (eq. 1.1). Thus, slip on a fault is more likely since the critical shear stress, that the fault can withstand, becomes smaller. In other words, P_f shifts the Mohr cycle to the left, so that it comes closer to the failure envelope defined by the static coefficient of friction μ (Fig. 1.9). In the model an effective coefficient of friction μ' is assigned to the faults that accounts for P_f and whose magnitude is discussed in 3.2. Pore fluids can get relevant on motions and effective stresses both during the months before (Scholz et al., 1973) and after large earthquakes (Masterlark and Wang, 2002; Jónsson et al., 2003). During the long interseismic loading time however, possible changes in pore space and P_f develop slow enough that the fluids can follow without significant delay.

Strong crust-mantle coupling

It is assumed, that on crustal scale there are no major vertical gradients in horizontal velocity. This issue is related to the question, whether lithospheric plates are driven by viscous flow in the mantle or by lateral push and pull from the adjacent plates or both, which is a matter of debate. In case of plates driven by basal shear, the vertical gradient in viscosity determines the coupling between mantle and crust and hence the depth gradient of lateral velocities. Here, vertically uniform velocity boundary conditions are applied to drive the model from the sides. This implies a strong crust-mantle coupling. From the east, most probably the lateral push from the Arabian Plate is dominant in conformity to the assumption. From the southwest it is possible, that a corner flow cell is established in the Hellenic subduction zone, which would pull the Marmara region from beneath. Hatzfeld et al. (2001) found shear wave anisotropy in the broader Aegean with the direction of fast polarization and the magnitude of delay times in good correlation with the present-day strain rate observed at the surface deduced from both geodetic measurements and seismicity. This may be interpretable as strong crust-mantle coupling. Biryol et al. (2008) made the same observation for the NAF and concluded "that the upper mantle and upper crust are deforming coherently, suggesting the existence of either strong coupling or similar boundary conditions". Thus, this is conform to the assumption. Anyway, this work focuses on upper and mid crustal levels, where the origin of plate motion should play a subsidiary role compared to interactions within the brittle crust.

Elastic rheology

Based on the above assumption it is consequent to assume elastic rheology. In one special case plasticity will be considered but only as a postprocessing rheology, which means that a modelled stress state obtained with elastic rheology is compared to a failure criterion afterwards (4.2.3.1).

At first glance, the assumption of elastic rheology seems to disregard the fact that on longer time-scales rock behaves like a viscous fluid in response to differential stresses, given temperature and pressure are high enough. This is evident from laboratory experiments (e.g. Tsenn and Carter, 1987), from postglacial rebound (e.g. Larsen et al., 2005), from postseismic viscoelastic stress relaxation (e.g. Pollitz et al., 2001) and from the anisotropy of seismic velocities and shear wave splitting due to the arrangement of olivine minerals in a preferred orientation during flow (e.g. Hatzfeld et al., 2001).

The role of viscoelasticity might be most important in transient phenomena such as creep of decreasing rate in response to a sudden stress change caused by an earthquake. Lorenzo-Martin et al. (2006) modelled the effect of postseismic stress relaxation following the earthquakes of the recent sequence along the NAF and found that the stress changes due to viscoelastic relaxation partly reach rates of the same order as the secular loading rate. However, they assumed linear, i.e. time-independent, and decidedly low viscosities of $5 \cdot 10^{17} - 10^{18}\,\mathrm{Pa} \cdot \mathrm{s}$ and provide no comparison with postseismic GPS observations. Viscosities in this range are reported for areas of much higher temperatures, in case of non-linear power-law creep and only during a few months after an earthquake (Pollitz et al., 2001; Pollitz, 2003; Hergert and Heidbach, 2006). Bürgmann et al. (2002) and Hearn et al. (2002) attributed the postseismic motion following the 1999 Izmit earthquake to frictional afterslip on and below the rupture plane.

Assuming uniform viscosity would not meet the present heterogeneities in temperature (Tezcan and Turgay, 1991; Pfister et al., 1998; Aydın et al., 2005) and lithology (e.g. Elmas, 2003) which are difficult to quantify. The question is, however, whether viscous rock behaviour is necessary to accomplish the goal of a meaningful stress and strain field that can be used for seismic hazard assessment. The presence of seismicity down to ~ 20 km depth in the Marmara region (e.g., Barış et al., 2002; Sato et al., 2004) can be taken as hint, that significant viscous creep rates are not expectable in upper and mid crustal levels, which is the zone of interest. Besides, a ductile shear zone beneath a fault may be effectively represented by a prolonged contact surface allowing frictional slip at depth.

The influence of viscoelasticity should increase in long-lasting processes. However, there are examples suggesting that viscous rock behaviour is not relevant even on long timescales. Hubert-Ferrari et al. (2003) successfully modelled the propagation process of the NAF with purely elastic rheology although this process developed during geological timescales. Similarly, Armijo et al. (2003) explained the past and present evolution of the Aegean by linear elastic fracture mechanics. ‘Long-term’ elasticity was evoked to explain the effective elastic-brittle behaviour of continental crust although it is not elastic at all depths, as well as its capability to preserve strength over long periods (Armijo et al., 2003; Hubert-Ferrari et al., 2003). This holds even more for the timescales considered in this work.

2.4 Agenda

Here, it is described how to attain the absolute stress state in the crust practically, and the workflow putting the model concept into practice is outlined. The explanation of the steps leading to this goal concurrently imparts an overview on this thesis.

Fig. 2.3 enumerates the various input information to the model and sketches how the output is used in several regards. The “ingredients” of the model are described in detail in chapter 3. Accomplishing the objective of the absolute stress state requires comprehensive information especially on geometrical constraints. Topography and bathymetry (3.1.1) predominantly influence the vertical stress in the subsurface but also horizontal stress magnitudes and their orientations and not least the normal stresses on faults. The same accounts for basement topography and Moho, that represent spatial changes in density and elastic properties (3.1.1). The active 3D fault system is implemented as set of curved and dipping contact surfaces, whose slipping behaviour is governed by Coulomb friction (3.1.2).

The model is subjected to gravity and also the hydrostatic pressure exerted by the water load is considered (3.4). Plate tectonic boundary conditions accounting for the regional geodynamical setting of the Marmara Sea area drive the model by applying the sub-modelling technique (3.6).

A decisive step within this approach is the provision of an initial stress state in the model in order to obtain realistic stress magnitudes. The background expounding the necessity of prestressing is given in 3.5.1. A technique of how to appropriately prestress a geomechanical earth model was developed (3.5.2), that employs the state of stress proposed by Sheorey (1994). The impact of prestress on stress regime, critical stress states and kinematics is demonstrated in 4.2.4.

The model output is the 3D displacement and stress field. Whether or not the model output is reasonable is controlled by comparing modelled stress and displacements or derivative quantities with independent observations such as GPS observations, fault slip rates, seismicity, stress orientations from earthquake focal mechanisms or morphology (chapter 4).

Once appropriate boundary conditions and material properties are found that yield a velocity and stress field that is in good agreement to observations, the full 3D stress and displacement field in the model volume is available and conduces to the comprehension of ongoing processes (chapter 4). In particular, the resulting velocity and stress fields provide information related to seismic hazard (4.3).

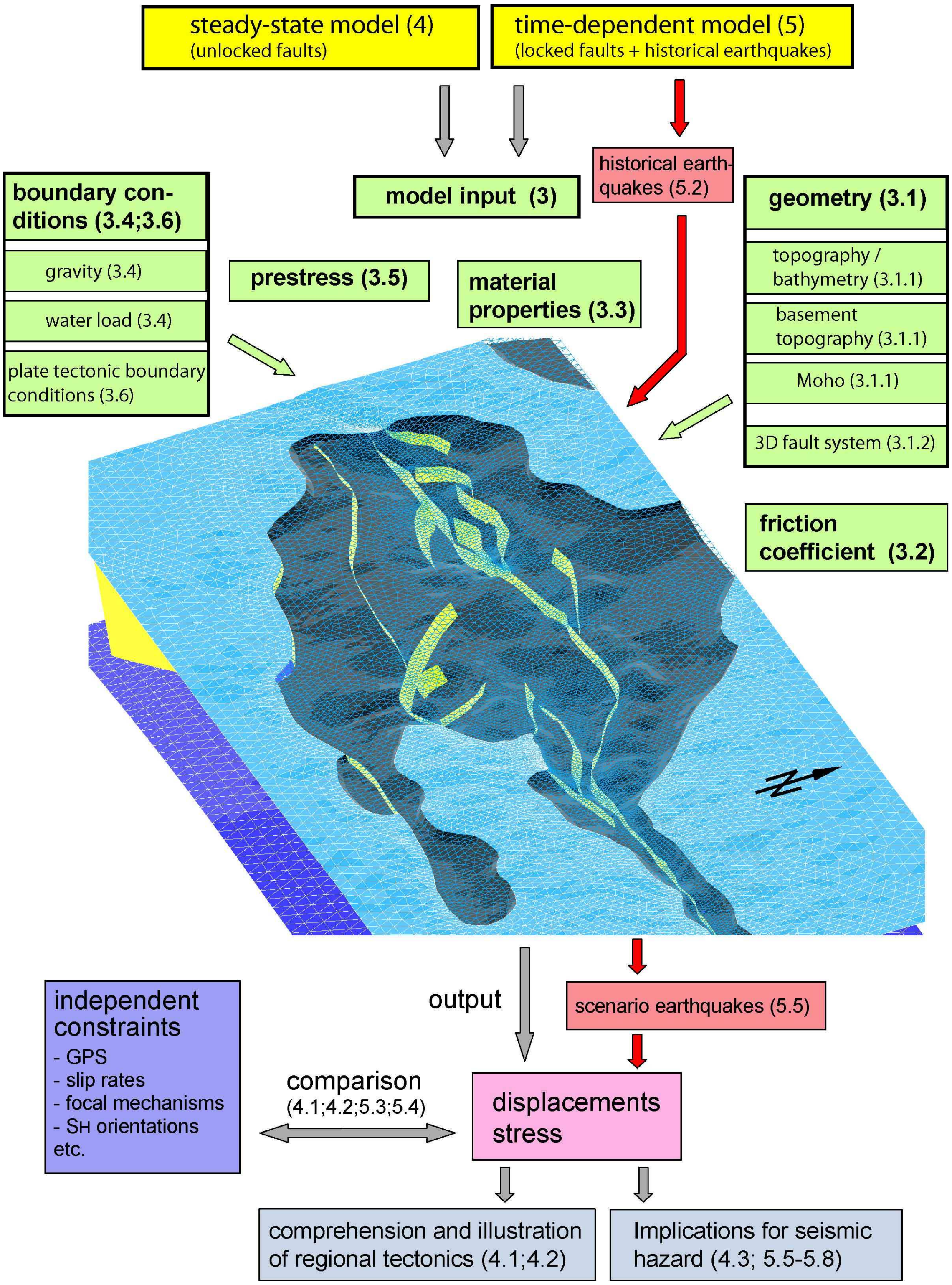

Fig. 2.3: Workflow of this thesis. The model geometry incorporates the active fault system (yellow), topography and bathymetry (solid and transparent light blue, respectively), basement topography (dark grey) and the Moho (blue). Green boxes indicate the model input, pink box the model output and purple the validation procedure. Red boxes and arrows refer to the time-dependent stress and strain evolution considering the seismic cycle, used to estimate source parameters of potential earthquakes. Light blue boxes indicate qualitative and quantitative conclusions for regional geodynamics and seismic hazard based on the model output. Numbers in parentheses refer to the corresponding chapter.

Basically, two versions of the model are considered. Whereas the first addresses the steady-state evolution of stress and strain (chapter 4) the second incorporates the effects of the seismic cycle (chapter 5). Practically, the difference between the two is that in the steady-state model faults are unlocked allowing continuous slip on the faults, whereas in the time-dependent model faults are locked at seismogenic depths accounting for stress accumulation on the fault. Stress is released by slip when the fault is unlocked.

The steady-state model is dedicated to infer fault slip rates and to reveal and apprehend the characteristics of the stress field that emerge during the secular process of relative plate motion. The time-dependent model is used for accomplishing the contemporary state of stress on the NAF that accounts for the effects of historical earthquakes (5.1+5.2) in order to estimate source parameters of future earthquakes. The performance of the model is demonstrated by comparing the modelled interseismic velocity field and coseismic displacements of the 1999 Izmit earthquake to observations (5.3+5.4). Using testing earthquakes by releasing accumulated shear stress moment magnitudes of potential earthquakes are estimated (5.5) and the likelihood of their occurrence (5.6). The influence of sediments on earthquake magnitudes is investigated (5.7) as well as the likelyhood of a rupture passing the bend near Istanbul (5.8).

Chapter 6 summarises the approach applied here, states the main results and gives an outlook on what can be further done to improve the model concerning the expected future earthquake.

Chapter 3

Model input and preparation

Within this chapter the model input sketched in Fig. 2.3 (upper part) is described in more detail. Geometry data (3.1) and material properties are presented and discussed (3.2+3.3). The requirement of an initial stress field is explained (3.5.1) as well as how to obtain it (3.5.2). Static loads (3.4) and plate tectonic boundary conditions (3.6) are introduced. For obtaining the latter, a separate model of the broader northwest Anatolian region is set up, which serves to drive the local Marmara model using the sub-modelling technique.

3.1 Geometry

The Marmara Model covers the Sea of Marmara and the adjacent onshore areas with Istanbul in the North, Lake Sapanca in the east, Bursa graben in the South and Ganos mountain in the west. It is of rectangular shape (27.25-30.25°E and 40.25-41.15°N) with 250 km length and 100 km NS extent. The model is georeferenced and realized in UTM projection zone 35N, 24-30°E. It reaches down to 38 km depth and consists of 639.640 linear tetrahedral elements allowing a resolution in the sub-kilometre range in the most critical areas and 2-3 km near the model sides.

3.1.1 Horizons

Topography and bathymetry

Topography was incorporated in the FE model using the GTOPO30 digital elevation model (USGS), which provides a resolution of 30’’ (~1 km) . The high-resolution bathymetry in the Marmara Trough was taken from Ifremer (http://www.ifremer.fr/drogm/marmara/asea.htm). The actual topography and bathymetry in the model is smoothed to some extent due to the local element size (~400-2500m). The flat shelf areas between the trough and the shores of the Marmara Sea are less than 100 m bsl. and were bridged by a linear interpolation between the z=-100m isoline from the Ifremer dataset and the shoreline. The bathymetry of the Black Sea and the Aegean in the regional model of northwest Anatolia (3.6) was adapted from the ETOPO2 dataset, which provides a resolution of 2’.

Basement-topography

The role of sediments on movements and stresses is investigated. Therefore, information on sediment thickness and their properties have to be gathered or assumed. The steps in generating a basement-topography map of the Marmara region is described in the following.

A major step forward in knowledge about the sediment thickness in the Marmara Sea was brought about by the seismic surveys during the last decade. Especially the SEISMARMARA Leg1 (2001) experiment contributed a lot to elucidate structures at greater depths. The combined performance of a dense grid of seismic reflection-refraction profiles and an Ocean Bottom Seismometer (OBS) experiment allowed imaging of the upper 6 km and in part down to the Moho (Carton et al., 2007; Laigle et al., 2008; Bécel et al., 2009). The data from this experiment form the basis of the used basement-topography map and were kindly provided by A. Bécel and A. Hirn (pers. comm.).

The uppermost basement rock in the Marmara Sea is limestone (Parke et al., 2002). Therefore, a first version of the basement-topography was generated by creating the iso-surface from the 3D velocity model corresponding to $v_p = 4.5$ km/s, which is a representative value for limestone.

This surface was then modified in several aspects. First, the depths of the points at which the seismic profiles cut the faults at the sediment-basement interface were estimated from both seismic images and the velocity model. The surface was recomputed to compulsorily contain these points. Second, in a similar way hard constraints on the basement-topography from the stratigraphy observed in boreholes were considered (Ergün and Özel, 1995; Elmas, 2003). Third, the surface was adjusted near faults exhibiting dip-slip. Seismic profiles show vertical offsets of the basement-topography across normal faults, e.g. along the Prince Islands segment or across the Imralı Fault (Parke et al., 2002; Carton et al., 2007). The surface from the velocity model shows a gradual change in depth across these normal faults. Therefore, the portions of the surface in the vicinity of normal faults were replaced by surfaces, which were obtained by laterally projecting the surface at some distance from the fault onto the fault, on both the hanging wall and the footwall. Thereby, a vertical step-like offset in the basement-topography at these faults was established.

Apart from the Marmara Trough, where the SEISMARMARA Leg1 experiment was conducted, there is little information available on sediment thickness. For this reason geological maps marking the sediment-basement boundary onshore as well as estimates based on the morphology were used to extend the coverage of the map. Over wide areas surrounding the Marmara Sea basement rocks crop out (e.g. Elmas and Yiğitbaş, 2001). In between, where sedimentary rocks are present, the basement-topography was constructed following reasonable assumptions. For instance, it can be expected that valleys or river planes are favoured areas for sediment accumulation, whereas in mountainous areas rock is rather eroded than deposited. Sediment thickness should also be increased near releasing bends of faults or in local depressions such as Iznik Lake (Fig. 1.5). It might be suggestive to assume that sediment thickness correlates in some sense with topography. In areas where sediments are present at the surface, the basement topography was generated by simply taking the topography and multiplying it by a linear function leading to decreased sediment thickness in elevated areas and increased sediment thickness in shallow areas. The basement-topography beneath the Thrace Basin was constructed following the constraints placed by the maximum sediment thickness, which was reported to be ~ 9 km (Görür and Okay, 1996; Okay et al., 2000) and by the sediment-basement boundary at the surface. In the Black Sea, thick layers of sediments are reported (Hurtig et al., 1991; Starostenko et al., 2004).

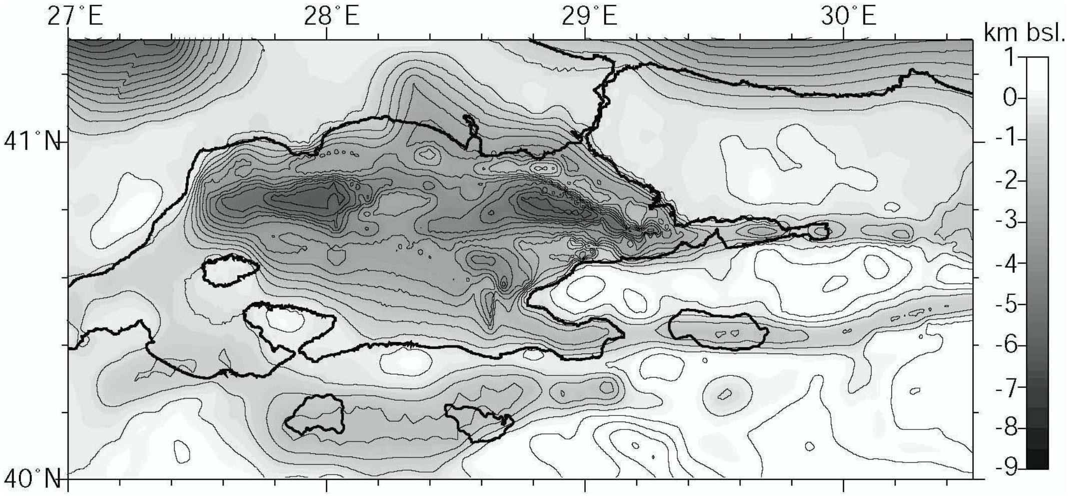

Fig. 3.1: Basement-topography in the Marmara region. Depths are bsl., not relative to the surface.

Fig. 3.1 shows the basement-topography map before constructing the vertical offsets at normal faults. Recent data on sediment thickness in the northwest of the Marmara Sea by Siyako and

Huvaz (2007) are not incorporated into this map as they were published after constructing the model geometry.

A final adjustment of the basement-topography was required by technical reasons. When incorporating the obtained basement-topography map into the finite element model the necessity arose to eliminate those parts, where the sediment-topography comes close to the surface. Since material properties in the model are assigned to the finite elements, a shallow basement-topography would imply small sized elements and hence a high number of them, which is costly in terms of computing time. For this reason the basement-topography was cut out where it is less than 800 m beneath the surface. Near the cutting line the basement-topography was connected to the surface. This was done in a gradual manner within several kilometres in order to avoid artefacts due to an artificial vertical step in material properties. As a consequence, the sediments are only considered in those areas where their thickness exceeds ~ 800 m (Fig. 3.3, middle).

Moho

The Moho beneath the Marmara Sea and its surroundings is characterised by significant undulations. From east Anatolia to the Aegean, there is a Moho uplift of 10-20 km and also towards the Black Sea. The shallow Moho depth beneath the Aegean is probably a result of backarc extension to the north of the Hellenic subduction zone, which caused crustal thinning. The thick crust beneath Anatolia supports the Anatolian plateau, which is ~ 1000 m above sea level. Towards northern Greece and Bulgaria the Moho deepens beneath the Rhodopian Massif.

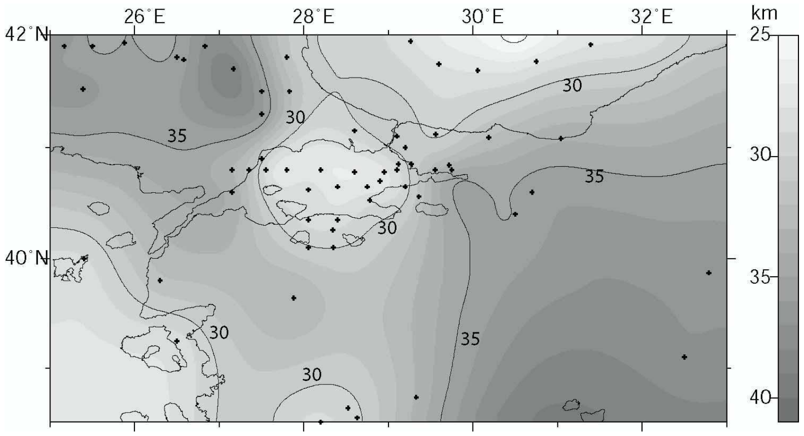

Fig. 3.2: Moho depth map (contours; bsl.) interpolated between compiled data points (black crosses).

There is agreement on these general characteristics of the Moho as shown by numerous Moho maps (Makris, 1985; Meissner et al., 1987; Gurbüz et al., 1992; Papazachos et al., 1995; Genç et al., 1996; Klingele and Medici, 1997; Tsokas and Hansen, 1997; Toksöz et al., 2002; Tirel et al., 2004; Karagianni et al., 2005). However, when trying to constrain Moho depths, inconsistencies appear as published depths differ by several kilometres in a sometimes unsystematic manner. Moho depths are no direct measure but rely on assumptions, e.g. on a density model or on a seismic velocity model. Some Moho maps are very smooth neglecting local deviations, others show strong undulations. For this reason, it is suggestive to create a new Moho map integrating also recent data and trying to reconcile reported depths, considering single points deviating from other results if they seem reliable or to exclude them if not.

Fig. 3.2 shows locations of the compiled Moho depth data as well as the map created by kriging. Used data come from refraction seismics, deep seismic sounding and receiver functions (Makris, 1978; Necioglu et al., 1981; Geiss, 1987 and references therein; Hurtig et al., 1991; Saunders et al., 1998; Boykova, 1999 and references therein; Gürbüz et al., 2003; Li et al., 2003; Toksöz et al., 2003; van der Meijde et al., 2003; Starostenko et al., 2004; Sodoudi et al., 2006; Zhu et al., 2006; Zor et al., 2006; Bécel et al., 2009). Part of the data is from beyond the area shown in Fig. 3.2, so that also data points from the surrounding contribute to this map. Following the arguments of Geiss (1987), Moho depths from gravity measurement surveys were not considered. Data from Necioglu et al. (1981) were mostly not used and if so, then their upper bound. Local strong Moho undulations are possible, they would however cause dominant anomalies in the stress field. In order to avoid this in case of inaccurate data, a smoothed Moho surface may be more reliable to get the first order influence of the Moho on the stresses in the crust. Thus, a Gauss filter was applied to the Moho surface, so that the resulting map may be regarded as a compromise between local variations and general trends.

The Marmara Sea marks a distinct high in the regional Moho depth pattern with a minimum depth of ~26 km (Bécel et al., 2009). Towards the south of the sea the Moho deepens, but not as sharply as to the west and east of the Marmara Sea. In the eastern Marmara region, the value from Zor et al. (2006) for station KAL (31 km) was not considered and instead replaced by depth values from the SEISMARMARA Leg1 seismic refraction survey (Bécel et al., 2009), which inferred a deeper Moho there. A deep Moho beneath the Strandja Massif in the northwest may reflect the presence of an ancient subduction zone or suture (Okay et al., 2001a; Bayrak et al., 2004). The map largely agrees with other data published without specific position, e.g. ~32 km beneath Izmit Bay (Horasan et al., 2002) and 36-42 km beneath central Anatolia (Bekler et al., 2005).

3.1.2 Geometry of the 3D fault system

The geometry of the active fault system is a key feature among the various inputs to the model, for it controls the kinematics and stress field evolution in the Marmara region in response to the outer driving forces.

It was proposed, that the fault system of the NAF in the Marmara region emerged as reactivation of pre-existent faults and generation of new faults (Okay et al., 2000; Alpar and Yaltırak, 2002; Hubert-Ferrari et al., 2003) during the westward propagation of the NAF. As this work focuses on the contemporary situation the present fault system is implemented in the model geometry. The time period of interest here is at most a few seismic cycles, within which no fundamental changes of the fault geometry are expected, e.g. that a unfavourably oriented fault becomes inactive and is replaced by the emergence of another fault.

Before several campaigns of high-resolution bathymetry mapping and seismics were conducted commencing about a decade ago, the opinions of how the fault system at the seafloor and beneath may look like were quite diverse. There is a number of fault maps based on seismic images that differ considerably from each other (e.g. Barka and Kadinsky-Cade, 1988; Wong et al., 1995; Okay et al., 2000; İmren et al., 2001; Parke et al., 2002; Gökaşan et al., 2003; Rangin et al., 2004). The most comprehensive fault maps for the whole Marmara Sea are those of Le Pichon et al. (2001, 2003) and Armijo et al. (2002; 2005). In the view of Le Pichon et al. (2001; 2003) there is mainly the MMF as a single through going strike-slip fault, whereas Armijo et al. (2002) interpret the fault system as a sequence of pull-apart structures. For specific parts of the Marmara Sea recent fault maps were published for the Çınarcık Basin (Carton et al., 2007), for the Gulf of Izmit (Cormier et al., 2006) and the southeast Marmara Sea (Kurtuluş and Canbay, 2007). The surface traces of the main faults in the Marmara Sea according to Armijo et al. (2002) are mapped and named in Fig. 1.6, supplemented by faults identified by Carton et al. (2007).

At least for the Marmara Trough down to mid-crustal depths results from the SEISMARMARA Leg-1 experiment (Carton et al., 2007; Laigle et al., 2008; Bécel et al., 2009) provide good insight into the fault system. While the traces of the faults at the seafloor and their general picture at depth are known today, the precise geometry is locally difficult to interpret and still under debate. Apart from a few exceptions for specific areas (Okay et al., 2000; Kanbur et al., 2007; Bécel et al., 2009) seismic sections are generally shown in terms of two-way-travel time, which complicates estimation of true fault dips. It is not straightforward to migrate them into depth images without knowledge of the probably heterogeneous distribution of seismic velocities. Fault dips are a crucial parameter since it controls the style of deformation, in particular the dip-slip rate at a fault, in response to an acting stress field. At least, relative dips of different faults in the same seismic section can be estimated more reliably than the absolute dips. Some authors provided numbers for fault dips (Okay et al., 1999; Seeber et al., 2004; Kanbur et al., 2007) or discussed them for modelling the fault-related kinematics in the Marmara Sea (Muller and Aydin, 2005). It can be generally said that faults dip rather steeply, also those which are referred to as normal faults, e.g. the Imralı and Çınarcık Faults.

The fault system for the model geometry (Fig. 3.3) was constructed based on the mapped fault traces at the seafloor, seismic sections and reasonable assumptions. (1) Fault traces at the sea bottom in the model coincide with the major faults shown in Fig. 1.6. (2) For each fault segment a dip was assumed, either from references or by guessing. Often it is clear from a mechanical point of view, whether a fault dips non-vertically and in which direction. The presence of sedimentary basins, fault bends and morphological features give hints on fault dips. Vertical faults were assumed where the surface traces strike straight and are embedded in rather flat bathymetry as the MMF beneath Izmit Bay, the Central Segment linking the Istanbul Bend and the Central Basin and underneath the Western High. Local sediment accumulation near fault bends and subsided sea floor along scarps suggest non-vertical dip of the fault, e.g. at the various basins. This holds also for the smaller basins as the Kumburgaz Basin or the Darica, Karamürsel and Izmit Basins in the Gulf of Izmit (Cormier et al., 2006), which are correspondingly associated with smaller bends and steeper dips.

(3) A fault representing a plate boundary and accommodating significant relative motion like the NAF is likely to strike as straight as possible. This means that local bends or apparent step-overs at the surface may be present only near the surface and do not necessarily need to continue at depth in the same manner but rather should tend to a more plane fault surface. It was therefore assumed that curvatures of the surface trace prolong at depth but with increasing curvature radii. An argument supporting this view at least for Izmit Bay may be the 1999 Izmit earthquake, which revealed that the NAF resembles more a single strike-slip fault (Alpar and Yaltırak, 2002; Cormier et al., 2006) than a series of small pull-apart basins as presumed before (e.g. Barka and Kadinsky-Cade, 1988).

(4) Due to the west migration of the Anatolian block with respect to Eurasia, the strike of the fault at the surface should be shifted to the west at depth. In case of changes in fault strike the “retarded” strike at depth is linked to the surface trace through a non-vertical dip of the fault. Following this principle the fault in the westernmost part of the Marmara Sea was assumed to dip to the north as claimed by Kanbur et al. (2007) in opposition to previous work.

(5) It was assumed that below 15 km bsl. all faults are vertical. (This pertains only to the MMF and the middle branch as the next point reveals). (6) Second order faults were assumed to cease at 7.5 km depth. The Southern Border Fault extends to 10 km depth. The Çınarcık Fault, Imralı Fault and the Tekirdağ Fault (Fig. 1.6) reach down to 15 km depth and the middle branch of the NAF to 20 km. The MMF was assumed to penetrate the whole model (38 km). This may be an appropriate assumption for a plate boundary fault and it was proposed by Aksu et al. (2000) that the MMF extends to depths greater than 30 km. The fault system in the middle and lower crust beneath the Marmara Sea is not clearly revealed by seismics. It was proposed, that the Marmara Sea fault system may represent a large scale negative flower structure (Aksu et al., 2000; Koral, 2007; Laigle et al., 2008), which is not accounted for in the chosen fault geometry.

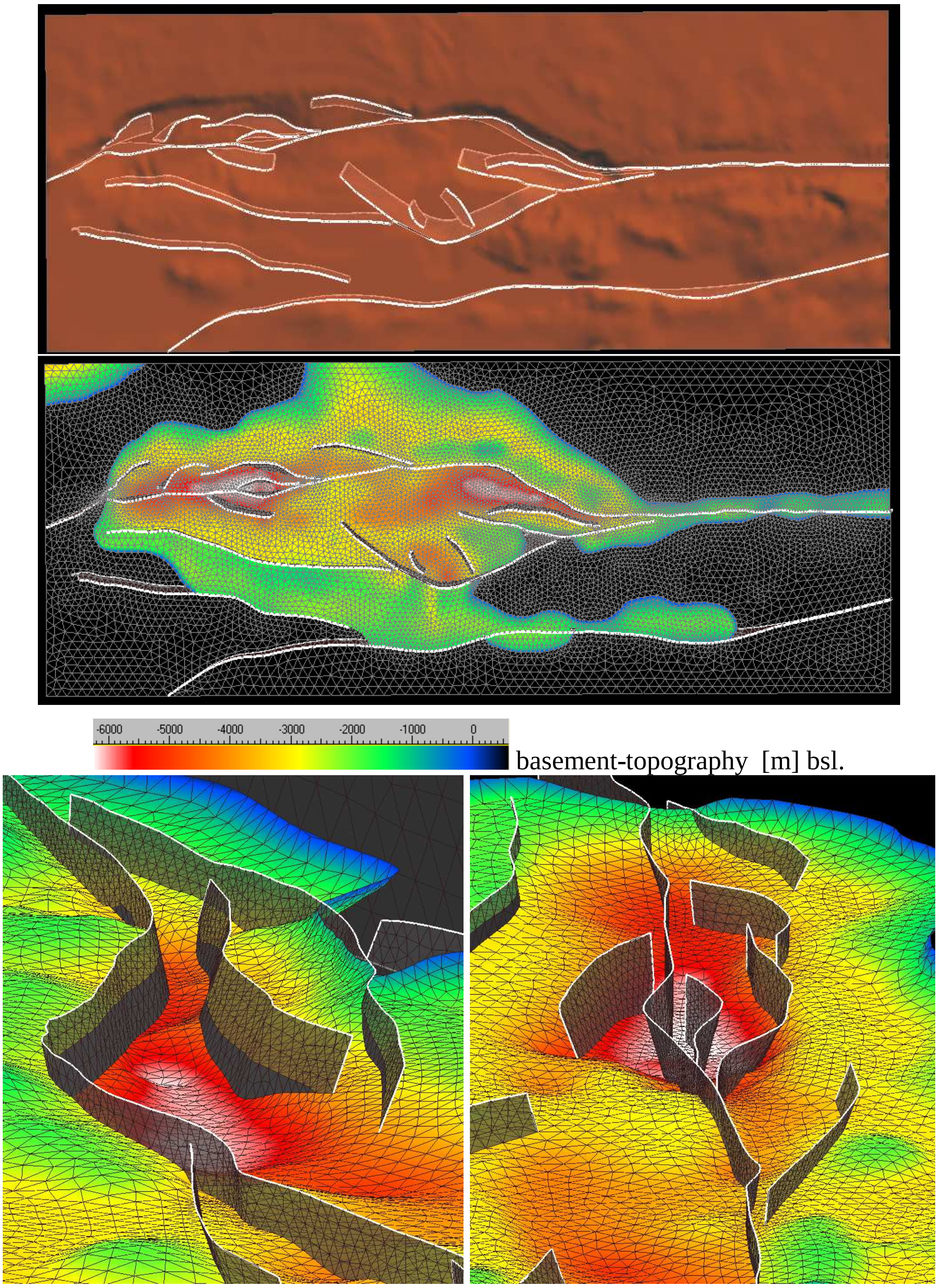

Fig. 3.3: Fault system. Top: Topography and bathymetry (three times vertically exaggerated). Fault surface traces (bright white lines) and fault traces at their lower end (brownish lines) indicate fault dips. Middle: Surface FE-mesh (grey), incorporated part of the basement-topography (coloured) and faults. Lower left: Çınarcık Basin (without vertical exaggeration). View from the northern shelf to ESE. Istanbul Bend (left), Izmit Bay (background, left), Central High (foreground, right), MMF (from background, left to foreground, right), inner (middle) and outer (right to background, left) Çınarcık Faults. White lines mark fault traces at the sea bottom. Visible parts of the faults are within the sediments. Note the vertical step in basement-topography across the basin bounding faults as revealed by Carton et al. (2007). Lower right: View from east to west. Central High (foreground), Central Basin (middle) and Tekirdağ Basin (background). Note that the MMF was assumed as a through going fault joining the southern inner rim of the Central Basin.

The fault structure beneath the Central Basin is difficult to interpret (Armijo et al., 2002; Le Pichon et al., 2003; Laigle et al., 2008). It was not assumed as a pull-apart basin with a fault step-over. The MMF was rather assumed as a through going fault with a local bend in its uppermost part marking the southern inner rim of the basin. The constructed fault system is presented in Fig. 3.3.

3.2 Coefficient of friction

The faults implemented in the model (3.1.2) obey the Coulomb friction law (eq. 1.1). Technically this is done by creating two surfaces for each fault, a so-called master and slave surface, where the slave surface is not allowed to penetrate the master surface and to separate from it. The tangential behaviour of the interface is determined by the coefficient of friction μ. It is a sensitive parameter since it influences the slip rate on a fault and the stress field in the surrounding. In the following the choice of μ is discussed.

i) Byerlee's law

μ of crustal rocks ranges between 0.6 and 0.85 as found by Byerlee (1978) from frictional sliding experiments for a broad range of rock types. Based on these experiments Byerlee's law relates the critical shear stress τ under a given normal stress σ_n at which brittle fracturing of the rock occurs:

$$\tau = 0.85\,\sigma_n \qquad \text{for } 5 < \sigma_n < 200 \text{ MPa}$$

$$\tau = 50 + 0.6\,\sigma_n \qquad \text{for } \sigma_n > 200 \text{ MPa},$$

which is basically the Mohr-Coulomb criterion (eq. 1.1) applied to crustal rocks. Byerlee friction coefficients ($0.6 < \mu < 0.85$) have been found widely applicable to natural sliding surfaces in the Earth's crust (e.g. Sibson, 1994). Also stress magnitude measurements in boreholes strongly support the general validity of Byerlee's law in the crust (Townend and Zoback, 2000). From these observations there is agreement, that the state of stress in the brittle crust is maintained by fractures whose frictional failure is governed by Byerlee friction coefficients and hydrostatic fluid pressures (Townend and Zoback, 2000; Townend, 2007). Thus, it is suggestive to assume coefficients of friction in the range of 0.6-0.85 according to Byerlee's law for the faults to be implemented in the finite element model.

ii) Observational indicators for weak large plate boundary faults

There are a number of observations that cast doubts on Byerlee friction coefficients to be characteristic for large-scale plate boundary faults and lead to the ongoing debate on whether the San Andreas Fault (SAF) is a weak fault or a strong fault (Zoback, 2000). From these observations it could be concluded that large-offset faults exhibit much lower effective friction coefficients. (1) The axis of maximum horizontal compression σ_H is oriented at high angles to the strike of major strike-slip faults (Townend, 2007), the most prominent example of which is the SAF with nearly fault-normal compression (Zoback et al., 1987; Townend and Zoback, 2004). This is much more than ~30° between the maximum principle stress σ_1 and fault strike expectable for an optimally oriented fault with Byerlee friction coefficients (Sibson, 1994) and suggests that these faults have "extremely low shear strength" (Zoback et al., 1987). (2) Stress magnitude measurements in the Cajon Pass drill hole and the SAFOD Pilot Hole near the SAF revealed that lateral shear stress is compatible with a weak fault (Zoback et al., 1987; Hickman and Zoback, 2004). (3) Ongoing slip at high rates with Byerlee friction coefficients should develop a heat flow anomaly at major strike-slip faults which, however, is not observed (Lachenbruch and Sass, 1980; Fulton et al., 2004). (4) Analysis of seismicity induced by stress changes due to major earthquakes revealed that the temporal and spatial occurrence of seismicity is best explained by effective coefficients of friction of ~0.2 for the SAF system (Raesenberg and Simpson, 1992; Gross and Bürgmann, 1998). (5) Weak plate boundaries were also suggested for subduction zones. Based on shear stress tests on clay minerals Brown et al. (2003) estimated effective friction coefficients of 0.2-32 for the Nankei Trough, Japan. Lamb (2006) inferred values <0.1 from calculation of shear stresses at various subduction zones and Wang and He (1999) reported values of ~0.05 for Nankai and Cascadia.

iii) Lessons from numerical models

In recent years several approaches were undertaken to model faults considering their frictional properties. The conclusion from these models was that realistic slip rates in accordance with geodetic observations are only obtained with very low coefficients of friction. With global finite element models Bird (1998) found the lowest misfits of the model to observed velocities and stress orientations for μ only 0.03. Also from numerical modelling Geist and Andrews (2000) found μ=0.09 at the SAF to best explain geodetic observations and orientations of σ_H. Results of numerical models from Bird and Kong (1994) imply μ=0.17 for the faults in California and an even lower value of μ=0.12 for the SAF due to velocity weakening. Similar optimum effective friction values of ~0.17 were found for faults in Alaska by Bird (1996) and for New Zealand' faults by Liu and Bird (2002). Vernant and Chéry (2006) modelled faults in the Zagros belt and found minimum residuals between modelled slip rates and GPS observations for apparent coefficients of friction of only 0.02. d'Alessio et al. (2006) inferred from numerical modelling that observed heat flow data at the SAF are best explained by apparent friction coefficients of ~0.1. Hence, these results differ considerably from what would be expected from Byerlee friction coefficients.

iv) Effective coefficient of friction μ'

It seems contradictory that a fault should have other frictional properties than the very rocks in contact at the fault. The lowest friction coefficients of rock expectable in considerable quantity in fault zones were found in the range of $0.2 < \mu < 0.4$ for montmorillonite clay, which represents a rare exception from Byerlee friction coefficients. Hence, apparent friction coefficients of < 0.2 cannot be explained by low values of μ alone. A glance on eq. (1.1) reveals that not only μ pertains to frictional resistance against shear stress but also cohesion, normal stress and pore fluid pressure. For this reason a low apparent or effective coefficient of friction on a fault does not necessarily imply a low coefficient of friction of the rock. An effective coefficient of friction μ' can be introduced in the Mohr-Coulomb criterion (eq. 1.1), which accounts for the effect of pore pressure:

$$\tau = \mu' \sigma_n + C_0, \tag{3.1}$$

where

$$\mu' = \mu\,(1-B).$$

B is the Skempton coefficient, which ranges between zero for drained rock and one for completely undrained conditions (Rice, 1992).

Low shear strength on a fault was mostly attributed to high pore fluid pressures (Blanpied et al., 1992; Hardebeck and Hauksson, 1999; Faulkner and Rutter, 2001). Theories on how high pore fluid pressures could emerge and be maintained in fault zones, in contrast to presumably hydrostatic pore pressures in the surrounding crust, concentrate on sealing due to clay fault gauge with vanishing permeability.

Byerlee (1990) himself proposed a theory relying on the observation that below a certain pressure gradient water cannot flow through dense clay, which is expectable in fault zones. Within the central zone of the fault, pore pressure may be as high as the lithostatic pressure, which yields low shear strength of the fault and slip is possible under fault normal compression. Byerlee (1990) calculated a minimum width of the fault zone of zero at the surface and an increase by 60 m per kilometre depth for this mechanism to work. In case of the NAF this precondition is fulfilled since a fault zone width of 80 m near the surface was reported by Dietrich et al. (2004) who inferred this width from a sharp decrease of seismic velocities and the damping parameter within the fault zone.

Apart from low inherent friction coefficients μ and high pore fluid pressures P_f, also reduced normal stresses σ_n may contribute to low apparent fault friction according to eq.(3.1). Parsons (2002) proposed nearly frictionless faulting from fault unclamping in long-term interactions with other faults. From finite element modelling he found that increased complexity of a fault system causes locally reduction of fault-normal stress down to hydrostatic values, which implies an almost frictionless fault.

Holdsworth (2004) explained the weakness of faults by repeated deformation during their existence ending up in rotten fault cores. He found evidence for this by investigating ancient fault cores exposed at the surface. Cataclastic textures were overprinted by platy weak minerals like micas and clays due to alteration by fluid influx. The resulting permanent weakening effect is expressed in shear strengths, which are more than 50 % lower than shear strength expectable from Byerlee’s law (Holdsworth, 2004).

To summarise, stresses in the crust seem to be controlled by fractures governed by Byerlee friction and hydrostatic pore fluid pressures, whereas this mechanical behaviour breaks down on large-offset plate boundary faults (Townend, 2007). Although the view of strong plate boundary faults as strong as the surrounding crust is defended (Scholz, 2000), low apparent frictional strength is characteristic of large-displacement faults, most probably due to high pore fluid pressures.

v) Choice of μ' in the finite element model

Although there is debate on the amount of total offset across the NAF in the Marmara region (Şengör et al., 2005), the NAF is supposed to be a large-offset plate boundary fault. Several of the above mentioned indicators ascribed to weak faults pertain also to the NAF. Data from the World Stress Map (WSM) (Reinecker et al., 2005) reveal that maximum horizontal stress is oriented either at rather high angles or subparallel to the strike of the NAF which can be interpreted as low shear strength of the fault (Fig. 3.12). It has to be mentioned, however, that WSM data near the NAF originate predominantly from earthquake focal mechanisms and it was suggested that stress orientations from focal mechanisms at plate boundary faults may be controlled by the plate boundary kinematics and fault geometry rather than being indicative of the prevailing stress field (Heidbach and Reinecker, 2004). In terms of heat-flow observations, no pronounced anomalies of fault-related origin are recognisable near the NAF (Pfister et al., 1998). High heat-flow is locally observed but mainly associated with geothermal fields.

In ΔCFS analyses most authors assume $\mu' \sim 0.4$ (Stein et al., 1997; Nalbant et al., 1998; Çakir et al., 2003a), which implies $\mu=0.85$ according to Byerlee friction and $B\sim0.5$. Parsons (2004) used a lower value of $\mu'=0.2$. From numerical modelling of the geodynamics of Anatolia Jiménez-Munt and Sabadini (2002), Jiménez-Munt et al. (2003) and Provost et al. (2003) agree on $\mu'=0.05$ for the NAF as the optimum value, when taking minimum deviations between model results and geodetic velocities, seismic strain rates and σ_H orientations as a measure for appropriate μ'. For $\mu'=0.2$ they found much too low velocities incompatible with the geodetic constraints.

The friction coefficient assigned to the faults in the model is an effective coefficient of friction accounting for the effect of pore pressure, which is not directly considered in the model (2.3). A parameter study will be performed to find an optimum µ' that minimises deviations between model results and data (3.6). Based on the above discussion, low µ' for the MMF and Byerlee friction coefficients for the smaller faults are tested as well (ch. 4).

Cohesion, which is difficult to ascertain, is neglected in this study. At greater depth of several kilometres, cementation processes due to hydrothermal flow were proposed by Angevine et al. (1982). Based on in situ stress measurements it was suggested, that cohesion is negligible at least near the surface (Jamison and Cook, 1980). Though µ' was shown to vary with slip rate and temperature at elevated temperatures in wet rocks (Blanpied et al., 1995), it is assumed that µ' is constant.

3.3 Rock properties

As discussed in 2.3, elastic rheology is assumed in the model. The elastic rock properties are provided in terms of Young's Modulus E and Poisson's ratio ν and are assigned to the finite elements. Four different material distributions are considered (Tab. 3.1). First, a homogeneous material distribution MAT_hom with average rock properties of continental crust (Turcotte and Schubert, 2002). A second rock distribution studies the influence of the Moho (MAT_moho), a third one addresses the role of sediments taking the basement-topography into account (MAT_sedi).

Table 3.1: Elastic parameters and densities for four different material distributions. In the inhomogeneous models the first number refers to the sediments above the basement-topography, the third number to the mantle beneath the Moho and the second one addresses the crustal basement in between. Values for MAT_grad are explained in Fig. 3.4.

Label	**Description**	**E [GPa]**	**ν**	**ρ [g/cm³]**
MAT_hom	homogeneous	70	0.25	2.65
MAT_moho	Moho	70/70/150	0.25	2.65/2.65/3.3
MAT_sedi	basement-topo	10/70/70	0.35/0.25/0.25	2.2/2.65/2.65
MAT_grad	depth-gradient	1-20/50-75-120 /150	0.47-0.27/0.25/0.25	1.7-2.3/2.5-2.7-3.0 /3.3

The fourth material distribution is intended to incorporate material parameters as deducible from data. Due to the geologic history of Anatolia with the collision of continents and accompanying processes, the lithology in the region is quite heterogeneous as evident on geologic maps (e.g. Okay et al., 2001b). It is difficult to assign representative material parameters to these heterogeneous lithologies since their distribution at depth is not clear in most cases. Information on the distribution of elastic parameters and density is contained in seismic velocities. Therefore, seismic velocities derived from various seismic or seismological experiments were used to estimate the elastic rock parameters. The relations linking Poisson's ratio and Young's modulus to seismic velocities and density are given by:

$$\nu = \frac{v_p^2 - 2v_s^2}{2(v_p^2 - v_s^2)} \qquad (3.2)$$

$$E = \rho v_s^2 \frac{3v_p^2 - 4v_s^2}{v_p^2 - v_s^2} \qquad (3.3)$$

where v_p and v_s are the p-wave and s-wave velocities, respectively, and ρ density. Since in most cases only v_p is available, empirical relations are employed for deriving v_s and ρ from v_p (Brocher, 2005):

$$v_s\ (\text{km/s}) = 0.7858 - 1.2344\, v_p + 0.7949\, v_p^2 - 0.1238\, v_p^3 + 0.0064\, v_p^4 \qquad (3.4)$$

$$\rho\ (\text{g/cm}^3) = 1.6612\, v_p - 0.4721\, v_p^2 + 0.0671\, v_p^3 - 0.0043\, v_p^4 + 0.000106\, v_p^5 \qquad (3.5).$$

Equation 3.5 is the Nafe-Drake curve (Ludwig et al., 1970) expressed in polynomials. It has to be kept in mind that the Young's modulus derived from seismic velocities is the dynamic Young's modulus that is generally not the same as the static Young's modulus and in most cases somewhat higher than the latter (Ciccotti and Mulargia, 2004) for the reasons explained by Sayers and Schutjens (2007). Furthermore, inferred seismic velocities may be affected by anisotropy, that can emerge from the acting stress field (e.g. Sayers and Schutjens, 2007). However, in view of the remaining uncertainties in the distribution of seismic velocities this is neglected.

Vertical profiles of seismic velocities in the Marmara region were given e.g. by Gürbüz et al. (2000), Horasan et al. (2002) and Clévédé et al. (2004). They differ by the resolved depth intervals but show no fundamental discrepancies. Table 3.2 shows the 1D-velocity model by (Gürbüz et al., 2000) as well as the calculated elastic properties and densities using equations (3.2)-(3.5).

Tab. 3.2: v_p*(z)-profile from Gürbüz et al. (2000) for the Marmara region and calculated elastic properties and density using eq. 3.2-3.5.*

depth [km]	**v_p [m/s]**	**v_s [m/s] (eq. 3.4)**	**ρ [g/cm³] (eq. 3.5)**	**ν (eq. 3.2)**	**E [GPa] (eq. 3.3)**
0	3000	1413	2.224	0.36	12
4.8	5300	3191	2.583	0.22	64
9.5	5900	3503	2.696	0.23	81
12.5	6200	3640	2.761	0.24	91
17	6500	3773	2.833	0.25	100
24	7300	4150	3.058	0.26	133
29	7900	4534	3.256	0.25	168

However, a 1D distribution can only be a first order approximation in view of the pronounced undulations in the basement-topography in the Marmara region. Velocities in the basins of the Marmara Sea are as low as 1.5-1.7 km/s in the uppermost layer with maximum thickness of ~750 m (Carton et al., 2007; Kanbur et al., 2007), which means $E \leq 1$ GPa, $\nu \approx 0.47$ and $\rho \approx 1.7$ g/cm³. Velocity increases below to 3.8 km/s ($E = 27$ GPa, $\nu = 0.27$ and $\rho = 2.35$ g/cm³). Average velocities of the sediments in the basins are in the range of 2-2.5 km/s (Carton et al., 2007), which corresponds to $E \approx 4$ GPa, $\nu \approx 0.43$ and $\rho \approx 2.0$ g/cm³. The limestone basement-topography, which was taken as the 4.5 km/s iso-surface, implies $E = 43$ GPa, $\nu = 0.23$ and $\rho = 2.46$ g/cm³. From refraction seismics along a EW profile crossing the whole Marmara Sea Bécel et al. (2009) inferred $v_p = 5.7$-6.3 km/s for the crystalline basement ($E = 75$-94 GPa, $\rho = 2.66$–2.78 g/cm³) and $v_p = 6.7$ km/s ($E = 108$ GPa, $\rho = 2.88$ g/cm³) for a ~10 km thick lower crust.

This information is incorporated into the fourth material distribution (MAT_grad) that accounts for the local geometry of topography/bathymetry, basement-topography and Moho and additionally for a vertically stratified velocity profile in the crust. This is done by introducing vertical gradients in rock properties within the implemented geometric volumes, with predefined values at the top and base of the respective layers as sketched in Fig. 3.4. As a result, the combined constraints on geometry and the $v_p(z)$-profile reflect lateral changes in density and elastic properties since the respective horizons vary laterally with depth. Poisson's ratio is assumed as constant ($\nu = 0.25$) throughout the crust and mantle, except for the sediments that exhibit higher values (Brocher, 2005). Rock properties in the mantle are assumed as constant.

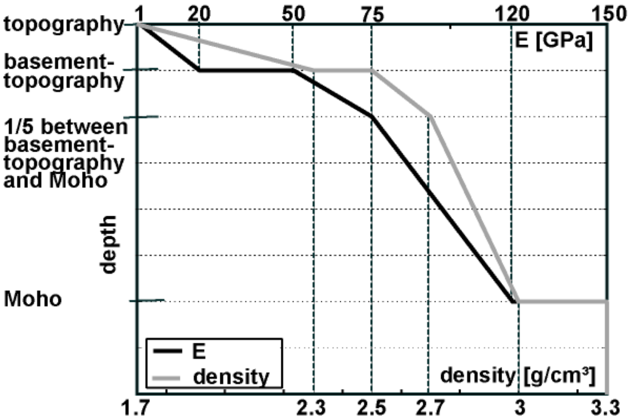

Fig. 3.4: MAT_grad rock property distribution: Depth-dependent E and ρ accounting for both published 1D-velocity profiles and geometrical constraints from topography/bathymetry, basement-topography and Moho. In those areas, where basement-topography coincides with topography (i.e. no sediments; Fig. 3.3 middle), E and ρ start with the values for the basement-topography at the surface. This pertains also to the regional model introduced in 3.6 in which sediments are not incorporated.

3.4 Static loads

Gravity is applied as a distributed load on each finite element in negative z-direction with an acceleration of 9.81 m/s². Areas below sea level are subjected to hydrostatic pressure due to the weight of the water column above. This is performed by applying a distributed surface load acting perpendicular to the local bathymetry at a pressure corresponding to the local water depth. At the bottom of the model vertical displacements are constrained to zero, whereas lateral motions are permitted. Except the water load the upper surface of the model is free.

3.5 Prestressing

Within this subchapter it will be shown that numerical geomechanical models focussing on the absolute stress state need to be appropriately prestressed (3.5.1), and a way to do so will be presented (3.5.2). The conceptions shown in the following were developed within the Tectonic Stress Group at the Geophysical Institute at the University of Karlsruhe and were presented by Eckert et al. (2007) and Hergert and Heidbach (2007).

3.5.1 Gravity requires prestressing.

Subjecting a model to gravity poses two key demands on the initial stress field in the model. This will be explained in the following.

Fig. 3.5 depicts a rectangular portion of the Earth's crust such as the hitherto described model. Subjecting this model to gravity while constraining lateral displacements at the sides of the model and vertical displacements at its bottom to zero, leads to subsidence in the model volume due to elastic compaction. The model is squeezed under its own weight. The reason for this is that the model is initially stress free. Therefore, in order to avoid this compaction the model requires an initial stress field that acts to maintain the original shape of the model volume by balancing the gravitational forces. One of the possible stress fields that fulfil this condition is simply that one, which results from the procedure just explained (Fig. 3.5). Including this state of stress as initial conditions in a non-deformed mesh keeps the model in equilibrium with gravity so that the initially defined model geometry remains preserved.

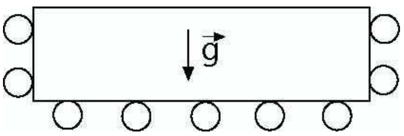

Fig. 3.5: Intuitive model set-up for obtaining gravitational prestress. The model is subjected to gravity with uniaxial strain condition.

The acquired prestress described above with zero displacement at the boundaries and acting gravity is an intuitive stress state commonly assumed for the Earth's crust in the absence of plate tectonic stresses (McGarr, 1988). The horizontal stress in this configuration is defined by the Poisson's ratio ν and vertical stress σ_V,

$$\sigma_{\bar{H}} = \frac{\nu}{1-\nu}\sigma_V = k\sigma_V \tag{3.6}$$

where k denotes the ratio of mean horizontal stress $\sigma_{\bar{H}} = (\sigma_H + \sigma_h)/2$ to vertical stress σ_V. σ_V can be approximated by the load due to the weight of the overburden. Assuming a Poisson's ratio of 0.25 as an average for crustal rocks (Turcotte and Schubert, 2002) yields a k-ratio of ~1/3 in the crust. In view of the comparably low horizontal stresses predicted by this assumption it is hardly imaginable how strike-slip or even compressive stress regimes (i.e. $\sigma_H > \sigma_V$) (Anderson, 1905) can exist in the Earth's crust. However, these stress regimes are common as seen, e.g. in the World Stress Map (Reinecker et al., 2005).

A global dataset of ~ 600 stress magnitude measurements was compiled with depth > 300 m (Fig. 3.6). The state of stress reflected by the data is clearly more compressive than implied by the uniaxial strain condition. It has to be concluded that the k-ratio observed in the crust is not solely due to Poisson's constraint. Evoking plate tectonic stresses to account for this discrepancy seems suggestive. However, the data originate from a broad range of tectonic stress regimes and even the k-ratio in provinces under extension exceeds the value resulting from the approach sketched in Fig. 3.5.

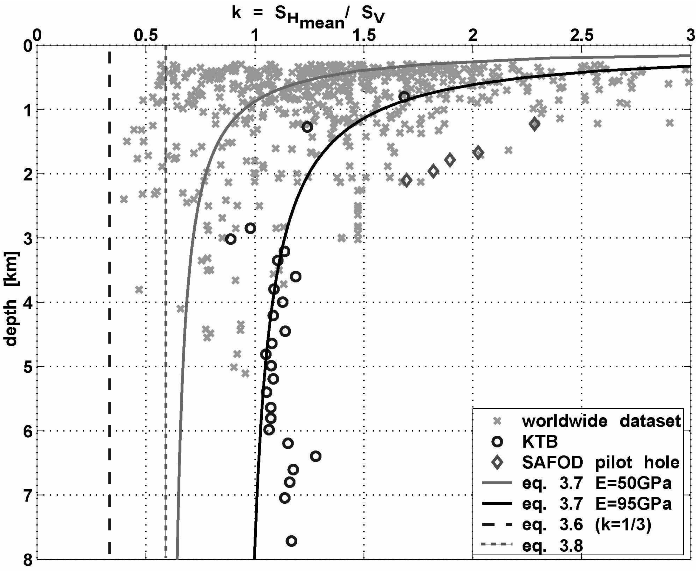

Fig. 3.6: Global compilation of stress magnitude measurements (>300m depth) including data from the KTB site (Brudy et al., 1997) and the SAFOD pilot hole (Hickman and Zoback, 2004). Solid curves represent k-ratios ($k=\sigma_H/\sigma_V$) after Sheorey (1994) for different Young's moduli (eq. 3.7). Dashed line is k-ratio from Poisson's constraint for ν=0.25 (eq. 3.6; Fig. 3.5). Dotted line is the same in poroelastic rock with P_f hydrostatic, α =1 and ρ=2.65 g/cm³ (eq. 3.8).

A comprehensive approach to describe stress magnitudes in the crust was proposed by Sheorey (1994). He assumed a 1D layered spherical model of the Earth and considered the structure of crust and mantle in terms of elastic properties, density, temperature gradient and the temperature dependent thermal expansion coefficient. Sheorey (1994) showed that stress in the upper crust and thus the k-ratio is a result of equilibrium between gravitational compaction and thermal expansion in a sphere. This means that surface stress depends on material properties and state variables down to the Earth's core. For the uppermost kilometres of the crust Sheorey (1994) provides the following approximation for the k-ratio:

$$k = 0.25 + 7E\,(0.001 + 1/z) \tag{3.7}$$

where E is the Young's modulus [GPa] and H depth [m]. The behaviour of the k-ratio against depth according to this formula is shown by the two curves in Fig. 3.6, which correspond to two different Young's moduli. The first one for E = 50 GPa, which is a typical value of crustal rock, represents the data cloud from worldwide stress measurements. The second curve addresses the KTB borehole in southeast Germany, where Brudy et al. (1997) reported the Young's modulus to be ~95 GPa. The KTB project probably represents the most thoroughly investigated dataset on deep *in situ* stresses (Brudy et al., 1997). The prediction of Sheorey (1994) yields a remarkable fit to the KTB borehole data (Fig. 3.6).

The theoretical model of Sheorey (1994) is of spherical symmetry as mentioned above. Hence, if preconditions such as flat topography and the absence of geological structures and plate tectonic forces are fulfilled, this theory should be applicable to estimate the k-ratio. The KTB drilling site is located in a tectonically relatively quiet area with no pronounced topography and thus satisfies the mentioned preconditions. An example for a place at which the presence of geological structures like faults, plate tectonics or topography becomes relevant is the SAFOD pilot hole near the San Andreas Fault (Hickman and Zoback, 2004). Here, the k-ratio is tectonically increased (Fig. 3.6).

The lesson from these observations for the modelling is that the application of gravity requires not only a prestress acting against the downward directed gravitational load of the rock mass but also an appropriate initial ratio of horizontal to vertical stress. Eq. 3.7 obviously describes the data. For this reason the k-ratio given by Sheorey (1994) is used to prestress the model.

Actually, the observed k-ratios probably reflect also other contributions. In poroelastic rock another term adds to the horizontal stress under uniaxial strain conditions (Engelder and Fischer, 1994):

$$\sigma_{\bar{\mathrm{H}}} = \frac{\nu}{1-\nu}\sigma_{\mathrm{V}} + \alpha\frac{1-2\nu}{1-\nu}P_{\mathrm{f}} \tag{3.8}$$

where P_f is pore fluid pressure and α the Biot coefficient of effective stress (Fabricius, 2006). Assuming hydrostatic pore fluid pressure and α=1, the k-ratio is significantly increased compared to k=1/3 from eq. 3.6 (Fig. 3.6). Nevertheless, the k-ratio proposed by Sheorey (1994) is used since it fairly represents the data.

How to obtain this stress state technically in the model is explained in the following subchapter 3.5.2. The role of prestress on the model results is discussed in 4.2.4 by comparing the effects of the two different prestress definitions given by eq. 3.6 and 3.7.

3.5.2 Obtaining an initial stress state

The k-ratio proposed by Sheorey (1994) that was identified to largely represent the observed ratio of horizontal to vertical stress in the crust, is established in the model by a modelling procedure presented in the following. Whether or not the physical processes behind Sheorey's (1994) concept are actually responsible for the stress state, is not investigated here. The k-ratio proposed by Sheorey (1994) is established in the model not by simulating physical processes resulting in the desired stress state but instead in a technically most simple way, as explained in the following.

The model is extended laterally and underlain by a second layer (Fig. 3.7a). The sides of the outer layer are inclined at an angle, which is defined by lines linking the upper corners of the model to the centre of the Earth. The upper model boundary remains unconstrained. At the lateral and lower model boundaries displacements perpendicular to the faces are not allowed.

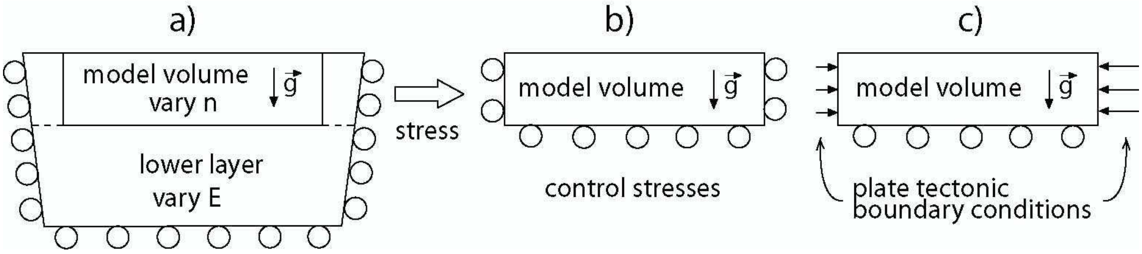

Fig. 3.7: Prestressing procedure. a) Model set-up for employing the effect of elastic compaction to simultaneously obtain gravitational prestress and fulfilling the k-ratio given by Sheorey (1994) (eq. 3.7). b) Stresses from model a) are included in an non-deformed mesh with uniaxial strain condition and gravity is applied. After a stabilising step, stresses at test sites are compared to the stresses proposed by Sheorey (1994). Once, this state of stress is obtained, c) boundary conditions addressing the problem to be solved are applied to the internally deformed and prestressed model b).

The effect of elastic compaction is used as a technical way to obtain the k-ratio according to Sheorey's formula (eq. 3.7) in the model. Depending on the model dimensions and on the thickness of the lower layer the Poisson's ratio in the upper layer and the Young's modulus in the lower layer has to be increased until the stress state in the model corresponds to that of Sheorey (1994). The effect of changing E in the lower layer is to alter the slope of the k(z)-curve in the model. Increasing Poisson's ratio in the upper layer shifts the k-ratio uniformly to higher values.

To control the initial stress in the model three vertical profiles were selected, one in the NE, one in the NW and one in the S of the model area (Fig. 3.8). The sites were chosen as a compromise between the following criteria. On the one hand, the sites should be close to the area of interest at the centre of the model and at some distance to the model boundaries that may be influenced by boundary effects. On the other hand, the sites should not be located in the vicinity of faults and near pronounced gradients of the topography since these cause perturbations of the stress field that are not included in Sheorey's formula.

Due to faults and lateral density and stiffness contrasts the original model volume is non-uniformly deformed within the enlarged model in Fig. 3.7a). Therefore, when inserting the stress field from this model into the non-deformed mesh with uniaxial strain condition, an unstable state is present that eventually causes an altered stress field. For this reason, stresses have to be controlled after a balancing step in the original model volume (Fig. 3.7b). Normally, the displacements during this balancing step are at most in the order of a few metres so that the constructed geometry is not affected in its precision.

At each of the three sites depth profiles of σ_V, σ_H and σ_h were extracted and the corresponding k-ratio was compared to the theoretical k-ratio after Sheorey (1994). For the homogeneous material model (Tab. 3.1) the best fit was obtained for $\nu = 0.425$ in the upper layer and E = 400 GPa in the lower layer (Fig. 3.7a; 3.8). The mismatch at depths less than ~2 km is related to the size of the finite elements. The stresses in a linear finite element are determined only at one integration point within the element. As a consequence, high stress gradients cannot be resolved and the extracted stress from an element is the stress at the depth of this single integration point. Apart from that, the upper one or two element layers are generally found to yield inadequate stresses, which is probably related to the free surface and displacement boundary conditions at the model sides. As a consequence, the resulting stresses at shallow depths are not as compressive as they should be.

It is emphasised that the values for Young's modulus and Poisson's ratio used in this step are not physically meaningful and do not reflect the true properties of the rock! The effect of elastic compaction and Poisson's constraint is only used as a technical way to simply obtain the stress state according to the k-ratio proposed by Sheorey (1994) in the model as an initial stress state. Surely, in the consecutive modelling steps (Fig. 3.7b;c) a realistic Poisson's ratio is used.

Proceeding from this initial stress state in Fig. 3.7b) that represents a stable stress state, plate tectonic boundary conditions are applied, that are presented in the next chapter 3.6. The initial stress state is laterally isotropic, given effects of topography, lateral density variations, faults and other complexities are negligible. The plate tectonic boundary conditions act to change the stress regime by altering mainly the horizontal stresses so that σ_H and σ_h start to diverge.

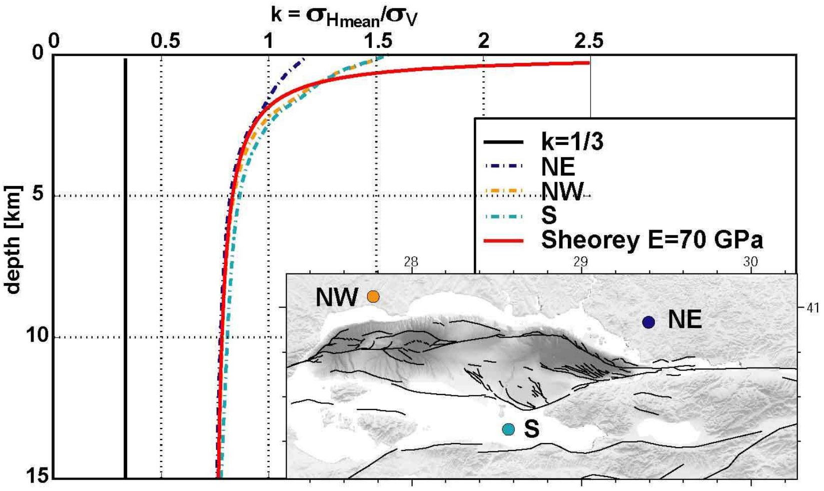

Fig. 3.8: Modelled k(z)-profiles (dashed lines) at three test sites indicated on the map using the approach sketched in Fig. 3.7a and b. Solid red line marks the theoretical stress state given by eq. (3.7) (Sheorey, 1994), against which the model is calibrated. For comparison, the low k-ratio resulting from eq. (3.6) is shown (black line).

3.6 Plate tectonic boundary conditions - regional model

Plate tectonic forces determine the pattern of stress and strain within the region of interest, depending on the structure and constitutive behaviour in its interior. Therefore, appropriate boundary conditions have to be found for the model described so far (Fig. 2.2 and 3.3), which is termed as the Marmara model in the following. To obtain suitable plate tectonic boundary conditions for the Marmara model, a second model is used, that covers northwest Anatolia and hence a wider area (Fig. 3.9). This model will be referred to as the regional model. The regional model serves to generate a velocity field of Northwest Anatolia, that is used to drive the local Marmara model at its boundaries by interpolating the nodal velocities of the regional model onto the boundary nodes of the Marmara model. The advantage of this so-called sub-modelling approach is that the complicated boundary conditions for the Marmara model evolve consistently with the surrounding of the model area and can be obtained with relatively simple boundary conditions for the regional model (2.1).

The regional model covers an area given by 25-33°E and 38.8-42°N (735x395 km) and reaches down to 42 km bsl. The regional model includes topography, the Moho and the northern, middle and southern branch of the NAF but not the basement-topography and the smaller faults included in the Marmara model. The mesh of the regional model is coarser than that of the Marmara model, which implies a lower resolution of 1-5 km (1.541.892 linear elements).

The regional model is run for 20 kyrs. Several variations of the regional model are tested concerning boundary conditions, coefficient of friction and distribution of density and Young's modulus. The goodness of a model is evaluated by comparing the model results to independent constraints as GPS observations (3.6.1) and maximum horizontal stress orientations (3.6.2). A velocity misfit is defined as

$$m = \frac{\sum_i \left| \vec{v}_{GPS} - \vec{v}_{mod} \right|}{\sum_i \left| \vec{v}_{GPS} \right| + \sum_i \left| \vec{v}_{mod} \right|} \tag{3.9}$$

where $\vec{v}_{GPS}$ and $\vec{v}_{mod}$ denote the observed and modelled horizontal velocities, respectively, and it is summed over all observation sites. The misfit parameter is however not committing for two reasons. First, the seismic cycle with locked faults is not implemented here. As a consequence, the modelled velocities near the faults have to differ from the observed ones, which contain the effect of interseismic deformation. Further explanation on this issue is given in 3.6.1. Second, the model results should fit the data particularly well near the boundary of the Marmara model since the Marmara model is driven by the nodes of the regional model, which are closest to the boundaries of the Marmara model. Correspondingly, deviations at greater distance from the boundary do not matter for the results of the Marmara model.

3.6.1 Lateral boundary conditions and velocity field

Different boundary conditions for the regional model are set up in order to find out how to optimally drive the Marmara region. A first set of boundary conditions for the regional model makes use of published rotation rates around the Euler poles of the involved tectonic plates. These block rotations rely on the assumption of rigid plates and are determined as to best explain the GPS observations on each plate. Of course, the model is not rigid but compressible. Nevertheless, the geodetic observations can be well represented by rigid body rotations over wide areas of the region and are therefore used as a first approximation. This model series is run with μ=0.05 and homogeneous rock properties (E=70 GPa, ν = 0.25, ρ = 2.65 g/cm^3, i.e material distribution MAT_hom in Tab. 3.1).

Regional Model 1 (REG_1) applies the rotation of the Anatolian Plate with respect to Eurasia after Reilinger et al. (2006) (32.1°E, 30.8°N, 1.231°/Myr) at the boundary of the regional model south of the northern branch of the NAF. The nodes at the northern model boundary are laterally fixed, since vanishing velocities are observed there. The nodes at the eastern and western model boundary north of the NAF are constrained to zero in EW direction and are free parallel to the boundary (rollers). REG_2 is the same as REG_1 except that it applies the rotation of the Marmara Plate after Reilinger et al. (2006) (28.4°E, 35.1°N, 2.370°/Myr) at the western model boundary between the northern and southern branch of the NAF. REG_3 is the same as REG_2 south of the northern branch of the NAF. At the whole boundary north of the NAF the Black Sea Plate rotation after Reilinger et al. (2006) (31.4°E, 43.3°N, 0.231°/Myr) is applied. The results of these three models are very similar (Tab. 3.3). REG_2 fits the observations slightly better than the other two and is shown in Fig. 3.9. The rather stable northern block as well as the westward motion south of the NAF with a turn to southwest in the west is well reproduced. However, the modelled velocities along the southern shore of the Marmara Sea and on Armutlu Peninsula are too southerly directed and too small in magnitude. Right there, between the middle and southern branch of the NAF, the modelled velocities should match the observed ones as good as possible since the southern boundary of the Marmara model passes along there (Fig. 3.9). Using the velocity field of REG_2 to drive the Marmara model would introduce an artificial NS-extension into the Marmara model due to the overrated south component in velocity. Besides, slip rates along the NAF would be underestimated due to the deficient EW-rate.

Other descriptions of the Anatolian Plate rotation south of the northern branch of the NAF were tested. REG_4 and REG_5 apply the Anatolian Plate rotation after McClusky et al. (2000) (32.6°E, 30.8°N, 1.2°/Myr) and Meade et al. (2002) (31.72°E, 32.37°N, 1.59°/Myr), respectively (the value of the latter was published by Le Pichon et al., 2003). Due to the more easterly located Euler Pole and the smaller rotation rate by McClusky et al. (2000) compared to Reilinger et al. (2006) the former rotation suits not as good as the latter for northwest Anatolia and the situation near the southern shore of the Marmara Sea outlined in the previous paragraph becomes worse. In contrast, the rotation by Meade et al. (2002) slightly improves the modelled velocity field (Fig. 3.9; Tab. 3.3). The smaller misfit is mainly due to increased rates. The modelled velocities in the east have too high north components due to the more northerly located Euler Pole and the smaller circle. This is however well beyond the area, which is relevant for the Marmara model.

It has to be noted, that the rotations from the respective authors rely on GPS observations in similar but different defined Eurasia-fixed reference frames and therefore the modelled velocities should be compared only with the corresponding observations and in the associated reference frame. The aim here is however finding optimum boundary conditions for one observed velocity field in its reference frame and it is irrelevant, where the optimum boundary conditions come from. The velocity field observed by Reilinger et al. (2006) is used as comparison since this dataset comprises the longest record and more observation sites.

In order to find more appropriate boundary conditions the observed velocity field is decomposed into its NS- and EW-velocity field (Fig. 3.10). A velocity pattern appears that is difficult to reconcile with rigid body rotations. East of 28-29°E observed velocities are remarkably straight and uniformly EW directed. Stations KPKL and FIST with small south and north components, respectively, do not impair this conclusion. Both stations have an observation period of 1 ½ years, which is much less than the other stations in the region and is reason for their higher standard deviations. The north component of station FIST is not observed in more recent observations (Ergintav et al., 2007). West of 28°E observed velocities show significant south components. It seems that there is a relatively sharp transition between 29° and 28°E, where velocities experience this change in the NS-component (Fig. 3.10). Mechanically, this can be understood by the presence of a number of grabens in west Anatolia, such as the Akçay, Kütahya, Simav, Bakircay, Gediz and Menderes grabens (Akman and Tüfekçi, 2004; Bozkurt and Sözbılır, 2004). These grabens are mostly EW oriented and accommodate NS extension originating from the Hellenic subduction zone. Maybe also elevated heat flow observed in distinct areas around 28°E (Pfister et al., 1998) is related to this transition.

The presence of a transition as described implies that the assumption of rigid body rotation of the Anatolian Plate is misleading in west Anatolia since with pure rotation the onset of southward motion would be considerably farther east than observed and the rather sharp transition in southward motion would not be accounted for. Based on this finding, the hitherto models are modified. REG_6 attempts to incorporate the transition in southward motion by applying the rigid block rotation velocity of REG_2 at 32°E uniformly between 32°E and 29°E along the southern boundary (Fig. 3.9). Between 29°E and 28°E a linear interpolation bridges the accrued gap to the Euler rotation west of 28°E. The results of REG_6 show a clear

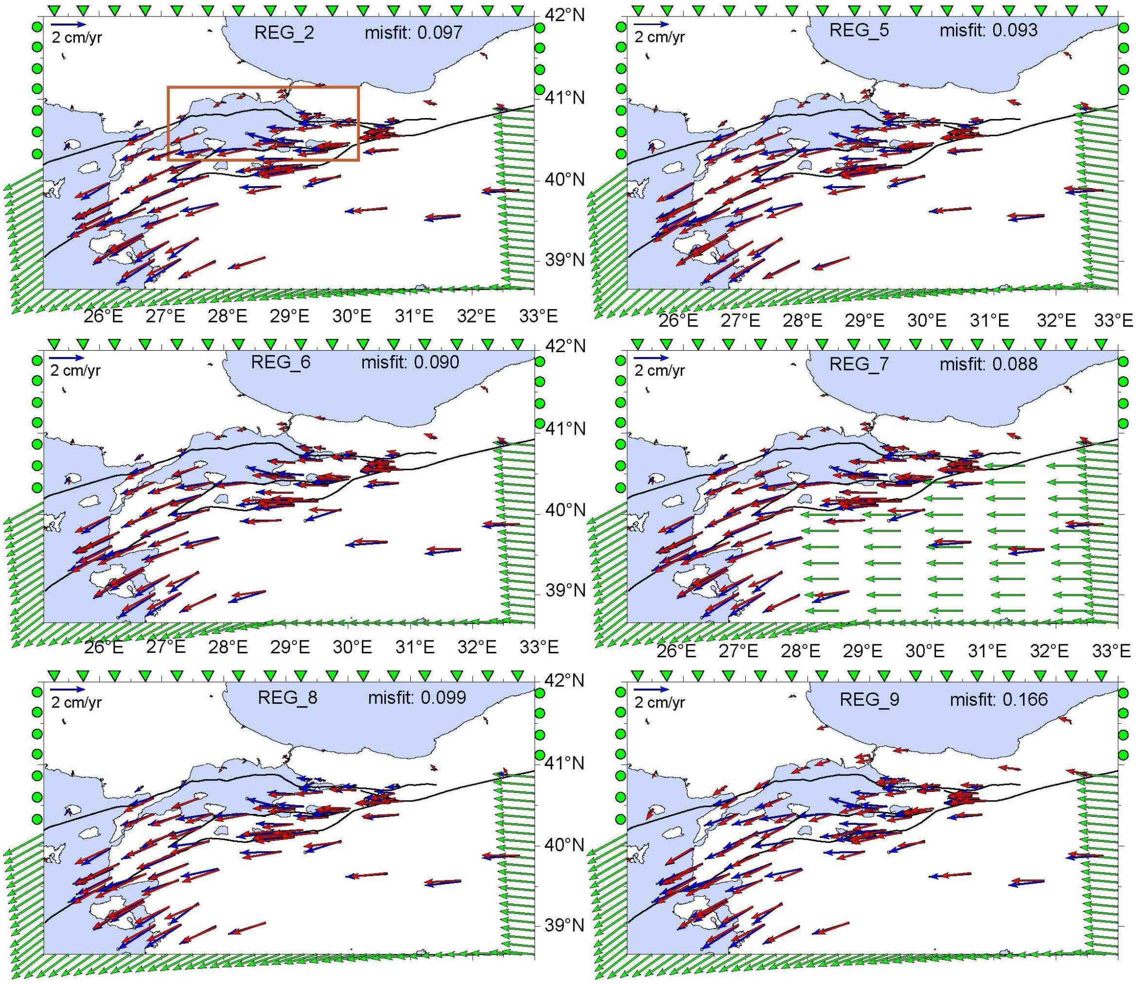

Fig. 3.9: Regional model: Comparison between modelled (red arrows) and GPS derived velocities (blue arrows, Reilinger et al., 2006). Green symbols indicate applied plate tectonic boundary conditions. Orange box marks boundary of the Marmara Model.

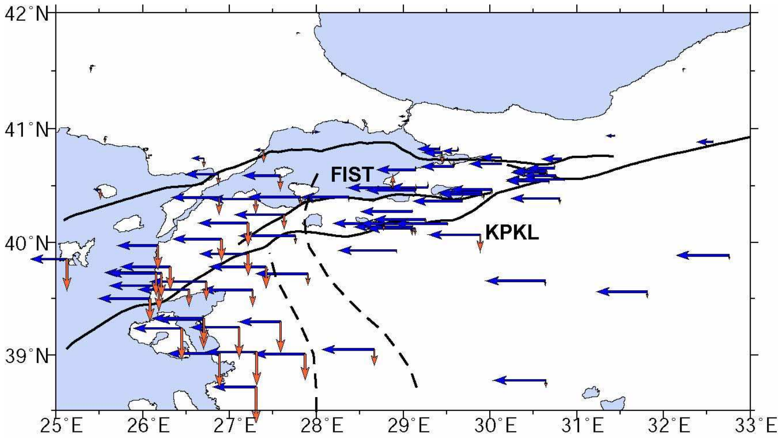

Fig. 3.10: Observed velocity field (Reilinger et al., 2006) decomposed into EW (blue) and NS (red) components. A transition at ~28-29°E (dashed lines) separates uniform EW directed velocities in the east from motion with clear south components west of it.

improvement and most important, the modelled velocities are now in good agreement in direction with the GPS observations near the southern shore of the Marmara Sea (Fig. 3.9). But still, they are somewhat too small in rate. For this reason, REG_7 applies additionally the EW components of the rotation of the Anatolian Plate at the bottom nodes south of the NAF east of

28°E (Fig. 3.9). In the previous models the bottom nodes are laterally unconstrained. The modelled velocity field of REG_7 shows only minor deviations from the GPS observations near the southern shore of the Marmara Sea.

Tab. 3.3: Regional model: description and misfits with respect to observed velocities and stress orientations.

No.	**Model description**			**Model results**	
	boundary conditions (more detailed in the text)	**µ’**	**material distr. (Tab. 3.1)**	**vel. misfit (eq. 3.9)**	**mean abs. σ_H dev.**
1	N fixed, S+W Anatolia rotation (Reilinger et al., 2006)	0.05	MAT_hom	0.097	19.5°
2	REG_1, but W Marmara rotation (Reilinger et al., 2006)	“	“	0.097	20.2°
3	REG_2, but N Black Sea rotation (Reilinger et al., 2006)	“	“	0.101	19.7°
4	REG_1/2, but S+W McClusky et al. (2000)	“	“	0.102	21.1°
5	REG_1/2, but S+W Meade et al. (2002)	“	“	0.093	19.2°
6	REG_2, but Anat. rot (Reil. et al., 2006) at 32°E uniform between 32°E and 29°E, transition between 28 and 29°E	“	“	0.096	22.7°
7	REG_6, east of 28°E south of NAF east comp. of vel. from Anat. rot. (Reilinger et al., 2006) at bottom nodes	“	“	0.088	23.2°
8	REG_2	0.0	“	0.099	30.7°
9	“	0.6	“	0.166	17.8°
10	“	0.05	MAT_moho	0.099	20.2°
11	“	“	MAT_grad	0.099	20.4°

A parameter study was performed for the effective coefficient of friction µ’ on the faults. REG_2 was run with µ’ in the range of 0 ≤ µ’ ≤ 0.7. These values cover the full range between µ’ at elevated pore fluid pressures and friction values from laboratory experiments (3.2). The results depicted in Fig. 3.11 reveal almost constant misfits above µ’~0.2. For lower µ’, the misfit decreases and reaches a minimum for µ’ = 0.03. For µ approaching zero, modelled velocities become worse again.

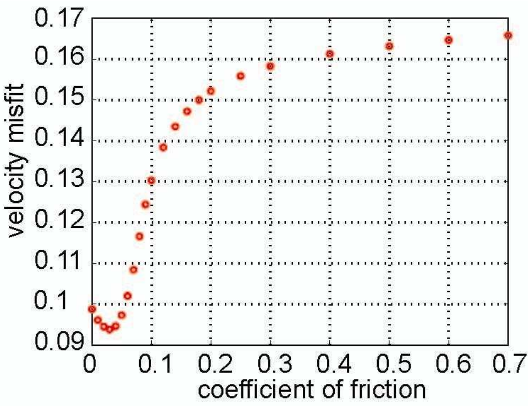

Fig. 3.11: Variability of the velocity misfit (eq. 3.9) with coefficient of friction for regional model REG_2.

The velocity field obtained for µ’ = 0.0 and µ’ = 0.6 (REG_8 and REG_9, respectively) is shown in Fig. 3.9. In the former case, the blocks are decoupled from each other. In contrast, for high µ’ the northern block is pulled to the west due to the drag exerted from the west moving southern block, which is in turn decelerated. Since the seismic cycle with locked faults is not incorporated here, optimum values of µ’ have to result in overestimated velocities south of the NAF and lower velocities than observed north of it. This pertains in particular to the northern branch of the NAF that accommodates most of the relative plate motion. For this reason, modelled velocities just south of the Ganos Fault and Izmit Bay are fine though they exceed the observed velocities. With $\mu' = 0.6$, the much too fast velocities on the northern block and the too slow velocities south of the NAF imply that laboratory friction coefficients are not applicable to the NAF. Optimum values for μ' are right below 0.1. A value of $\mu'=0.05$ will be used in all following models. In 5.3 it will be shown that a model with locked faults at seismogenic depths and otherwise $\mu'=0.05$ widely reproduces the observations.

The influence of inhomogeneous distribution of rock properties on the velocity field and stress orientations was investigated with two additional models. REG_10 and REG_11 include the Moho and the latter additionally a vertical gradient in rock properties in the crust (MAT_moho and MAT_grad in Table 3.1, respectively).

Increasing E in the whole model volume or parts of it should lead to faster velocities in the centre of the model since the dissipation of strain energy with distance from the model boundary is reduced. However, the models show that introducing inhomogeneous rock properties does not substantially alter the modelled velocities (Tab. 3.3).

It can be concluded that at least for the kinematics, density and elastic rock properties are of minor importance and that boundary conditions and discontinuities by faults and their frictional behaviour are the key elements controlling the model results.

3.6.2 Stress orientations

The World Stress Map (WSM) database[2] is a global compilation of the orientation of maximum horizontal stress σ_H and provides independent constraints to check the model results. In northwest Anatolia information on σ_H comes predominantly from earthquake focal mechanisms using the definition of Zoback (1992) that considers the plunges of the PTB axes. Besides, there are geological indicators for σ_H orientation and a few data points from overcoring stress measurements in the study area. The WSM data set was extended by ~200 data records so that in total ~300 data records are available in the model area (Fig. 3.12). The broader Marmara region is characterised by a NW-SE orientation of σ_H, which turns to WNW-ESE towards the Aegean and is NNW-SSE oriented in the east. Stress orientations in west Anatolia reflect the back-arc extension in the broader Aegean.

The trajectories in Fig. 3.12 were calculated excluding the data from geological indicators and WSM D quality data. It appears that the geological indicators in the northwest Aegean, that are EW to WSW-ENE oriented, do not reflect the contemporary stress orientations represented by the focal mechanism solutions (~WNW-ESE), so that a temporal change in σ_H orientation may have occurred. Stress data relying on the acoustic emission technique (Tuncay et al., 2002; not shown in Fig. 3.12) confirm the coast-normal orientation of σ_H at the Black Sea coast in the northeast of the model area and NS to NW-SE orientations in the east but are otherwise difficult to reconcile with the focal mechanism data. This may be due the shallow depths the specimens were taken from in mines so that local effects or topography could overprint regional stress orientations. This may also hold for the overcoring data point in the centre of Fig. 3.12 close by Uludag mountain.

The maximum horizontal stress orientations of the models presented in Fig. 3.9 were compared with the data (without geological and WSM D quality data) (Fig. 3.13). The modelled orientations were calculated from the stress tensor at grid points using the definition of Lund and Townend (2007), i.e. both the orientations and magnitudes of all three principle stresses are

---

[2] http://www.world-stress-map.org

considered. Comparison was performed at constant depth of 5 km since many of the focal mechanisms are without depth information or tabulated with a standard depth.

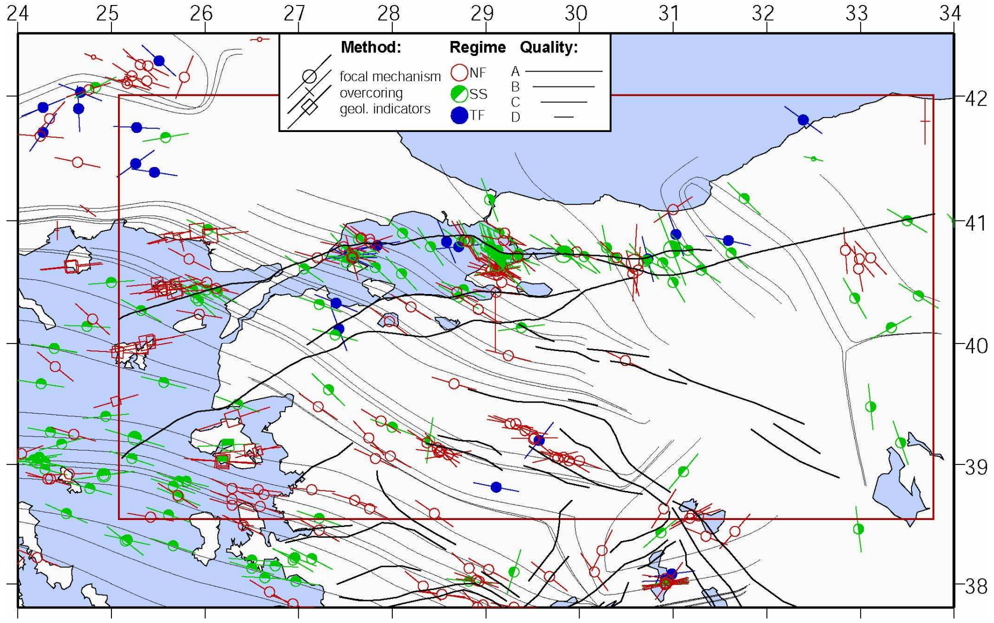

Fig. 3.12: Maximum horizontal stress orientations and stress regime in Northwest Anatolia from the supplemented World Stress Map (WSM) 2005 release. Red box indicates boundaries of the regional model (3.6). Thick black lines show major faults. Thin black lines show trajectories calculated from the stress data using a search radius of 70 km and requiring that at least three data points are within that range (data from geological indicators and WSM D quality data excluded for this purpose).

North of the NAF the models show the same pattern of σ_H orientations since the same boundary conditions were applied (Fig. 3.9). The modelled NNW-SSE orientation in the NE reflect WSW extension due to the boundary constraint in EW direction and the SW directed pull in the SW of the model. In contrast, σ_H is oriented perpendicular to the northwest model boundary since the northern block experiences drag from the west moving southern block but is not allowed to move to the west at the boundary and is accordingly compressed in EW direction. Although in this way modelled σ_H orientations are a result of the boundary conditions, the data nevertheless show this rotation of σ_H from NS to EW orientations north of the NAF as well.

The section between the northern and southern branch of the NAF along the western model boundary is characterised by NNW to NW trending modelled σ_H whereas the data trend NW to W. Since an extensional displacement boundary condition implies σ_H to be oriented perpendicular to the pulling direction it is difficult to simultaneously obtain a good velocity field and σ_H orientations with displacement boundary conditions here.

With vanishing fault friction modelled σ_H orientations become scattered since zero fault friction implies that the fault cannot withstand any shear stress, so that σ_H is oriented either parallel or perpendicular to the local fault strike (Fig. 3.13; REG_8). In contrast, with high fault friction the stress field is smooth across the faults (REG_9).

Apart from REG_8 (μ'=0.0) all models resemble the observed WNW-ESE oriented σ_H along the coast of northwest Anatolia in the southwest of the model area. In the southeast model quadrant however, only some of the tested boundary conditions are capable of reproducing the observed σ_H pattern. The observed σ_H orientations in the south show a fan-like arrangement with WNW trending σ_H west of an inflection point at ~30°E and NE trending σ_H east of it. Only the models

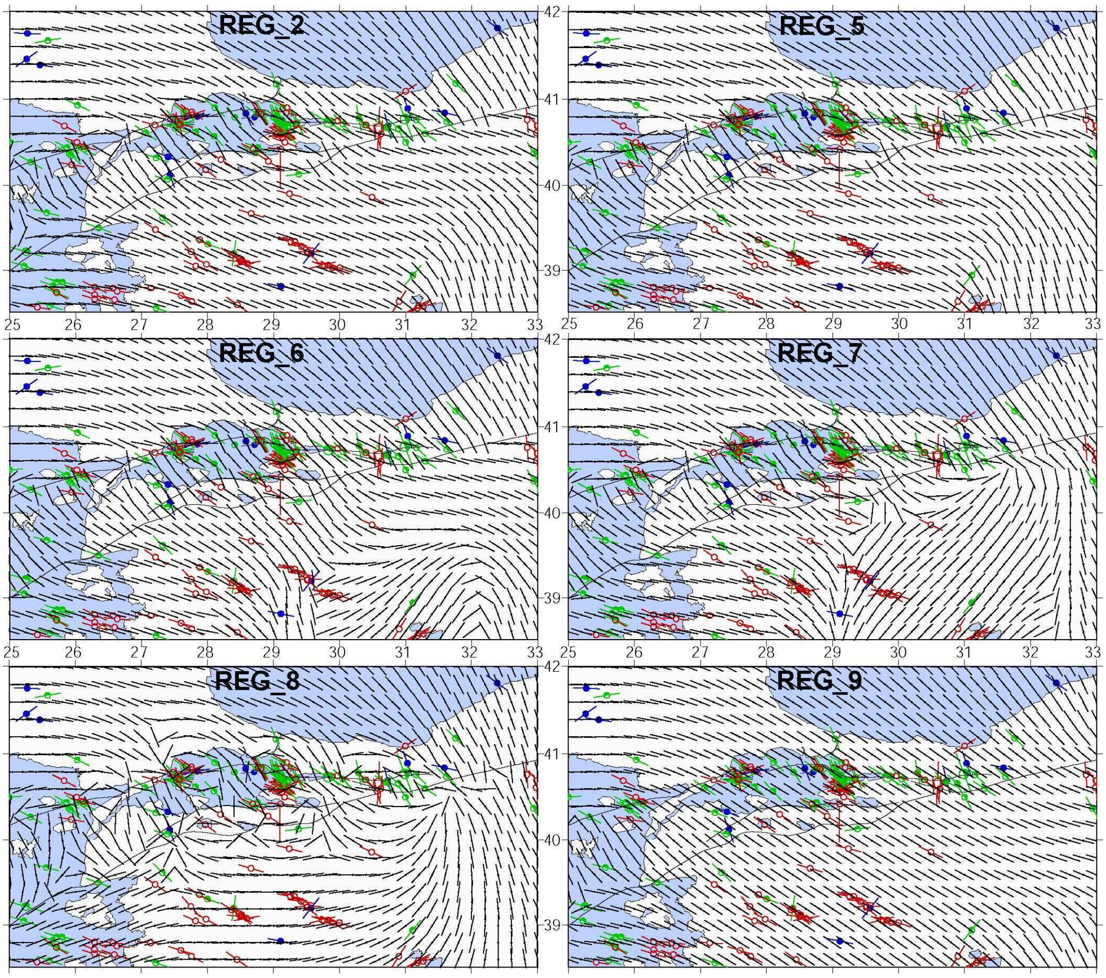

Fig. 3.13: Modelled σ_H *orientations (black lines) at 5 km bsl. in comparison to WSM data (coloured lines; without geological indicators and D quality data). Legend see Fig. 3.11.*

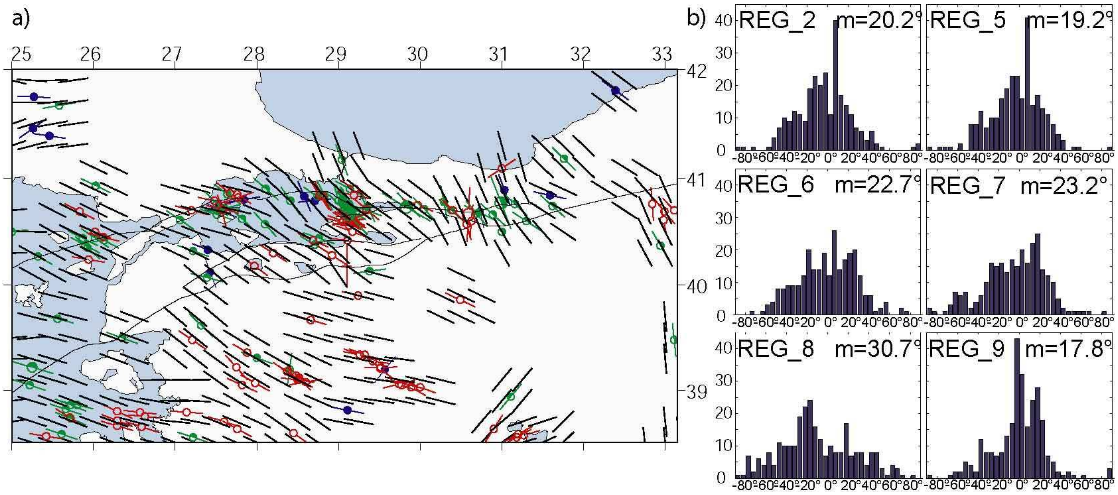

Fig. 3.14 a) Black lines indicate smoothed WSM data (coloured lines; excluding geological and D quality data) on a grid (0.25°E x 0.2°N), requiring at least one data point within 30 km distance to a grid point. Only data within the search radius (30 km) pertain to the orientation at a grid point. b) Histograms of the deviations between the modelled σ_H *orientations and the smoothed WSM data at grid points in (a). Positive values indicate clockwise deviations of the model with respect to the data and negative counter-clockwise. The mean absolute deviation m at all grid points is shown in the right top corner.*

with either µ’=0.0 (REG_8) or boundary conditions that deviate from pure rotations (REG_6 and REG_7) yield NE-SW oriented σ_H in the SE, whereas all other models show roughly perpendicular orientations there.

A quantitative measure of the deviations between modelled orientations and data is shown in Fig. 3.14. In order to reduce the influence of spatial data distribution on overall deviation, the WSM data were smoothed. The smoothed data points in Fig. 3.14a) represent a compromise between data coverage and resolution and the modelled orientations were compared to these (Fig. 3.14b). Models with rotation as boundary condition south of the NAF (REG_2 and REG_5) show more or less Gauss-like distributions around ~0°. The mean absolute deviation of ~20° is less than the accuracy of the data, which is ±25° for WSM C quality data as all single focal mechanisms. For REG_6 and REG_7 the distribution is wider and subgroups of data are not matched as the data cluster from normal faulting earthquakes in the Kütahya graben. The smallest deviation is obtained for µ’=0.6 (REG_9), whereas REG_8 with µ’=0.0 yields a clearly asymmetric distribution and the highest mean absolute deviation.

3.6.3 The preferred regional model

Coming back to the question which model to choose for providing boundary conditions for the local Marmara model, it turns out that the best model in terms of kinematics (REG_7) is not the best in terms of stress orientations (Fig. 3.13; 3.14b). The stress orientations of REG_6 and REG_7 indicate, that the presumed transition point is not between 28 and 29°E but somewhat farther east (Fig. 3.13). Placing the transition between 29 and 30°E (REG_6#) yields a smaller deviation and σ_H orientations that meet the principle features of the data in the south (Fig. 3.15). However, velocities of REG_6# (not shown) are too southerly directed south of the Marmara Sea (velocity misfit 0.095).

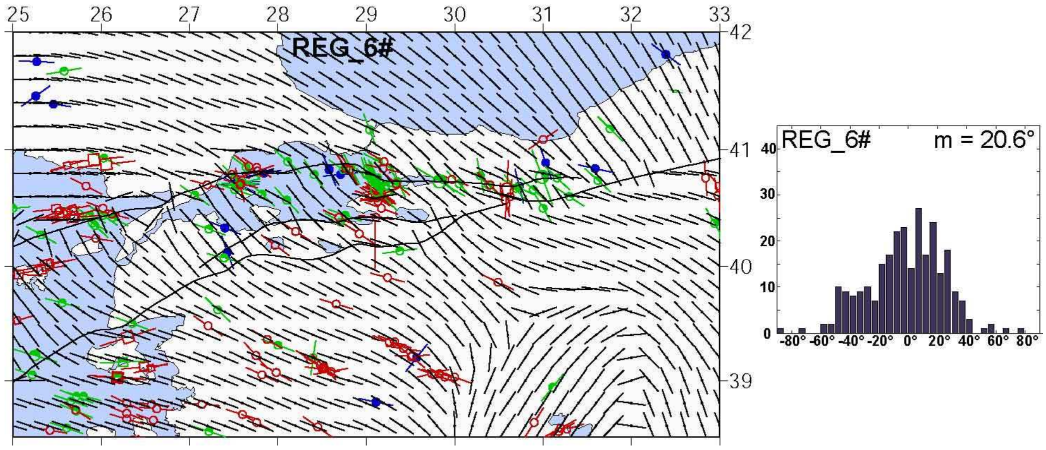

Fig. 3.15: Like REG_6, except the presumed transition shifted 1° to the east (29-30°E).

REG_7, which provides the best velocity field, is chosen as the one to drive the Marmara model although the observed orientations in the south are partly not well reproduced. Taking the observed velocity field as key criterion is consequent since not the modelled stress field but the modelled velocity field is used as boundary condition for the Marmara model. Besides, WSM C quality data, as all data from single focal mechanisms, have an accuracy of ±25°, which falls short of the precision of GPS observations. Eventually, stress orientations in the area of the Marmara Model hardly differ among the various models (except the models with extreme µ’) (Fig. 3.13).

Fig. 3.16 provides some observations and suggestions based on the results that may explain why the presented models can either reproduce the velocity field in the southern Marmara Sea area (REG_7) or the stress orientations in the south of the regional model area (REG_6#). GPS observations demonstrate that the area south of the Marmara Sea clearly deviates from the small circle rotation of the Anatolian Plate (Fig. 3.16). Several reasons may account for that. First, slip along the Eskişehir Fault. Velocities east of the Eskişehir Fault point inward of small circles whereas velocities west of it have an outward component. This can be explained by right-lateral slip along the Eskişehir Fault. Geological fault slip analyses found this normal fault to be active with a right-lateral component (Koçyığıt and Özacar, 2003; Tokay and Altunel, 2005; Ocakoğlu, 2007; Okay et al., 2008). Therefore, a model with boundary conditions as in REG_6# including the Eskişehir and other NW-SE striking normal faults with right-lateral slip component might result in EW directed velocities along the southern shore of the Marmara Sea due to relative motion on these faults. Second, it cannot be excluded that the geometry of the middle and in particular the southern branch of the NAF is oversimplified in the model and that a more detailed representation of the fault system in this area could explain the observed velocity field. Third, the deviation from plate rotation may be related to the Izmir-Ankara Suture, which approximately borders this area to the south (Fig. 3.16). The Sakarya Zone encompassed by the Izmir-Ankara and Intra-Pontide Sutures is made up of subduction-accretion units. Different lithologies on each side of the Izmir-Ankara Suture (Okay and Tüysüz, 1999; Okay et al., 2008) may imply contrasts in rock stiffness and different styles of deformation in the Sakarya Zone and the Anatolide-Tauride Block (Fig. 3.16). Eventually, stress orientations in the south of the regional model could be influenced by faults, which are not included in the model such as the faults encompassing the Simav and Kütahya grabens, the faults forming the Isparta Angle and the Eskişehir fault system (Fig. 3.16). Whatever the reason for the deviation from Anatolian Plate rotation south of the Marmara Sea may be, the boundary conditions of REG_7 effectively account for them, so that the observed velocity field is satisfactorily matched in this area.

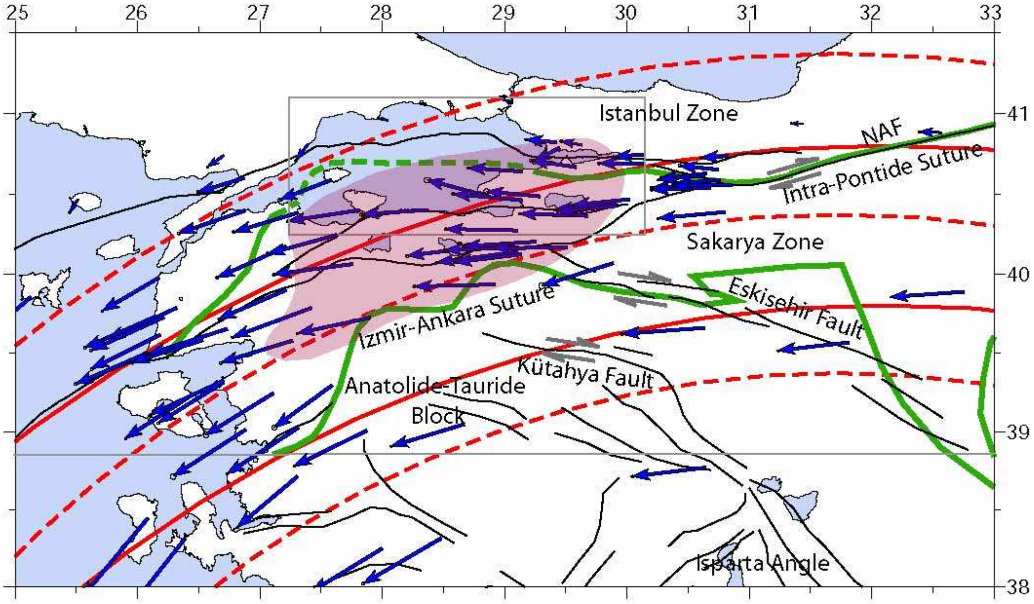

Fig. 3.16: Pink shaded area deviates from Anatolian Plate rotation. Blue arrows indicate GPS observations after Reilinger et al. (2006), solid red lines are small circles around the Euler Pole of the Anatolian Plate after Reilinger et al. (2006) and dashed red lines after Meade et al. (2002). Green lines mark sutures, grey line marks southern boundary of the regional model and grey box the boundary of the Marmara Model.

3.6.4 Stress regime and decomposition of the stress field in Northwest Anatolia

Before applying the modelled velocity field to the Marmara Model, additional results from the regional model are presented in the following as a contribution to the geodynamics of northwest Anatolia. Fig. 3.17 shows the stress regime for REG_7 representatively for all models. A common characteristic of all models is a dominant strike-slip regime north of the NAF, whereas south of the NAF extension prevails. This general pattern is largely reflected by the WSM data (Fig. 3.12). Near the eastern model boundary south of the NAF REG_7 shows extension due to the applied bottom pull whereas the other models show a strike-slip regime there. Areas under compression in the model are confined to a few restraining fault bends, which is confirmed by the data apart from some additional local thrust faulting events (Fig. 3.12). The most significant difference among the models results from the models with zero and high fault friction (REG_8 and REG_9). In the first case extension spreads north of the NAF, whereas in the latter case a coherent strike-slip regime reaches to the southern branch of the NAF.

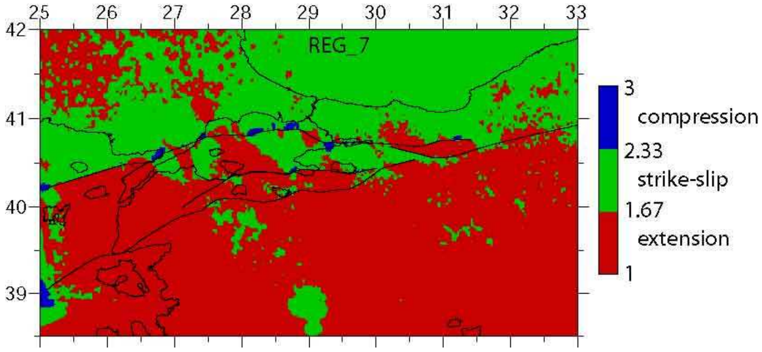

Fig. 3.17: Modelled stress regime for REG_7 at 5 km depth. See Fig. 3.12 for comparison with WSM data.

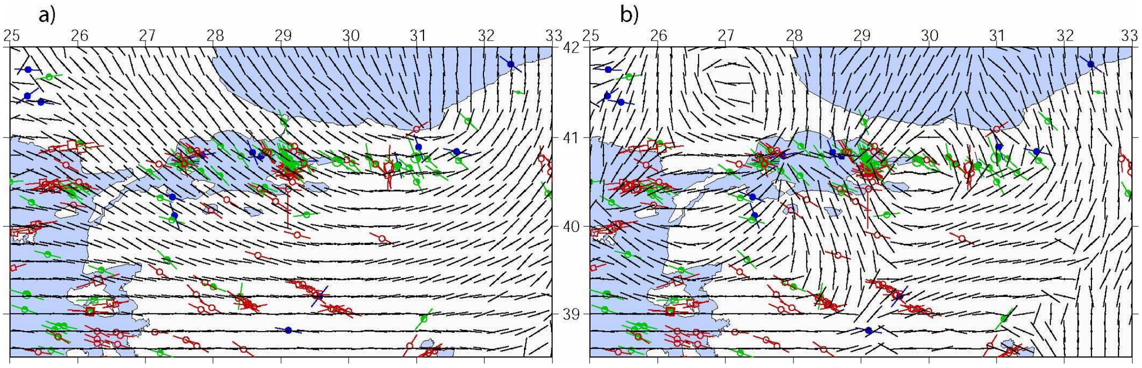

Fig. 3.18: Maximum horizontal stress orientations (black lines) at 5 km depth without plate tectonic boundary conditions in comparison to WSM data (coloured lines). a) Homogeneous model (MAT_hom; Tab. 3.1), i.e. only topography and water load determine σ_H orientations. b) MAT_moho, i.e. combined effects of topography and Moho.

In general, it has to be noted that the stress regime depends on the directions and relative magnitudes of the principle stresses and that small changes, in particular in transitional stress regimes, can flip the axes and the regime. This is one reason why the scattered patterns of both data and model results not fully agree. All in all this result agrees with the general view that the Marmara region is in a transitional stress regime between strike-slip and extension.

Some characteristics of the regional stress field are revealed by decomposing the stress field into its various components. Fig. 3.18 shows stress orientations due to gravitational potential energy, without the influence of plate tectonic stresses. Stress orientations from topography (Fig. 3.18a) resemble the orientations from plate tectonic boundary conditions (Fig. 3.13) in most parts of the model area. This can be explained by the elevated Anatolian Plateau (Fig. 1.2), which exerts stresses oriented towards the topographic lows of the Black Sea, Marmara Sea and Aegean Sea. One may conclude, that at least to some extent gravitational potential energy contributes to the plate tectonic stresses in this region. Similarly, the Moho acts to compress the overlying crust in the surrounding of shallow Moho areas. So σ_H is oriented radially with respect to the Marmara Sea (Fig. 3.18b), which was found as an area of relatively thin crust (Fig. 3.2). The same holds for the elevated Moho beneath the Black Sea and the Aegean.

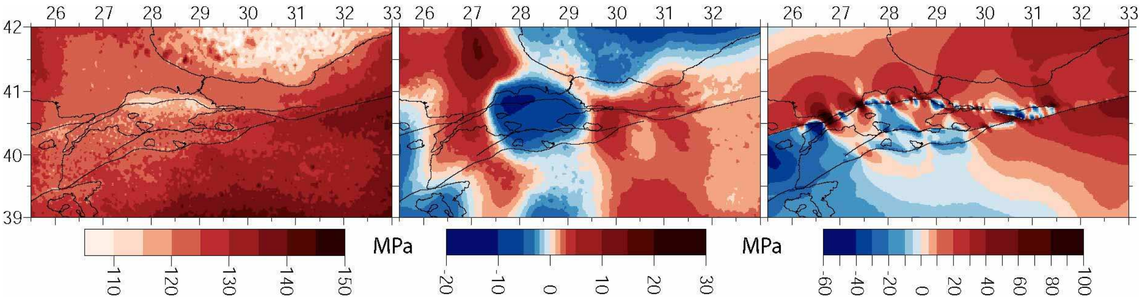

Fig. 3.19: a) σ_H magnitude at 5 km bsl. due to the overlying rock and water column for material distribution MAT_hom. b) Effect of Moho on σ_H magnitudes. Difference of σ_H magnitude at 5 km depth between material distribution MAT_moho and MAT_hom (Tab. 3.1), both models without plate tectonic boundary conditions. c) Effect of plate tectonic boundary conditions on σ_H magnitudes. Difference in σ_H magnitude at 5 km depth for MAT_hom (Tab. 3.1) between REG_2 (Tab. 3.3) including plate tectonic boundary conditions and the same model without plate tectonic boundary conditions. The total stress field (not shown) is approximately the sum of a), b) and c).

In Fig. 3.19 maximum horizontal stress magnitudes at 5 km bsl. due to the load of the overlying rock and water column (a), the influence of the Moho (b) and plate tectonic stresses (c) are separately shown. These three sources of stress contribute to the total stress field. The stress magnitudes in Fig. 3.19a) roughly reflect the topography since in first order the stresses are determined by the density (ρ=2.65 g/cm^3), the local topography and the k-ratio at 5 km depth given in Fig. 3.7. The extensional influence of the elevated Moho beneath the Marmara Sea amounts to a decrease of ~10 MPa in horizontal stress at 5 km depth beneath the Marmara Sea (Fig. 3.19b). The area from Biga Peninsula over Çanakkale Street to Strandja Massif as well as the area east of the Marmara Sea experience an amount of compression by the Moho. Areas of high depth gradients and depth differences of the Moho correspond to high stress changes, whereas areas of flat Moho hardly alter stress magnitudes in the upper crust (Fig. 3.2; 3.19b). Therefore, the influence of Moho variations on horizontal stress magnitudes might be even higher when using not a smoothed Moho surface as here, but the actual one with shorter wavelengths and steeper flanks. On the other hand the contrast in density and elastic properties between crust and mantle was chosen appreciably in this example (material distributions MAT_hom and MAT_moho in Table 3.1, respectively). Nevertheless, this result shows that the Moho influences stress magnitudes at seismogenic depths and hence the normal and shear stress on faults and by that the criticality of a fault, when assuming the Coulomb criterion (eq.1.1) as failure criterion. The question whether the uplifted Moho is a result of ongoing tectonics or whether an uplifted Moho caused the Marmara Sea depression and the features of extension there like normal faulting, remains open. Fig. 3.19c) shows the influence of plate tectonic boundary conditions on σ_H. The northern and eastern model area is compressed by plate tectonic stresses whereas in the southwest horizontal stresses decrease. In this way, the plate tectonic stress pattern reflects the relative orientations of the NAF's strike and the Anatolian Plate motion indicated by the small circles (Fig. 3.16). In most areas, the plate tectonic stresses clearly exceed the stresses caused by the Moho and form a significant fraction of the stresses by gravitational potential energy. The highest stresses and the highest stress gradients arising from plate tectonics are induced near faults so that the stress field beneath the Marmara Sea is strongly perturbed.

Having presented the data to be incorporated into the finite element model and a suitable velocity field for the northwest Anatolian region as boundary conditions for the Marmara model, it is passed over to the latter model in the following.

Chapter 4

Steady-state Marmara model

Within this chapter the steady state evolution of the velocity and stress field of the Marmara model introduced in chapter 3 is presented and discussed. “Steady state” refers to the secular evolution of stress and strain without the effects of the seismic cycle. In other words, it means the sum of interseismic velocity and coseismic displacement and of interseismic stress accumulation and coseismic stress drop averaged over a period of several seismic cycles. In some respects it is more relevant to know steady-state quantities than time-dependent ones that are affected by the seismic cycle, as for instance in case of slip rates on a fault. During the interseismic period the slip rate at the Earth’s surface is zero since the fault is locked. Instead we want to know the secular rate at which the two blocks are passing by each other since the slip rate is a key parameter for estimating the accrued slip deficit that will eventually be released during an earthquake. Therefore, kinematic results of a steady-state Marmara model are presented excluding the influence of the seismic cycle. In a technical sense this simply means that effective fault friction is uniform and low (μ’=0.05) throughout the whole depth extent of the faults, as already done in case of the regional model (3.6).

The boundary conditions for the Marmara model are as follows. The northern model boundary is laterally fixed and at the NW and NE boundaries EW displacements are constraint to zero as for the models presented in Fig. 3.9. The lateral velocity field of Regional model REG_7 (Fig. 3.9) is used to drive the Marmara model south of the main branch of the NAF. The model is run for 20 kyrs starting from the initial stress state (3.5).

Results of the Marmara model are presented in terms of kinematics (4.1), stress regime (4.2.1), stress orientations (4.2.2) and stress magnitudes (4.2.3). The results are compared with independent data and discussed. Chapter 4.3 summarises what the results of the steady-state Marmara model imply for seismic hazard.

4.1 Kinematics of the Marmara model

The nodal displacements of the finite element mesh are part of the model output of the performed stress-displacement analysis (Fig. 2.3). The kinematics of the Marmara model is shown in terms of the horizontal (4.1.1) and vertical (4.1.2) velocity field, including lateral and dip-slip rates on faults as well as profiles of relative plate motion across the plate boundary zone and of vertical motion across the Marmara Trough.

4.1.1 Horizontal velocity field

The modelled steady state horizontal velocity field is shown in Fig. 4.1. North of the NAF the modelled velocities are almost vanishing due to the applied boundary conditions, which constrain velocities to zero at the northern model boundary and prevent east-west motion at the eastern and western model sides north of the NAF. The counter-clockwise rotation of the Anatolian plate is visible in the southern part of the model area where the EW directed velocities in the SE turn gradually to SW in the southwest part of the model area. North of the NAF velocities are uniformly EW directed east of the Central Basin (hardly visible due to small rates) and at about the longitude of this basin they experience a clear south component so that velocities are directed in southwest directions in the NW model area.

The MMF represents a major discontinuity in the velocity field as velocities south of it are clearly increased by more than 1 cm/yr compared to north of it and velocities further increase to the south. Also smaller faults coincide with discrete changes in velocity. The change in rate across the NAF is more sharp at Sapanca Lake (eastern model boundary) and at the Ganos fault (western model boundary) than in the Marmara Sea, where the same velocity change is taken up between the northern and southern rim of the North Marmara Trough rather than exclusively at the MMF. This becomes apparent when tracing the 1 mm/yr and 17 mm/yr velocity isolines, which more or less border the North Marmara Trough. Velocities in the Çınarcık Basin show a slight north component and are significantly reduced compared to other areas south of the NAF.

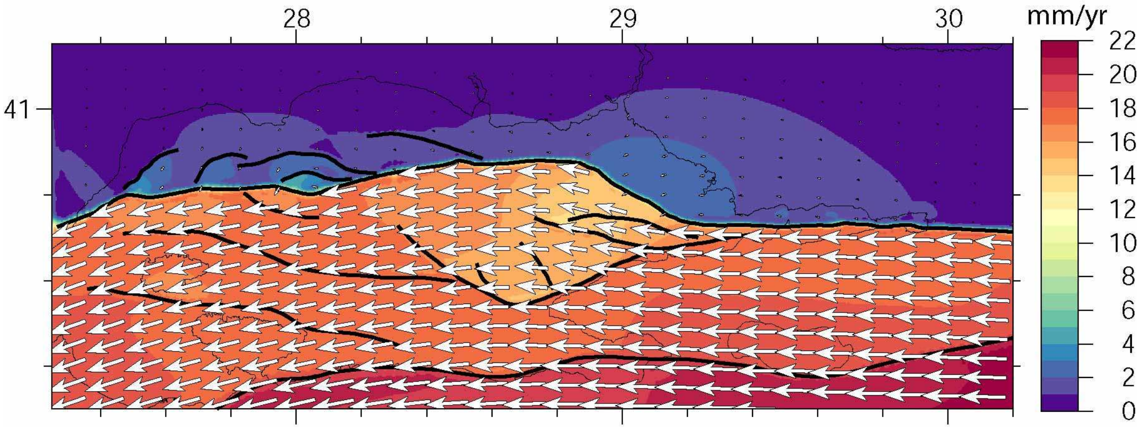

Fig. 4.1: Modelled horizontal surface velocity field in terms of rate (contours) and direction (arrows) relative to stable Eurasia (MAT_hom; Tab.3.1). Black lines mark implemented faults.

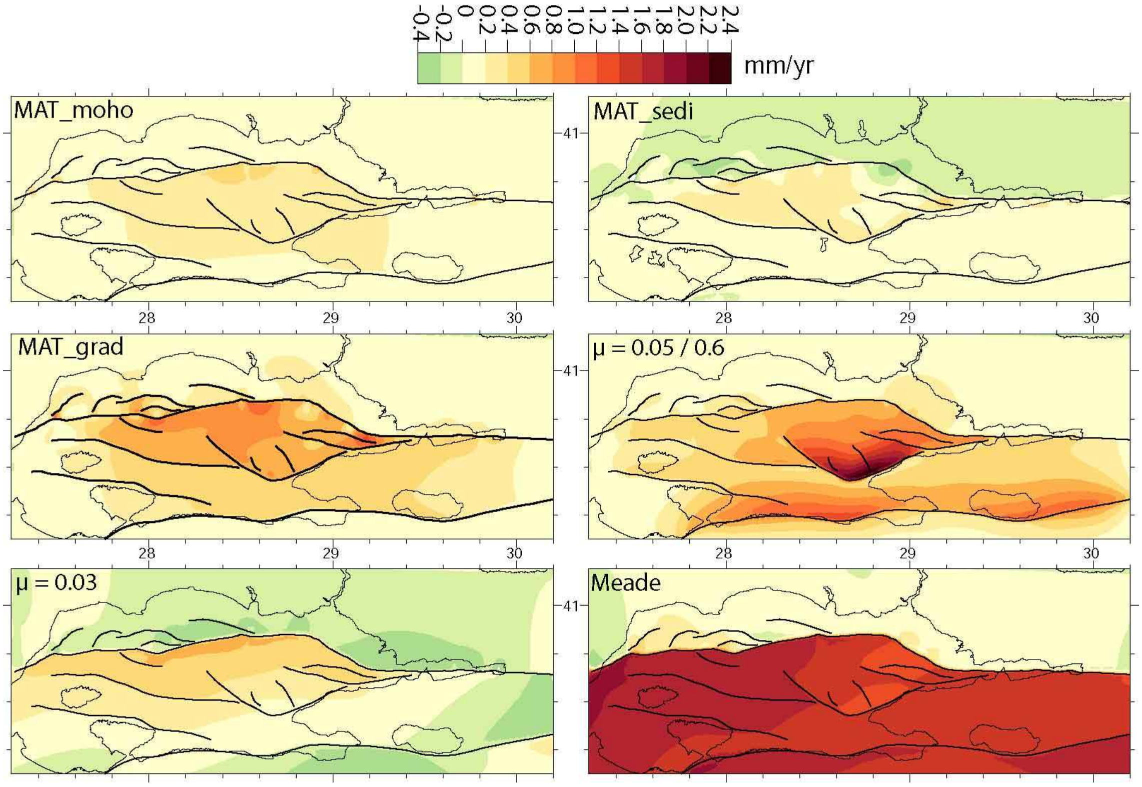

Fig. 4.2: Difference in horizontal velocity with respect to the homogeneous reference model in Fig. 4.1 of three inhomogeneous models (Tab. 3.1), two models with modified coefficient of friction (μ' = 0.6 except MMF and μ' = 0.03, respectively) and one with modified boundary conditions (Meade). Strictly speaking, also the model with μ' = 0.03 has changed boundary conditions since here the regional model with μ' = 0.03 was used to drive the Marmara model.

The homogeneous reference model (Fig. 4.1) with µ’ = 0.05 and boundary conditions from regional Model REG_7 was modified in order to assess the effects of rock properties, coefficient of friction and boundary conditions on velocities (Fig. 4.2). All three inhomogeneous rock distributions introduced in Tab. 3.1 yield higher horizontal velocities south of the MMF than the homogeneous model in Fig. 4.1 by up to 0.7, 0.9 and 1.3 mm/yr, respectively. A model with µ’ = 0.6 on all faults except the MMF (µ’ = 0.05) yields maximum increase of 2.4 mm/yr in the eastern Imralı Basin. Lowering µ’ on all faults to 0.03 yields moderate positive velocity changes in the North Marmara Trough and decrease of the same amount in the north and south. This model was driven by the velocity field generated by the same regional Model REG_7 as the models before except that µ’ = 0.03 was assigned to the faults. Two further models with changed boundary conditions were tested. The first is a modification of regional Model REG_7 using the Euler pole and rotation rate from Meade et al. (2002) instead of Reilinger et al. (2006). In response to this boundary condition the southern block of the Marmara model is faster by 1.5-2 mm/yr. Finally, a model driven not only laterally but also in z-direction according to regional Model REG_7 was run. However, horizontal velocities are not much influenced by that (< 0.1 mm/yr, not shown in Fig. 4.2).

4.1.1.1 Lateral fault slip rates

From the nodal displacements on top of the contact surfaces (faults) the lateral relative displacements between the nodes on either side of the fault were calculated. The result are the right-lateral slip rates at the surface presented in Fig. 4.3 for the homogeneous model. The northern branch is found to accommodate the largest part of the relative plate motion. Slip rates vary significantly along fault strike. In the eastern Marmara Sea and especially along the Prince Islands segment the slip rate is smaller than in the Gulf of Izmit and in the western Marmara Sea. A minimum slip rate of 12.4 mm/yr is found on the Prince Islands segment and a maximum rate of 17.8 mm/yr at the easternmost part of the Ganos Fault. Between the eastern end of Izmit Bay and Tuzla Bend the slip rate decreases from 17.0 mm/yr to ~14 mm/yr, which is a reduction of ~20 %.

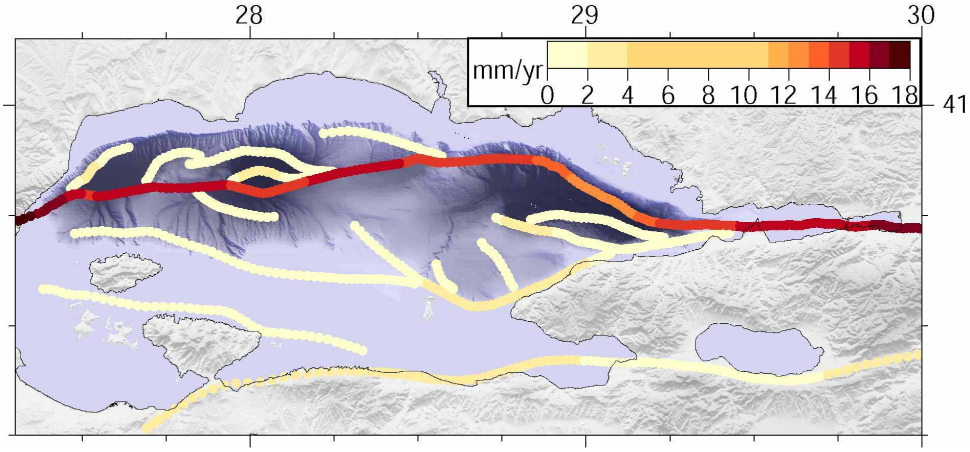

Fig. 4.3: Right-lateral surface fault slip rates for the homogeneous model (MAT_hom, Tab. 3.1).

The other faults exhibit right-lateral slip rates in the range of 0-3.2 mm/yr. Generally, the segments striking EW to ENE-WSW, which is the direction of plate motion, slip at higher rates than those oriented oblique to it. The modelled slip rates also depend on the length and depth extent of the faults. The main branch, which transects the whole model and reaches down to its base, shows the highest slip rates. The middle branch (reaching down to 20 km depth), Imralı Fault, outer Çınarcık Fault and Tekirdağ Fault (all 15 km), Southern Border Fault and the one between Marmara Island and Kapıdağ Penisnula (10 km) and the other faults (7.5 km) show decreasing rates.

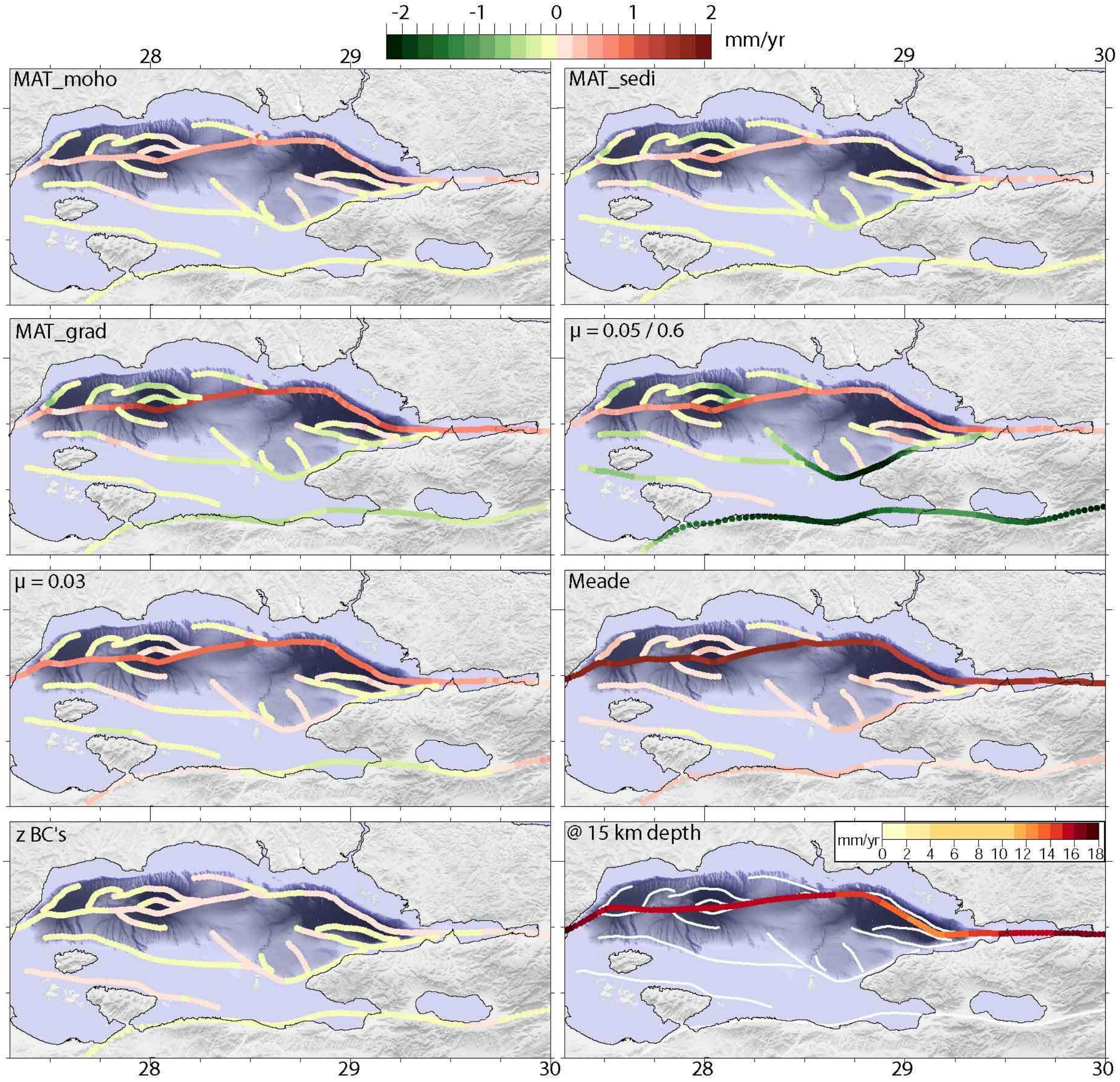

Fig. 4.4: Difference in lateral fault slip rate with respect to the homogeneous reference model in Fig. 4.2 of three inhomogeneous models (Tab. 3.1), two models with modified coefficient of friction (µ' = 0.6 except MMF and µ' = 0.03, respectively) and two models with modified boundary conditions (also in z-direction at the lateral boundaries and Meade). Strictly speaking, also the model with µ' = 0.03 has changed boundary conditions since here the regional model with µ' = 0.03 was used to drive the Marmara model. The figure on the lower right shows slip rate on the MMF of the homogeneous reference model in Fig. 4.3 at 15 km depth. Here, white lines mark surface traces of implemented faults.

The model variations introduced above affect right-lateral slip rates (Fig. 4.4) as implied by the results previously presented (Fig. 4.2). Incorporation of the Moho raises the slip rate by 0-0.6 mm/yr on the MMF, whereas rates slightly decrease on the other faults. Consideration of the sediments yields an increase of slip rates on the MMF by up to 0.5 mm/yr for material distribution MAT_sedi and by 1.5 mm/yr for MAT_grad. Assigning µ' = 0.6 to all faults apart from the northern branch reduces slip rates on the smaller faults by up to 2.2 mm/yr on the middle branch of the NAF while the slip rate on the MMF moderately increases (< 1.2 mm/yr). By about the same amount the slip rate increases on the MMF with µ' = 0.03 whereas rates on the other faults show only minor changes. Applying the other definition of Anatolia's rotation as boundary condition (Meade) brings about significant increase of slip rate by up to 1.8 mm/yr on the MMF and also moderate increase on the other faults. In contrast to the other model variations the maximum changes here are not concentrated in the central parts of the MMF but instead more or less uniformly increased through the whole model. Slip rates remain unchanged when driving the Marmara model also in z-direction at the model sides.

The right-lateral slip rate on the MMF of the reference model (Fig. 4.3) was also controlled at 15 km depth (Fig. 4.4, bottom right). Slip rates at depth are similar compared to surface slip rates. However, the rate is constant between Istanbul Bend and Ganos Bend while surface slip rates show small variations. The minimum in slip rate on the Prince's Islands Segment is shifted to the southeast at depth.

4.1.1.2 EW velocities across the plate boundary

Fig. 4.5 shows how relative plate motion is accommodated across the plate boundary zone based on the velocity field shown in Fig. 4.1. Since relative plate motion is roughly EW directed in the Marmara region, EW velocities across the plate boundary zone were controlled at four NS profiles at 28, 28.5, 29 and 29.5°E. The northern branch accounts for the dominating part of relative plate motion with strong increase of westward motion from north to south across this fault. Qualitatively, this is a common feature at all longitudes, but the importance of the slip rate on the MMF with respect to total relative plate motion across the model area is different at the respective longitudes.

The profile at 29°E crosses from north to south the MMF, the inner and outer Çınarcık Faults, the Imralı Fault and the middle branch of the NAF, which is expressed by the five steps in Fig. 4.5 from north to south. In contrast, the profile at 29.5°E crosses only the main and middle branches of the NAF, visible by the two pronounced steps in Fig. 4.5. The EW velocity just south of the Imralı Fault at profile 29°E is the same as on profile 29.5°E just south of the main branch of the NAF, and also north of the main branch EW velocity is the same on both profiles, so that the difference in EW velocity across the main branch at 29.5°E is jointly taken up by four faults at 29°E (Fig. 4.5).

Between the steps in EW velocity indicating slip on faults, EW velocities are mostly not constant with latitude. For instance, EW velocity increases by 1 mm/yr between the main and middle branch of the NAF at 29.5°E.

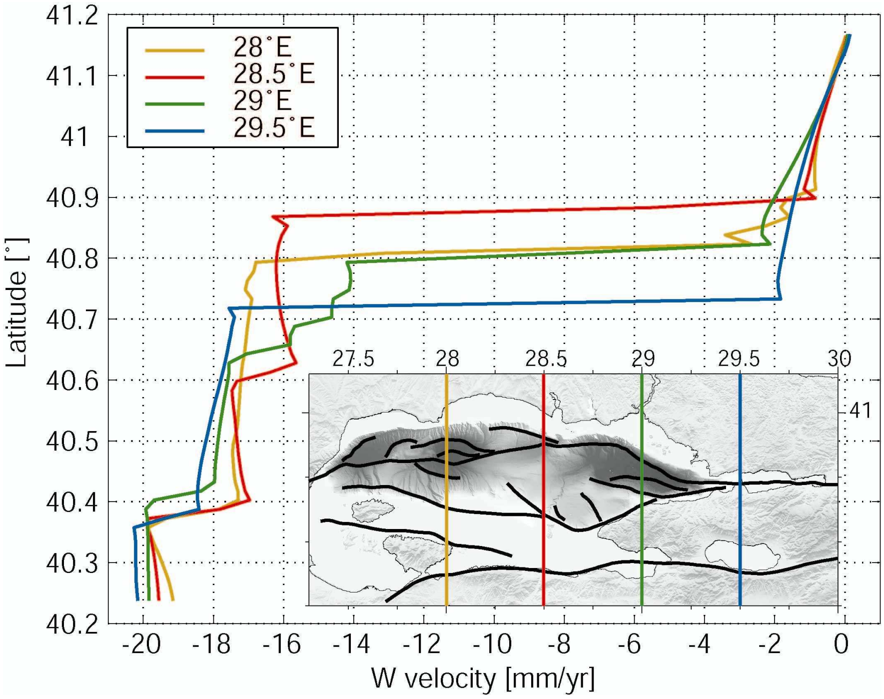

Fig. 4.5: EW velocities along four NS-profiles at longitudes shown on the inlay map.

Tab. 4.1: Summation of slip on the MMF, on the other faults and of internal deformation to total relative EW velocities between northern and southern model boundary at the four longitudes shown in Fig. 4.5. Percentage numbers indicate fraction of slip rate on the MMF to total relative EW velocity across the model width.

	Right-lateral slip rate on the MMF [mm/yr]	**Sum of right-lateral slip rate on the other faults [mm/yr]**	**Internal deformation [mm/yr]**	**Σ [mm/yr]**
28°E	14.4 / 75 %	7.6	-2.8	19.2
28.5°E	14.7 / 75 %	5.4	-0.5	19.6
29°E	12.8 / 64 %	5.7	1.4	19.9
29.5°E	15.3 / 76 %	1.7	3.2	20.2

4.1.1.3 Rotation rates

From the modelled horizontal velocity field shown in Fig. 4.1 rotation rates were calculated (Fig. 4.6). More precisely, the anti-symmetric part of the velocity gradient field at the surface

$$\frac{1}{2}\left(\frac{dV_E}{dN}-\frac{dV_N}{dE}\right),$$

which can be identified with the rotation rate, was computed at the centre of each surface triangle element from the velocities at the elements' nodes (e.g. Cai and Grafarend, 2007).

The eastern Çınarcık Basin, Armutlu Peninsula and the area north of the NAF are found to rotate clockwise, whereas the Tekirdağ Basin, Central Basin, Imralı Basin and Western Çınarcık Basin as well as the area south of the basins show counter-clockwise rotations. The highest rotation rates are associated with fault bends.

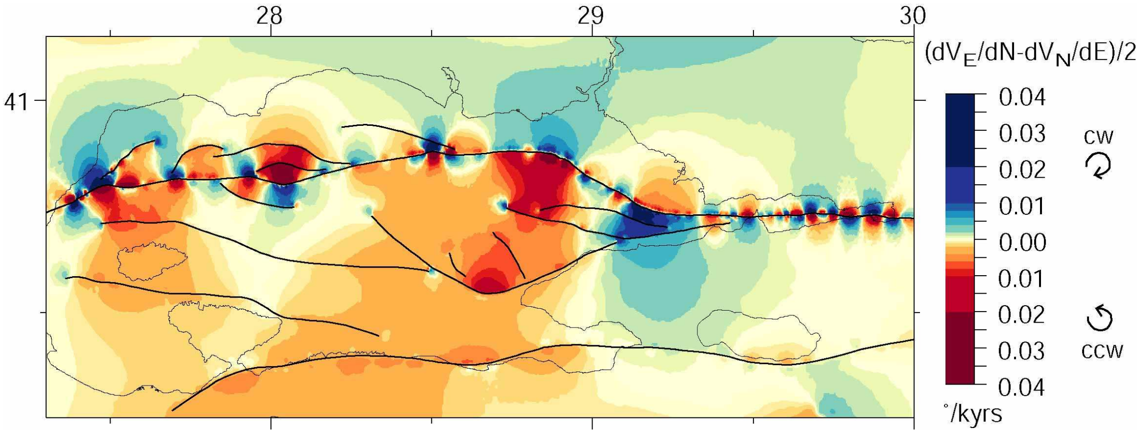

Fig. 4.6: Rotation rates calculated from the modelled velocity field. Blue colours indicate clockwise rotation, red colours counter-clockwise rotations. Black lines indicate implemented faults.

4.1.2 Vertical velocity field

The modelled vertical velocities are shown in Fig. 4.7. The most striking characteristic of the vertical motion pattern is subsidence of rather sharply bounded areas in the Marmara Sea with clearly increased subsidence rates compared to the surrounding. Pronounced changes in vertical velocity coincide with implemented faults. Modelled subsidence rates reach 3.4 mm/yr in the Tekirdağ Basin, 2.6 mm/yr in the Central Basin and 1.5 mm/yr in the Imralı Basin. The maximum subsidence rate is found in the Çınarcık Basin with 4.1 mm/yr.

Uplift is confined to basically two areas. Between the western shore of the Marmara Sea and the western model boundary the maximum uplift rate reaches 1.2 mm/yr and the plateau in uplift pattern there is raised at rates of ~ 0.7 mm/yr. South of Izmit Bay between the northern and middle branch of the NAF and further to the south the model shows uplift at a peak uplift rate of 0.8 mm/yr just south of the northern branch and rates of 0.1-0.4 mm/yr over most of the uplifted area. Another area of uplift, though at moderate rates of 0-0.2 mm/yr, is the northern shelf and coastal area to the north of the Central Segment of the MMF.

The footwalls of faults are quite stable with minor subsidence rates or slight uplift as along the Prince Islands segment, the western part of the Imralı Fault, the Southern Border Fault, the Tekirdağ Fault and the MMF south of the Tekirdağ Basin. The block south of the Southern Border Fault hosting Marmara Island is tilting to the south. This can be seen by the increasing modelled subsidence rate across the Island from north to south between the two faults adjacent to the Island.

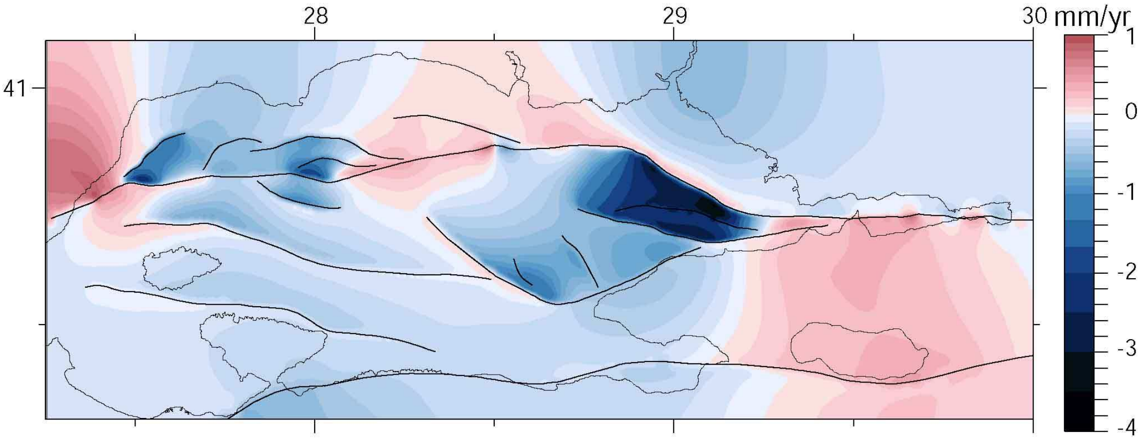

Fig. 4.7: Modelled vertical motion pattern at the surface for the homogeneous model. Blue colours indicate subsidence, red colours uplift.

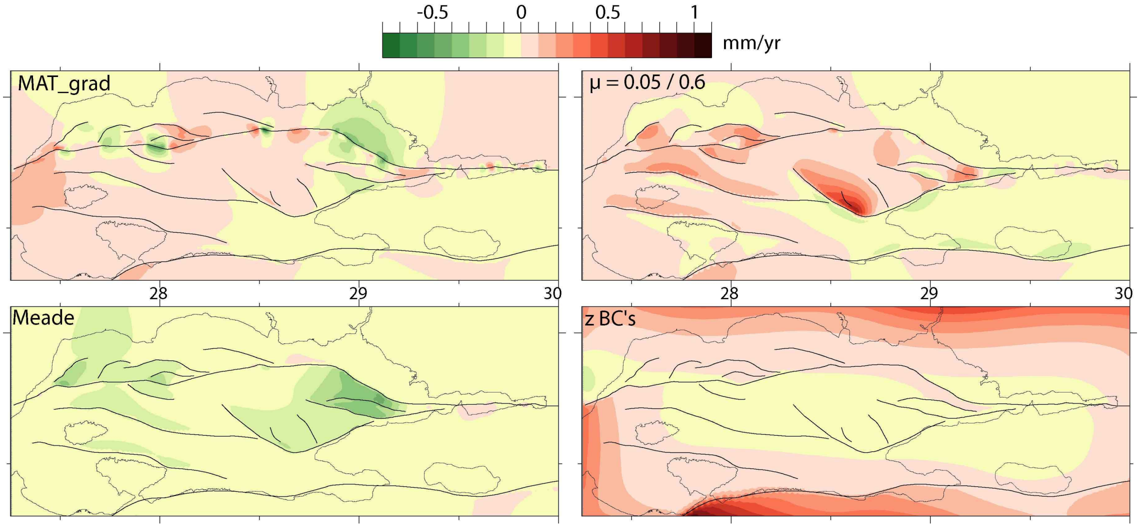

Fig. 4.8: Difference in vertical velocity with respect to the homogeneous reference model in Fig. 4.7 of an inhomogeneous model (MAT_grad; Tab. 3.1), a model with modified coefficient of friction (μ' = 0.6 except MMF and μ' = 0.03, respectively) and two with modified boundary conditions (also in z-direction at the lateral boundaries and Meade). The other models in Fig. 4.4 show negligible deviations (< 0.2 mm/yr) in vertical velocity from the reference model.

Both positive (1.1 mm/yr) and negative (-0.8 mm/yr) maximum changes in vertical velocity of the various models were obtained by the model using the rock distribution MAT_grad (Fig.

4.8). The additional subsidence holds for the Çınarcık and Central Basins while the positive changes concentrate on the southwest model area. Assigning a high friction coefficient to the smaller faults results in an uplift component with respect to the reference model which is highest close to the faults. In contrast a subsidence component of up to –0.5 mm/yr which is similar in pattern to that of the reference model (Fig. 4.7) results from applying the Meade boundary conditions. Constraining vertical velocities at the model boundaries by the corresponding velocities in the regional model yields primarily an uplift component (< 1.1 mm/yr) which drops towards the model centre. All other model variations show only small changes in vertical velocity (< 0.3 mm/yr but mostly < 0.1 mm/yr).

4.1.2.1 Dip-slip rates at faults

The vertical relative motion between neighbouring nodes on the northern and southern sides of the faults at the surface is shown in Fig. 4.9. Due to the steep dips of the faults the presented rates are almost the same as dip-slip rates within the fault planes (for the fault segments with the lowest dips the deviation is less than 5 %).

The highest dip-slip rates occur on the on the faults along the rims of the basins. Slip rates vary along strike of these basin bounding faults indicating preferred sections for subsidence. Generally, high dip-slip rates are found at fault segments that dip at the lowest angles (Fig. 3.3) and which also exhibit relatively high lateral slip rates. The fault segments linking the Çınarcık and the Central Basin and the latter with the Tekirdağ Basin as well as the fault in the Izmit Bay hardly show dip-slip since these faults were implemented almost vertical. Maximum dip-slip rates reach up to 4.3 mm/yr at the Prince’s Islands Segment and 3.8 mm/yr at the MMF just east of the Ganos Bend. These values are a little higher than absolute subsidence rates since the footwalls show small uplift rates there (Fig. 4.7).

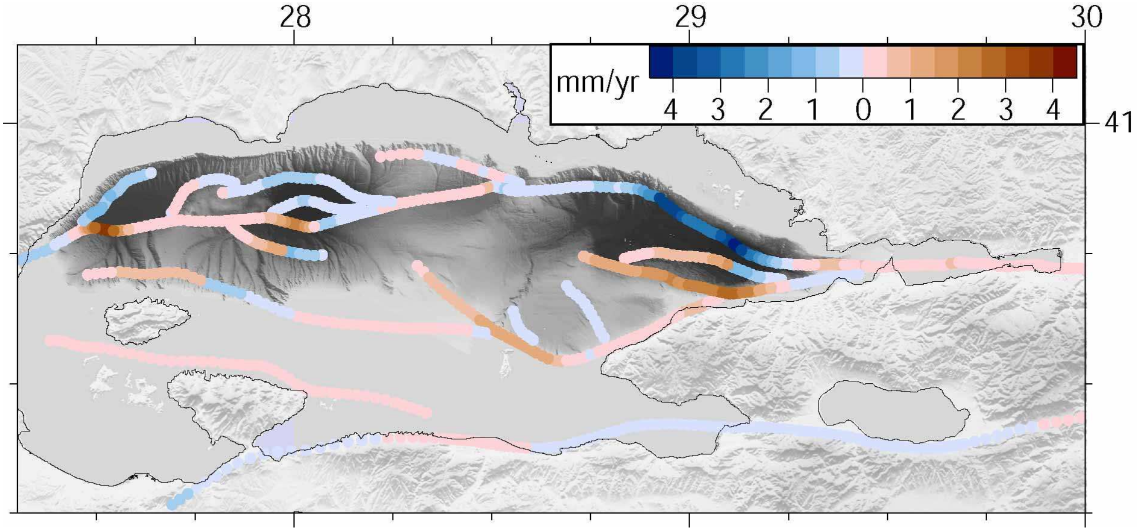

Fig. 4.9: Vertical slip rate on the faults. Red colours indicate that the northern block subsides relative to the southern one. Blue vice verca.

4.1.2.2 Vertical motion across the basins

The vertical motion on a profile crossing the Imralı and Çınarcık Basins is shown in Fig. 4.10. Subsidence in these basins is clearly expressed by higher subsidence rates within the basin bounding faults. The footwalls of the normal faults are rather stable. Modelled subsidence in the Çınarcık Basin is faster in the north than in the south and the Imralı Basin tilts to the south.

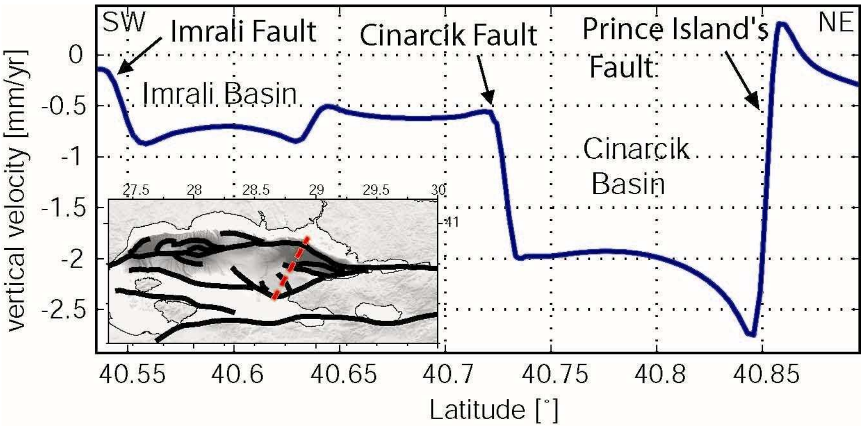

Fig. 4.10: Vertical velocity on a SW-NE profile crossing the Imralı and Çınarcık Basins (dashed line on inlay map).

4.1.3 Discussion kinematics

How do the presented results agree or disagree with observational data, other calculations and suppositions in the literature? Investigating this is not only important to range in the presented kinematics whether it approximates the actual situation or not. A comparison with independent data provides also the basis for assessing the reliability of the combined stress-displacement analysis. Though kinematics does not provide direct information on stress, it nevertheless sets some constraints on the stress field. Any correct stress field should yield kinematic results consistent with observations.

4.1.3.1 Horizontal velocity field

From the results presented in chapter 4.1, the relative plate motion between the Anatolian and Eurasian Plates across the Marmara Sea can be understood as an interplay between several processes. Though the major part (60-80 % in the model area) of relative plate motion is accommodated by the MMF (Fig. 4.3; 4.5; Tab. 4.1) other factors contribute as well. Slip partitioning is evident from Fig. 4.3 and 4.5, so that the cumulative slip rates on the smaller faults of the Marmara fault system account for a significant fraction of total relative plate motion (Tab. 4.1). Changes in EW velocity in NS-profiles are however not restricted to faults as visible in Fig. 4.5. West velocities are not constant between the faults which means that also deformation within the blocks is involved. The distributed deformation in the volume can be understood as the sum of rotations (Fig. 4.6), slip on second order faults not included in the model and permanent strain. From Fig. 4.8 it becomes clear that also dip-slip on normal faults oriented oblique to plate motion take up some portion of relative plate motion, e.g. the western part of the Imralı Fault or the Prince's Islands Segment. The change in west velocity across these normal faults due to dip-slip is however small since the faults dip steeply.

Both the Moho and the sediments enhance horizontal surface velocities and right-lateral slip rate on the MMF (Fig. 4.2; 4.4). This can be explained by a decrease in fault normal stress in both cases. The bulge of the Moho with a local minimum in depth beneath the Marmara Sea causes extension above. Therefore, at a given coefficient of friction the reduced normal stresses facilitate fault slip (eq. 1.1). Besides, the stiffer Moho transmits the displacements applied at the lateral model boundaries more effectively into the model's interior than a weaker material does since in the latter case stronger deformation makes the provided energy to dissipate within a shorter range from the boundaries. The sediments reduce fault normal stress by their lower density, which results in a lower vertical load and by that in lower horizontal and hence fault normal stresses (eq. 3.6). The mentioned effects of higher Young's modulus and less dense sediments are also responsible for the still faster rates with rock distribution MAT_grad since here the average crustal Young’s modulus is higher and the average sediment density lower than in the other inhomogeneous rock property distributions (Fig. 3.4; Tab. 3.1). The higher slip rate along the MMF comes along with reduced slip rates on the other faults (Fig. 4.4) since total relative motion between northern and southern boundary remains the same for the same boundary conditions were applied.

The model with $\mu' = 0.6$ on all faults but the MMF represents an upper bound slip rate for the MMF as far as the coefficient of friction is concerned since $\mu' = 0.6$ implies Byerlee friction values under completely drained conditions at the faults. Accordingly, the slip rates on the faults with high friction strongly fall off whereas the rate on the MMF increases (Fig. 4.4). The decrease of slip rates on the former faults is highest on fault segments oriented oblique in a restraining sense with respect to plate motion (Fig. 4.4) so that the push from the southern block is transmitted across the faults as can be seen by the increased velocities on the northwest sides of those fault segments. The model with overall reduced coefficient of friction ($\mu' = 0.03$) concentrates relative plate motion in the model area on the MMF, whereas the role of internal deformation becomes less important (Fig. 4.2; 4.4). This is even more apparent when noticing that total relative motion between the northern and southern model boundary is reduced in this model (Fig. 4.2) since in the regional model the southern branch, which is beyond the southern model boundary of the Marmara model, accommodates a higher portion of total relative plate motion due to the reduced μ'. By that the model approves that deformation is localised at faults in case of widely decoupled blocks whereas distributed deformation in the volume gains importance as the degree of coupling increases with higher fault friction.

In case of increased velocities at the model boundaries (Meade) the additional relative motion between northern and southern model boundary is nearly entirely taken up by the MMF (up to 1.8 mm/yr slip rate increase at a maximum velocity increase of 1.9 mm/yr).

Information on slip rates comes from different sources, the most common of which are briefly introduced in the following. Geodetic observations by GPS, InSAR or other techniques are either directly used to evaluate the slip rate on a fault by taking the velocity difference on either side of a fault while assuming that the two blocks are rigid (geod). Geodetic observations are also used within the framework of pole analyses, which aim to evaluate the velocities of rotating blocks describing piecewise circles along a fault trace (pole). Furthermore, geodetic observations form the basis for finding optimum dislocation rates at faults in numerical or block models (mod). Slip rates are inferred from earthquake catalogues by summing seismic moments and deriving the shear strain rate (seism). In paleo-seismological investigations measurements of coseismic displacements of subsequent historical earthquakes in the subsurface (and dating of the appertaining soil specimens in case of unknown event times) are used to infer fault slip rates (paleo). Geological investigations infer slip rates from offsets at a fault during a certain period, either total offset since initiation of a fault or offsets of markers preserved in datable sedimentary strata (geol).

An overview on published slip rates of the NAF is given by Tab. 4.2 and Fig. 4.11. The published slip rates comprise a broad range of values between less than 10 and 30 mm/yr. Generally, geodetic slip rates or those derived with methods relying on them (pole, mod) exceed slip rates from geological or paleo-seismological analyses. However, there are also differences between reported slip rates relying on the same method. Explanatory remarks on that will be given later on during discussion.

The modelled slip rates (Fig. 4.3) largely agree with those from paleo-seismological investigations (Tab. 4.2). Restrictively, one should say that the paleo-data listed in Tab. 4.2 refer almost exclusively to the Ganos Fault and only the easternmost part of which is included in the Marmara model. The model predicts slip rates of 17-18 mm/yr at this short section in good agreement to the reported values. The town of Gerede is located beyond the eastern model boundary east of Almacik lens and represents the slip rate of the NAF, where it is constituted of only one single fault strand. Nevertheless, the 14-19 mm/yr reported there (Tab. 4.2) do not contradict the modelled slip rate of ~17 mm/yr at the eastern model boundary.

Tab. 4.2: Overview on reported slip rates / relative plate motion / right-lateral shear rates

Slip rate [mm/yr]	**Fault / Location**	**Method**	**Reference**
25	NAF	geod.	Oral et al. (1995)
22 ± 3	Marmara region	geod.	Straub et al. (1997)
≤ 24 ± 1	NAF	geod.	McClusky et al. (2000)
24-25	NAF	geod	Reilinger et al. (2006)
22.9	NAF	geod	Noomen et al. (1996)
≤ 30 ± 2	NAF	geod.	Reilinger et al. (1997)
11 / 13 / 26	Izmit / Izmit Bay / Marmara Sea	geod	Ayhan et al. (2002)
16 / 19	NAF: at 30°E / Marmara	pole	Westaway (1994)
28	NAF	pole	Le Pichon et al. (1995)
23	MMF, including Prince Isl. Seg.	pole	Le Pichon et al. (2003)
24/6	Northern/southern branch	mod	Meade et al. (2002)
18-24	Ganos Fault	mod	Motagh et al. (2007)
17	NAF	mod	Provost et al. (2003)
16 / 12.1	Western NAF / Marmara Sea	seism	Kiratzi and Papazachos (1995)
5.6 (at 31°E)	Marmara region	seism.	Pınar et al. (1996)
20 ± 4	Marmara region	seism.	Ambraseys (2006)
24	Marmara region	seism.	Eyidoğan (1988)
16	NAF western part	seism	Kiratzi (1993)
~ 20	Marmara region	seism	Papazachos and Kiratzi (1996)
16-24 / 3	Marmara region / southern branch	seism	Ambraseys (2002)
18	Ganos Fault	paleo	Rockwell et al. (2006)
14-18/19	NAF (Gerede / 1944 eq.)	paleo	Rockwell et al. (2006)
17.5-20	Ganos Fault	paleo	Aksoy et al. (2006)
18	Ganos Fault (Saros Bay)	paleo	Rockwell et al. (2001)
6.3	Yenice-Gönen Fault	paleo	Kürçer et al. (2008)
≥ 17	Ganos Fault	paleo	Meghraoui et al. (2004)
20.5 ± 5.5	NAF (Eksik)	geol	Kozacı et al. (2007)
18.6 ± 3.5	NAF (Tahtaköprü)	geol	Kozacı et al. (in press)
5-8	NAF	geol	Barka and Kadinsky-Cade (1988)
18 ± 3.5	NAF	geol.	Hubert-Ferrari et al. (2002)
17	Marmara region	geol.	Armijo et al. (1999)
14	MMF	geol.	Armijo et al. (1999)
10.5 ± 1.5	NAF in western Izmit Bay	geol.	Polonia et al. (2004)

Observed coseismic surface displacements are often quite heterogeneous along the fault trace, e.g. as documented for the 1999 Izmit earthquake (Aydin and Kalafat, 2002; Barka et al., 2002) and accordingly resulting slip rates can depend on which place a trench is excavated. If disposed soil layers cannot be related to known historical earthquakes, dating of soil specimens becomes necessary and these are generally afflicted with considerable uncertainties. Nevertheless, the published paleo-slip rates in Tab. 4.2 well agree to each other, which strengthens confidence in them.

Reported seismic slip rates for the Marmara Sea region are 12-24 mm/yr, which is markedly greater in range compared to the paleo-data (Tab. 4.2), and the modelled slip rates are well included within this range. This uncertainty is related to basically two circumstances. First, seismic slip rates are only as good as the used seismic catalogue concerning its completeness in magnitude, its spatial resolution and particularly its covered time period. Second, in a complex fault system as present beneath the Marmara Sea, seismic slip rates denote the right-lateral shear rate of the whole region rather than the slip rate on a single fault strand. For this reason, the slip rate on the MMF should be lower than the corresponding values in Tab. 4.2. On the other hand, a pre-requirement for identifying seismic slip rates with true slip rates on a fault is the absence of aseismic creep. In this respect, seismic slip rates represent a lower bound. When taking the seismic slip rates as dextral regional shear rate of the Marmara region, the model results also agree with the data as can be seen on Fig. 4.1 and 4.5 showing that relative motion between northern and southern model boundary is ~18-22 mm/yr.

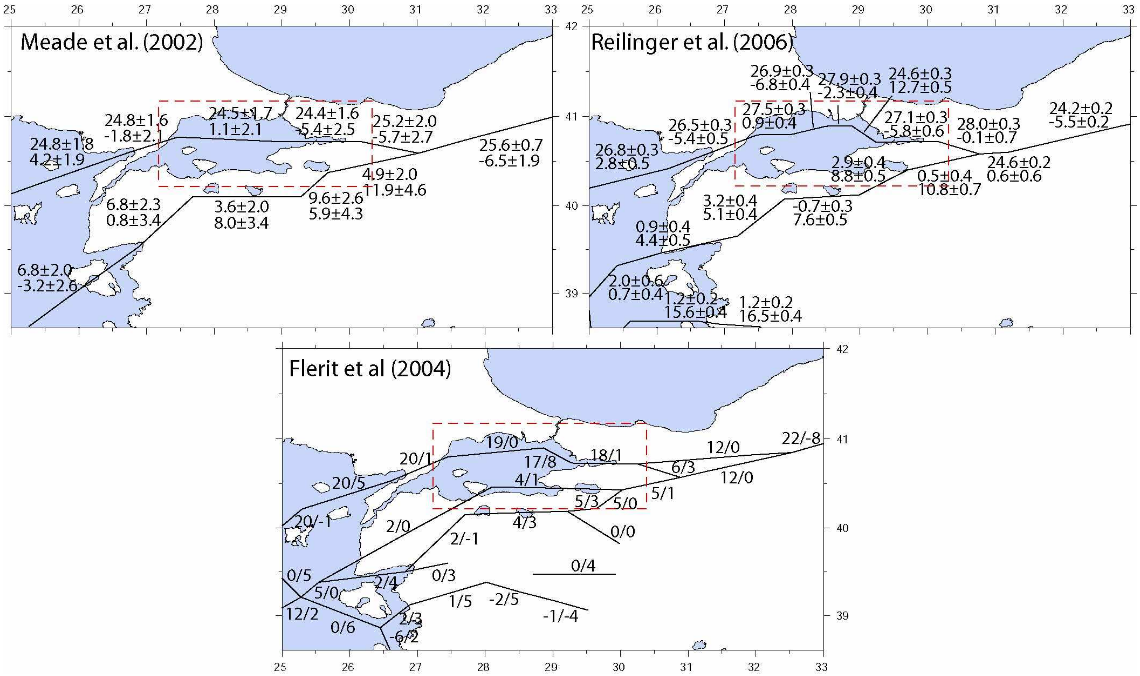

Fig. 4.11: Published slip rates for faults in the Marmara region from block models (Meade et al, 2002; Reilinger et al. 2006) and an elastic dislocation model (Flerit et al., 2004). The first number at each segment stands for the right-lateral slip rate and the second one for opening (positive) or closing (negative) rate in mm/yr. Dashed boxes mark boundaries of the Marmara Model.

Geological slip rates are also diverse (Tab. 4.2), which reflects the respective assumptions on total fault offset and uncertainties in dating. E.g. Barka (1997) estimated a total offset of 10-15 km and Schindler (1997) 55-60 km meaning slip rates of 2-4 mm/yr and 15-22 mm/yr, respectively. The most frequently cited geological slip rate for the MMF is the one from Armijo et al. (1999) with 70 km total offset at Gelibolu Peninsula and 85 km across the Marmara region implying 14 mm/yr on the MMF and 17 mm/yr between Anatolia and Eurasia. This is only slightly less than the rate quantified in this study (Fig. 4.3).

Published slip rates from numerical models based on geodetic observations are also similar to the results presented in Fig. 4.3 (Provost et al., 2003; Motagh et al., 2007). There are three references providing slip rates for single segments of the fault system in the Marmara region based on evaluation of GPS observations (Fig. 4.11). Meade et al. (2002) and Reilinger et al. (2006) used block models and Flerit et al. (2004) an elastic dislocation model to evaluate fault slip rates, which fit the observed GPS velocities best for their presumed fault geometry. They considered the interseismic effect in the observations by locking the faults above a seismogenic depth and determined optimum slip rates by varying the displacement rates, which they imposed at the lower portions of the faults beneath the locking depth. Fig. 4.11 shows their used fault geometries and the appertaining slip rates. Meade et al. (2002) found a right-lateral slip rate of 24.4-25.2 mm/yr for the northern branch of the NAF with simplified fault geometry, which considers only three segments in the area of the Marmara model of this study. Reilinger et al. (2006) used a similar fault geometry consisting of the northern and southern branch, but with a few additional segments for a better representation of the curvature of the fault trace. The resulting right-lateral slip rates of 24.6-28.0 mm/yr on the northern branch show more variation compared to those of Meade et al. (2002) and are 2-3 mm/yr higher. Flerit et al. (2004) used a more detailed fault geometry including not only the northern and southern branches of the NAF but also the middle branch along the southern shore of the Marmara Sea and accounted also for deformation in the blocks between the faults. They obtained slip rates of 17-20 mm/yr for the northern branch, which is 6-9 mm/yr or ~30 % less than the rates obtained by Reilinger et al. (2006). The above presented slip rates (Fig. 4.3) are a few (1-5) mm/yr less than those obtained by Flerit et al. (2004) but drastically fall below the rates reported by Meade et al. (2002) (7-12 mm/yr less) and Reilinger et al. (2006) (9-14 mm/yr less).

Similarly, slip rates directly deduced from geodetic observations (Tab. 4.2) are in the range of 22-25 mm/yr and decidedly exceed the previously presented results (Fig. 4.3). Nowadays, mostly geodetic slip rates are referred to and recent publications state a slip rate of ~20 mm/yr for the northern branch of the NAF. This value comes from the consideration that total relative plate motion observed by GPS is 24-25 mm/yr (McClusky et al., 2000; Reilinger et al., 2006) and the assumption that the northern branch accommodates 80 % of the relative plate motion, which was proposed by Meade et al. (2002) based on the above mentioned block model (Fig. 4.11).

The presented model results (Fig. 4.3) differ from this literature value (20 mm/yr) in two respects. First, modelled slip rates vary along fault strike and second they are lower by ~2-7 mm/yr. This difference has to be thoroughly discussed since geodetic slip rates are widely thought of being most reliable for they are based on very precise measurements in contrast to e.g. the dating of soils and they reflect the contemporary situation rather than an average over long time periods.

The reported slip rates in Tab. 4.2 generally imply a constant slip rate along the NAF. At least Le Pichon et al. (2003) stresses this circumstance explicitly while saying that the MMF slips at uniform rate “on its whole length”, including “the northern Çınarcık margin”. In contrast to the view of uniform slip rate the presented results (Fig. 4.3) show significant (>5 mm/yr) variability of slip rate along the MMF. The effect of slip rate variability along the MMF would be even more pronounced if a velocity weakening friction law would be applied. Slip rate variability is supported by the block and elastic dislocation models in Fig. 4.11, which all agree at least on reduced right-lateral slip rates on the Prince’s Islands Segment.

The discrepancy in slip rate on the MMF between the model and the literature value (20 mm/yr) can be referred to basically two reasons already mentioned in the first paragraph of this subchapter (4.1.3.1). First, the role of slip partitioning on several faults. As shown in Fig. 4.3 and Tab. 4.1 the other faults besides the MMF accommodate a small but in sum not negligible slip rate of a few (~1-7) mm/yr and by that a significant fraction of total relative plate motion. These smaller faults were not considered in the above mentioned block and elastic dislocation models, except the middle branch of the NAF in the latter case (Fig. 4.11). The additional faults permit a lower slip rate on the MMF while total relative plate motion is maintained.

Second, the role of internal deformation. Occasionally, total relative plate motion geodetically observed at some distance from a plate boundary fault is taken as the slip rate on this fault. This is however only valid if the two blocks are rigid and slide relative to each other without internal deformation. Because of this, McClusky et al. (2000) and Reilinger et al. (2006) correctly state that such geodetic slip rates represent upper bounds. They proofed by GPS observations that this pre-requirement is approximately fulfilled in most parts of Anatolia where internal deformation is small (<1-2 mm/yr). Localised deformation at the NAF east of Bolu (31.4°E) was also found from the characteristics of fault related offsets during geological times (Hubert-Ferrari et al., 2002). In its western part however the NAF is not any more a single vertical and rather straight strike-slip fault but exhibits marked bends and splits into several branches forming a broad and complex system of faults which elastically interact trough the rock masses in between. At least, this is shown by the modelled rotations (Fig. 4.6) and deformation in the volume visible in the gradients of west velocity between the faults in Fig. 4.5. Internal deformation can explain the difference between the high slip rates predicted by the block models (Meade et al., 2002; Reilinger et al. 2006), which are made up of rigid blocks, and the lower slip rates resulting from the elastic dislocation model (Flerit et al., 2004) and the model of this study, which both allow for internal deformation (Fig. 4.11). Keeping the role of slip partitioning and internal deformation in mind Straub et al. (1997) reported the observed relative velocity across the whole Marmara region instead of a fault slip rate (Tab. 4.2).

As previously declared, the term “internal deformation” summarises the effects of rotations, slip on not considered second order faults and permanent strain. To better illustrate the deformation the velocity gradient field calculated from the modelled velocity field could be further decomposed into dilation and strain beside the rotation shown in Fig. 4.6, which however was not done here. In agreement to the model results clockwise rotation of Armutlu Peninsula was reported based on structural fault characteristics indicating dextral shear, GPS observations and paleomagnetic measurements (Schindler, 1997; Straub et al., 1997; Alpar and Yaltırak, 2002). Clockwise rotation in the eastern Çınarcık Basin was quantified by Seeber et al. (2006) to 0.018°/kyr based on geometrical considerations which fits quite well the modelled rotation rates there (Fig. 4.6). Modelled clockwise rotations on Kocaeli and Istanbul Peninsulas are confirmed by left-lateral faults emerged in a dextral shearing setting (Oktay et al., 2002). Counter-clockwise modelled rotation characterises most of the Marmara Sea area south of the MMF and in particular the basins. This agrees to the interpretation of Aksu et al. (2000) who suggested this from the structural setting revealed by seismics as interplay of plate motion and southward retreat of the southern border of the North Marmara Trough. Overall counter-clockwise rotation of the Anatolian Plate is evident from GPS observations (Fig. 1.3).

Third, the implemented fault geometry accounts for the lower slip rate on the MMF. The faults of the block and elastic dislocation models in Fig. 4.11 comprise plane and vertical segments and hence are “highly idealised”, as Reilinger et al. (2006) admitted. Though the fault system used in the present study (Fig. 3.3) is necessarily also reliant on simplifications, it nevertheless considers mapped and seismically imaged structures in a smooth representation concerning fault orientations and dips. Fault bends, also small ones, tend to lower the slip rate compared to plane segments. Modelled dip-slip on non-vertical faults whose strike encloses an angle relative to the direction of plate motion produce an additional relative EW velocity not accounted for by the other models.

Modifications of the model brought about some changes compared to the reference model (Fig. 4.3; 4.4). Based on the investigated elastic rock property and density distributions lithology may account for an increase of right-lateral slip rate on the MMF by <1.5 mm/yr (Fig. 4.4). Though with higher Young’s modulus and lower densities slip rate on the MMF increases at the expense of internal deformation, expectable rock properties cannot account for the total difference between the model results and the literature value of ~20 mm/yr. Also both of the tested alternative friction hypotheses cannot account for the full difference, at least for 1.2 mm/yr. The same holds for the alternative boundary conditions (Meade) which enhances slip rate on the MMF by <1.8 mm/yr.

As noticed during description of the results, modelled slip rates depend on the extensions of a fault. While the length of the implemented faults are mostly well known from bathymetric mapping surveys and shallow seismics, the deeper structures are uncertain and in part unknown. The faults could be assumed as essentially vertical terminating at some depth or could merge at depth forming a large scale negative flower structure including the middle branch of the NAF (Aksu et al., 2000; Koral, 2007; Laigle et al., 2008) which could have fundamental consequences for surface velocities and slip rates. Given the smaller faults apart from the MMF would cease at shallower depths than assumed, some fraction of the cumulative slip rate on these faults would be additionally taken up by the main branch. In turn, if their lower end is at greater depth than presumed, the slip rate on the MMF would decrease whereas rates would increase in particular on the middle branch of the NAF.

Higher slip rates at depth could be imagined when remembering that all but the MMF and the middle branch of the NAF terminate at mid crustal depths (15 km) or yet above so that the MMF should take over at depth some part of the relative motion accommodated by the smaller faults at shallow depths. However, at least at 15 km depth there is only a small increase of slip rate on the MMF compared to the surface (Fig. 4.4).

In summary, uncertainties in the model parameters due to elastic parameters, friction coefficient and boundary conditions may each account for at most 1-2 mm/yr of the difference to the common 20 mm/yr. It can however not be excluded that their cumulative effect could make up the whole difference at least at some fault sections.

Within the discussion of reliable fault slip rates it is mandatory to check whether observed total relative plate motion is reproduced by the model. As explained previously, deformation gradually loses its localised character at the NAF from east to west and the plate boundary zone becomes distributed over a width of ~100 km and more in the Marmara region. The relative EW-velocity across the plate boundary zone between Istanbul (station ITAY) on stable Eurasia and sites ULUD on Uludag mountain and GIRE, both stations are south of the southern branch of the NAF (Fig. 5.5), were observed to be 22±3 mm/yr (Straub et al., 1997), which was recently affirmed (21.4±1.5 mm/yr) by Reilinger et al. (2006). This is slightly less than observed further east (~24 mm/yr; McClusky et al., 2000), suggesting that a small fraction of relative plate motion is accommodated still south of this GPS site. Modelled relative EW-velocities between the northern and southern model boundary are between 17.2 mm/yr right west of where the middle branch quits the model and 21.3 mm/yr at the southeast edge of the model (Fig. 4.1; 4.5). It is important to note, that the former value does not include slip on the middle branch, since the model boundary transects this fault, and in particular the southern branch of the NAF runs beyond the southern model boundary. This means that the model does not cover the whole plate boundary zone and consequently predicts a lower total relative motion between its northern and southern boundaries. The missing fraction to the observed relative motion at site ULUD, which is located right south of the southern branch of the NAF, can be referred to slip on this fault. Okay et al. (2008) ascribed a slip rate of 1-2 mm/yr to the southern branch based on the GPS observations of Straub et al. (1997) so that the model is in agreement to the data there. Of course, further to the west a few mm/yr are left since the plate boundary zone widens to the west.

Another crucial issue with geodetic slip rates is to discriminate between interseismically observed velocities and long-term fault slip rates. Disregarding effects of the seismic cycle leads to very small apparent slip rates when interseismic velocity differences at GPS sites close to the fault are used (Tab. 4.2; Ayhan et al., 2002). E.g. this is obvious from the interseismic velocities at stations SISL and SMAS nearby the main branch of the NAF (Fig. 4.12). Since during the interseismic period the fault is locked the observed small relative velocities across a fault are due to the associated deformation, which gradually extends over several kilometres on either side of the fault (Deniz et al., 1993). Also the relatively high amount of internal deformation of 7 mm/yr on Armutlu Peninsula reported by Straub et al. (1997) and their observed 7 mm/yr across Izmit Bay have to be understood in the context of interseismic strain accumulation rather than as the long-term value. Because of this interseismic signal in geodetic observations they cannot be directly used to evaluate fault slip rates. As a consequence, the modelled velocities should coincide with observations only at some distance from faults but not nearby. Fig. 4.12 shows that this is largely fulfilled when comparing modelled steady-state and GPS derived velocities at stations ITAY and DTAS. Modelled steady-state velocities north of the NAF are so small that they are hardly visible in Fig. 4.12. Although geodetic observations provide no direct information on fault slip rates, geodetic observations represent a hard constraint for fault slip rates. Therefore, the model has to be modified by incorporating the seismic cycle so that modelled velocities can be fully compared with observed ones. This will be presented and further discussed in chapter 5.

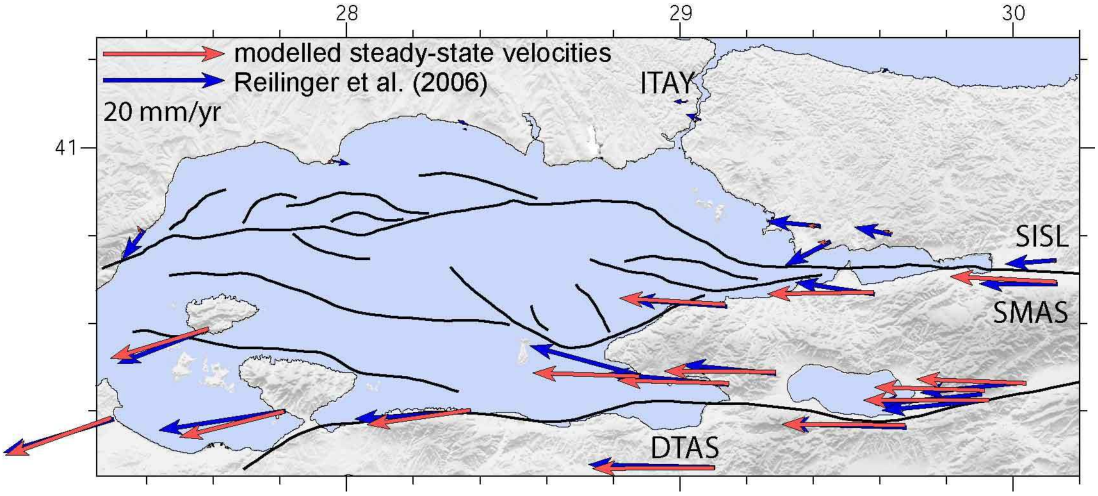

Fig. 4.12: Modelled steady-state velocities (from the velocity field in Fig. 4.1) in comparison with (interseismic) GPS observations. Note, that coincidence is expectable only at some distance to the NAF, not in its vicinity.

4.1.3.2 Vertical velocity field

The highest dip-slip rates occur on the faults along the rims of the basins (Fig. 4.9). This illustrates that the modelled subsidence in the basins (Fig. 4.7) is fault related. The modelled dip-slip rates correlate with implemented fault dips which are lowest along the Prince's Islands Segment, Tekirdağ Basin and Imralı Fault. Furthermore, dip-slip rates depend on the orientation of the fault with respect to plate motion (EW) and the acting direction of extension (~NE-SW) so that the releasing sides of bends and NW-SE striking faults are preferred fault sections for increased dip-slip rates. Eventually, dip-slip rates depend on the lateral slip rate on a fault so that dip-slip rates on the MMF exceed those on the smaller faults.

A comparison of the subsidence pattern in the Marmara Sea with the bathymetry reveals that the striking areas of high subsidence rates coincide with the location and extent of the deep basins, namely the Tekirdağ Basin in the west, the Central Basin in the middle, the Çınarcık Basin in the east and the Imralı Basin in the south (Fig. 1.6). Subsidence is slower between the Tekirdağ and Central Basins and the area between the latter and the Çınarcık Basin is quite stable in correlation with the Western High and Central High, respectively (Fig. 1.6).

In agreement to observations the highest modelled dip-slip rates are found at the narrow ends of the Çınarcık and Tekirdağ Basins (Seeber et al., 2004; 2006). The depocentres of these basins are visible in seismic profiles where fanning of sediments in the basins towards the depocentres is observed (Seeber et al., 2004; 2006; Carton et al., 2007; Laigle et al., 2008).

The footwalls of the implemented oblique-normal faults are quite stable or show slight uplift (Fig. 4.7). This agrees to the findings of Seeber et al. (2004; 2006) and is generally characteristic for large normal faults in areas under extension (Okay and Okay, 2002). Okay and Okay (2002) reported footwall uplift on the MMF relative to the present sea level at a rate corresponding to 13 % of the hanging wall's subsidence at the Tekirdağ Basin. This is similar to the model results which show footwall uplift adjacent to the Tekirdağ and Çınarcık Basins of 8-12 % of the subsiding hanging-walls.

In the following the modelled vertical motion pattern is discussed for single subareas of the model one after another.

Imralı Basin

In contrast to the other basins the Imralı Basin is hardly expressed in the bathymetry whereas the model predicts relatively high subsidence rates there. The explanation for this is elucidated by seismic profiles crossing the basin showing that the basement is submerged by ~4 s TWT (Parke et al., 2002; Laigle et al., 2008) corresponding to a vertical offset of up to 4 km across the Imralı Fault at the southern rim of the basin. The depression is almost filled by sediments concealing the downthrown basement. For sedimentation processes are not included in the model, the Imralı Basin is expressed in the modelled subsidence rates but hardly in the actual seafloor morphology. The Imralı Basin is located just north of the mouth of the Kocasu River which carries about 90 % of the total fluvial sediment influx into the Marmara Sea (Okay and Ergün, 2005). At the Imralı Fault near its southernmost point McHugh et al. (2006) report subsidence due to footwall collapse at a scarp at a rate of 1 mm/yr based on radiocarbon dating. They consider an additional 1 mm/yr as possible when taking into account a receding normal fault scarp. At the place of investigation the model yields a dip-slip rate of 0.5-1 mm/yr which is further increasing to the west (Fig. 4.9) and an absolute subsidence of the same amount (Fig. 4.7) in rough agreement to this finding.

Çınarcık Basin

The maximum subsidence rate in the model area is 4.1 mm/yr in the eastern Çınarcık Basin. In agreement to that Seeber et al. (2006) found that the depocentre of this basin is located in its eastern part. Concerning subsidence rate at the depocentre the maximum modelled rate is in the same order of magnitude but less than the 7.7 ± 1.3 mm/yr subsidence inferred by Seeber et al. (2006). They used the interaction between fault-controlled subsidence and sedimentation, which changed in rate at the lake–sea transition in the Marmara Sea ~14 kyrs ago, to infer this subsidence rate. Some part of the discrepancy could be explained by the performed modifications of the reference model. Using the boundary conditions "Meade" increases subsidence by up to 0.5 mm/yr, which is due to the faster relative plate motion. Increased subsidence rates of locally up to 0.8 mm/yr arise from another distribution of density and elastic parameters (Fig. 4.8). The effect of sedimentation, which leads to compaction and hence subsidence, can be excluded since reported sedimentation rates inferred to be 3.4±0.3 mm/yr (Seeber et al., 2006) are much too low. A probable explanation for the underestimation of subsidence concerns the fault geometry - in two respects. First, the dip of the Prince's Islands Segment in the model is 75-85° and hence relatively steep. Earlier simple test models showed a strong dependence of fault dip and dip-slip motion with increasing dip-slip rate as fault dip decreases. Therefore, higher subsidence rates would be obtained with a less steeply dipping fault. Seeber et al. (2006) and Okay et al. (2000) calculated and interpreted distinct lower dips of 60/74° and ~45-80° (their Fig. 6), respectively. The second aspect of potentially improper fault geometry is related to the discovery that there are actually two faults along the northern rim of the Çınarcık Basin, a steeper inner one and a shallower outer one (Carton et al., 2007). Therefore, lateral and dip-slip on the Prince Islands Segment may be partitioned and more complex than captured by the anticipated geometry.

The Çınarcık Fault was modelled with dominant dip-slip near its southern turning point where it joins the Imralı Fault (Fig. 4.9) and dominant right-lateral slip in the west (Fig. 4.3). From seismic images the contrary is more likely (Carton et al. 2007). This is either due to an improper deep geometry of this fault in the model or due to reasons that will be discussed later (chapter stress regime).

For the Central Basin Armijo et al. (2005) report a 2-6 mm/yr throw rate at the inner faults of the Basin. Laigle et al. (2008) assumed a 2 mm/yr subsidence rate. The maximum modelled dip-slip rate is 2.1 mm/yr on the southern inner rim (Fig. 4.9) and maximum subsidence rate 2.6 mm/yr (Fig. 4.7).

At the western end of the Tekirdağ Basin Seeber et al. (2004) inferred a subsidence rate of 2.8 mm/yr based on a back-stripping analysis of the from east to west progressively tilted and subsided sediments resulting in a rake of 8° and under the assumption of a 20 mm/yr right-lateral slip rate. This is similar to the modelled subsidence rates of <3.4 mm/yr there (Fig. 4.7). To the west of the Tekirdağ Basin on the shelf close to the coast however Seeber et al. (2004) derived subsidence of 4-6 mm/yr from an unconformity in sedimentary strata vertically disposed by the MMF since the lake-sea transition. Seeber et al. (2004) concluded that this rapid subsidence is recent and has to be seen in the context of west-moving subsidence on the laterally fixed northern block while the westmoving southern block and the Ganos bend belonging to it are stable. Though time dependent vertical motion would not be captured in Fig. 4.7 since steady-state velocities were controlled, this contradicts the uplift modelled there and may be due to an oversimplified fault geometry.

Southern and northern rim of the Marmara Trough

With increased subsidence north of the Southern Border Fault this fault marks the shelf break in the southwest of the Marmara Trough (Fig. 4.7). The higher subsidence rates in the western part of this fault and lower rates in the east are confirmed by the increase in vertical offset of the basement topography in seismic NS profiles from east to west (Parke et al., 2002) and is also seen but less pronounced in the bathymetric gradients which steepen from east to west.

In contrast, the northern margin of the Marmara Trough is hardly imaged by a distinct change in modelled subsidence rates. This is not what one would expect from the rather sharp break in the bathymetry. The model does not include a deep rooted fault at the northern rim of the trough since several authors agree on the lack of active faults there from seismic profiles (Le Pichon et al., 2001; Parke et al., 2002). Possibly landslides on the steep slopes are responsible for the shelf break at the northern side of the trough. At least for some sections landslides are documented (Armijo et al. 2002). This kind of mass movement is not considered in the model.

The modelled southward tilt of Marmara Island and Kapıdağ Peninsula to the south of the Southern Border Fault agrees with a series of tilted basement blocks found by Parke et al. (2002) from seismic sections.

Western shore

The uplifting area near the western model boundary (Fig. 4.7) is characterised by pronounced topography. The Ganos Mountain near the western shore of the Marmara Sea reaches 924 m above sea level (Fig. 1.5). The presence of this anticline was ascribed to uplift related to the Ganos Bend (Seeber et al., 2004), which is the restraining bend of the MMF near the western shore of the Marmara Sea. The Ganos Mountain is located at the transpressive side of the bend. Along the western shore of the Marmara Sea marine terraces are present onshore. Yaltırak et al. (2002) dated shells from these marine deposits using radiometric methods. Under consideration of sea level changes they found neogene uplift rates of 0.3 mm/yr in Gaziköy, which is located close to where the NAF enters the Marmara Sea. The model shows uplift only north of the fault whereas the southern block is stable. In contrast, Yaltırak et al. (2002) found average uplift rates of ~0.4 mm/yr also south of the NAF on the entire western shore of the Marmara Sea including the Strait of Çanakkale (Dardanelles). The model applying the MAT_grad rock property distribution shows 0.1-0.2 mm/yr uplift relative to the reference model there and thus better approaches these observations (Fig. 4.8). This holds also for the model applying the vertical velocities of the regional model as additional boundary conditions (Fig. 4.8). In this case the uplift cannot be explained by processes within the model area but have to be seen in context of the surrounding which influences the stress-displacement pattern there. Probably, this is in relation to the southwestward turn of the middle branch of the NAF near Kapıdağ Peninsula and of the southern branch near Gönen (Kürçer et al., 2008) compressing the area to the west similar to the restraining Ganos bend. If so, this in an argument in favour of the applied sub-modelling technique since the regional model implicitly includes this effect.

Southern shore

Along the middle branch of the NAF modelled relative vertical motion due to dip-slip is mostly absent (Fig. 4.9) which is confirmed by seismic profiles lacking appreciable throw components perpendicular to this vertical strike-slip fault (Kurtuluş and Canbay, 2007). However, at Bandırma Bay next to Kapıdağ Peninsula and around Iznik Lake the southern side subsides with respect to the northern side while one would expect the contrary. Several inadequacies of the model may could account for this mismatch. The southern boundary of the model was unfavourably chosen since it follows the Bursa graben and the fault along the southern rim of which is beyond the southern model boundary. This seems to cause an improper accommodation of the NS-extension in the volume resulting in subsidence south of the middle branch instead of dip-slip on a normal fault. The regional model accounting for this roughly reverses the subsidence south of Bandırma Bay (Fig. 4.7; 4.8). There is evidence for the presence of normal faults in Bandırma Bay (Kurtuluş and Canbay, 2007) and the fault along the northern edge of Kapıdağ Peninsula obviously exhibits a significant dip-slip component with the hanging wall being the northern one since Parke et al. (2002) imaged a vertical offset in the basement of ~1.5 s TWT across this fault (their profile Mar97-13). Implementing this fault less steep and consideration of omitted normal faults could therefore avoid the obtained subsidence pattern. Accordingly, a north dipping middle branch near Iznik Lake and incorporation of the south dipping normal fault north of this Lake may yield improved results there as well as usage of stiffer material in the model volume (Fig. 4.8).

Armutlu Peninsula, Samanlıda massive and Izmit Bay

A striking mountain range (Samanlıda Massive) elongates along the middle branch of the NAF to the north of it where the model shows uplift (Fig. 1.5; 4.7). This mountain range may be a consequence of the vertical WSW oriented middle branch and the EW directed plate motion. Emre et al. (1998) interpreted the mountainous area of the Samanlıda Massive as a large scale pressure ridge between the northern and middle strand of the NAF. Uplift to the south of Izmit Bay is indicated by marine terraces including oysters that are found 12-15 m above the present sea level. Çağatay et al. (2003) inferred an age of ~36 kyr for the top of these terraces from ^{14}C-dating which would imply an average uplift rate of ~0.4 mm/yr. Yaltırak and Alpar (2002) inferred an uplift rate of 0.224 mm/yr of the block south of Izmit Bay. In good agreement to that the modelled uplift is 0.2-0.4 mm/yr there (Fig. 4.7). The Karamürsel Basin in the Izmit Bay however is not reproduced by the model, which may be related to the observation that the high subsidence rates there are localised (Cormier et al., 2006) due to not considered smaller structures. In any case, the model shows the primary pattern of relative uplift of the southern side of Izmit Bay with respect to the northern side.

There is evidence for moderate subsidence north of Izmit Bay as predicted by the model. Cormier et al. (2006) found an escarpment between the NAF and the northern shore of Izmit Bay by bathymetry mapping and high-resolution seismics and interpreted it as a paleoshoreline of the Marmara Lake during the last glacial maximum. In the western Izmit Bay this escarpment is 90-95 m bsl. Southwest of Istanbul, at ~4.5 km distance from the NAF, this escarpment is 87 m bsl. Cormier et al. (2006) assumed the latter site to be hardly affected by fault tectonics and therefore to represent the reference for the ancient sea level ~12 kyrs before present. They conclude that the northern block in the Izmit Bay subsides at a rate of <1 mm/yr. In agreement to that the modelled subsidence rates there are in the range of 0.2-0.3 mm/yr. Also the modelled relative vertical velocities between the discovered paleoshoreline southwest of Istanbul and the one in the western Izmit Bay match the observed ~3-8 m subsidence of the latter site with respect to the former one since the last glacial maximum quite well. The model predicts uplift of ~0.2 mm/yr and subsidence of 0.2-0.3 mm/yr, respectively, at these sites which means a vertical offset of 4.8-6.0 m between them after 12 kyrs.

Northern shore and Istanbul

There is evidence for uplift of the northern shore of the Marmara Sea in the past. Okay and Okay (2002) draw this conclusion from the presence of steep cliffs along the northern shore, from marine terrace deposits onshore, from the drainage diversion of the Maritsa River which once was flowing into the Marmara Sea but today into the Aegean and from northward tilt of the Thracian erosion surface. They referred the uplift to a tectonic origin related to the NAF. Oktay et al. (2002) reported 75 m of uplift on the northern part of Istanbul Peninsula during the Late Quaternary. The model shows a stable central part of the northern coast whereas subsidence prevails in the northwest and northeast (Fig. 4.7). Again, uplift at small rates is obtained when constraining the vertical velocity at the model boundary by the velocity field emerged in he regional model (Fig. 4.8).

Within the Terrafirma project of the European Space Agency (ESA) the vertical motion of Istanbul was investigated using the technique of Persistent Scatterer Interferometry. Comprising numerous satellite images out of 15 years, average subsidence rates of 0-2 mm/yr were found in Istanbul but locally also subsidence rates of up to 5 mm/yr[3]. The model results show subsidence in Istanbul at a rate of 0.3-0.6 mm/yr (Fig. 4.7). Thus, the modelled rates are comparable in magnitude to the observed ones but they do not reflect the observed heterogeneous pattern of subsidence since the resolution of the finite element mesh in this area is ≥1.5 km and local heterogeneities may be due to soft soils or unstable foundation geology as well as ground water effects. In view of the reported uplift in the past and the contemporary subsidence a temporal change in vertical motion pattern could have occurred which may be related to the spreading influence of extension arising from the retreating slab in the Hellenic subduction zone.

Marmara region

GPS based vertical velocities are available for the whole Marmara region (Ergintav et al., 2007). They show a heterogeneous pattern and in part quite rapid vertical motion exceeding ±10 mm/yr with uncertainties of several mm/yr. Vertical velocities by GPS are known to be less accurate than horizontal ones due to a number of bothering signals from e.g. the troposhpere or electron content in the ionosphere. Besides, it is difficult to discriminate between vertical motion of tectonic origin and local signals from ground water fluctuations and extraction, compaction, creeping slopes and others which often reach rates of the same order.

The published slip rate models in Fig. 4.11 found maxima in fault-normal opening rates at the Prince’s Islands Segment, which is consistent with dip-slip on this segment and subsidence of the hanging wall (Fig. 4.7; 4.9). Muller and Aydin (2005) modelled vertical motion of the seafloor of the Marmara Sea using different fault geometries in an elastic boundary element dislocation model. They obtained maximum subsidence in the basins of 6 mm/yr but also subsidence for the whole Marmara region exceeding 2 mm/yr. By that their relative subsidence rate across e.g. the Prince’s Islands Segment is maximum 3 mm/yr, which is similar to the dip-

---

[3] http://www.spiegel.de/wissenschaft/weltall/0,1518,437204,00.html

slip rates in Fig. 4.9. Eydoğan et al. (1988) calculated a crustal thinning rate for the Marmara region of 0.13 mm/yr from seismic moment tensors of major earthquakes. This may be taken as an average subsidence rate for this region and is consistent with the prevailing extensional influence from the Hellenic subduction zone.

Several tectonic models were proposed on how to interpret the origin of the basins and the pertaining role and nature of the fault geometry (Wong et al., 1995, Aksu et al. 2000; Okay et al. 2000; Imren et al. 2001, Armijo et al. 2002, Le Pichon et al. 2001; 2003, Parke et al. 2002). Debate came to a head between mainly two hypothesis. Le Pichon et al. (2001; 2003) claimed that there is only one single through going strike-slip fault in the Marmara trough. In contrast, Armijo et al. (2002) resisted on the view that the Marmara trough as a whole is a pull-apart basin and also the single basins.

In order to take a stand on that by means of the model the vertical motion on a profile crossing the Çınarcık and Imralı Basins was considered (Fig. 4.10) which corresponds to profile No. 8 of the SEISMARMARA seismic experiment (Laigle et al., 2008). The vertical motion on this cross section clearly expresses the subsidence in the basins due to oblique slip with down component at the Prince's Islands Segment, Outer Çınarcık Fault and Imralı Fault. Evidence for more rapid subsidence along the northern rim of the Çınarcık Basin compared to the south is found by north tilting sediments (Carton et al. 2007) and likewise south dipping sedimentary layers in the Imralı Basin (Laigle et al. 2008). The small south dipping fault in the northern Imralı Basin seems not to cut into the basement on seismic images (Laigle et al., 2008) so that this fault was erroneously implemented to penetrate also the basement producing a greater vertical throw rate relative to the other faults than observed. The footwall south of the Çınarcık Basin slowly subsides relative to the footwall of the Imralı Fault which is by the seismically imaged basement topography (Laigle et al, 2008). By that, the modelled subsidence pattern across the basins agrees to the interpretation of Laigle et al. (2008) that submergence and tilting of a huge basement block is involved which is downthrown on its southern side at the Imralı Fault and retreats to the south.

These results cannot be fully integrated into either of the existing two main kinematic models of the Marmara region. At greater depth the fault geometry in the FE model is comparable to the point of view represented by Le Pichon et al. (2001; 2003) since beneath 15 km only the MMF is implement beneath the Marmara Sea. Although one single through going strike-slip fault seems to be prevalent at greater depth as proposed by Le Pichon et al. (2001; 2003) the model shows also significant dip-slip components and slip on subsidiary faults at shallower depths. The FE model includes the faults according to the surface trace fault map of Armijo et al. (2002) and the FE results agree on their opinion that several faults are involved in the accommodation of relative plate motion. However, the FE results were obtained using a fault geometry at depth which does not represent classical pull-apart structures as they emphasize to exist and fault step-overs at depth in earlier models yielded strongly decreased slip rates. The preferred fault geometry in this study can be described as a through going main fault with dominant strike-slip character which however also comprises non-vertical sections exhibiting oblique slip and is accompanied by normal faults. Thereby, a prominent role is exerted by the bends of the main branch. Near the Tuzla and Ganos Bends the fault becomes less steep allowing dip-slip at the releasing sides of the bends. The Çınarcık and Tekirdağ Basins can be interpreted as half grabens that tilt toward the dipping border fault. An extensional component is taken up by dip-slip on normal faults with the footwall blocks remaining stable leading to subsidence and tilting of basement blocks (Fig. 4.10).

4.1.4 Conclusions kinematics

The main results of the modelled kinematics are as follows

- Right-lateral slip rate on the MMF is variable along strike and is in the range of 12.5-18 mm/yr in the model area and amounts to ~15 mm/yr on the Central Segment. Slip rate may be higher by up to ~2-4 mm/yr depending on rock properties, coefficient of friction and the preferred regional velocity field.
- The inferred fault slip rates are not a result of new observations but due to another physical conception. Fault slip rates cannot be directly determined from geodetic observations. A physical model based on assumptions is required to deduce fault slip rates from observed surface velocities. In contrast to plane and vertical first-order faults as boundaries of rigid blocks, a 3D fault geometry, including second-order faults, with reasonable effective coefficient of friction, embedded in a deforming medium, was set up. Fault slip rates were quantified, not by forcing fault slip rates to match kinematic observations but instead by establishing a stress field by applying remote velocity boundary conditions to an initially stressed volume. This enables slip rates to evolve freely in response to stress, and the resulting velocity field is in agreement to observations. The lower slip rates with respect to the frequently reported 20 mm/yr are primarily explained by slip partitioning on several faults and by internal deformation that involves also rotations. Though the MMF accounts for the dominant part of relative plate motion the model results rise the demand to distinguish relative plate motion from slip rate on the MMF. The view of localised deformation restricted to the two main strands of the NAF in the Marmara region has to be questioned.
- The modelled uplift and subsidence rates largely coincide with the observed pattern and rates.
- The present morphology is reflected by the modelled vertical motion suggesting that the surface was shaped at least to some extent by tectonic processes which are still ongoing.
- The largely properly modelled characteristics of the subsidence in the basins suggest that the implemented fault geometry is reasonable, i.e. asymmetric half-grabens bounded by a dominating throughgoing MMF on one side and synthetic normal faults on the other.
- vertical motion is fault controlled, either directly by dip-slip on non-vertical faults or as deformation caused by stresses exerted by the faults in response to plate motion.
- the modelled vertical velocity field can be taken to reflect though not an appropriate but consistent stress field.

4.2 Stress

The stress tensor at the element’s integration points is the second basic output from the finite element analysis besides the previously presented nodal displacements (Fig. 2.3). The absolute stress at 5 km depth resulting from the homogeneous reference model is shown in Fig. 4.13 in terms of orientations (trend and plunge) and magnitudes of the principle stresses.

The maximum principle stress σ_1 plunges at low angles in the western model area, beneath the Samanlıda Massive and in most of the area north of the NAF whereas it plunges steeply beneath the basins in the Marmara Sea and south of the middle branch of the NAF (Fig. 4.13). In contrast, the intermediate principle stress σ_2 plunges at almost complementary angles with respect to σ_1 about the bisector plunge of 45°. This is a consequence of the very low plunges of σ_3 throughout almost the whole model area so that the three principle stresses are mutually perpendicular.

The trend of the maximum principle stress is oriented approximately colinear with the maximum horizontal stress σ_H in areas in which σ_1 plunges subhorizontally. Accordingly, the trend of σ_2 corresponds to σ_H in areas of steeply plunging σ_1. Thus, maximum compression is found in a NW-

SE orientation in most of the model area. The trend of σ_3 is oriented mostly NE-SW and can be identified with the minimum horizontal stress σ_h since σ_3 plunges subhorizontally.

The maximum principle stress plunging at high angles means an extensional stress regime and σ_1 and σ_3 plunging subhorizontally is equivalent to a strike-slip regime. Hence, the basins are under an extensional stress regime as well as the southern model area whereas the area south of Izmit Bay and the northern and southern shelf are in a strike-slip regime. There are four distinct small areas with steeply plunging minimum principle stress axis which is equivalent to a compressional stress regime. These are the area between Hersek Peninsula and Tuzla Bend, the area east of the Central Basin, around Ganos Bend and less pronounced in the eastern part of the Central Segment.

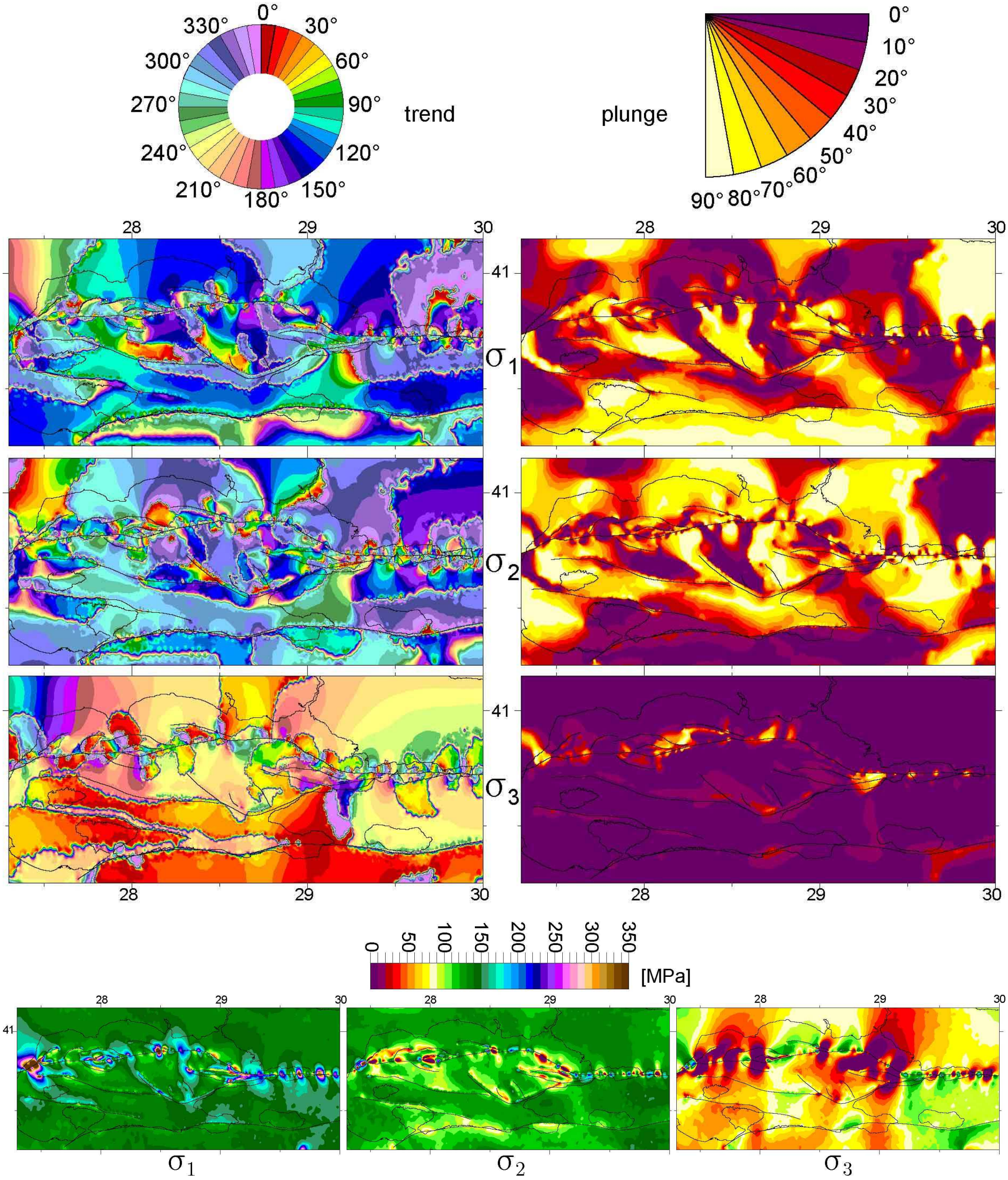

Fig. 4.13: Full stress tensor at 5 km bsl. from the homogeneous model in terms of orientations (trends left column, plunges right column) and magnitudes (bottom) of the three principle stresses.

The modelled stress field displayed in Fig. 4.13 is presented in more convenient quantities in the following which allow comparison to various observations. The stress regime will be shown in chapter 4.2.1. Stress orientations will be shown as maximum horizontal stress orientations at 5 km depth and as trend and plunge at earthquake hypocentres (4.2.2). Stress magnitudes will be shown in terms of differential stress at 5 km depth and normal stress on the MMF (4.2.3). Eventually, the crucial role of prestress on resulting stresses is demonstrated and discussed in chapter 4.2.4.

4.2.1 Stress regime

The modelled stress regime at 5 km bsl is presented in Fig. 4.14 in terms of the regime stress ratio (RSR), that is defined in App. 2. Most of the model area is in a strike-slip regime (1<RSR<2). More precisely, within this range RSR values between 1 and 1.5 prevail indicating a stress regime between strike-slip and transtension.

While transtension is quite widespread, a pure extensional stress regime characterises only relatively small areas. These are the depressions of the North Marmara Trough, in particular the Çınarcık and Imralı Basins as well as between the Central and Tekirdağ Basins and further a NS oriented band across Armutlu Peninsula, east of Kapıdağ Peninsula along the southern shore of the Marmara Sea and south of it.

Areas of transpression or compression (RSR > 2) are rather small and are confined to the vicinity of faults. The most prominent area of transpression and compression among these is located between Hersek Peninsula in the Izmit Bay and the Tuzla Bend as noticed previously. In the western Marmara Sea around the Ganos Bend a transpressional state of stress results from the model as well as in the eastern Central Basin, a few kilometres to the west of the Istanbul Bend and around some small restraining bends in the Izmit Bay.

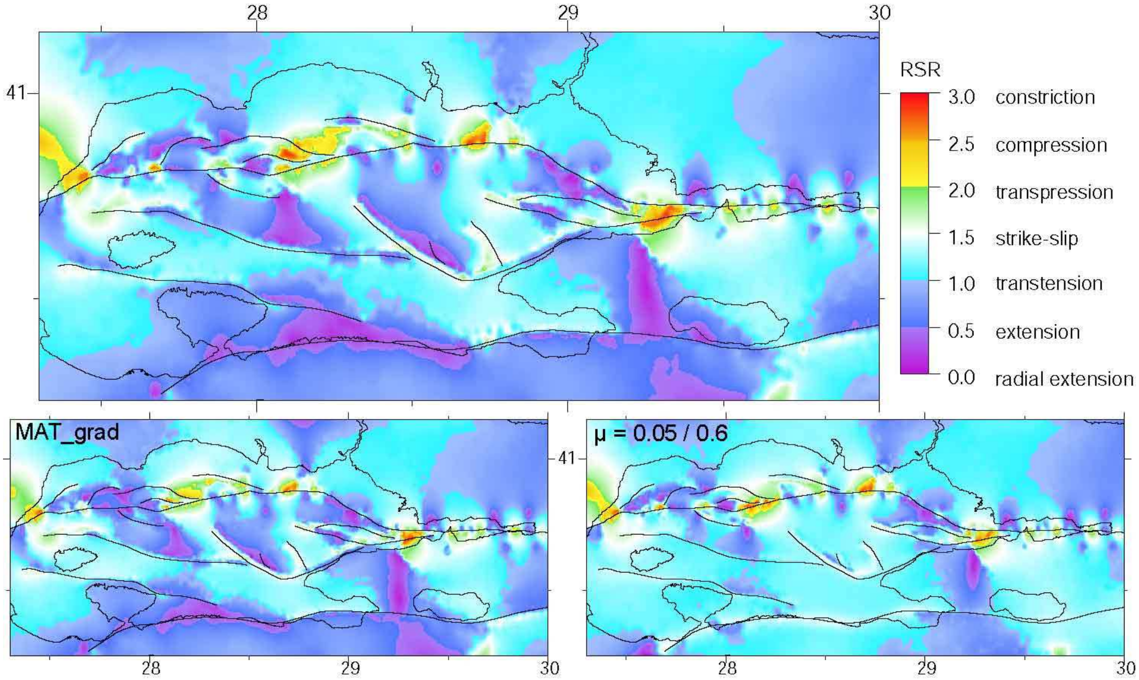

Fig. 4.14: Modelled stress regime at 5 km bsl. in terms of RSR (App. 2). Homogeneous reference model (top), MAT_grad rock properties (lower left) and Byerlee friction coefficients on all faults but the MMF (lower right).

The modelled dominant strike-slip regime with a tendency to extension agrees with the frequently proposed general view that the Marmara region is under a strike-slip stress regime characteristic for the NAF throughout most of its length from east Anatolia to the Marmara Sea but in transition to extension which prevails in west Anatolia and Greece (e.g. Taymaz et al., 1991).

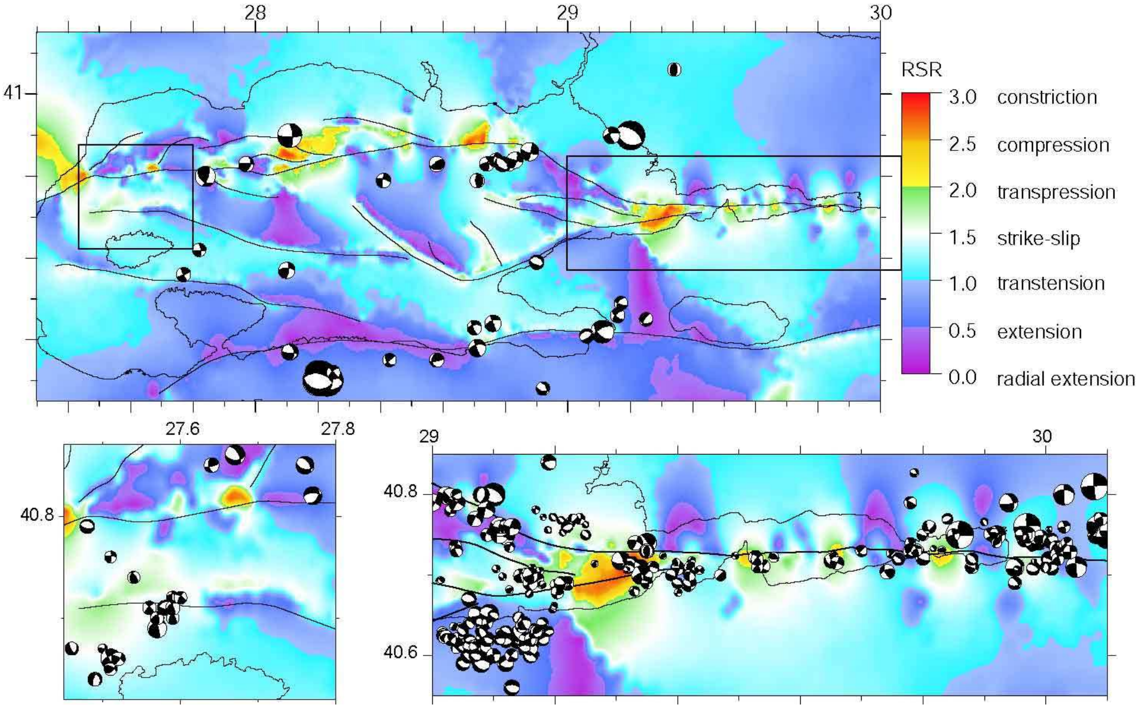

Fig. 4.15: Modelled stress regime from Fig. 4.14 in comparison to earthquake focal mechanisms reported by Eydoğan et al. (1988) and references therein, Taymaz et al. (1991), Polat et al. (2002a), Pınar et al. (2003), Bohnhoff et al. (2006), Pondrelli et al. (2004; 2007), Harvard CMT. The two lower figures show enlarged areas framed by the black boxes in the top figure.

Conclusions on the stress regime are often drawn from earthquake focal mechanisms. So they are used as independent information for comparison with the modelled stress regime. Before, however, it has to be pointed out that this comparison is not unconditional for the following reasons:

- The type of faulting does not necessarily reflect the prevailing stress regime. Slip occurs not only on optimally oriented faults emerged under the present stress field but also on non-optimally oriented reactivated faults. E.g. slip on a vertical fault will occur in a strike-slip sense even though the stress regime may exhibit components of extension or compression (e.g. Célérier, 1995). Often sets of different fault types altogether represent the associated stress regime rather than one single fault with its specific type of faulting. In particular focal mechanisms of aftershocks can be quite different from the prevailing stress regime (e.g. Gahalaut and Gahalaut, 2008).
- Focal mechanisms of large earthquakes cannot resolve local properties of the stress regime since they represent an average over an extended area.
- The fact that the accuracy of earthquake hypocentre determination is generally in the kilometre range, may lead in unfavourable cases to comparison of the focal mechanism at one place with the modelled stress regime at another place. An extreme case in this respect may be the 1963 M=6.3 normal faulting event originally located near the shore between Istanbul and Tuzla (Taymaz et al., 1991) but was relocated by Bulut and Aktar (2007) on Armutlu Peninsula.

Therefore, given the focal mechanisms are unequivocal solutions, one has to be aware of these issues when comparing the modelled RSR to focal mechanisms (Fig. 4.15). It is not distinguished between different depths and most of the displayed focal mechanisms are from aftershocks which may reflect stress perturbations due to the main rupture. On the one hand this further weakens the basis for comparison, on the other hand a better coverage of focal mechanisms is provided.

In the western Marmara Sea near the western end of the Southern Border Fault a cluster of strike-slip and thrust faulting focal mechanisms was observed. The model shows slight transpression there. In the Tekirdağ Basin, Western High and Central Basin mostly normal faulting earthquakes occurred as expectable from the modelled stress regime.

Strike-slip faulting prevails on the Prince's Islands Segment. The model however shows almost extension there. Possible reason for this discrepancy is that the type of faulting may not represent the stress regime here as pointed out above. Apart, the type of faulting may be depth dependent with normal faulting earthquakes at shallow depths and pure strike-slip earthquakes at greater depth as reported by Karabulut et al. (2003) or the strike-slip earthquakes may have all occurred on the steeper southern splay of the Prince's Islands Segment that actually comprises two faults as revealed by seismic sections (Carton et al. 2007; 4.1.3).

Focal mechanisms to the northwest of the Çınarcık Basin show mainly strike-slip to normal faulting events in rough agreement to the modelled stress regime ranging between strike-slip and extension in this area. A cluster of small normal faulting earthquakes north of the Tuzla Bend is not reflected by the modelled strike-slip stress regime. However, Bulut and Aktar (2007) reported that these hypocentres are aligned on a vertical plane contrary to the reported normal faulting mechanisms. In the southeastern Çınarcık Basin near the Çınarcık Fault dominant strike-slip events agree with the modelled strike-slip regime.

The prominent cluster of earthquakes near Yalova on Armutlu Peninsula shows predominantly normal faulting focal mechanisms on EW striking fault planes. In agreement to that the modelled stress regime is close to extension there (Fig. 4.14) with EW oriented σ_2 corresponding to σ_H and NS oriented σ_3 corresponding to σ_h (Fig. 4.13). Interestingly, the eastern termination of this cluster is right about where a sharp transition from extension to transpression is modelled. Strike-slip earthquakes in the southern Marmara Sea between the western tip of Armutlu Peninsula and the southern shore correspond to the modelled strike-slip regime there. The earthquakes to the east and west of these show dominant normal faulting which is reflected by a modelled transtensional to extensional stress regime.

The area between the westernmost Izmit Bay and the eastern end of the Çınarcık Basin is characterised by a transpressive stress regime which is supported by a number of thrust faulting mechanisms reported for this area though also some strike-slip and normal faulting events indicate a complex stress field. Of course, the observed thrust faulting earthquakes are at most of moderate magnitude since the modelled area of compression is small. Other indicators affirming compression in this area are a mountain emerging on Hersek Peninsula near a restraining bend of the NAF (Özaksoy et al., 2006) and mud volcanoes on the sea floor to the west of Hersek Peninsula (Cormier et al., 2006).

The effect of the sediments is a slight increase in extension which is visible in the western Central Basin and the western Çınarcık Basin and the areas under compression are still smaller (Fig. 4.14). Byerlee friction coefficients on all but the main fault shifts the stress regime in the Imralı Basin, the southern shelf and southern onshore areas from transtension/extension to strike-slip/transtension.

To summarise, the modelled stress regime largely reflects the earthquake focal mechanisms while keeping in mind that the preconditions for full coincidence between model results and focal mechanisms may be not fulfilled in any case. The areas under strike-slip regime or compression widely correspond to stable or uplifting areas, whereas areas under extension tend to subside (Fig. 4.7). By that, the modelled state of stress and kinematics are related meaningfully.

4.2.2 Stress orientations

Fig. 4.16 shows the orientation of maximum horizontal stress σ_H calculated from Fig. 4.13 using the definition of Lund and Townend (2007). σ_H is oriented basically NW-SE in the Marmara region as noticed previously while analysing the regional model (Fig. 3.11). The Marmara model reveals locally deviations from this regional orientation. The swing towards NS orientations in the northwest model edge is due to boundary conditions and is not present in the regional models (Fig. 3.12). Near the faults orientations are in part scattered due to the low friction coefficient requiring either very low or high angles of σ_H orientation with respect to the local fault strike. However, WSM data confirm a NNW-SSE oriented compression northwest of the Çınarcık Basin and more or less EW orientations in the western Sea of Marmara beneath the Western High, Tekirdağ Basin and to the south towards Marmara Island. Modelled σ_H orientations at the earthquake cluster near Yalova on Armutlu Peninsula clearly show EW orientations as affirmed by the orientations derived from the focal mechanism solutions. At fault segments for which a significant dip-slip component was modelled (Fig. 4.9) σ_H is oriented widely parallel to fault strike e.g. at the western part of Imralı Fault, along the MMF on the southern side of the Tekirdağ Basin and at the faults bounding the Çınarcık Basin. This is consistent with σ_3 or σ_h oriented perpendicular to these basin bounding faults in opening direction (Fig. 4.13). Remembering that most of the WSM data in this region come from focal mechanism solutions of small to intermediate earthquakes that potentially are affected by small-scale structures not considered in the model and that the accuracy of WSM C quality data is ± 25 °, most of the data points in the model region are matched fairly well by the model. The sediments and fault friction have only minor influence on the σ_H orientations.

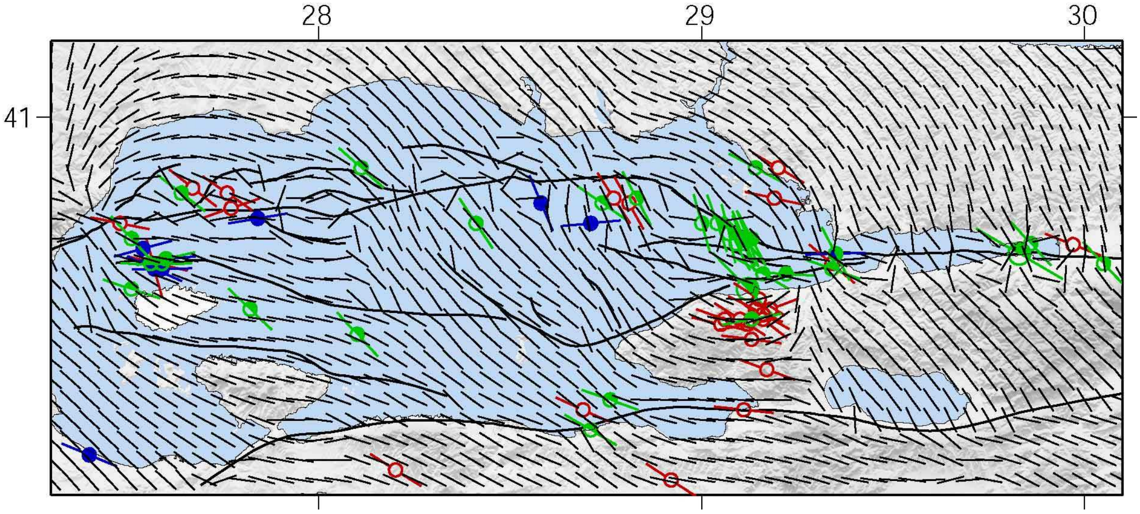

Fig. 4.16: Modelled maximum horizontal stress orientations (black lines) calculated from the stress field displayed in Fig. 4.13. Coloured lines show WSM data.

A more profound comparison than between modelled σ_H orientations and WSM data can be performed based on the numerous reported analyses of earthquake focal mechanisms in the Marmara region. P and T axes for single earthquakes are compared with modelled minimum and maximum principle strain axes respectively at the hypocentres. Additionally, principle stress orientations from stress tensor inversions are compared with modelled stress orientations.

Three datasets of earthquake focal mechanisms were employed for the comparison, which are each divided into two subsets specific for particular areas. The first dataset comprises aftershocks of the 1999 Izmit earthquake (Bohnhoff et al., 2006). This dataset is composed of a subset of events occurred in the eastern Marmara Sea including events on Armutlu Peninsula (termed Seg. 1 in Bohnhoff et al., 2006) and a subset of earthquakes in Izmit Bay and farther to the east (Seg. 2; Fig. 4.17). The second dataset by Pınar et al. (2003) is a compilation of earthquakes in the whole Marmara Sea, divided in a western (W) and an eastern (E) subset (Fig. 4.17). Some of the events in the eastern part are aftershocks of the Izmit earthquake and are also contained in the dataset of Bohnhoff et al. (2006). The third dataset from Polat et al. (2002a) comprises focal mechanisms from the whole Marmara Sea occurred in the two months after the 1999 Izmit earthquake and separately considers the area west of Izmit Bay (Fig. 4.17). Additionally, there are two more stress inversion analyses for the whole Marmara region on which will be referred to. The first one is based on microearthquakes in the whole Marmara Sea area from 1995 and the second one on M>5 earthquakes between 1943 and 1997 (Gurbuz et al., 2000; Polat et al., 2002b).

Fig. 4.18 shows the orientations of the three principle stresses at 5 km depth on a dense grid of 0.01°E x 0.01°N (i.e. ~ 0.85 x 1.1 km) spacing over the whole model area. This is simply another representation of the results shown in Fig. 4.13. Both σ_1 and σ_2 show either a preferred trend in NW or SE directions or are steeply dipping, thus both principle stresses either correspond to σ_H or σ_V. This clearly expresses the transitional stress regime between strike-slip and extension. All in all steeply plunging σ_2 is little more frequent than σ_1 whereas σ_1 slightly prevails at near horizontal orientations. The minimum principle stress is almost horizontal trending in NE or SW directions.

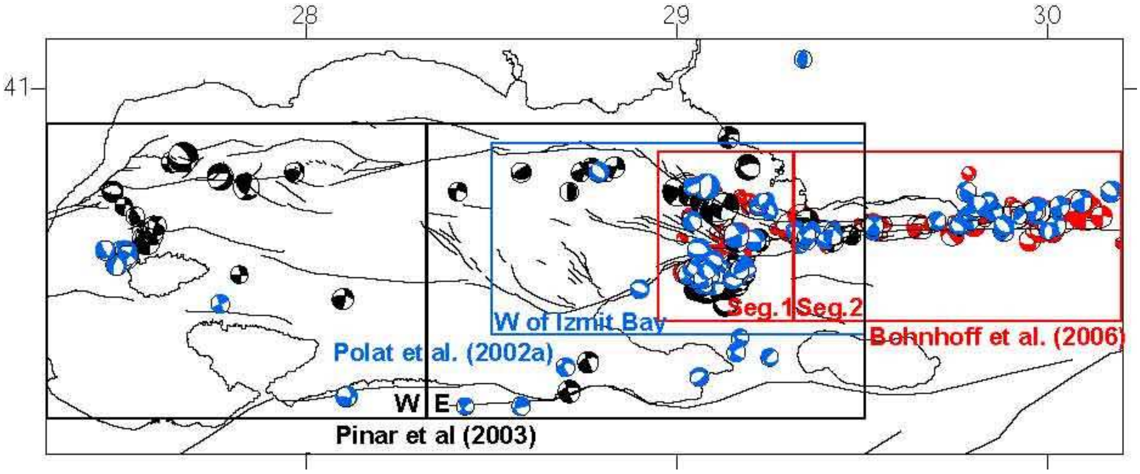

Fig. 4.17: Overview map of focal mechanism data sets and areas for which results of stress tensor inversions are available. This map refers to Fig. 4.19.

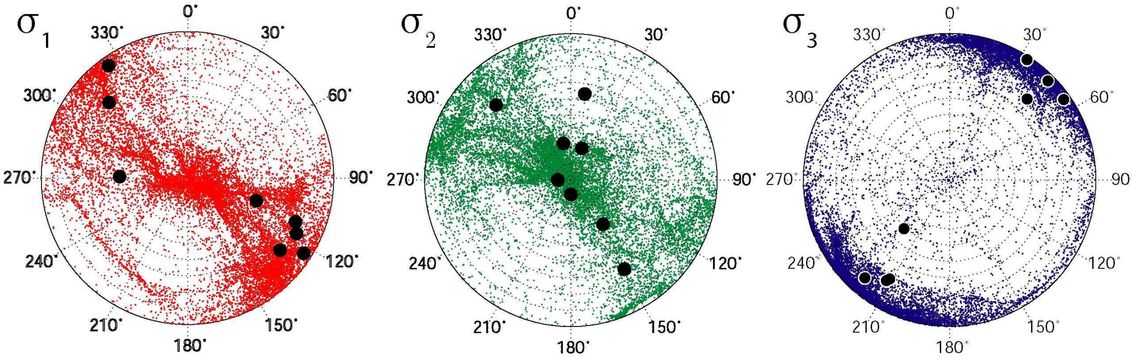

Fig. 4.18: Modelled principle stresses (σ_1 left, σ_2 middle, σ_3 right) at 5 km depth at grid points (0.01°E x 0.01°N) over the whole model area. Black dots mark reported orientations of the principle stresses from stress tensor inversions of earthquake focal mechanisms in various subareas (Gurbuz et al., 2000; Polat et al., 2002a; Pınar et al., 2003; Bohnhoff et al., 2006).

This result is in good agreement to published stress tensor inversions of focal mechanisms. Almost every point denoting the published orientation of a principle stress axis can be correlated with a cloud indicating the modelled stress orientations (Fig. 4.18). The only exception is the western subset of Pınar et al. (2003) which may be due to the relatively few and heterogeneous focal mechanism in this set. Fig. 4.19 correlates the reported stress orientations shown in Fig. 4.18 to their respective area and it becomes clear that the modelled stress orientations in Fig. 4.18, which represent the whole model area, better match the inversions from the regional scale datasets than those from the smaller subareas (Fig. 4.17). The regional datasets in which aftershocks are absent and the one comprising major earthquakes (Gürbüz et al., 2000; Polat et al., 2000b) yield the best coincidence. Most of the published inversions show a strike-slip regime while Polat et al. (2002a) found extension with σ_2 being the steepest principle stress. As explained above both can be well reconciled with the modelled stress orientations.

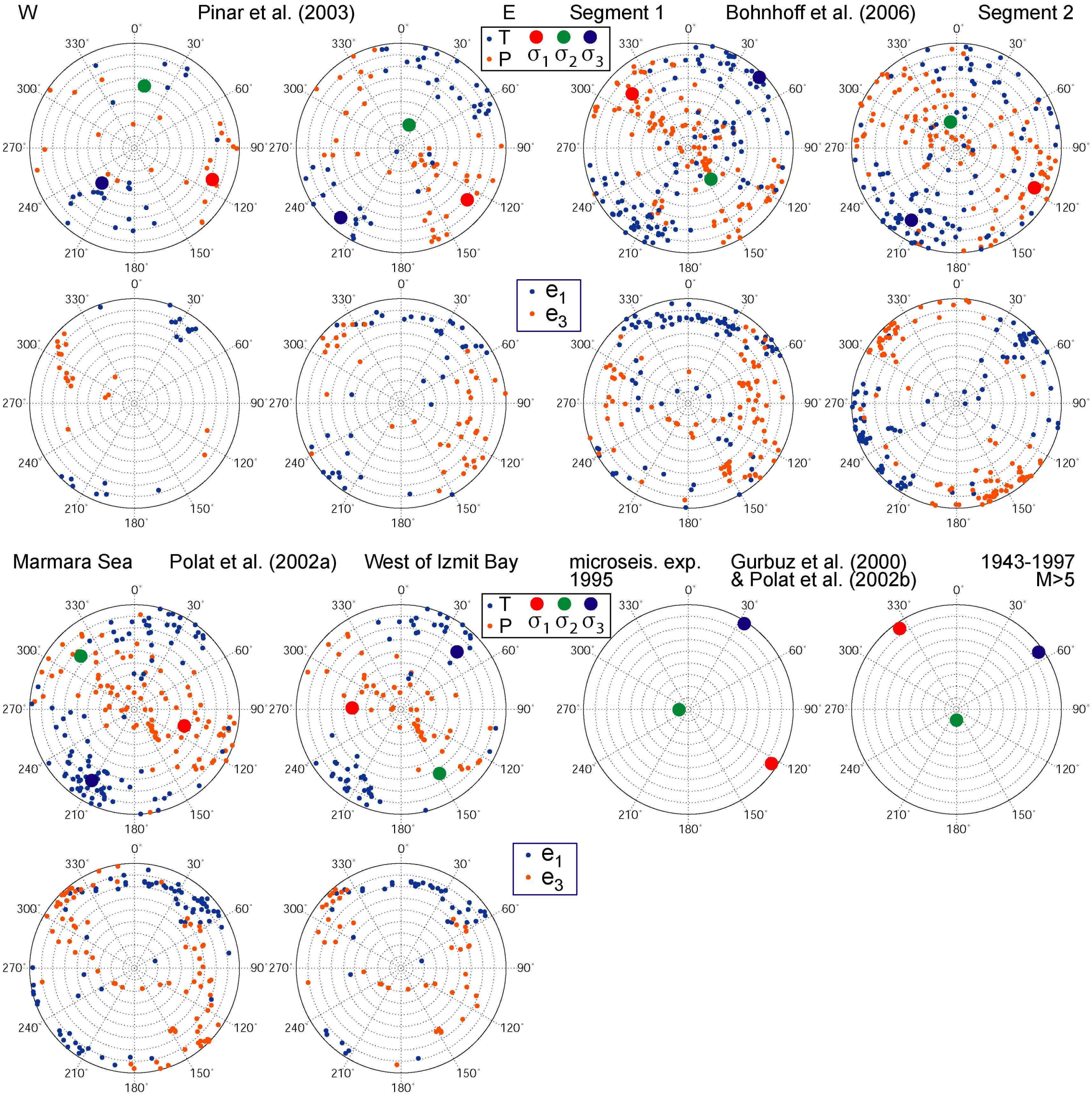

Fig. 4.19: First and third row show reported P/T axes of earthquake focal mechanisms as well as results of stress tensor inversions for the datasets displayed in Fig. 4.17. The figures below, in the second and fourth row, show orientations of modelled minimum and maximum principle strain axes at the hypocentres of the earthquakes whose P/T axes are shown in the plots above, respectively.

The polar plots in the first and third row of Fig. 4.19 also show the orientations of the reported P- and T axes of the focal mechanisms. The plots below them show the modelled minimum and maximum principle strain axes e_3 and e_1, respectively, at the hypocentres for comparison. The pattern of single dots is mostly not well reproduced but the general behaviour of all data is well modelled. In general, e_3 axes point in NW or SE directions as the P axes do, while the e_1 axes trend in NE or SW directions like the reported T axes. The modelled orientations are more focused whereas the reported axes are more distributed. This is surely because most of the analysed earthquakes occurred close to each other and the model provides only one orientation at one point whereas focal mechanisms may exhibit significant variety even in small volumes. It should also be noted that the reported focal mechanisms of those earthquakes which were reported by at least two authors in part differ from each other by an amount that inhibits rejection of single modelled orientations.

4.2.3 Stress magnitudes

One of the main goals of this thesis is to model the absolute stress field in the Marmara region. However, it is difficult to validate whether this goal is actually accomplished since there are no stress magnitude measurement data at greater depths available. Nevertheless, qualitative conclusions from the modelled stress magnitudes can be drawn and there are observations that might provide indirect constraints on the stress field as will be explained.

4.2.3.1 Differential stress

The modelled differential stress σ_1 - σ_3 at 5 km bsl. based on the stress field in Fig. 4.13 is shown in Fig. 4.20 (upper row). High differential stresses are confined to the vicinity of faults in particular at the Ganos Bend, Central Basin and Çınarcık Basin where faults are strongly curved or different faults approach each other. Low differential stresses are predicted on the northern shelf between Istanbul and the Central Basin, Central High and at most of the southern shelf as well as around the four corners of the model area. The sediments act to reduce differential stresses (Fig. 4.20 upper row, middle figure) due to their lower density decreasing the load of the overlying rock mass and their much lower Young's modulus which responds by lower stresses to a given strain. In contrast, applying Byerlee friction coefficients on all but the main fault increases differential stress in particular on the southern shelf and the southern onshore areas (Fig. 4.20 upper row, right).

Rock strength is a certain differential stress at which intact rock subjected to this critical stress responds by brittle failure. Rock strength is basically determined by the internal coefficient of friction μ_i and by the cohesion C_o of the rock. A measure for the likelihood of fracture generation due to critical differential stresses is the Fracture Potential (FP) which is defined in App. 3. FP was calculated from the modelled differential stress using $\mu_i = 0.64$ and $C_o = 31$ MPa, which are the values reported for granite as a typical crustal rock (Jaeger and Cook, 1969). One could term this as post-processing rheology since the model was run with purely elastic rheology and the plastic yield criterion is applied afterwards to the modelled stress field. Of course, the FP values reflect the characteristics of the differential stress on which they are based on (Fig. 4.20, second row). Actually, it would be more meaningful to assume a lower rock strength for the model considering the sediments so that a lower differential stress would be sufficient for failure in this case.

Fracturing of rock is manifested by seismicity. Thus, the observed seismicity pattern could be used to check the modelled differential stress pattern in view of its meaningfulness. In turn, the modelled differential stress should predict the principle features of the spatial seismicity distribution. It is important to note that this issue does not directly concern seismic hazard since large damaging earthquakes normally rupture already existing faults whereas here the fracturing of an intact rock volume is addressed which is generally associated with earthquakes of moderate magnitude due to local peak differential stresses evolving during plate motion in the surrounding of a given fault geometry. Seismic hazard will be the topic of chapters 5 and 6.

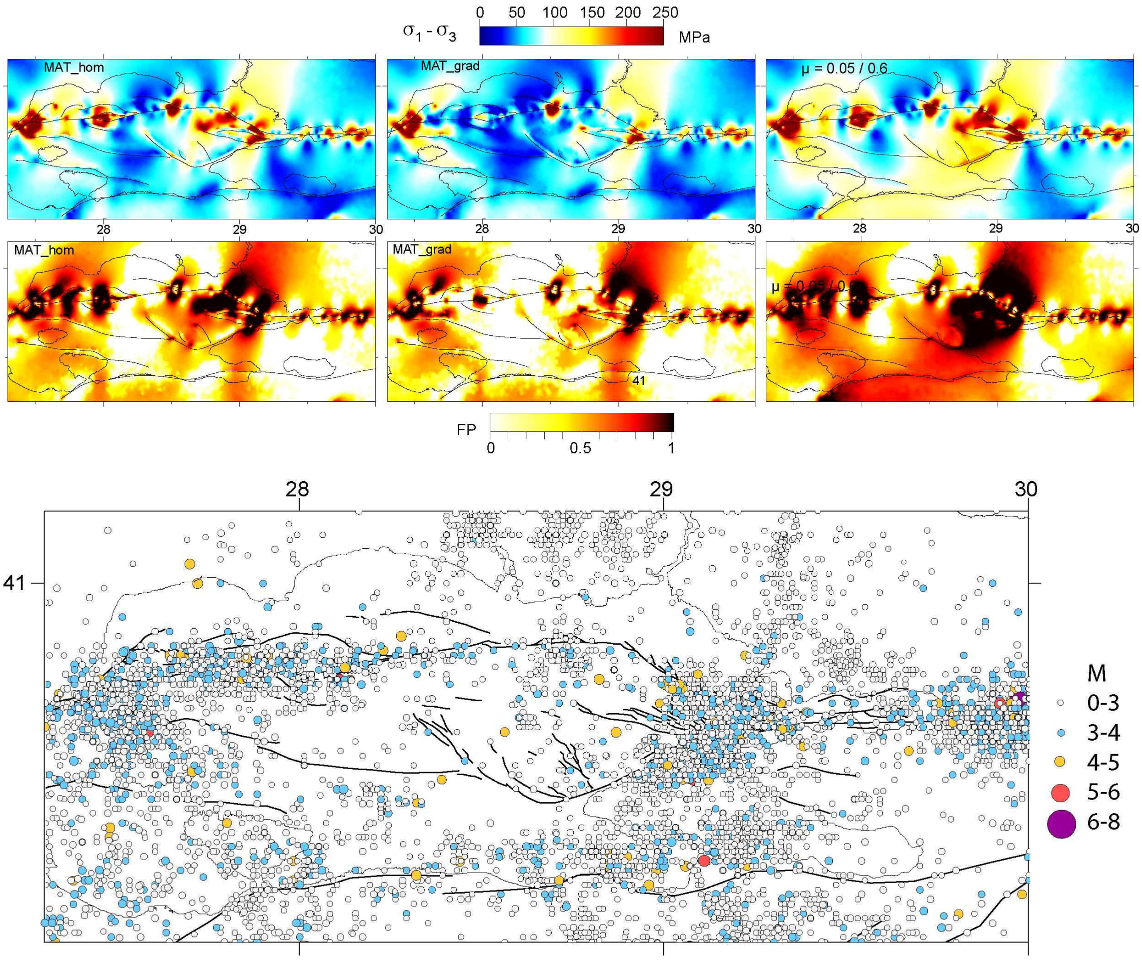

Fig. 4.20: Modelled differential stress σ_1 - σ_3 at 5 km depth (top row) and calculated fracture potential FP (App. 3) (middle row) in comparison to seismicity (bottom; 1973-1989 and 2005-August 2008 from USGS NEIC catalogue and 1990-2004 from Kandilli catalogue).

Fig. 4.20 (bottom) shows the seismicity between 1973 and 2008 from all depths for a better spatial coverage. Though not in detail, the main features of the FP pattern can be found in the seismicity distribution. High FP values in the Western Marmara Sea in the Central Basin, Western High, Tekirdağ Basin as well as south of it towards Marmara Island clearly correlate with increased seismicity. A high likelihood for fracture generation predicted for the eastern Çınarcık Basin and the northwest of Armutlu Peninsula are also confirmed by dense seismicity including the Yalova cluster. Good coincidence is also found for the central part of the Marmara Sea with low FP values on the northern shelf, Central High and the area to the west and southwest of Imralı Basin. Seismicity is almost absent or at a moderate level there supporting this result. Also the NW, NE and SE model areas for which low FP values are predicted are almost aseismic. In the southwestern part characterized by more or less uniform intermediate FP values distributed seismicity is observed at a likewise intermediate level. Increased seismicity in the southern part of Armutlu Peninsula, Gemlik Bay and along the southern shore of the Marmara Sea are best explained by the model with high fault friction.

In some areas the FP results cannot be correlated to the observed seismicity. In the middle of the Central Segment of the MMF a marked patch of high FP was inferred whereas seismicity was hardly observed there. A bend of the MMF in the model is responsible for the high differential stresses there. However, there is no evidence for the presence of this fault bend at depth in seismic profiles and the bend was only anticipated from the peculiarities of the mapped surface trace of the MMF there. Thus, the stress concentrations could be due to a misinterpreted fault geometry and with a plane fault segment differential stresses could be as low as in the surrounding. Similarly, in the northwest of the Prince’s Islands Segment high FP values occur right were a slight fault bend was constructed widening the Çınarcık Basin and associated with a lower fault dip than nearby. This leads to a local increase in dip-slip motion (Fig. 4.9) and consequently to a reduction in σ_h (Fig. 4.13) and thus increase in differential stress. The stress concentration spreads to the southwest towards the western tip of the Çınarcık Fault. A M = 4.8 event occurred there but seismicity is otherwise sparse. Again, it is not clear whether this fault bend actually exists at depth. High FP values to the northeast of the Prince Island`s Segment are supported by increased seismicity only in the southeastern part, a M = 4.1 earthquake near the coast among them, but not in the northwestern part towards Istanbul.

Low FP values in areas of increased seismicity such as west of Iznik Lake and south of it, along the southern shore of the Marmara Sea and west of Istanbul may be explained by the omission of faults in the model which were found to be there (Gökaşan et al., 2002; Yaltırak and Alpar, 2002; Kurtuluş and Canbay, 2007; Öztürk et al., in press). Incorporation of these faults should increase differential stresses there since these generally arise in the vicinity of faults in case of complex geometry, fault interactions and near fault tips. Besides, most of the seismicity around Istanbul, particular to the west, are of artificial origin due to quarry blasts (Horasan et al., 2009).

In summary, apart from the deficiencies due to the reasons discussed the distribution of seismicity of low to intermediate magnitude in the Marmara region could be widely explained by fracture generation due to critical differential stresses which are mainly a result of interaction between fault geometry and plate motion. By that, the modelled differential stress is largely appropriate at least in view of the observed seismicity.

4.2.3.2 Normal stress on the MMF

The last stress quantity presented from the model addressing the steady-state situation is the normal stress on the MMF (Fig. 4.21). Of course, fault normal stress increases with depth. But most interestingly, along its path from one model boundary to the other the MMF experiences considerable changes in fault normal stress laterally. The Prince’s Islands Segment is characterised by a much lower increase of normal stress with depth than the other fault segments. At mid-crustal depths the difference in normal stress between the Prince’s Islands Segment and the adjacent segments is in the order of several hundreds of MPa (200-500) or at least a factor of two. The lateral differences in fault-normal stress found here are in the same order of those inferred for the San Andreas Fault by Parsons (2002) from numerical modelling. Also in the western Marmara Sea and in particular below the Tekirdağ Basin fault-normal stress is markedly reduced. In contrast, the fault normal stress depth gradient is higher in the Izmit Bay and on the Central Segment. Peak values in normal stress are modelled on the restraining side of the Ganos Bend and east of Tuzla Bend and less pronounced west of Istanbul Bend.

For the MAT_grad rock properties the lateral contrast in normal stress between different fault segments is still more drastically. The fault sections experiencing extension (Prince’s Islands Segment and MMF along the southern rim of the Tekirdağ Basin) show lower normal stresses over the entire model thickness. The other segments show lower normal stresses only at shallow depths due to the lower density and Young’s modulus of the sediments whereas at greater depths fault-normal stresses are higher since the MAT_grad rock property distribution assumes a denser and stiffer basement than the homogeneous model (Tab. 3.1; Fig. 3.4).

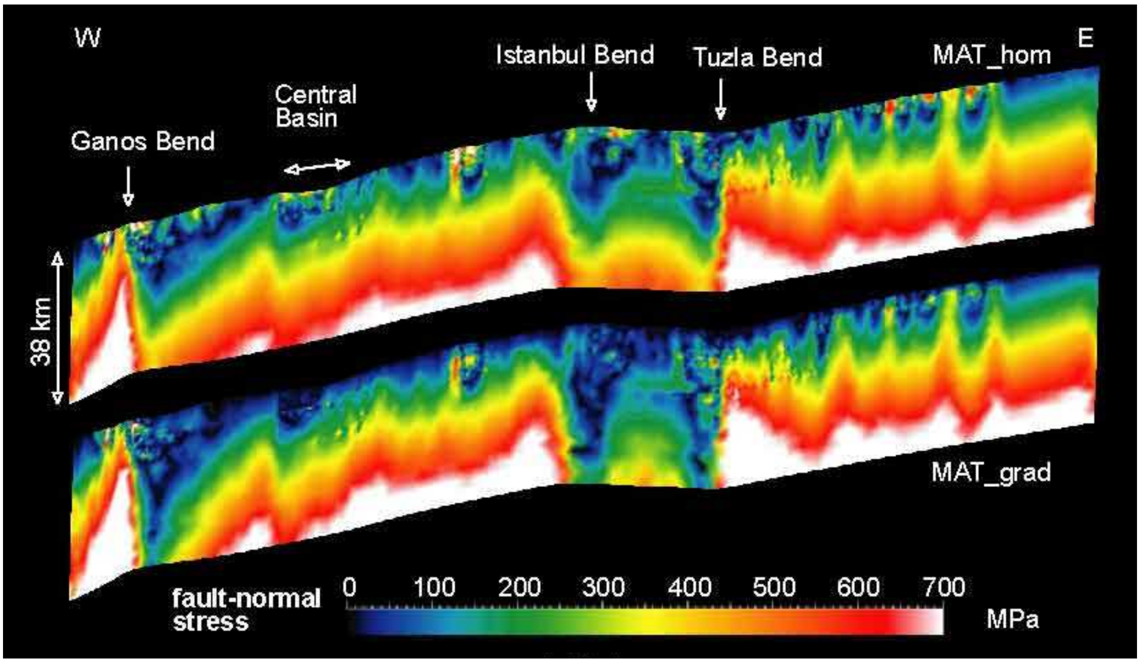

Fig. 4.21: Normal stress on the main branch of the NAF for the homogeneous model and the one with MAT_grad rock properties.

4.2.4 The role of prestressing

This chapter is intended to address the role of prestressing in models that aim at the absolute stress field. For this purpose a model is considered that is only gravitationally prestressed using the uniaxial strain condition as depicted in Fig. 3.5. and thus without the initial ratio of horizontal to vertical stress proposed by Sheorey (1994). This model is referred to as Model A in the following. The model presented in the previous chapters which was prestressed accounting for both gravitational equilibrium and a ratio of horizontal to vertical stress according to Sheorey (1994) as described in chapter 3.5.2 (Fig. 3.7) is referred to as Model B in the following.

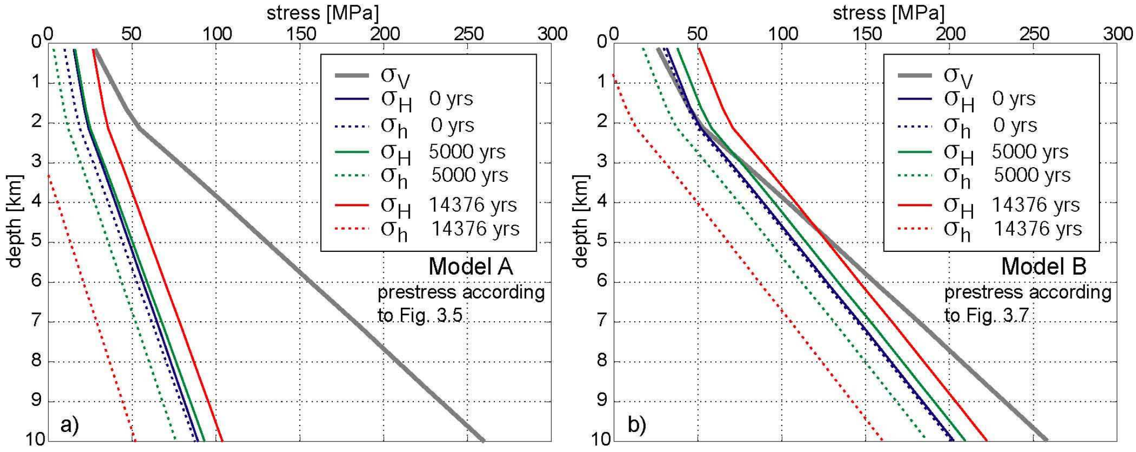

Fig. 4.22: Stress paths at site „NE“ (Fig. 3.8) after prestressing (0 yrs) and temporal evolution due to plate tectonic boundary conditions. a) Model A: the vertical stress far exceeds the horizontal stresses resulting in an extensional stress regime ($\sigma_V >> \sigma_H > \sigma_h$). b) Model B: A strike-slip regime evolves with time ($\sigma_H > \sigma_V > \sigma_h$). (The bends at ~ 2 km depth in the stress paths are due to element size as explained in 3.5.2, so that stresses at shallow depths are to be discarded).

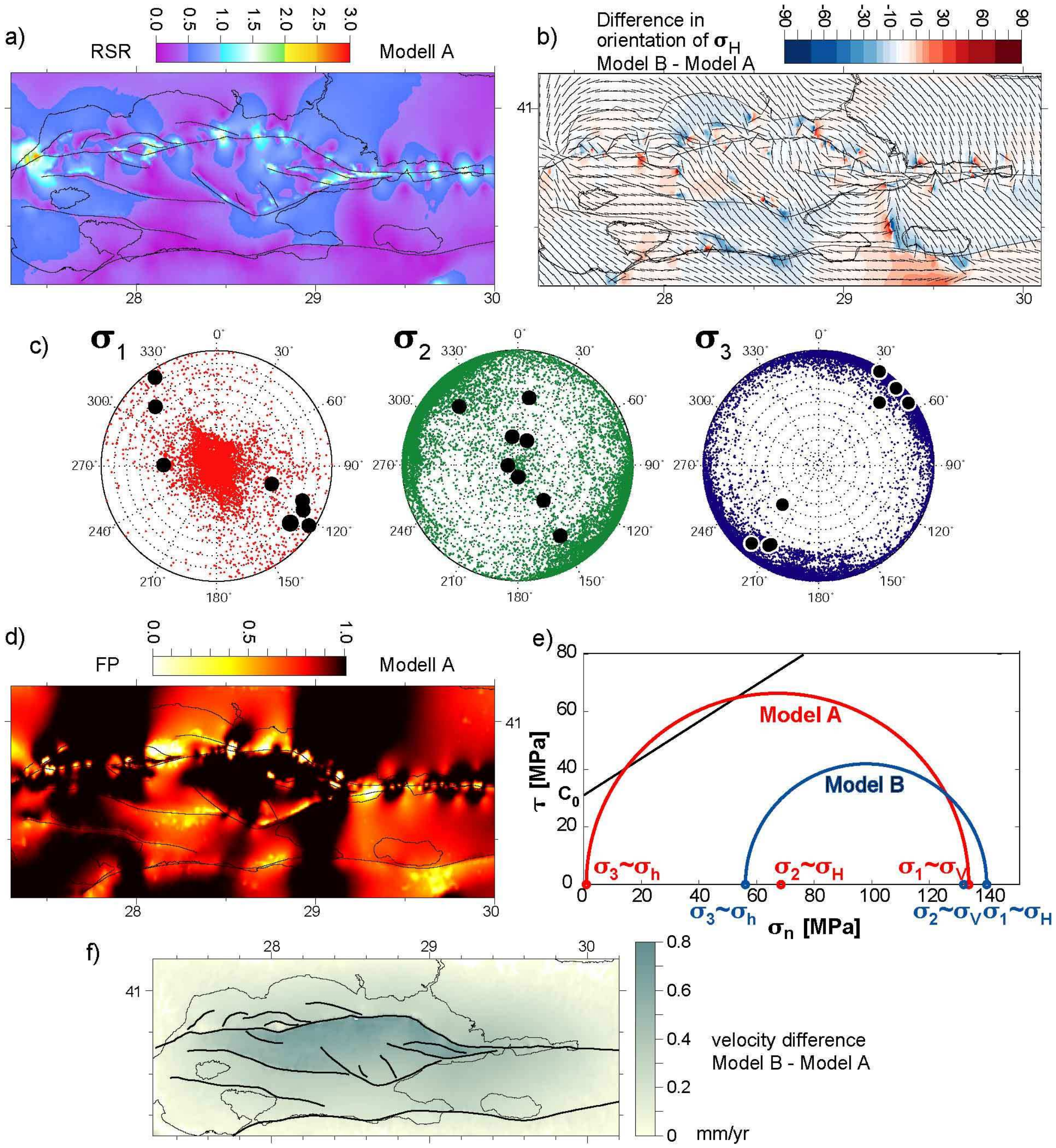

Fig. 4.23: Consequences of prestress on stress regime, stress orientations, differential stress / failure and kinematics. a) RSR (App. 1) at 5 km bsl. for Model A. Note that extension / radial extension prevails in contrast to strike-slip / transtension in the properly prestressed Model B (Fig. 4.14). b) Orientations of maximum horizontal stress for Model A (black lines) and difference Model B – Model A (contours). c) Principle stress orientations for Model A. Note that σ_1 is the vertical stress whereas in Model B it is σ_2 (Fig. 4.18). d) Fracture Potential FP (App. 2) at 5 km bsl. for Model A. Note, that most of the model area is prone to failure, in contrast to the properly prestressed Model B (Fig. 4.20, middle left). e) Mohr circles at site "NE" (Fig. 3.8) at 5 km bsl. for Model A and B. Failure envelope assumes C_0 = 31 MPa and μ_i = 0.64. Note, that in Model A failure occurs due to differential stress between the vertical and minimum horizontal stress, whereas in Model B differential stress is uncritical and given by the two horizontal stresses. d) Difference in horizontal velocity between Model A and B. Conclusions: 1) Initial stress has strong impact on stress regime and differential stresses / rock failure. 2) Meaningful maximum horizontal stress orientations and kinematics do not imply a meaningful 3D stress state.

Proceeding from Fig. 3.8 that shows the state of stress after prestressing in Model A (k=1/3) and B (dashed lines), tectonic boundary conditions were applied (Fig. 3.9). Fig. 4.22a) and b) show the stress paths of the vertical stress σ_V and of the maximum and minimum horizontal stresses σ_H and σ_h at site "NE" (Fig. 3.8) for Model A and B, respectively, and their temporal evolution. The temporal changes of the vertical stress are negligible small. Initially, i.e. right after prestressing, σ_H and σ_h have roughly the same magnitude. The tectonic boundary conditions make σ_H and σ_h move apart from each other.

Model A is in an extensional tectonic stress regime throughout the crust since the vertical stress far exceeds the horizontal stresses ($\sigma_V >> \sigma_H > \sigma_h$) (Fig. 4.22a). This corresponds to RSR values around 0.5 indicating extension (Fig. 4.23a) in marked contrast to the results of Model B (Fig. 4.14 top) which yielded a strike slip to transtensional stress regime. In Model B a strike-slip regime evolves with time as σ_H becomes gradually higher than the vertical stress, which is initially higher (Fig. 4.22b).

The extensional stress regime in Model A is manifested in the vertically dipping maximum principle stress (Fig. 4.23c) whereas σ_1 was found almost horizontal in Model B in agreement with stress inversions of earthquake focal mechanisms (Fig. 4.18). While principle stress orientations differ fundamentally between Models A and B, they result in almost the same maximum horizontal stress orientations (Fig. 4.23b). Deviations in σ_H between the two models are <5° over most of the model area. This is simply due to the fact that in Model A σ_H is given by σ_2 whereas in Model B it is either σ_1 or σ_2 – while trend is the same. This demonstrates, that a model matching observed σ_H orientations, does not necessarily represent a meaningful 3D stress state or in other words stress regime.

The large differences between horizontal and vertical stress in Model A cannot be overcome by the acting boundary conditions which are slightly extensional (σ_h decreases at a higher rate than σ_H increases; Fig. 4.22). At less than 10 km depth the differential stress already exceeds the shear strength of intact crustal rock (Fig. 4.22). This is also demonstrated by the inferred fracture potential for Model A indicating that in most of the model area fracturing would occur (Fig. 4.23b) whereas in Model B areas under critical differential stresses were found much smaller (Fig. 4.20 middle).

Fig. 4.23c depicts the Mohr circles at 5 km bsl. at site "NE" (Fig. 3.8) together with a failure envelope assuming C_0 = 31 MPa and μ_i = 0.64. Differential stress in Model A is high and critical whereas differential stress in Model B is much smaller and far below critical values. In Model A σ_1 corresponds to σ_V, while in Model B σ_V represents σ_2. The large differential stress in Model A exceeding the yield stress is a consequence of the too low horizontal stresses compared to the vertical stress ($\sigma_1 \approx \sigma_V >> \sigma_3 \approx \sigma_h$). However, near a major lateral shear zone such as the NAF shear failure is not expected to arise from differential stresses between the vertical stress and the minimum horizontal stress. Instead, failure should be due to critical differences between maximum and minimum horizontal stress arising from the horizontal shear exerted by the relative plate motion. In Model B horizontal stresses are much higher and closer to the vertical stress due to the additional prestress so that differential stress is much lower than in Model A, far below the failure envelope (Fig. 4.22; 4.23c). In Model B high fracture potential is predicted only locally near the fault where high differential stresses due to the fault geometry and plate motion evolve (Fig. 4.20 middle).

In Fig. 4.23d) the difference in horizontal surface velocity between Model A and B is shown. Of course, the deviations are zero at the boundaries since the same displacement boundary conditions were applied, and they are higher in the middle. The velocity differences between both models are smaller than 1 mm/yr and negligible with respect to absolute velocities and similar or even below the accuracy of GPS measurements. This illustrates that the different prestress in both models hardly affects the resulting kinematics. Thus, Model A fits the GPS observations equally well than Model B presented in chapter 4.1.

To conclude, two different initial stresses were considered, namely only gravitational prestress (Model A; Fig. 3.5) and both gravitational prestress and horizontal to vertical initial stress according to Sheorey (1994) (Model B; Fig. 3.7), depicted in Fig. 3.8; and 4.22 (0 yrs). The following consequences of prestressing arise on stress regime, stress orientations, differential stress and kinematics:

- A solely gravitationally prestressed model (Model A) is capable of reproducing kinematic observations and maximum horizontal stress orientations. In this respect it is essentially equal to a model that is prestressed according to the more advanced prestressing approach presented in 3.5.2 (Model B).
- However, the models result in completely different stress states with fundamental consequences. Model A fails both to predict
  - a realistic stress regime (Fig. 4.22a; 4.23a)
  - and rock failure (Fig. 4.23b and c)

since the vertical stress far dominates about the horizontal stresses (4.22a). In contrast, the higher initial horizontal stresses according to Sheorey (1994) are capable of reproducing meaningful stresses.

This underlines the fact that a model that fulfils the kinematic observations must not necessarily fulfil the dynamic constraints. With the prestressing approach taking into account an appropriate initial ratio of horizontal to vertical stress after Sheorey (1994) (3.5) it is possible to simultaneously model both the kinematics and dynamics according to observations. Thus, appropriate prestressing is of fundamental importance in models aiming at the absolute stress state.

4.2.5 Conclusions stresses

- This model probably represents the first attempt to obtain the absolute stress state in the Marmara region in contrast to relative stresses or stress differences commonly addressed.
- Maximum horizontal stress has a preferred NW-SE orientation in the Marmara region with local deviations associated with the fault system.
- The maximum and intermediate principle stresses are either the vertical stress or trend at low plunges in NW or SE directions, depending on location. The minimum principle stress is nearly horizontal and oriented in NE-SW directions. By that, the model agrees with stress tensor inversions from focal mechanism solutions.
- The stress regime is a strike-slip regime but close to extension for most of the Marmara Sea region.
- Modelled differential stress reflects the primary features of the observed seismicty pattern with increased activity in the western Marmara Sea, eastern Çınarcık Basin and adjacent areas. In contrast, the central part of the Marmara Sea is quite silent.
- Normal stress on the main Marmara Fault undergoes enormous changes in excess of 100 MPa along its path through the Marmara Sea with clearly reduced values on the Prince’s Islands Segment and at the southern rim of the Tekirdağ Basin, whereas normal stress is high on the Central Segment.

In particular the orientations of the three principle stresses put constraints on stress magnitudes. Since the vertical stress σ_V is primarily given by the density distribution and depth, σ_V should be well established in the model based on reported seismic velocities at depth. In most cases σ_V can be associated with one principle stress. Since the three principle stresses are ranked by their relative magnitudes, knowledge of the absolute magnitude of σ_V places constraints on the magnitudes of the two more horizontal principle stresses. However, a direct validation of modelled stress magnitudes by stress measurement data remains open since they are not available at relevant depths. It is conceivable that stress magnitude measurements were conducted in some of the numerous wells for oil and gas exploration in the Thrace Basin to the NW of the Marmara Sea. However, given such data actually exist, they may be of limited value for the whole Marmara region since there is a number of examples demonstrating that stress within sedimentary basins sometimes is decoupled from the stress field in the underlying basement (Tingay et al., 2005). To date, it is planned to drill a borehole for scientific purposes on Sivriada which is one of the Prince's Islands at only a few kilometres distance from the NAF (Dresen et al., 2008). Apart from establishing a borehole observatory allowing detection and accurate localisation of low-magnitude earthquakes it is planned to conduct stress magnitude measurements. This would provide an opportunity to better validate the modelled stress, in particular if drilling will not cease within the sediments but will penetrate the basement that is at ~2 km depth according to the constructed basement-topography (Fig. 3.3).

The steady-state Marmara Model focussing on the secular velocity and stress fields was found to simultaneously yield meaningful results with respect to observations. In this respect, a consistent model for stress and strain evolution is available that can be used to address open questions the most relevant of which are concerned with seismic hazard. During discussion of the results seismic hazard was left aside so far. The conclusions of these findings on seismic hazard will be drawn in 4.3.

4.3 Implications of the steady-state model on seismic hazard

Unless a fault accommodates relative plate motion by aseismic creep, the slip rate on a fault is directly related to seismic hazard. For greater slip rates a critical stress level is reached within a shorter period than at smaller slip rates. Furthermore, if the change in slip rate is significant along fault strike, the fault will most probably fail in segments due to the different loading conditions along the fault. With regard to the Marmara region the disastrous dependency of seismic hazard on fault slip rates was stated by Özalaybey et al. (2002) as follows:

"At present, it is not well known how this total slip rate is partitioned and taken up between these branches … In particular, the role of aseismic creep and strain partitioning remains a critical issue for any realistic assessment of seismic risk in the Marmara region."

In this respect, the fault slip rates that were presented (Fig. 4.3) and satisfactorily explained here (4.1.3.1; 4.1.4), represent a major contribution to seismic hazard assessment in the Marmara region.

Though aseismic creep on the NAF cannot be excluded and a creeping section on the NAF at shallow depths at a length of ~70 km around Ismetpasa (~32.6°E) is known from geodetic observations (Cakir et al., 2005), the NAF is generally seismogenic since historical times (Ambraseys and Jackson, 1998). For the Marmara region Ambraseys and Jackson (2000) calculated right-lateral shear-velocities from released seismic moment. Since their result is right the same than geodetic observations suggest they concluded that "perhaps effectively all" fault slip is seismogenic and that "aseismic creep is relatively unimportant" in the Marmara region.

The consequences of the presented slip rates on seismic hazard are outlined in the following. As explained in 1.3.2 and 1.3.3 slip rates are commonly used as integral part of time-dependent probability analyses of earthquake occurrence. (1) Slip rates were used to constrain the recurrence interval on the MMF for probability calculations. For this purpose, Parsons et al.

(2000) and Erdik et al. (2004) assumed a slip rate of 22 mm/yr which is 20-75 % higher than inferred here. (2) Slip rates were used to infer the activity rate of characteristic earthquakes of particular magnitude on each fault segment. For this purpose, Kalkan et al. (2008; in press) used fault slip rates that are in part far beyond from what was found here, e.g. 20 mm/yr on the Southern Border Fault in contrast to < 2 mm/yr (Fig. 4.3), and as a consequence the summed slip rates along cross sections over the Marmara region imply a total relative plate motion that is 2-3 times faster than observed. This is a marked example of how important it is for resulting ground motion probabilities to apply fault slip rates that are consistent with a mechanical model. (3) If fault interactions are considered by using the concept of Coulomb failure stress changes, the slip rate is required to deduce an annual stressing rate that allows estimation of the probability change associated with a coseismic stress change from a nearby earthquake. The slip rates on the MMF applied in ΔCFS studies are in part considerably higher than those presented in Fig. 4.3, namely 16 mm/yr (Stein et al., 1997), 17-20 mm/yr (Armijo et al., 2005; Lorenzo-Martin et al., 2006; Pondard et al., 2007) based on the slip model from Flerit et al. (2004), 24 mm/yr (Hubert-Ferrari et al., 2000; Muller et al., 2006) and 30 mm/yr (Çakir et al., 2003a). (4) Slip rates were also used to estimate contemporary potential slip on particular fault segments based on the elapsed time since the last earthquake. Pınar et al. (2003) assumed a slip rate of 20 mm/yr on the Prince’s Islands Segment, which is 50-60 % faster than inferred in this study, and end up in a contemporary potential slip of 4.5 m. Armijo et al. (2005) deduced a slip deficit of 4-5 m on the Central Segment since 1766, which implies slip rates in the range of 17-21 mm/yr, whereas in this thesis 14-17 mm/yr were found. Hubert-Ferrari et al. (2000) expect 5.5 m of slip deficit to have accrued on the Central Segment since 1766 based on their assumed slip rate of 24 mm/yr whereas the results here suggest only about 2/3 of this value.

It is necessary to point out that reported estimations of seismic hazard by the authors above are based on reported slip rates or assumed slip rates due to a lack of information. However, for future probability calculations of seismic hazard in the Marmara region, two issues are emphasised here. First, total relative plate motion is not the slip rate on the MMF and second, used slip rates have to be consistent with a thorough mechanical model that agrees with the kinematic observations.

The inferred high variations in normal stress along strike of the MMF (Fig. 4.21) should considerably affect seismic hazard in the Marmara Sea. Presuming the validity of Mohr-Coulomb theory here, a reduction in normal stress shifts the Mohr circle to the left. Hence, a lower shear stress is required to exceed the failure envelope. This is basically equivalent to a reduction in inter-event time since a critical shear stress is reached after a shorter period of loading. In this respect, the recurrence rate of earthquakes on the Prince’s Islands Segment should be smaller than on the adjacent segments. This conclusion holds for a homogeneous medium and uniform slip-rate along the entire fault. While this is not the case, as the right-lateral slip rate undergoes a local minimum along this segment (Fig. 4.3), dip-slip rates are however much higher than on neighbouring segments (Fig. 4.9) so that total slip rate along the Prince’s Islands Segment differs not as drastically from the rates on the adjacent segments than the normal stress does. Considering inhomogeneities, the conclusion of more frequent earthquakes on the Prince’s Islands Segment can be maintained since lateral differences in normal stress are even greater in the inhomogeneous case than in the homogeneous model (Fig. 4.21) and also dip-slip rate (Fig. 4.8), while right-lateral slip rate increases slightly less than on the neighbouring segments (Fig. 4.4). Reported damage descriptions of historical earthquakes (Ambraseys and Finkel, 1991) can be reconciled with more frequent events on the Prince’s Islands Segment. Marked peaks in fault normal stress e.g. at the Ganos Bend and less pronounced at the Istanbul and Tuzla Bends and small ones in the Izmit Bay and Central Basin (Fig. 4.21) may act as barriers for seismic ruptures so that earthquakes terminate at these locations.

The deduced characteristics of slip rate and normal stress can be valuable in explaining the occurrence of past earthquakes or even to figure out their locations and give reasons for the presence of a seismic gap in the Marmara Sea. Historical earthquakes gather in the Izmit Bay and on the Ganos Fault (Ambraseys, 2002). For these fault segments higher slip rates were modelled than for those in the Marmara Sea, thus providing an explanation for this pattern (Fig. 4.3). The remarkable decrease in slip rate between the eastern Izmit Bay and Tuzla Bend (3-4 mm/yr) as well as the increasing fault normal stress towards Tuzla Bend may have contributed to stop the 1999 Izmit earthquake in the western Izmit Bay. The relative rareness of large earthquakes on the Central Segment, which at present is considered as the segment being unbroken for the longest time of all segments, can be in part explained by the lower slip rate (~2-4 mm/yr) compared to the NAF onshore (Fig. 4.3) and by the highest mean fault normal stress of all MMF segments in the Marmara region (Fig. 4.21).

The seismic gap on the Central Segment can be related to another result of the steady-state model. The analysis of differential stress revealed that the Central High is characterised by much lower differential stresses than the western Marmara Sea or Izmit Bay (Fig. 4.20). This circumstance was shown to correlate with the seismicity pattern that indicates areas of critical differential stresses. One may argue that the surrounding of the Central Segment is capable of sustaining long loading periods, based on the low rates in differential stress modelled in the rock adjacent to this fault. The evolution of differential stresses is primarily governed by the interaction between fault geometry and plate motion. In the western Marmara Sea, the Çınarcık Basin or the Izmit Bay locally high differential stresses evolve due to small bends of the MMF and second order faults approaching the main branch. These peak differential stresses are more or less continuously released by microseismicity and eventually inhibit the fault to accrue shear stress levels as high as expectable on the Central Segment. The plane and comparably simple nature of the Central Segment is therefore responsible for its apparent capacity to accumulate high shear stress levels without reaching critical differential stresses in the surrounding, and hence for long interevent periods on this segment.

The modelled slip rate and normal stress along the NAF in the Marmara Sea provide a basis for answering the question whether propagating earthquake sequences such as the one starting in 1939 in east Anatolia and migrating to the eastern Marmara Sea till the end of the 20th century (Fig. 1.1) are also characteristic for the Marmara Sea. From the modelled variations in slip rate it has to be concluded that the loading conditions on the faults beneath the Marmara Sea are not as uniform as on the NAF in the rest of Anatolia where the NAF has a rather simple structure. Besides, the deduced normal stress pattern favours particular fault sections for earlier rupture compared to others. Therefore, propagating earthquake sequences typical for the NAF east of the Marmara region are not likely to continue in that remarkable chronological and spatial order in the Marmara Sea – at least not in every seismic cycle. Armijo et al. (2002; 2005) and Pondard et al. (2007) came to the same conclusion from the presence of the rather complex fault structure in the Marmara Sea placing natural barriers like bends or interacting faults which inhibit uniform propagation of earthquakes. In contrast, Le Pichon et al. (2003) claim that the slip rate is uniform throughout the whole length of the MMF and consequently consider a large rupture through the whole Marmara Sea as possible.

The direct consequence of a lower slip rate on the MMF would be that reported slip rate-based probabilities for an earthquake on a given fault segment were smaller. The probabilities for the expected future earthquake by Parsons (2004), to which is mostly referred to when stating earthquake probabilities for the Marmara Sea, are however not based on slip rates but instead on recurrence rates. According to this outstanding work, the regional time-dependent probability of a M>7 earthquake within the next 30 years, considering the coseismic stress change of the 1999 event, is 53 ± 18 % or 69 ± 28 %, depending on the adopted aperiodicity values of the mean earthquake recurrence rate. For obtaining mean recurrence rates and aperiodicities two or at most three earthquakes for each fault segment were considered, due to a lack of reliable information on historical earthquakes. In a later work, Parsons (2005) analysed the reliability of probability calculations for earthquake occurrence and concluded: “Time-dependent probability calculations may not be warranted for paleoseismic catalogs with fewer than ~10 events”. East of Bolu, where the NAF is a single and rather straight and vertical fault, probabilities based on recurrence rates is surely the best approach to follow. The results presented here provide information that contributes to an understanding of recurrence rates in the Marmara Sea since they elucidate their physical background. However, in view of the uncertainties with locations of historical earthquakes and the various interconnections within the fault system it seems worthwhile to attempt estimation of earthquake occurrence in the Marmara Sea under avoidance of recurrence rates. With this intention, in the next chapter an approach will be presented for quantification of time-dependent potential seismic moment and a very rough estimate of occurrence time in the order of decades. It is implicitly accounted for the variability in slip rates, coseismic stress changes due to historical earthquakes and for the stress-strain interconnections within the fault system. Thus, at least part of the uncertainties afflicting mean recurrence rates are taken into account.

Chapter 5

Time-dependent Marmara model

The model presented in the previous chapter represents the steady-state situation with uniform continuous motion on the faults. However, actually the secular velocity and stress field are perturbed by the seismic cycle. The stress field to a certain time depends on the time elapsed since the last earthquake and is thus a time-dependent quantity not addressable by the previous steady-state model. In order to estimate the contemporary state of stress on the faults, the seismic cycle needs to be incorporated into the model. This basically means that the faults within the seismogenic zone need to be locked and intermittently released during historical earthquakes in the Marmara region while steady state boundary conditions representing plate motion are further on continuously applied.

This chapter deals with the displacements and stress field related to the seismic cycle, both during the interseismic and coseismic stages. It is dedicated to assess seismic hazard in the Marmara region. In chapter 5.1 the elastic rebound theory is introduced and it is explained how the seismic cycle including earthquakes is modelled according to this theory. Using this technique, in 5.2 the contemporary state of stress on the MMF is modelled by incorporating the major historical earthquakes into the model. In chapters 5.3 and 5.4 the reliability of the technique of modelling the seismic cycle introduced in 5.1 is assessed. The modelled interseismic velocity field (5.3) and coseismic displacements due to the well documented 1999 Izmit earthquake (5.4) are compared with observations. Then testing earthquakes are modelled in order to assess what coseismic slip and earthquake magnitudes are to be expected if these earthquakes would happen in the near future (5.5). The likelihood of occurrence of these testing earthquakes is estimated in 5.6 based on the absolute stress state. The role of the sediments on seismic hazard in the Marmara Sea is investigated in 5.7 and the circumstances that facilitate or impede continuation of rupture propagation at Istanbul Bend are addressed in 5.8.

5.1 Stress-based modelling of earthquakes

The elastic rebound theory (Reid, 1910) is widely accepted as the basic explanation for earthquakes at major transform faults. Within this theory earthquakes are thought to arise from the elastic rebound of previously stored elastic strain energy in the rocks on either side of a fault (Fig. 5.1b). During the interseismic period the two plates adjacent to the fault move relatively to each other while the fault is locked. The far field plate motions cause the rock in the neighbourhood of the locked fault to accrue elastic deformation. Once the accumulated strain is great enough that the associated shear stresses exceed the frictional strength of the rocks, the accumulated strain energy is suddenly released as rocks snap back to their original non-deformed shape.

Commonly, elastic dislocation models of earthquakes focus on mainly two aspects. Numerical models were used to infer the heterogeneous slip distribution on a rupture plane from the geodetically observed coseismic surface displacements (e.g. Bürgmann et al., 2002; Çakir et al., 2003b; Reilinger et al., 2006). Numerical models were also used to calculate changes of Coulomb failure stress on potential future rupture planes due to an earthquake nearby (Stein et al., 1997; Hubert-Ferrari et al., 2000; Parsons et al., 2000; Muller et al., 2003; Lorenzo-Martin et al., 2006). In both cases slip is imposed on the fault in an elastic half-space and coseismic displacements and stress changes at any point in the model volume in response to the imposed slip are determined. This kind of modelling suits well for the mentioned tasks. However, it is dynamically inconsistent as shown in Fig. 5.1a). Coseismic displacements and stress changes are correct but not the absolute stress state. Stress is built up and not released since energy is brought into the model while imposing coseismic slip. As a consequence, without further assumptions these kind of models do not provide any information on the state of stress on a fault, on its proximity towards failure or on potential slip on a fault.

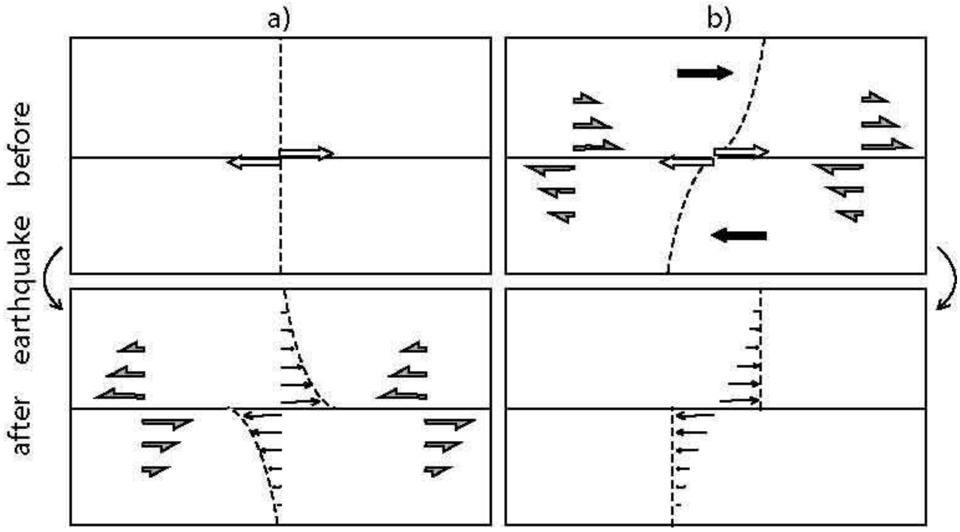

Fig. 5.1: Displacements and stress associated with the seismic cycle around a strike-slip fault (solid horizontal line; top view) prior to (upper sketches) and after (lower sketches) an earthquake. Thick white arrows indicate coseismic slip on the fault, bold black arrows in b) interseismic velocity and bold grey arrows indicate shear stress, respectively. Dashed lines denote a profile that is initially perpendicular to the fault strike and deforms during loading and coseismic slip. a) Modelling an earthquake by imposing slip on the fault. b) Modelling an earthquake by loading a locked fault and releasing the accumulated stress. Note that coseismic displacements (thin black arrows) and stress changes are the same in a) and b), whereas absolute stresses are different.

In this work, it is attempted to model the seismic cycle in a consistent way with respect to stress according to elastic rebound theory as illustrated in Fig. 5.1b). If this can be accomplished then to any time the potential slip due to the accumulated stress is inferable by unlocking the fault so that the stored stress is released by slip on the fault.

5.2 The contemporary state of stress on the MMF

The time-dependent model for seismic hazard analysis focuses on the MMF since it is located closest to Istanbul, accommodates the highest slip rates and due to its length and depth extent it has the greatest potential for strong earthquakes in the region. For obtaining the contemporary state of stress on the MMF all major recent earthquakes have to be considered and incorporated into the model since the present state of stress on the NAF depends on the time elapsed since and extent of past earthquakes. Therefore, an overview and discussion on historical earthquakes on the MMF is given at first.

5.2.1 Historical earthquakes on the MMF

The noteworthy earthquakes on the MMF during the last 500 years were the 1509, 1719, 1754, May 1766, August 1766, 1894, 1912 and 1999 earthquakes (Fig. 5.2). Only earthquakes with $M \geq 7$ are considered since the influence of small earthquakes on today's stress field should be negligible compared to these and since their locations are mostly not known precisely. Although the rupture locations and lengths in Fig. 5.2 widely rely on the same damage descriptions reported by Ambraseys and Finkel (1991) the interpretations differ in part considerably from each other so that the fault sections ruptured during these earthquakes cannot be unequivocally determined. This however is of fundamental importance for the assessment of contemporary seismic hazard. In the following, the respective earthquakes are each briefly introduced and a preferred set of rupture locations is chosen.

1509

The 1509 earthquake is thought to have hit the eastern Marmara Sea, and Ambraseys (2001b) placed it on the Central Segment so that this earthquake would be much smaller than they previously reported. From paleo-seismological investigations it was concluded that this earthquake also occurred in the Izmit Bay (McHugh et al., 2006; Özaksoy et al., 2006; Pavlides et al., 2006) supporting the interpretation of Parsons (2004) (Fig. 5.2) and even reached the Gulf of Saros (Rockwell et al., 2001) which is however based on Ambrasey's earlier publications.

1719

The 1719 earthquake was similar in location and extent as the 1999 Izmit earthquake but damage in Istanbul was higher so that it either had a higher magnitude or terminated further to the west (King et al., 2001) which is rewarded by most of the interpretations in Fig. 5.2.

1754

Since the 1754 earthquake was accompanied by a seismic sea wave most authors preferred a non-vertical fault segment to have hosted this event, either the Prince's Islands Segment or the Çınarcık Fault (Fig. 5.2). Damage was reported for Istanbul but destruction occurred around the Izmit Bay and further to the east (Ambraseys and Finkel, 1991) so that a more eastward location of this earthquake would be also justified (Papadimitriou et al., 2001). Considering the fact that the 1754 tsunami was not damaging, hence probably small, and that the 1999 Izmit earthquake, though it ruptured a widely vertical fault, generated a tsunami (Altınok et al., 2001; Yalçıner et al., 2002; Tinti et al., 2006) that was also observed in Istanbul (Altınok et al., 2003), a location of the 1754 event in the Izmit Bay seems also likely.

May 1766

The May 1766 earthquake caused a damaging seismic sea-wave and heavy damage in Istanbul (Ambraseys and Finkel, 1991) so that again the Prince Islands segment is a likely fault segment. However, rupture must have been longer since damage occurred all around the Marmara Sea from Edirne to Izmit and also in Gelibolu and Bursa. McHugh et al. (2006) concluded from dated perturbed sea floor sediments that this earthquake occurred also in the western Izmit Bay. Generally, the accuracy of dating is not as precise as to exclude the 1754 event to be responsible for the documented mass flow. An eastern termination in the western Izmit Bay can be reconciled with the interpretations of Ambraseys and Jackson (2000), Papadimitriou et al. (2001) and Parsons (2004) whereas Hubert-Ferrari et al. (2000), Barka et al. (2002) and Pondard et al. (2007) place the eastern end of this event at the Istanbul Bend omitting the Prince's Islands Segment (Fig. 5.2). They preferred a more western location for this earthquake due to the damage reported in the north and west of the Marmara Sea (Ambraseys and Finkel, 1991).

August 1766

The August 1766 earthquake struck the broader Gelibolu Peninsula area with heaviest damages around Tekirdağ, Gelibolu and in the north and northwest of the Marmara Sea (Ambraseys and Finkel, 1991). Damage extended to Istanbul and Bursa. Most authors assume the centre of this event in the Gulf of Saros at the northern shore of Gelibolu Peninsula. Whereas Hubert-Ferrari et al. (2000) and Ambraseys and Jackson (2000) placed the eastern termination near the western shore of the Marmara Sea, Barka et al. (2002), Parsons (2004) and Pondard et al. (2007) suggested that this event reached the Central Basin (Fig. 5.2). Thus, two authors assume that the two 1766 earthquakes occurred adjacent to each other whereas the interpretations of two other authors imply considerable gaps between the two earthquakes of ~ 45 km (Parsons, 2004) and over 100 km (Ambraseys and Jackson, 2000).

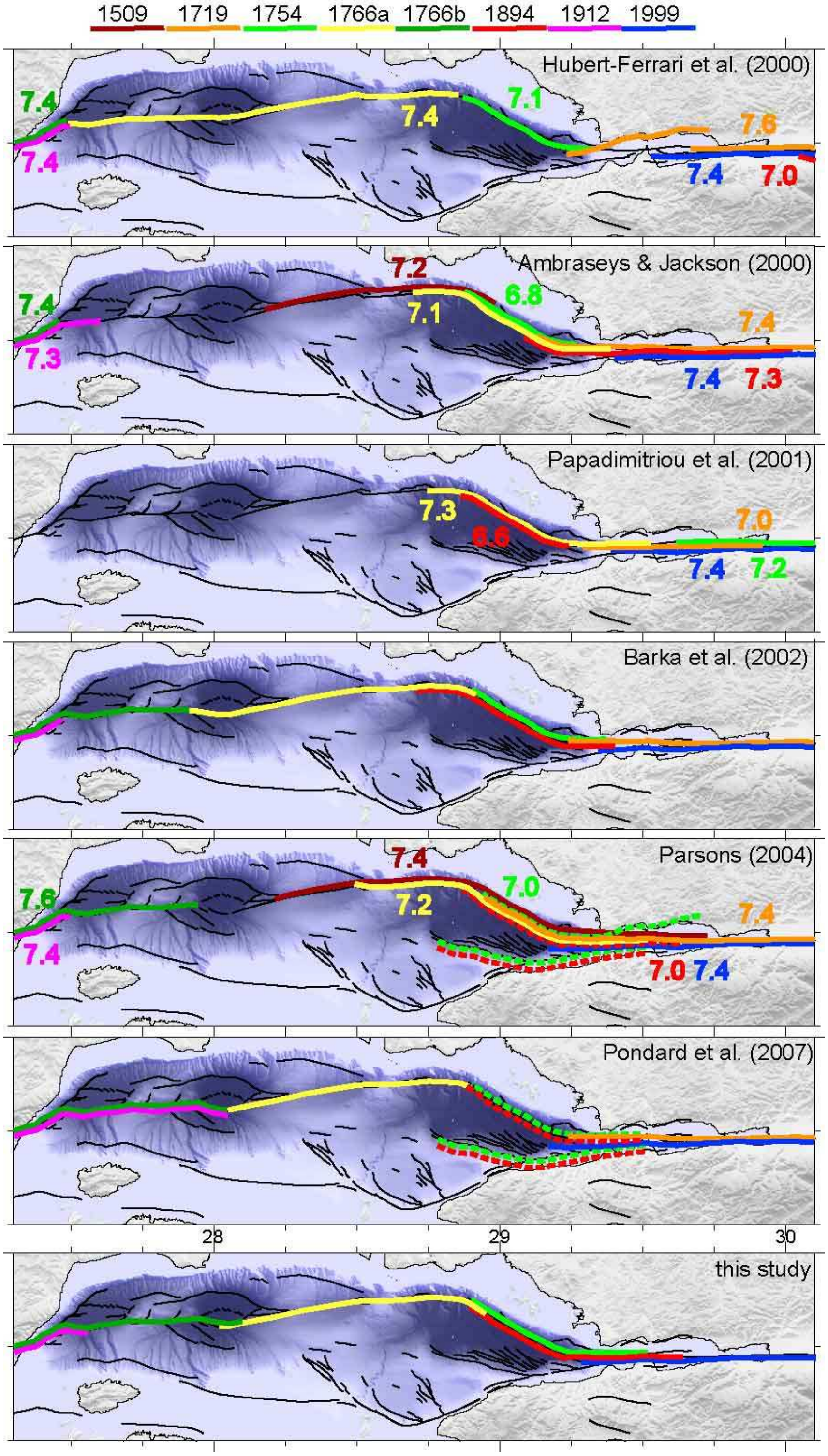

Fig. 5.2: Published rupture locations and lengths for M ≥ 7 historical earthquakes on the MMF. Dashed lines indicate different possibilities. Lines for Ambraseys and Jackson (2000) were drawn using their epicentres and rupture lengths assuming the epicentres in the middle. Bottom figure displays the preferred set of rupture locations used in this work (the 1719 earthquake is omitted here since at that time fault locking starts).

1894

The most affected area of the 1894 earthquake was the Gulf of Izmit and further to the east, between Yalova and Adapazari (Ambraseys, 2001a). Heavy damage was reported also in Istanbul and on the Prince Islands, a seismic sea wave was documented, the Sakarya river flooded its banks and landslides concentrated in the area east of Sapanca. According to this damage description the interpretation of Ambraseys and Jackson (2000) seems probable (Fig. 5.2). Hubert-Ferrari et al. (2000) placed this earthquake to the east of Sapanca Lake which hardly can explain the sea wave of 4.5 m amplitude (Altınok et al., 2003) and over 250 deaths in Istanbul whereas those interpretations locating this event at the Prince's Islands Segment might underestimate the destruction in the Sapanca area with 990 deaths unless site effects due to soft sediments around Sapanca Lake and Akyazi Plane are responsible for the losses there.

1912

The 1912 Ganos earthquake caused extensive damage on Gelibolu Peninsula with hundreds of destroyed villages (Ambraseys and Finkel, 1991). Serious damages were also reported for Istanbul as well as a seismic sea-wave indicating that the surface break entered the Marmara Sea (Altınok et al., 2003). However, there is debate on the eastern termination of this event. Until Armijo et al. (2005) discovered fresh looking fault scarps on the sea floor the Ganos earthquake was thought to have ruptured not far into the Marmara Sea and terminating somewhere around Ganos Bend. Based on their observations Armijo et al. (2005) concluded that the 1912 event reached as far as to the Central Basin. This view is supported by Pondard et al. (2007) while the other authors keep to the former interpretation.

1999

The western end of the 1999 Izmit earthquake is supposed to be west of Hersek Peninsula although no surface displacement was observed on this peninsula (Muller et al., 2006; Cormier et al., 2006). Reconstructions of coseismic slip by means of elastic dislocations require slip on the MMF 10-30 km west of Hersek Peninsula in order meet the geodetic constraints (Reilinger et al., 2000; Wright et al., 2001; Feigl et al., 2002; Çakir et al., 2003b) and also inversions of strong motion waveform data for slip yielded slip west of Hersek (Bouchon et al., 2002; Delouis et al., 2002; Sekiguchi and Iwata, 2002). Aftershocks progressed into the Çınarcık Basin and along the fault on the northern rim of Armutlu Peninsula to ~35 km west of Hersek Peninsula (Ito et al., 2002; Karabulut et al., 2002; Özalaybey et al., 2002). Evidence for surface rupture west of Hersek Peninsula was also found from observations on the sea floor by sonar techniques and towed cameras (Gasperini et al., 2003; Armijo et al., 2005; Cormier et al., 2006; Uçarkuş et al., 2006). Gülen et al. (2002) even suggested a continuation of the Izmit rupture close to the Prince Islands based on inversion of teleseismic waves.

The authors referred in Fig. 5.2 followed different guide lines for their interpretations. Ambraseys and Jackson (2000), Papadimitriou et al. (2001) and Parsons (2004) considered the damage descriptions quantitatively by applying local attenuation relations to the seismic intensity distributions. In contrast, Hubert-Ferrari et al. (2000), Barka et al. (2002) and Pondard et al. (2007) seem to have assumed that the whole MMF broke since 1766 and grouped the single earthquakes in such a way that beside the damage distributions empirical scaling relations are rewarded, that ruptures terminate at geometrical complexities such as fault bends and that several earthquakes on the same segment in close temporal proximity are avoided. This implicitly assumes a widely uniform slip rate on the NAF or more precisely, that earthquakes are in principal equally frequent on all segments of the MMF. As concluded in 4.3 from the variations in slip rate and fault normal stress this is probably not the case. The interpretations of Ambraseys and Jackson (2000) and Parsons (2004) support the conclusion that in particular the Prince's Islands Segment fails more frequently than other segments of the MMF (Fig. 5.2). On the other hand it is unlikely that both the 1754 and 1766 May events (Ambraseys and Jackson, 2000) and also the 1719 event (Parsons, 2004) broke the Prince’s Islands Segment as loading time would be very short. Concerning tsunamis also submarine landslides due to ground shaking have to be kept in mind since Yalcıner et al. (2002) and Tinti et al. (2006) found from numerical modelling that landslides can account for tsunamis of similar or even higher wave amplitudes than earthquakes.

Implicitly, the interpretations in Fig. 5.2 assume that damage is determined by distance from the rupture plane. However, in the Marmara Sea one has to be aware of anisotropic wave propagation. The pronounced basement-topography and variations in sediment thickness in the order of several kilometres (Fig. 3.1; 3.3) implying enormous lateral velocity contrasts may cause seismic waves to propagate in preferred directions. The low-velocity sediments in the basins of the North Marmara Trough may act as some kind of wave guide focussing the wave field, so that there possibly is a preferred EW propagation. For most of the earthquakes in the Izmit Bay damage was reported on the western coast of the Marmara Sea and even as far as Edirne beyond the Thrace Basin with up to 9 km thick sediments, whereas south of the Marmara Sea, though much closer, damage seemed generally less severe. In turn, waves coming from the west may be channelled by the narrowing Çınarcık Basin concentrating energy onto Armutlu Peninsula and directing it into the Gulf of Izmit. At least this can be concluded from finite difference modelling of wave propagation (A. Oth, pers. communication). The reported distribution of large historical earthquakes during the last 2000 years reveals a concentration of events in the Izmit Bay and at the Ganos Fault whereas events between Istanbul and Tekirdağ occurred comparably rarely (Ambraseys, 2002; Fig. 1.7). Either this was actually the case or it is a hint for a preferred EW wave propagation so that based on the damage distribution, earthquakes in the centre of the Marmara Sea would appear to have occurred in the east or west though the northern shore is closer to the rupture plane. Even without conjecturing a preferred EW wave propagation, earthquakes may be located too far in the east than they actually were. Erdik et al. (2004) calculated the intensity distribution of a hypothetical M=7.5 earthquake between Hersek Peninsula and the Central Basin and it turns out that the dominant part of onshore areas with high intensities concentrate around the Izmit Bay although only a small fraction of the total rupture length is there. Besides, the distribution of damage surely reflects soil conditions to some extent. Kudo et al. (2002) analysed aftershocks of the 1999 earthquake and found that ground motion at Avcilar (SW Istanbul) and Adapazari (Fig. 1.5) was much stronger than at other sites closer to the epicentres and referred this to thick soft sediments. However, for taking potential wave propagation and site effects on derived rupture locations and lengths into account quantitative investigations by means of wave propagation modelling are required, which however is an issue of its own.

Another obstacle for determining the locations of historical earthquakes is illustrated by the highly heterogeneous slip distribution inferred for the 1999 Izmit earthquake, both at the surface (e.g Barka et al., 2002; Aydin et Kalafat, 2002) and at depth (e.g. Clévédé et al., 2004). The sections of small coseismic displacements between the high slip patches can be referred to step-overs between single fault segments (Barka et al., 2002) or they are due to stress shadows from smaller earthquakes such as the 1878 M = 6.6 event between Sapanca Lake and east of Gölcük (Papadimitriou et al., 2001, Barka et al., 2002). Ambraseys (2001a) reported that the 1894 event was felt as three consecutive shocks separated by 12-18 seconds. This could be a hint that the displacement field left behind by this event was also quite heterogeneous for the same reasons and possibly involved different fault segments. Eventually, there are numerous obstacles complicating intensity determination from reported damages so that inferred rupture locations and lengths are necessarily approximate, in particular for large earthquakes at sea (Ambraseys, 2002).

The preferred set of rupture locations in this work is based on the assumptions stated in the following. First, the whole MMF broke since 1766. Hence, it is assumed that the two 1766 earthquakes occurred adjacent to each other which one may presume from the damage description (Ambraseys and Finkel, 1991) and from the quite short period of only 2 ½ months between the two earthquakes which gives reason to evoke triggering of the second event by the first one due to Coulomb failure stress increase. In this case it would be more likely that these events occurred adjacent to each other. The point at which the first one stopped and the second one progressed is taken as not relevant for today’s stress field due to the short inter-event time. Second, the May 1766 event is assumed not to have occurred in the Izmit Bay and along the southern Prince’s Islands Segment since these sections probably hosted the 1719 and 1754 events not long before. Third, the Prince Islands Segment experienced more earthquakes than the adjacent segments, based on the discussion in 4.3. All events that may be associated with the Çınarcık Fault are assumed to have occurred on the Prince’s Islands Segment based on the much higher modelled slip rate on the latter compared to the former (Fig. 4.3; 4.9). Fourth, the 1912 event is assumed to have terminated near the Ganos Bend. Fifth, based on the modelled slip rates the last earthquake at Gölcük prior to the 1999 event was the 1719 earthquake since the observed coseismic slip of ~ 4.5 m in 1999 would be accumulated in 281 years at the modelled slip rate of 16.0 mm/yr at Gölcük so that the previous earthquake should have occurred in 1718, just one year before the actual date. This excludes the 1894 event at Gölcük and most probably also the 1754 event unless modelled slip rates are underestimated. Sixth, the 1999 event stopped 20 km west of Hersek Peninsula. Seventh, the sections of the respective earthquakes overlap for a few kilometres in order to allow stress release also in the transitional area.

A precise knowledge of the locations of historical earthquakes is of crucial importance for assessing the contemporary slip deficit at a fault segment and hence for seismic hazard. In view of the conflicting interpretations it is hardly possible to determine one set of rupture locations without conjecture. Unfortunately, these uncertainties in historical earthquake locations will impede definite conclusions on the occurrence of future earthquakes from this model.

5.2.2 Incorporation of the seismic cycle

The starting point for the time-dependent Marmara model including the seismic cycle is the steady-state model presented in chapter 4. The latter model was driven for 20 kyrs with unlocked faults in order to establish a stress field reflecting the ongoing tectonics so that maximum and minimum horizontal stresses, which were initially roughly equal after prestressing, became different due to relative plate motion. Then, to incorporate the seismic cycle all faults in the study area above 15 km bsl. are locked which is technically implemented by assigning infinite friction. Most of the seismicity in the Marmara region is observed above this depth (Barış et al., 2002; Karabulut et al., 2002; Özalaybey et al., 2002; Sato et al., 2004; Bulut et al., 2007). Below 15 km bsl. the coefficient of friction remains unchanged (μ'=0.05) allowing continuous slip due to the relative plate motion which is further on ensured by the plate tectonic boundary conditions acting on the sides of the model. When the coefficient of friction at a locked fault portion is reduced to its original value at some time after locking, the accumulated stress is released by slip on the fault. This happens dynamically consistent, i.e. coseismic slip is driven by stress and slip occurs until equilibrium of forces is reached.

The beginning of fault locking should be as early as to ensure that every portion of the MMF experienced at least one earthquake. The influence of earthquakes that occurred prior to these should be negligible on today’s stress field. As assumed in 5.2.1 the 1719 earthquake in the Izmit Bay fulfils this requirement although it cannot be excluded that there is a seismic gap left since 1509 in the Marmara Sea (Fig. 5.2). Hence, fault locking started on May 25th 1719 and tectonic boundary conditions were continuously applied. On September 2nd 1754 the MMF was unlocked along the anticipated rupture length for this event as displayed in Fig. 5.2 and right after locked again while tectonic loading proceeded until on May 22nd 1766 where stress on the next segment was released. In this way, the seismic cycle was incorporated into the model until end of the year 2010. The whole series of tectonic loading and stress release on particular fault segments was run fully automatically from 1719 to 2010 without computing interruptions.

Fig. 5.3 shows shear stress on the MMF end of the year 2009. Shear stress is mostly smaller than ~20 MPa, however local maxima with much higher values above 100 MPa are visible that are associated with minor fault bends. Possibly, the maximum values were smaller if plastic rheology was applied. Interestingly, the differences in elapsed time since the last earthquake between the respective fault sections do not recognisably appear in total shear stress, suggesting that typical coseismic stress drops are much smaller than the residual stresses related to structures and driving stresses.

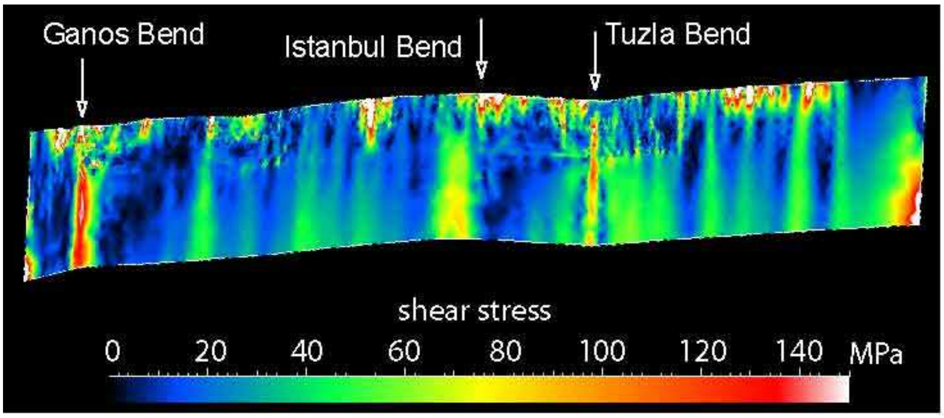

Fig. 5.3: Shear stress on the MMF in the homogeneous case end of the year 2009 including the accumulated stress due to tectonic loading since the last earthquake. No dependence of shear stress on elapsed time since the last earthquake is recognisable from this figure (Izmit segment ~10 years, Central Segment ~243 years) suggesting that typical coseismic stress drop is a small fraction of residual stress.

5.3 The interseismic velocity field

The hardest observable constraints on the seismic cycle are interseismic velocities and coseismic displacements. Thus, within this subchapter and the next one, the modelled interseismic velocity field and coseismic displacements during the 1999 Izmit earthquake are presented and compared to observations, respectively, in order to document whether the modelling technique yields agreeable results. In this subchapter additionally the observed interseismic velocity field is analysed and the discussion on slip rates intermitted in 4.1.3.1 is completed.

GPS observations during the interseismic period reflect an intrinsic part of the seismic cycle. Therefore, the velocities from the steady-state model with freely slipping faults presented in 4.1 could not be directly compared to GPS data. It was only qualitatively argued that velocities of the steady-state model should fit the observations at some distance to the faults whereas in their vicinity the steady-state velocities have to differ from observations (Fig. 4.12). The time-dependent model presented here, that considers the seismic cycle with locked faults, is thus fully comparable to GPS observations since both the observations and the model address the interseismic velocity field. Thus, the modelled interseismic velocities in relation to the GPS observations represent the basis for the reliability of the slip rates presented in Fig. 4.3.

Fig. 5.4 shows modelled velocities during the interseismic period between the 1912 and 1999 earthquakes together with the GPS velocities observed prior to the 1999 event. All in all the modelled velocities fit the observed ones quite well both in direction and rate. The modelled velocities at some stations south of the NAF tend to fall below the GPS velocities but residuals are generally small and mostly below 1-2 mm/yr. It was not tried to better fit the observations using modified locking depths.

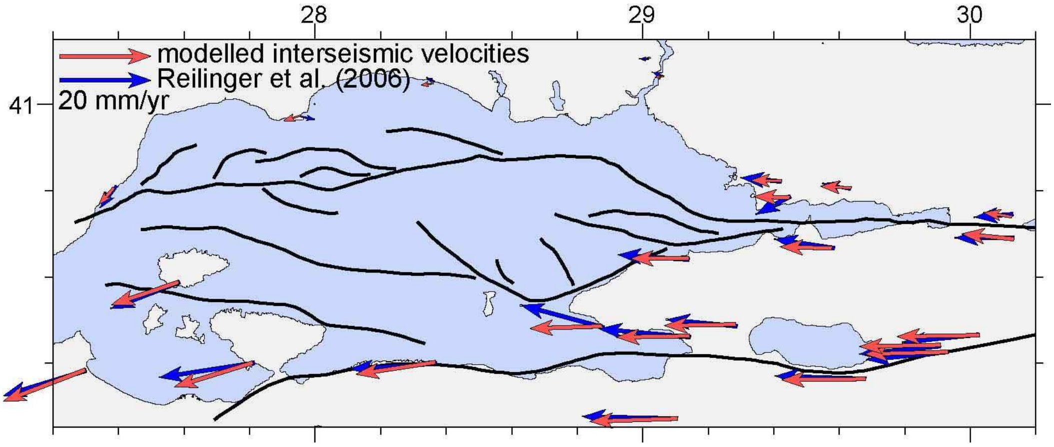

Fig. 5.4: Modelled interseismic velocities and GPS observations prior to the 1999 earthquake. Note the difference in modelled velocities near the NAF compared with Fig. 4.12.

Both the steady-state and the time-dependent models were driven by the same boundary conditions coming from the regional model with unlocked faults (3.6). This presumes that the seismic cycle does not affect the model boundary but perturbs the velocity and stress field only within the model area. In the following it is discussed whether this is actually the case. More precisely, it is analysed what the time averaged velocities at the boundaries may be and how much observed velocities deviate from the average velocities during different phases of the seismic cycle at the model boundary. Fig. 5.5 shows GPS observations both prior to (Reilinger et al., 2006) and after the 1999 Izmit earthquake (Ergintav et al., 2007). Although both datasets show phases of the interseismic period there is a striking change in velocity direction north of the NAF from EW before the earthquake to WE after, indicating that the interseismic velocity depends on the time window considered. The westward motion prior to the earthquake is easily explained by the drag exerted by the west moving Anatolian Block through the locked fault. The eastward motion after the earthquake is probably an expression of postseismic phenomena like aftershocks, afterslip or viscoelastic stress relaxation (Reilinger et al., 2000; Bürgmann et al., 2002; Hearn et al., 2002; Çakir et al., 2003b; Ergintav et al., 2007). During the 2 ½ years following the 1999 event, pairs of GPS stations opposite to the main branch showed clearly enhanced rates of relative plate motion compared to the long-term rate (e.g. 33.9±0.5 mm/yr in v_e component between stations DUMT and TUBI and 34.7±0.5 mm/yr between ULUT and KANT) (Lenk et al., 2003). The fact that the relative rates between the two pairs of stations are almost the same despite their different distances from the NAF gives reason to assume localised afterslip on the fault rather than distributed deformation as an explanation for the higher rates.

Taking the GPS site SILE as an example (located at 29.62°E 41.18°N and hence close to the northern boundary of the Marmara model; Fig. 5.5), an average velocity for this site can be estimated to v_e = -0.42±1.27 mm/yr, when taking the 1999 coseismic displacement of Δu_e = 11.91 cm to the east (Reilinger et al., 2000) and assuming the pre 1999 velocity of v_e = -0.85±1.25 mm/yr (Reilinger et al., 2006) during the whole interseismic period of 280 yrs (1719-1999). Since the east component of velocity v_e obviously decreases during the interseismic period reaching a minimum at the end of the seismic cycle and since the site probably reflects remaining strain from the locked faults farther west in the Marmara Sea, this velocity represents a lower bound in v_e. Based on that, it was assumed that the northern block is stable so that the boundary condition v_e = 0 mm/yr was set there.

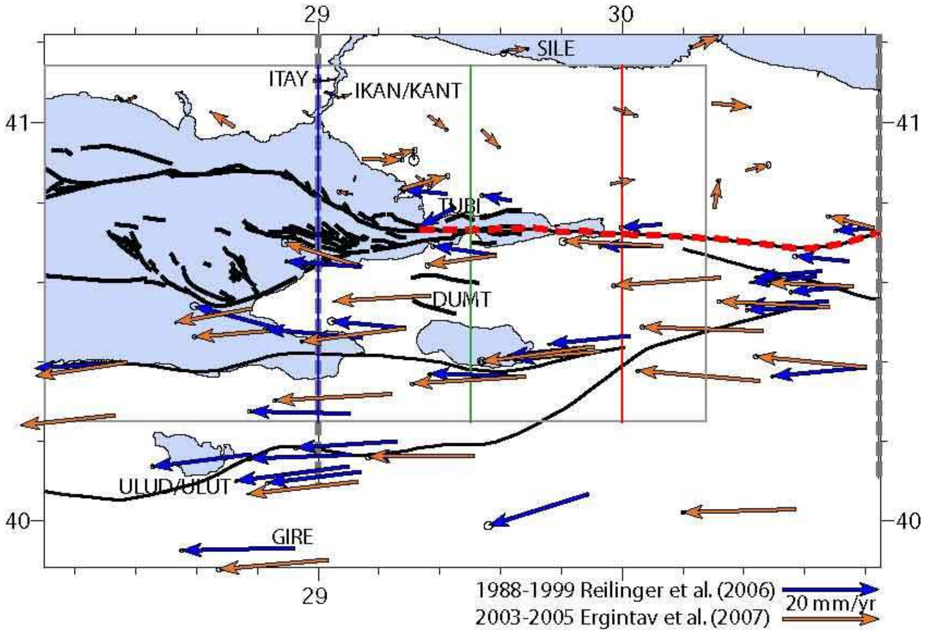

Fig. 5.5: GPS observations late (1988-1999) (blue, Reilinger et al., 2006) and early (2003-2005) (orange, Ergintav et al., 2007) in the interseismic period in the eastern Marmara region, where the 1999 Izmit earthquake occurred (dashed red line). Light grey box marks the boundaries of the Marmara model. Red, green, blue solid and thick dashed grey lines refer to Fig. 5.6.

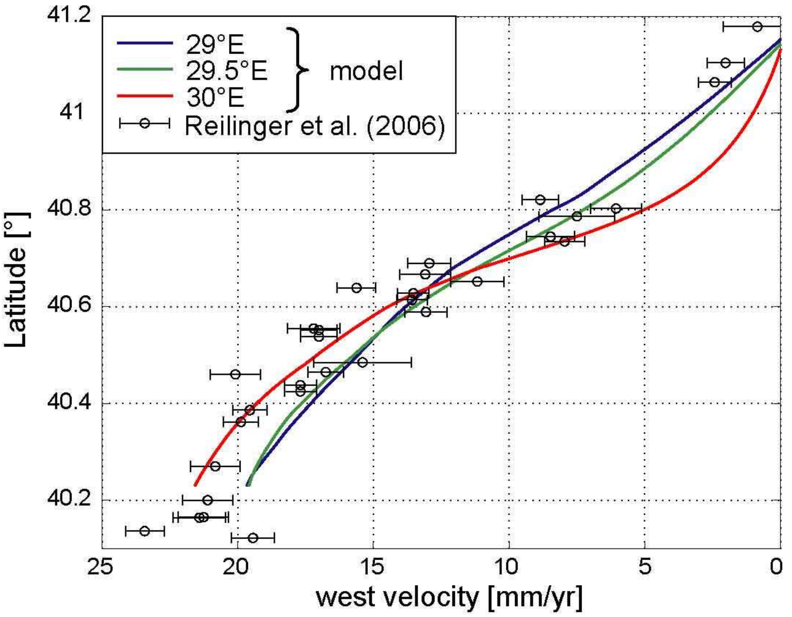

Fig. 5.6: Modelled interseismic EW velocities at longitudes 29, 29.5 and 30°E (s. Fig. 5.5). Circles show EW components of GPS derived velocities as well as their uncertainties (Reilinger et al., 2006) observed at the stations between the two thick dashed grey lines in Fig. 5.5.

Fig. 5.6 shows the modelled interseismic west velocities at three longitudes in comparison to the GPS observations. The step-like behaviour from the steady-state model vanished (Fig. 4.5). Instead, a continuous change in velocity across the plate boundary emerges in good agreement with the observations. Thus, the model reflects the interseismic strain accumulation in a meaningful way both in the overall pattern and quantitatively. It is also demonstrated that the model accommodates as much relative EW motion than observed which documents that the inferred slip rates on the main branch can be reconciled with GPS observations.

5.4 The 1999 Izmit earthquake

The well documented 1999 Izmit earthquake provides a basis for examining whether the performed modelling technique (5.1; 5.2.2) is capable of reproducing the observed characteristics of this event. If modelled coseismic displacements are similar to the observed ones the model technique should also be applicable to other fault segments for gaining information on the expectable size of future earthquakes.

After the period of fault locking and consecutive release of particular fault segments at the time of past earthquakes, as described in 5.2.2, the pre 1999 situation was attained, whose velocity field was presented in the previous subchapter. On August 17th 1999 the fault segment that ruptured during the Izmit earthquake (Fig. 5.2 bottom) was unlocked and the coefficient of friction was set to its original value (μ'= 0.05). The induced reduction in fault friction causes an unstable stress state due to the stored elastic strain energy in the volume adjacent to the fault. The new equilibrium is found by release of the accrued shear stress due to slip on the fault. During this coseismic step the boundary conditions were maintained. This means a laterally fixed northern model boundary, the east and west boundaries north of the NAF were constrained to zero in EW direction perpendicular to the boundary and the boundaries south of the northern branch of the NAF were laterally kept at their positions prior to fault unlocking.

Lateral surface displacements

Fig. 5.7 shows the modelled lateral coseismic displacements at GPS stations in comparison to observations. The model approximates the observed displacement field very well, both in direction and amount of slip. The pattern of the observed displacement field that describes a clockwise rotation south of the NAF and an anticlockwise north of it can be clearly recognised in the modelled displacement field. The maximum residual is 36 cm, all other pairs of modelled and observed displacements differ by less than 30 cm. At the five large displacement sites close to the fault with more than 1 m of slip, the difference in amount of slip between modelled and observed displacements is on average only 8 cm or 6 % of the observed displacements, and directions deviate on average by less than 9° from the observed ones.

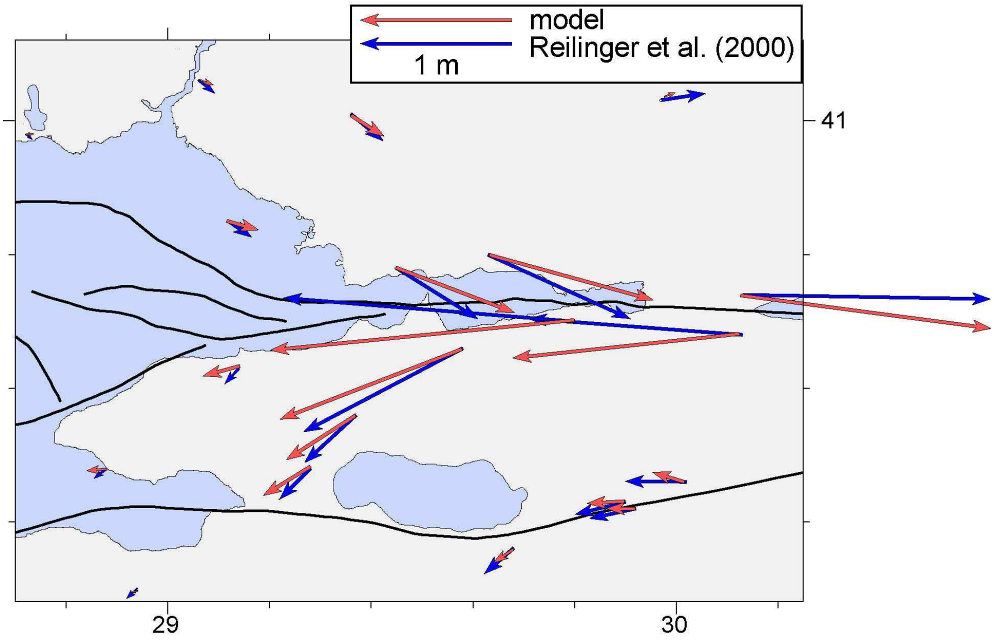

Fig. 5.7: Modelled coseismic displacements (red) in comparison to GPS observations (blue, Reilinger et al., 2000). Note that modelled displacements are a consequence of released shear stress and not a result of imposed slip on the rupture plane.

This result strengthens confidence in the applicability and reliability of the applied modelling technique. Furthermore, this result represents another indication for the reliability of the deduced slip rates presented in Fig. 4.3. Higher slip rates than those would therefore require that either the 1754 earthquake ruptured through Gölcük or that there is a significant level of microseismicity and/or aseismic creep.

Near the northern and southern boundary modelled displacements are smaller than observed. This is due to the applied boundary conditions which allow no lateral displacement at the boundaries during the coseismic phase, except NS displacements at the eastern and western model boundary north of the NAF. The model as a whole has to be pinned somewhere since otherwise it moves uncontrolled in space. Sophisticated surface loads maintaining the lithostatic and plate tectonic stresses and balancing the coseismic stress changes could overcome this problem, which however was not tried.

Following the Izmit earthquake there was a phase of rapid postseismic movements at decaying rates. Maximum postseismic displacements about two months after the earthquake were ~ 5 cm (Reilinger et al. 2000) and were ascribed to afterslip (Reilinger et al. 2000; Bürgmann et al. 2002; Hearn et al. 2002). Afterslip is an expression of prolonged shear stress release after the main shock at fault portions still under unrelieved stress. During a modelled earthquake however, shear stress is fully released down to a level determined by the coefficient of friction so that afterslip in the model is not meaningful. Prolonged slip on the unlocked fault would be simply determined by the secular slip rate shown in Fig. 4.3. Thus, modelled coseismic displacements should be compared to the sum of observed coseismic and postseismic displacements but as the latter represent only a small fraction of the coseismic displacements this hardly makes a difference in Fig. 5.7.

Admittedly, the modelled coseismic displacements fit the observations not as good as those obtained by Reilinger et al. (2000), Hearn et al. (2002), Çakir et al. (2003b), Bos et al. (2004) and Hamiel and Fialko (2007), who almost perfectly reproduced the GPS observations. However, it is necessary to point out that their goals and applied methods to accomplish these are substantially different from those in this study. The above mentioned works aim at obtaining a best fit between modelled and observed displacements by iteratively varying the slip distribution on the rupture plane in an elastic half space or they proceed from the GPS or InSAR observations and invert the observed displacements for slip on the fault. As mentioned earlier these approaches are useful to infer the slip distribution on the rupture plane but they lack any predictive strength since they are not consistent with total stress (Fig. 5.1a). The modelled coseismic displacement field in Fig. 5.7 could be improved to better reproduce the observations by introducing a heterogeneous distribution of fault friction during the interseismic period. However, this is consciously not intended here. The key point to be emphasised here is that this modelled coseismic displacement field is purely a consequence of the accumulated shear stresses on the NAF. There is no imposed slip. Slip is driven by stress. No assumptions were made on inhomogeneous fault friction responsible for asperities and heterogeneous slip distribution on the rupture plane. Since nevertheless observations are approximated fairly well, a reliable performance of the model is expectable on other fault segments as well for which asperities etc. are unknown either. Thus, the contemporary and future potential of earthquakes can be assessed.

Lateral surface fault slip

Fig. 5.8 shows the modelled lateral coseismic fault slip at the surface. Between Gölcük and the eastern model boundary it is in the range of 4-4.7 m. At about the Karamürsel Basin modelled slip rapidly decays to the west.

Observed surface expressions of the rupture indicate peak levels of slip at Gölcük and Adapazari with 4-5 m (Aydin and Kalafat, 2002; Barka et al., 2002) (Fig. 5.8). Thus, the model matches these observations well. In between, reported coseismic displacements are much smaller and do not exceed 3 m. Papadimitriou et al. (2001), Barka et al. (2002), and already prior to the 1999 event, Barka and Kadinsky-Cade (1988) reported that the NAF broke between Sapanca Lake and east of Gölcük during the 1878 M = 6.7 earthquake and hence right in between these two locations of observed maximum displacements. The fact that the 1878 event generated a tsunami that extended into the open Marmara Sea (Ambraseys and Finkel, 1991) supports the view that this earthquake entered the Izmit Bay. Since the 1878 earthquake was not considered in the modelling, the omission of this event explains at least part of the discrepancy between modelled and observed surface displacements there.

The onset of marked decrease in modelled surface slip west of Gölcük is due to the 1894 earthquake which was assumed to have terminated there one century before (Fig. 5.2). The fault to the east was unbroken since beginning of fault locking in 1719. Cormier et al. (2006) reported a dramatic decrease in surface slip at about 29.68° (right yellow arrow in Fig. 5.8) based on sonar data, which agrees with this assumption.

As mentioned earlier, on Hersek Peninsula surface rupture was absent (e.g. Barka et al. 2002) whereas the model yields a slip of ~ 2 m there (Fig. 5.8; middle yellow arrow). However, Gasperini et al. (2003) found evidence from sea floor observations that there was a surface slip of ~ 1 m right west of Hersek Peninsula. The best-fit slip distribution of Çakir et al. (2003b) relying on InSAR observations also shows 2 m of surface slip on Hersek Peninsula. Armijo et al. (2005) found a fresh fault scarp at the entrance of the NAF into the Çınarcık Basin (left yellow arrow in Fig. 5.8) and interpreted it as a consequence of the 1999 event.

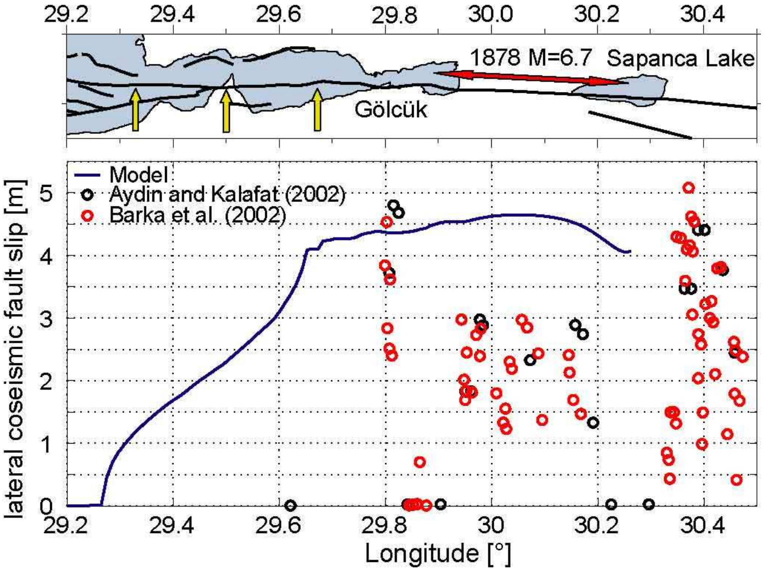

Fig. 5.8: Modelled lateral surface fault slip during the 1999 Izmit earthquake (blue line) in comparison to observations (circles). Lateral blanks in the data are due to water coverage of the NAF (see map above). Note that the fault section marked with a red double arrow was associated with the 1878 M=6.7 earthquake (Barka and Kadinsky-Cade, 1988; Papadimitriou et al., 2001; Barka et al., 2002). Yellow arrows indicate locations which are referred to in the text. The eastern model boundary is at 30.26°E.

Vertical surface displacements

Vertical surface displacements due to the Izmit earthquake reached maximum values near the western end of the rupture, with subsidence on the northern side and uplift south of the NAF (Fig. 5.9). The model reflects the observations quite well there. In all other areas however, correlation between model results and GPS observations is poor. The model predicts subsidence in the northwest and southeast area affected by the rupture whereas uplift is modelled in the northeast and southwest quadrants, which is opposite to the observations (Fig. 5.9). The reason for this is not easily discernable. Actually, one would expect the modelled pattern rather than the observed one since generally uplift is found in the compressive and subsidence in the extensional quadrants for right-lateral slip on a vertical fault. Three reasons may account for this mismatch. The first one concerns the applied boundary conditions during the coseismic phase which do not allow lateral slip at the boundaries. Therefore, the extension and compression arising at the boundaries due to the coseismic displacements is necessarily taken up by vertical displacements. Second, the heterogeneous slip distribution on the rupture plane (e.g. Clévédé et al. 2004; Fig. 5.10) in contrast to the quite homogeneous one of this study may be responsible for the observed pattern in vertical displacements. The slip models of Reilinger et al. (2000) and Çakir et al. (2003b) (published by Ergintav et al., 2007) show the same sense of vertical displacements in the near field as inferred in this study, whereas in the far field they are opposite and agree with the observed pattern. Third, poroelastic effects may account for the observations. The mechanism of poroelastic rebound produces the opposite signal of the coseismic rupture (Masterlark and Wang, 2002; Jónsson et al., 2003), that is to say uplift in the extensional and subsidence in the compressive quadrants. The omission of poroelastic effects in the model would therefore explain the mismatch if this mechanism is actually responsible for the observations. Yaltırak et al. (2005) reported water level changes in wells due to the 1999 Izmit and Düzce earthquakes even at distances of more than 100 km from the rupture plane that were recorded within minutes both prior to and after the earthquakes, which indicates that other mechanisms involving fluids may be involved as well.

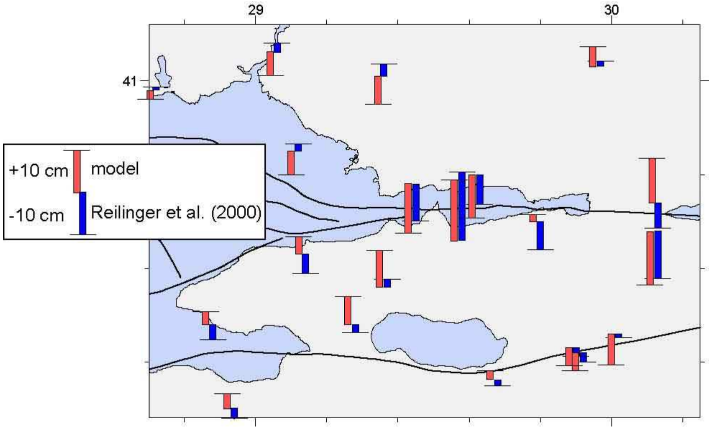

Fig. 5.9: Modelled vertical displacements during the 1999 Izmit earthquake (red bars) in comparison to GPS observations (blue bars; Reilinger et al. 2000).

Slip on the rupture plane

Modelled coseismic slip at depth on the rupture plane is shown in Fig. 5.10. The modelled slip is quite uniform vertically within the uppermost 15 km bsl. This portion of the fault was previously locked. Below, slip tapers to 0-1 m at the lower model boundary. East of Hersek Peninsula modelled slip decreases to about half of its value within a short distance of a few kilometres, then gradually decreases further to the west and at the western end of the rupture slip rapidly decreases to zero. Slip prolongs below the adjacent locked segment. Modelled maximum slip is 4.76 m.

Fig. 5.10 also shows the slip distribution after Çakir et al. (2003b) from inversion of InSAR data and field observations, including the early postseismic phase till one month after the event. The modelled 2 m contour closely follows the corresponding isoline inferred by Çakir et al. (2003b). The red coloured area indicating displacements > 4 m is framed by the reported 3 or 4 m isolines and slip decreases below between about 15-25 km similar to the inversion results. The marked decrease east of Hersek Peninsula is due to the 1894 earthquake which was assumed to have terminated there (Fig. 5.2). The slip distribution of Çakir et al. (2003b) also indicates a rapid decrease in slip there supporting this result. Between Hersek Peninsula and the western end of the rupture, modelled slip is right the same as the reported one at the surface (Fig. 5.10). Below however, modelled slip is higher and vanishes within a short distance at the western termination whereas the slip distribution of Çakir et al. (2003b) tapers gradually to zero over a distance of about 20-30 km. Because of this, the modelled surface displacements around the western Izmit Bay are slightly overrated (Fig. 5.7).

In the model slip extends down to the bottom of the model at 38 km depth and surely, slip in the lower crust and upper mantle is overestimated in the model. This can be ascribed to two assumptions made in 2.3. First, the adopted elastic rheology. During the interseismic phase viscoelastic rheology should allow relative motion at the bottom of the model at higher rates than modelled because of viscous flow, so that in turn coseismic slip would get smaller. Second, heightened modelled coseismic slip in the lower crust and upper mantle is a consequence of the assumption that plate tectonic forces act only laterally at the sides of the model. No basal lateral motions were applied since these would have impeded an independent evolution of the slip rates on the NAF. Technically, heightened slip below the locking depth could be otherwise avoided by setting the locking depth upward and/or by constraining slip at the bottom to zero during the coseismic phase. Though modelled slip below the locking depth is higher than reasonable, recent findings from Shaw and Wesnousky (2008) imply that large ruptures penetrate greater depths than commonly thought based on elastodynamic modelling. They proposed that ~1/3 of total seismic moment is due to slip below the seismogenic layer.

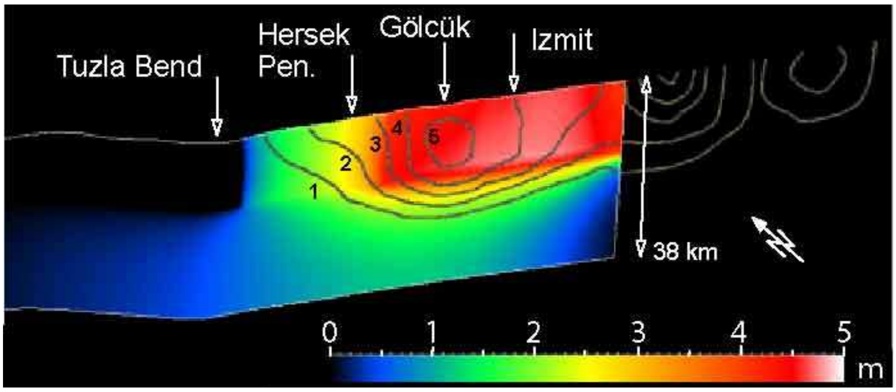

Fig. 5.10: Modelled coseismic total slip on the rupture plane for the 1999 Izmit earthquake due to shear stress release. Grey lines indicate slip model of Çakir et al. (2003b) for the sum of coseismic and postseismic displacement within one month after the earthquake from InSAR and field observations (1m-isolines).

Besides the work of Çakir et al. (2003b) there is a number of further slip distributions for the Izmit earthquake in the literature based on various methods such as inversion of geodetic observations (Reilinger et al, 2000; Feigl et al. 2002; Bürgmann et al., 2002; Hamiel and Fialko, 2007) and seismological data from teleseismic waves to strong motions (Yagi and Kikuchi, 2000; Bouchon et al., 2002; Gülen et al., 2002; Sekiguchi and Iwata, 2002) or joint inversions (Delouis et al., 2002). A comparison of some of these is provided by Beresnev (2003), Clévédé et al. (2004) and the following webpage http://www.seismo.ethz.ch/srcmod/.

A striking characteristic of these slip distributions is “that they have in fact little in common” (Beresnev, 2003). Probable reasons for the disparity in inferred slip patterns are the differing adopted fault geometries, the multiplicity of constraints, for some inversions are based on a single data source whereas others considered several kinds of geodetic or seismological data or surface slip observations, the applied inversion technique with assumed parameters and the resolution (Beresnev, 2003; Bos and Spakman, 2003). Based on elastic dislocations King and Wesnousky (2007) demonstrated that different slip-depth profiles on a fault can be found that produce the same surface displacement field. Bos and Spakman (2003) showed that inversions of geodetic data based on elastic dislocations in an elastic half-space yield ambiguous results for the deeper portions of a fault. From this perspective it is not astonishing that despite their differences the slip distribution presented in Fig. 5.10 and the various heterogeneous slip distributions based on elastic dislocations yield similar surface expressions. The general problem with slip inversions from teleseismic data is that the structural and lithological complexities the waves experience on their long way from the source to the receiver are projected into the source. Slip inversions from near-field strong motion data are often compatible with damage. Nevertheless, Beresnev (2003) summarized what can be expected from slip inversions of seismic data as “there is no basis currently available for distinguishing between artificial and real features” and “if anything can be said with confidence, it is that the fact of a particular solution matching the data well does not guarantee that this solution is close to the true one.” Two consequences arise from that. On the one hand, the fact that the model well reproduced observed coseismic slip at the surface does not imply that modelled slip is correct at depth. On the other hand, due to the inherent non-uniqueness of reported slip distributions the modelled slip distribution at depth does not need to agree with the reported slip distributions.

Tab. 5.1 provides a comparison of source parameters between the modelled Izmit earthquake and some of the published slip distributions. All numbers refer to the rupture within the model area, that is to say west of 30.26°E.

Modelled maximum slip (4.76 m) is lower whereas modelled mean slip (3.33 m) is higher than reported values. Since observed maximum surface slip reached almost 5 m in the model area (Fig. 5.8) the modelled maximum slip at depth of 4.76 m is probably too small since generally maximum slip at depth exceeds maximum slip at the surface (Wells and Coppersmith, 1994; e.g. Manighetti et al., 2007). Generally, damage is associated with asperities that are characterised by large slip. In this respect, the model cannot resolve areas, in which damage is particularly likely. Though it would be difficult to validate anticipated asperities based on the available slip distributions it would be technically possible to restrict fault locking to particular areas of the fault instead of the whole seismogenic area. However, this was not done since the focus of this work is on future earthquakes on the MMF on which asperities are not known in advance. It is attempted to quantify expectable seismic moment and for this purpose the detailed distribution of heterogeneous slip is not necessary. As discussed below, the example of the 1999 event shows that seismic moment can be approximated without any assumption on heterogeneous friction or stress.

While it is at present hardly possible to precisely locate where slip occurred at depth, the cumulative slip on the whole rupture plane or seismic moment are much more reliably inferable. Nevertheless, reported seismic moments for the whole rupture, that is also beyond the model boundaries, vary by up to a factor of two between $1.41 \cdot 10^{20}$ (Yagi and Kikuchi, 2000) and $2.88 \cdot 10^{20}$ Nm (Harvard CMT catalogue). The seismic moment $M_0 = \mu A u$ (eq. 1.4) was calculated using the standard value of $\mu = 30$ GPa for the reported slip distributions and $\mu = E/(2 \cdot (1+\nu)) = 28$ GPa for the modelled seismic moment based on the adopted elastic parameters in the model (Tab. 3.1). Moment magnitude M_w is given by eq. (1.5). For calculating modelled seismic moment, modelled slip was considered only above 20 km bsl., because of the discussed continuation of slip down to the bottom of the model. Modelled seismic moment above 20 km bsl. exceeds literature values by 23-54 %.

Tab. 5.1: Source parameters of the modelled Izmit earthquake in comparison to published slip distributions within the model area (west of 30.26°E).

	Type	**above depth [km]**	**area [km²]**	**max. slip [m]**	**mean slip [m]**	**M_0 [10^{20} Nm]**	**M_w**
Model		20	1668	4.76	3.33	1.5547	7.46
Çakir et al. (2003b)	InSAR & field obs.	24	2280	5.51	1.77	1.2100	7.39
Reilinger et al. (2000)	GPS	18.2	1562	5.65	2.15	1.0072	7.34
Yagi and Kikuchi (2000)	body waves & strong motions	21.6	1348	6.31	2.54	1.0271	7.34
Sekiguchi and Iwata (2002)	Strong motions	23.3	1816	8.52	1.88	1.0241	7.34
Bouchon et al. (2002)	Strong motions	18	1746	6.35	2.28	1.1943	7.38
Delouis et al. (2002)	InSAR, body waves, & strong motions	22.5	1856	7.99	2.27	1.2641	7.40

It can be concluded that the model approximates the reported seismic moment of the Izmit earthquake though it yields a somewhat higher seismic moment than the reported slip distributions. There are basically four reasons for the somewhat higher modelled seismic moment. (1) The neglected 1878 earthquake which becomes prevalent in the easternmost part of the fault where the 3 m isoline of Çakir et al (2003b) comes to the surface whereas modelled slip remains above 4 m (Fig. 5.10). (2) Modelled slip west of Hersek at depth is overestimated. Though there must have been slip far to the west based on geodetic observations, obviously not all portions of the fault broke whereas in the model stress was allowed to fully release. Thus, this is merely a wrong assumption than a deficient performance of the model. (3) The generally heightened slip below the locking depth. For the calculation of seismic moment only slip above 20 km was considered. (4) Reported slip distributions address coseismic release of seismic moment but not the postseismic whereas in the model stress is fully released during the earthquake. The numbers for the slip distribution of Çakir et al. (2003b) in Tab. 5.1 refer to their coseismic slip distribution. They inferred deep afterslip during the month following the main shock corresponding to a seismic moment of $0.3 \cdot 10^{20}$ Nm. Almost all of it released within the model area. This amount of postseismic moment roughly makes up the difference between the model results and the reported values (Tab. 5.1).

Though details of the slip distribution can not be deduced reliably from the presented modelling technique, it was shown that the magnitude of an earthquake can be approximated. As there are profound reasons for the somewhat higher modelled seismic moment, as just discussed, this result gives confidence to apply the modelling technique to other fault segments. When considering coseismic slip only above ~20 km, the contemporary potential of seismic moment can be estimated. Because of not considered smaller historical earthquakes, possible unbroken fault portions during an earthquake and afterslip the result will represent an upper bound.

Coseismic stress drop

Modelled coseismic stress drop on the rupture plane associated with the slip in Fig. 5.10 is shown in Fig. 5.11. In contrast to the rather uniform slip distribution, stress drop shows variations on the rupture plane. Between the eastern model boundary and Izmit stress drop is quite uniform at ~ 4 MPa and a maximum of 4.6 MPa. In agreement to that, a stress drop of 4 MPa was reported by Tibi et al. (2001). The fault is quite plane in this section. West of Izmit, however, the fault was constructed as to show several minor bends that were mapped at the surface (Cormier et al., 2006). Stress is hardly reduced in the upper part of the rupture and even locally increased, while stress drops at the lower portions of the rupture (by ~ 4 MPa), where the fault was constructed less bended. The stress drop shown in Fig. 5.11 is the mean of the shear stress on the northern and southern side of the fault and both sides show an alternating mutually opposite pattern of stress increase at restraining sections and stress drop at releasing parts of the fault, so that mean stress change is low. Maybe, this is an environment, in which particular large slips can arise as at Gölcük in 1999 and where ruptures arrest as the 1894 event. In other words, asperities may be characteristic for this fault portion or more generally for geometrical complexities. It would be interesting to test, whether in the model a more inhomogeneous slip pattern with high slip around Gölcük would develop during several seismic cycles.

Between Hersek Peninsula and the western termination of the rupture, coseismc stress drop is < 1 MPa. This portion ruptured more recently during the 1894 event (Fig. 5.2). Around Tuzla Bend, west of the rupture, shear stress is increased by 1-2 MPa, while rapidly decaying further to the west. This is similar to what was found in a number of ΔCFS studies (e.g., Lorenzo-Martin et al., 2006; Muller et al., 2006). Average stress drop on the whole rupture plane is 2.0 MPa.

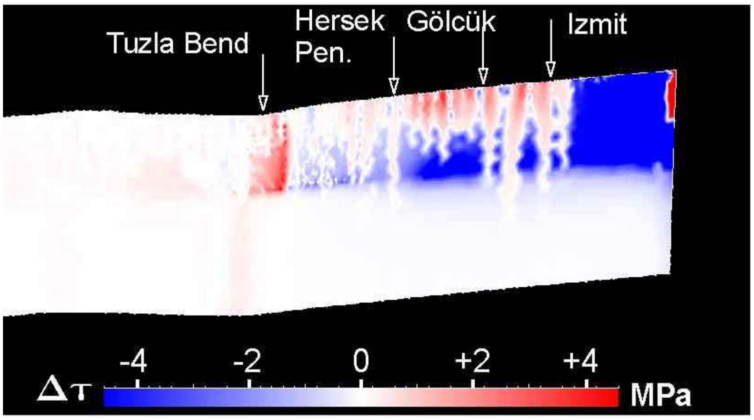

Fig. 5.11: Coseismic stress drop dring the 1999 Izmit earthquake. Between the eastern model boundary and Izmit stress drop is ~4 MPa, between Izmit and Hersek Peninsula stress is reduced only in the lower part of the seismogenic zone, between Hersek Peninsula and the western termination of the rupture stress drop is low due to the stress shadow of the 1894 event and right west of the rupture termination shear stress is increased by ~ 1-2 MPa.

5.5 Testing earthquakes in 2010

Testing earthquakes on selected fault segments of the MMF were modelled in order to test what the moment magnitudes of contemporary potential earthquakes in the Sea of Marmara would be. The basis for this analysis is the modelled state of stress on the MMF for the year 2010, from which potential slip can be deduced by unlocking the fault along the respective fault sections, in the same way as done for the 1999 event.

Following the 1999 Izmit earthquake the model was run with relocked faults until beginning of the year 2010 while plate tectonic boundary conditions were continuously applied. By that the contemporary state of stress in the model was established, as the starting point for this analysis. At the beginning of the year 2010 six different testing earthquakes were modelled. This was done by unlocking the MMF along certain sections. The predefined locations and lengths of these sections are shown in Fig. 5.12. These scenarios comprise the conceivable locations and lengths of possible earthquakes as they terminate at natural barriers such as fault bends or where the most recent 1912 and 1999 earthquakes stopped. The first testing earthquake is induced by unlocking the MMF along the Prince’s Islands segment and around the Tuzla Bend where the

1999 event ended (Fig. 5.12). In response to fault unlocking the accrued stress on this fault section is released by slip. In the same way the Central Segment between Istanbul Bend and Central Basin is released (scenario ii), the segment between the Central Basin and Ganos Bend (scenario iii) and combinations of these three scenarios (scenarios iv and v), including a worst case scenario with a through going rupture between the Tuzla and Ganos Bends (scenario vi) (Fig. 5.12). Of course, the respective testing earthquakes are treated independently.

The slip distributions of the six testing earthquakes are shown in Fig. 5.13 and their source parameters are listed in Tab. 5.2. Scenario i on the Prince’s Islands Segment yields the smallest magnitude of the six with $M_w = 6.8$. The Central Segment between Istanbul Bend and the Central Basin stores enough shear stress to produce a $M_w = 7.3$ event at present. A rupture in 2010 on the relatively small section between the Central Basin and Ganos Bend (scenario iii) would generate a considerable $M_w = 7.1$ event. The scenarios iv and v, involving two fault segments each, would produce earthquakes comparable to the 1999 Izmit event in magnitude, if these would occur in the very near future. The worst case scenario with the MMF breaking all the way between the terminations of the 1999 and 1912 events yields a moment magnitude of $M_w = 7.6$ at present.

As the results demonstrate, there is the potential of one or even two $M_w > 7$ earthquakes in the Marmara Sea at present. However, the results of the single scenarios need to be discussed. The lower moment magnitude on the Prince’s Islands Segment compared to the other scenarios is due to the 1894 event which released shear stress one century before (Fig. 5.2). If the 1894 event occurred in the Izmit Bay and did not rupture the Prince’s Islands Segment, the present hazard evolving from this segment is higher. However, even if the 1766 May or 1754 events were the last events on this segment, expectable contemporary magnitudes on this segment are clearly lower than a $M_w = 7.4$ event suggested by Pınar et al. (2003) based on a 20 mm/yr slip rate. This can be claimed based on the results for scenarios ii and iii which have a much greater length than scenario i and would yield events of lower magnitudes than 7.4 at a loading period since 1766 and at a higher slip rate than inferred for the Prince’s Islands Segment (Fig. 4.3; 5.2). The inferred potential magnitude for the Prince’s Islands Segment represents an upper bound if the May 1766 and/or 1963 M = 6.3 earthquakes ruptured part of it. Other locations proposed for the 1963 event are near the northeast coast (Taymaz et al., 1991), at the Çınarcık Fault (Nalbant et al. 1998; Parsons, 2004) and on Armutlu Peninsula (Bulut and Aktar, 2007).

The moment magnitudes inferred for scenarios ii and iii rely on the assumption that the two 1766 events accounted for a through going release of shear stress between the Istanbul and Ganos Bends. Otherwise, the longer loading period since 1509 would increase the potential magnitude on the Central Segment drastically. However, in 5.6 it will be shown that this is not likely. The magnitude inferred for scenario iii represents an upper bound if the 1912 event reached the Central Basin (5.2.1). As will be discussed in 5.6 it cannot be excluded that the 1912 event propagated further to the east than anticipated.

Based on the model results the highest possible magnitude of a contemporary earthquake filling the whole seismic gap between the 1912 and 1999 events at once is $M_w = 7.6$. If the inferred magnitudes for scenarios i and iii represent upper bounds due to intermittent release of shear stress by other earthquakes, as just discussed, then also the magnitudes inferred for the multi-segment ruptures iv, v and vi involving these segments represent upper bounds. In any case it can be concluded that a $M_w = 8$ earthquake in the Marmara Sea, as sometimes thought as possible, cannot be confirmed from the modelling results. Nevertheless, a $M_w = 7.6$ earthquake would still be disastrous for the Marmara region. Interestingly, Cisternas et al. (2004) and Le Pichon et al. (2003) found a maximum possible magnitude of $M_w = 7.6$ in the Marmara Sea at present which is right the same as the model outcome. The result of Cisternas et al. (2004) is based on the temporal evolution of cumulative released seismic moment in the Marmara region during the last 2000 years.

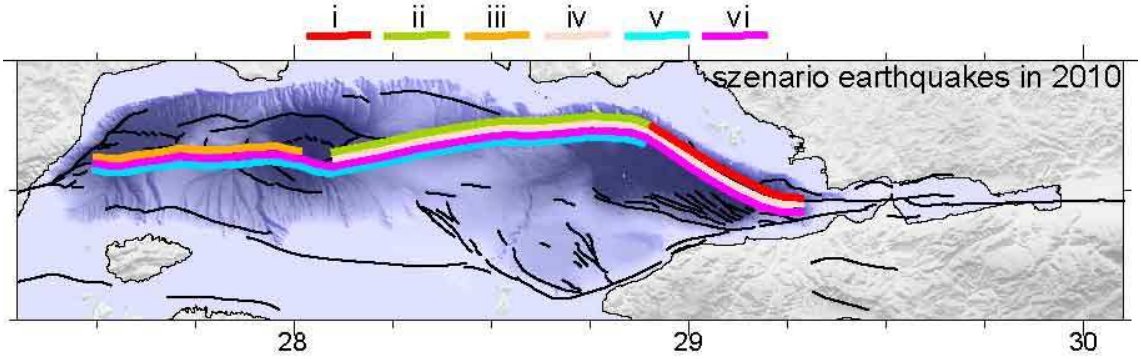

Fig. 5.12: Predefined lengths of six testing earthquakes in the year 2010. Three single segment ruptures are considered (best case) and a worst case scenario comprising all three segments.

Tab. 5.2: Source parameters of the six testing earthquakes according to the slip distributions in Fig. 5.13 above 20 km bsl.

Scenario	**area [km²]**	**max. slip [m]**	**mean slip [m]**	**M_0 [10^{20} Nm]**	**M_w**
i	741	1.28	0.86	0.1784	6.83
ii	1216	3.42	2.62	0.8938	7.30
iii	828	3.33	2.32	0.5385	7.15
iv	1931	3.98	2.85	1.5414	7.46
v	2125	4.70	3.59	2.1341	7.55
vi	2841	4.95	3.64	2.8979	7.64

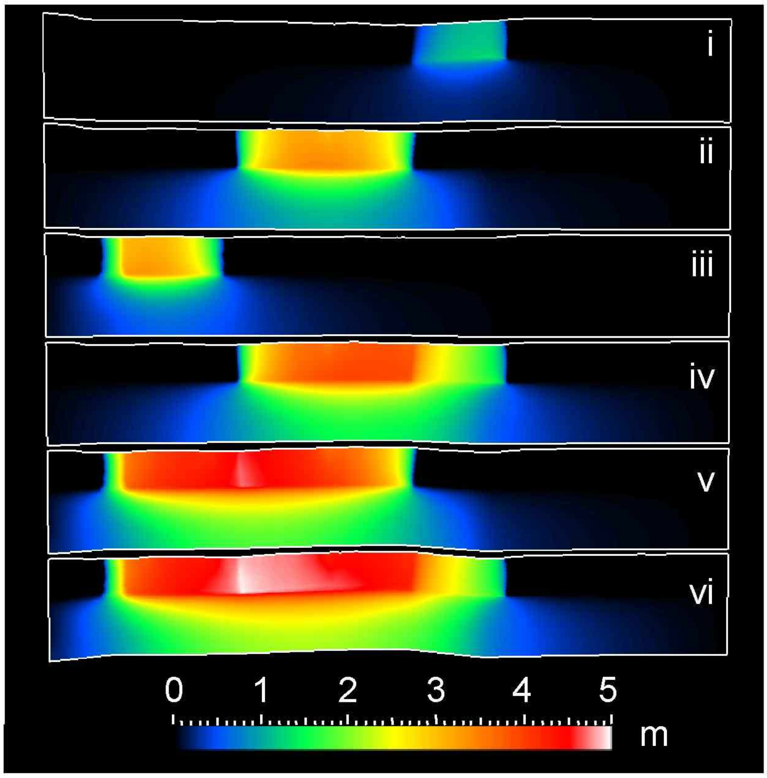

Fig. 5.13: Coseismic slip distributions for six testing earthquakes on January 1st 2010. Slip is a consequence of unlocking the respective fault segments depicted in Fig. 5.12 and determined by the accumulated shear stress.

A characteristic of the modelled testing earthquakes is that slip increases with rupture length (Fig. 5.13). The testing earthquakes involving more than one fault segment (iv-vi) show larger slip at one position than if only one segment is involved. This is in agreement with what is commonly observed. Based on compilations of earthquake source parameters Scholz et al. (1986) found the basic u~L and M_0~L² scaling relations for large earthquakes. Here, L stands for rupture length, W for rupture width and u for mean slip. This is the so called L-model in contrast to the W-model that scales u~W and M_0~L (Scholz, 1982). The W-model scaling relations were not observed except for very large earthquakes and were proposed since slip tends to saturate for very long rupture lengths (Romanowicz and Ruff, 2002; Manighetti et al., 2007).

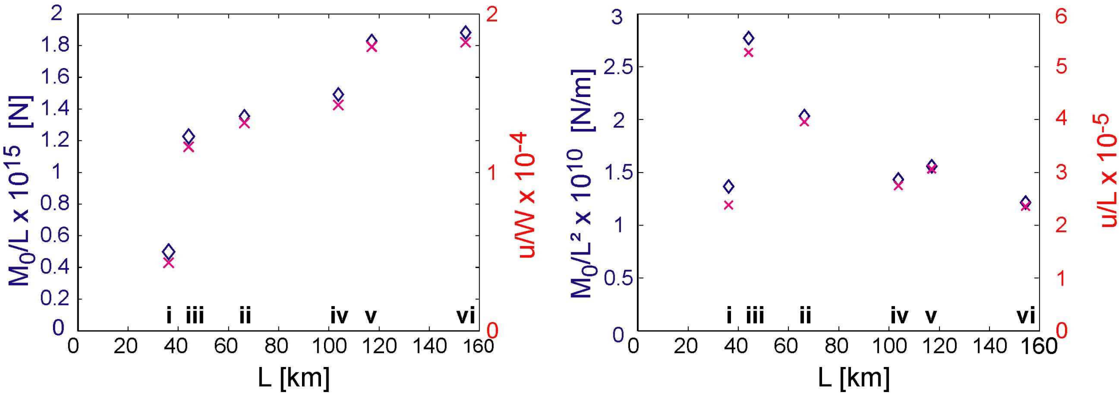

Fig. 5.14: Rupture length dependency of seismic moments for the six modelled testing earthquakes in Fig. 5.12 and 5.13. a) A M_0~L relationship as predicted by the W-model is not confirmed by the results. b) Instead, the model results can be reconciled with the M_0~L² and u~L relationships predicted by the L-model. The scatter is related to the different stages of the single fault segments within their seismic cycle.

Fig. 5.14a shows that applying the W-model scaling relations to the modelled u and M_0 does not eliminate the L dependence in these quantities. In contrast, division of modelled u by L and of M_0 by L² apparently eliminates the respective dependence of the rupture length (Fig. 5.14b). This can be concluded though these relations hold when the seismic cycle is completed, while the fault is in different stages of the seismic cycle along fault strike, which is expressed by the scatter. Therefore, the modelled testing earthquakes seem to keep to the observed scaling relations of the L-model. This is related to a second characteristic of the modelled slip distributions. The larger the rupture length, the deeper the rupture extends (Fig. 5.13). This is what the L-model implies as the base of the fault is free whereas the W-model assumes that the fault is pinned at its base (Scholz, 1982). Just recently, it was proposed that depth extent of large earthquakes is dependent on rupture length with slip occurring below the seismogenic depth (King and Wesnousky, 2007; Hillers and Wesnousky, 2008; Shaw and Wesnousky, 2008).

Whereas empirical scaling relations allow estimations of source parameters for a given fault segment, it is hardly possible to make reliable estimations analytically as the following calculation demonstrates. Taking scenario ii on the Central Segment as an example, which is of quite simple geometry and presumably late in its seismic cycle, the rupture area corresponds to a circular area of radius a=19.7 km $\left(=\sqrt{1216\text{km}^2/\pi}\right)$. Assuming a typical coseismic stress drop of $\Delta\sigma$ =3 MPa and a shear modulus of μ=28 GPa, just as used in the model, an average displacement of u = 1.53 m follows from eq. (1.3) in the circular fault case. The resulting seismic moment is $0.52\cdot10^{20}$ Nm (eq. 1.4), which is different from the modelled seismic moment $0.89\cdot10^{20}$ Nm. This shows that the geometry factor becomes important at the scale of large earthquakes and the model accounts for it.

The kind of testing earthquakes presented here can be initiated also later than 2010 at the same or other sections of the MMF. Due to the prolonged loading time, resulting slip will then be greater. It can be concluded that the model provides a tool for quantifying potential slip and seismic moment to any arbitrary time at any arbitrary fault section.

The modelled testing earthquakes implicitly include fault interactions. Coseismic slip during the historical earthquakes induced stress changes on the adjacent locked fault sections. These stress changes will influence the slip occurring during a future earthquake on these neighbouring fault sections. Thus, the model accounts not only for time-dependence as far as the secular loading rate is concerned but also considers the effects of coseismic stress changes on nearby fault segments. In other words, a common ΔCFS study is implicitly incorporated and the model therefore represents a valuable advance compared to these.

Concerning the inferred numbers on contemporary potential moment magnitudes and seismic hazard, three issues have to be boldly underlined.

(1) The inferred results depend on the anticipated locations of the major historical earthquakes (Fig. 5.2). The uncertainties in locations of historical earthquakes require further research on gathering and exploiting chronicles for mapping intensities, modelling of wave propagation in a realistic velocity and density structure and consideration of site effects, as proposed in 5.2.1. The model result can only be as reliable as the information on historical earthquakes.

(2) Modelled contemporary moment magnitudes represent upper bounds from three perspectives. First, smaller historical earthquakes with $M < 7$ were neglected due to a lack of reliable information so that present potential seismic moment release would be reduced. Second, shear stress is fully released on an unlocked fault segment in the model whereas actually some parts of the fault may remain unbroken during the main shock and afterwards released by aftershocks, afterslip or further smaller earthquakes later on so that the main event is smaller. Third, the width of the seismogenic layer beneath the Marmara Sea may be reduced due to the thick sedimentary cover. This will be investigated in chapter 5.7.

(3) Contemporary potential slip does not mean that occurrence of the pertaining testing earthquake is likely at present or at all. Some of the testing earthquakes are mutually exclusive, e.g. ii excludes iv, v and vi since the same segment will not rupture twice within a fraction of the regular seismic cycle. The seismic gap in the Marmara Sea may break at once or in several smaller earthquakes. It is necessary to investigate how likely the respective testing earthquakes are at present and to identify the most probable one. This will be done in the next subchapter.

5.6 Assessing the criticality of a fault segment

So far, slip and seismic moments of contemporary potential earthquakes in the Marmara Sea were quantified. Seismic hazard assessment requires additionally the likelihood of their occurrence or better, the time of earthquake occurrence. Within this subchapter it is investigated how far the respective fault segments are progressed in their seismic cycle in order to identify the most likely scenarios.

One way to assess the state of a particular fault segment within its seismic cycle and to identify the most likely scenarios among the six in Fig. 5.12 and 5.13 is to adopt empirical scaling relations as a criterion for critical source parameters of modelled testing earthquakes. Modelled seismic moment of a testing earthquake of predefined length is compared with the seismic moment calculated from empirical scaling relations for the same surface rupture length. The ratio of modelled to empirical seismic moment is taken as a measure for the fraction at which the seismic cycle is already completed on this fault segment.

For this analysis the empirical scaling relations of Wells and Coppersmith (1994) and Wesnousky (2008) were employed as well as the relation

$$M_0 = \mu W L^2 \alpha \tag{5.1}$$

where α stands for the ratio of incremental slip to fault length. The latter relation is based on the findings of Scholz et al. (1986) that for large earthquakes generally u~L and M_0~L². In the previous subchapter it was shown that the modelled testing earthquakes apparently keep to these relations. Scholz et al. (1986) originally found that $\alpha = 1.25 \cdot 10^{-5}$ and $\alpha = 6 \cdot 10^{-5}$ for interplate and intraplate earthquakes, respectively, based on global compilations of earthquake source parameters. For historical earthquakes in the Marmara Sea region Ambraseys and Jackson (2000) used $\alpha = 5 \cdot 10^{-5}$. Two different rupture widths W were considered (15 and 20 km) and μ was taken as 30 GPa.

Tab. 5.3 gives an overview on expected source parameters based on the above mentioned scaling relations for earthquakes of the same rupture length as the six testing earthquakes. The modelled source parameters from Tab. 5.2 are also shown. When comparing the modelled source parameters of the testing earthquakes to the expected ones for the same rupture lengths, one has to be aware that the intention of the comparison is to assess the current state of the particular fault segments within their seismic cycle. Therefore, similar numbers for modelled and expected source parameters are taken as indication that a fault segment is late in its seismic cycle. In turn, large discrepancies are taken as indication that a fault segment has not yet reached a critical state.

It strikes, that the modelled seismic moments exceed those expectable from the scaling relations of Wells and Coppersmith (1994) and Wesnousky (2008) for all but the first testing earthquake on the Prince’s Islands Segment (Tab. 5.3). According to the explanation above this would mean that these earthquakes should already have happened. In contrast, the scaling relation (5.1) yields much higher values for the seismic moment so that modelled seismic moments fall below these except for scenario iii for W=15 km. According to the relations of Wells and Coppersmith (1994) and eq. (5.1), the most likely of the six testing earthquakes is iii between the Central Basin and Ganos Bend, followed by ii on the Central Segment and v between the Istanbul and Ganos Bends. The latter scenario is the most likely one when taking the relations of Wesnousky (2008) and even the scenario rupturing the whole MMF is more likely for this scaling relation than the single segment scenarios (Tab. 5.3). The results in Tab. 5.3 are graphically represented in Fig. 5.15. The contemporary testing earthquakes (except i) already exceed the values from empirical relations but are within their standard deviations.

Based on the high ratios of modelled to empirical seismic moments the MMF beneath the Sea of Marmara is quite late in its seismic cycle. This holds in particular for the section between the Istanbul and Ganos Bends. Beside this qualitative conclusion, it is difficult to precisely quantify the proximity to failure due to the differences among the scaling relations and their huge standard deviations. It seems that the scaling relations by Wells and Coppersmith (1994) and Wesnousky (2008) which are based on global compilations of earthquake source parameters are not representative for the Marmara Sea region. Instead, relation (5.1), which was used by Ambraseys and Jackson (2000) and who are well acquainted with historical earthquakes in this region, seems to be better applicable here, at least for the three small testing earthquakes i-iii. For rupture lengths corresponding to the three larger testing earthquakes (iv-vi) however, relation (5.1) exceeds the 1σ intervals of the empirical relations (Fig. 5.15).

That scenario iii should have already occurred for W=15 km using eq. (5.1) (Tab. 5.3) not necessarily requires that W is greater. If the 1912 Ganos earthquake propagated farther to the east than assumed here (Armijo et al., 2005; Fig. 5.2) then the modelled seismic moment falls below the expected one. Maybe, also the high level of microseismicity in the western Marmara Sea is responsible for that (Fig. 4.20). Finally, in view of the fact that the modelled seismic moment for the 1999 Izmit earthquake exceeds the average of the published seismic moments in Tab. 5.1 by 11 %, which was referred to postseismic moment release and unbroken portions of the fault, then scenario iii might be right ready.

Tab. 5.3: Estimation of fault criticality by comparing modelled source parameters from Tab. 5.2 (white columns) to expectable source parameters from empirical scaling relations by Wells and Coppersmith (1994) (light yellow columns), Wesnousky (2008) (yellow columns) and eq. (5.1; Ambraseys and Jackson, 2000) (orange columns) for the surface rupture lengths of the six testing earthquakes in Fig. 5.12.

	L [km]	**area [km²]**		**max. slip [m]**			**av slip u [m]**		
1σ					±2.3·u	±1.86		±2.1·u	±0.77
i	36.122	741	623	1.28	1.31	2.80	0.86	0.83	1.29
ii	66.297	1216	1148	3.42	2.65	4.12	2.62	1.56	1.90
iii	44.083	828	761	3.33	1.65	3.23	2.32	1.02	1.49
iv	103.701	1931	1803	3.98	4.45	5.10	2.85	2.49	2.35
v	117.003	2125	2036	4.70	5.12	5.36	3.59	2.82	2.47
vi	154.406	2841	2693	4.95	7.06	5.97	3.64	3.77	2.75

	M_0 [10^{20} Nm]					**M_w**					**$M_{0,\text{ mod}}$ / $M_{0,\text{ scal. rel.}}$**			
1σ		*	±2.3 · M_0	W [km]			± 0.28	± 0.24	W [km]				W [km]	
				15	20				15	20			15	20
i	0.18	0.23	0.32	0.29	0.39	6.83	6.90	6.92	6.98	7.06	78 %	55 %	61 %	46 %
ii	0.89	0.63	0.72	0.99	1.32	7.30	7.20	7.14	7.33	7.41	142 %	124 %	90 %	68 %
iii	0.54	0.32	0.42	0.44	0.58	7.15	7.00	6.99	7.09	7.18	169 %	128 %	123 %	92 %
iv	1.54	1.34	1.29	2.42	3.23	7.46	7.42	7.31	7.59	7.67	115 %	119 %	64 %	48 %
v	2.13	1.64	1.51	3.08	4.11	7.55	7.48	7.36	7.66	7.74	130 %	141 %	69 %	52 %
vi	2.90	2.61	2.17	5.36	7.15	7.64	7.61	7.46	7.82	7.90	111 %	133 %	54 %	41 %

* calculated from M_w

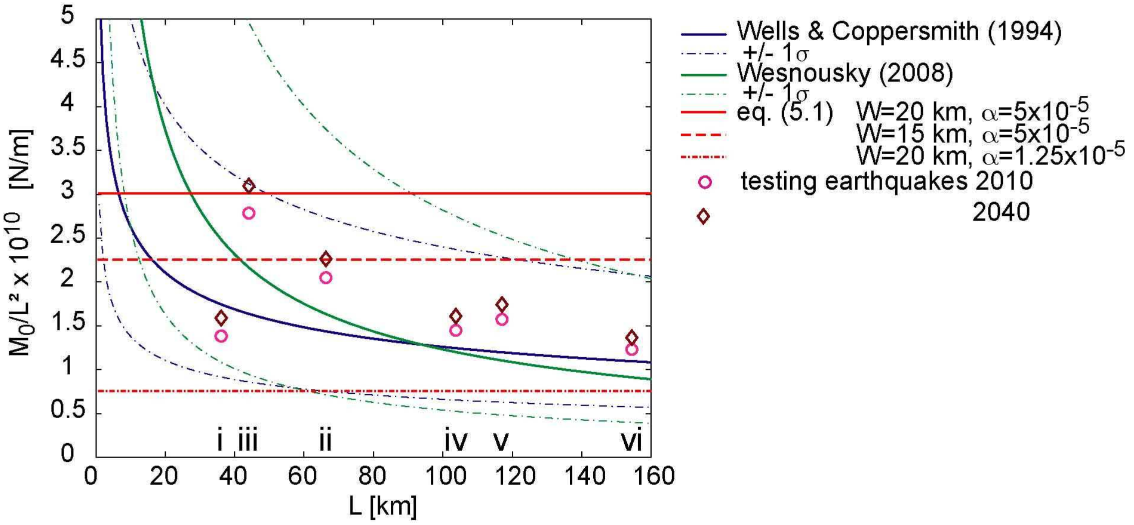

Fig. 5.15: Graphical representation of the comparison between modelled seismic moments and critical values based on scaling relations for the years 2010 and 2040 (Tab. 5.3 and 5.4). Roman numbers refer to the testing earthquakes in Fig. 5.10. Note, that in most cases modelled seismic moments already exceed expectable M_0 for the corresponding rupture length, indicating that fault segments are late in their seismic cycle.

In order to get an idea on time dependence of the modelled source parameters, the six testing earthquakes were also modelled at the beginning of the year 2040 instead of 2010 (Tab. 5.4 and Fig. 5.15). The ruptures of greater length show a stronger increase in amount of maximum and average slip compared to the earthquakes of smaller length. In contrast, the increase of seismic moment during these 30 years is constantly 11 % for scenarios ii through vi, while seismic moment of scenario i increases little more by 15 % (Tab. 5.4).

Concerning the time, the next earthquake has to be expected, some rough estimates can be made, though conditionally. If the 1912 Ganos earthquake reached the Central Basin, then the Central Segment between Istanbul Bend and Central Basin should host the next earthquake (scenario ii) in ~30 years based on the empirical relation (5.1) and assuming W=15 km (Tab. 5.4). If the 1912 event terminated at Ganos Bend, then the segment between Central Basin and Ganos Bend (scenario iii) should break very soon if W=15 km (Tab. 5.3) and in ~30 years for W=20 km (Tab. 5.4). Since seismic moment of the respective earthquakes increased by 11 % between 2010 and 2040 (Tab. 5.4), it can be argued that the above stated dates will be delayed by about 3 decades when accounting for an overestimate of the modelled seismic moments by 11 % due to postseismic moment release and unbroken portions of the fault, that was found for the 1999 event. On the other hand, since there is already sufficient shear stress accumulated to produce earthquakes of typical seismic moments and since the used $\alpha = 5 \cdot 10^{-5}$ is an unusually high value for plate boundary earthquakes (Scholz, 1986), these dates can be understood as upper bounds or as a time frame from now on. Eventually, the initiation of an earthquake is too complex to exclude that failure at a small portion of the fault to some time may extend to the whole near critically stressed segment. In 5.7 the role of the sediments on seismic moments will be investigated.

Tab. 5.4: Comparison of source parameters for the six testing earthquakes at locations shown in Fig. 5.12 in the years 2010 (white columns) and 2040 (purple columns). The ratios of modelled to empirical seismic moments indicated by the yellow columns (same relations as in Tab. 5.3) refer to the seismic moments in the year 2040.

	max. slip [m]		**av slip u [m]**		**M_0 [10^{20} Nm]**			**M_w**		**$M_{0,\,mod}$ / $M_{0,\,scal.\,rel.}$ (2040)**			
	2010	2040	2010	2040	2010	2040		2010	2040			15	20
i	1.28	1.47	0.86	0.99	0.18	0.21	+ 15 %	6.83	6.88	90 %	63 %	70 %	52 %
ii	3.42	3.79	2.62	2.90	0.89	0.99	+ 11 %	7.30	7.33	157 %	138 %	100 %	75 %
iii	3.33	3.68	2.32	2.58	0.54	0.60	+ 11 %	7.15	7.18	188 %	142 %	137 %	103 %
iv	3.98	4.40	2.85	3.17	1.54	1.72	+ 11 %	7.46	7.49	128 %	133 %	71 %	53 %
v	4.70	5.19	3.59	3.97	2.13	2.36	+ 11 %	7.55	7.58	144 %	156 %	77 %	58 %
vi	4.95	5.47	3.64	4.05	2.90	3.22	+ 11 %	7.64	7.67	123 %	148 %	60 %	45 %

To summarise, from the ratio of seismic moments of modelled testing earthquakes to seismic moments from scaling relations the following conclusions can be drawn in view of the likelihood of the six testing earthquakes in Fig. 5.12:

- Scenarios iii and ii are the most likely ones or both together (i.e. scenario v), depending on the applied scaling relation. Due to the fact that both segments have progressed in their seismic cycle, an earthquake at one of them may easily extend to the other one due to the coseismic shear stress increase on the other segment, provided that the complexity of the fault geometry beneath the Central Basin represents no impeding barrier.
- Since the segments between the Istanbul and Ganos Bends are quite late in their seismic cycle (Fig. 5.15) and since the model results are based on the assumption that the two 1766 events ruptured the MMF all the way between Istanbul Bend and Ganos Bend (Fig. 5.2) it is unlikely that there is a seismic gap left since 1509. If the Central Segment did not rupture during one of the 1766 events an earthquake should have occurred already there.

- The MMF beneath the Istanbul and Ganos Bends already accumulated enough and even higher shear stress than necessary to produce earthquakes with source parameters that are typically observed globally for the corresponding rupture lengths. From this point of view a M>7 earthquake beneath the Marmara Sea can in principle happen in the very near future.
- Based on the model results, a M>7 earthquake beneath the Marmara Sea is almost sure within a few decades. With conservative assumptions on rupture width, shear modulus and α in eq. (5.1), an expectable occurrence time is in ~30 years.

Besides their large uncertainties, a disadvantage of taking empirical scaling relations as a measure for the criticality of a fault segment is that they do not reflect specific stress patterns on the fault. From the inferred variations along strike in normal stress on the MMF it was concluded that recurrence rates of earthquakes should be variable as well, with shorter return periods on the Prince’s Islands Segment and along the Tekirdağ Basin and higher return periods on the Central Segment (4.2.3.2; 4.3). Therefore, a more appropriate measure for this purpose would be to directly apply critical stress states on the fault. These could come from frictional rock strength data.

5.7 The influence of rock properties on seismic moments

While the velocity field is not markedly affected by the elastic parameters of the rock (4.1), stress magnitudes are (Fig. 4.20; 4.21). Therefore, though coseismic slip may be similar for different elastic parameters, the associated seismic moments may be not. Here, the influence of elastic parameters on seismic moments of earthquakes on the MMF is investigated. In particular, the hypothesis is investigated on whether and how much seismic moment is reduced due to the thick sediments in the Marmara Sea.

For this purpose, the testing earthquakes ii and iii are modelled using the inhomogeneous rock property distributions MAT_sedi and MAT_grad (Tab. 3.1; Fig. 3.4). The basement-topography along the Central Segment hosting testing earthquake ii is 3-4 km below the sea bottom, whereas sediments are 4-6 km thick along the western segment of the MMF, where scenario iii is modelled (Fig. 3.3). For determining the modelled seismic moments in these cases, the local elastic parameters as well as the resulting mean slip using these rock property distributions were considered. As an alternative to estimating the effect of the sediments using rock property distribution MAT_sedi, one further possibility was tried. It may be, that the fault is not locked within the soft sediments but only within the basement so that there would be stable sliding above the basement-topography and interseismic shear stress accumulation only within the basement. This option of a reduced seismogenic width was tested using the homogeneous rock property distribution with freely slipping faults above the basement-topography and below 15 km depth and a locked fault only in between.

Tab. 5.5 shows the results of this analysis. For all applied rock property distributions resulting slip is higher than in the homogeneous reference model. Consideration of the Moho and a depth gradient in rock properties in the crust (MAT_grad) results in an increase of 5 % in seismic moment for sceanario earthquake ii and a decrease of 6 % for iii. The effect of the sediments (MAT_sedi) is to reduce seismic moment by 10 % on the Central Segment and by 19 % on the western segment of the MMF. The effect of a reduced seismogenic width in the homogeneous case is relatively small and even yields a little higher seismic moment compared to if the fault is locked also above the basement-topography.

The higher stiffness of the Moho and of the lower part of the crust in the depth dependent rock property distribution MAT_grad tends to increase seismic moments compared to the homogeneous reference model since stresses from plate tectonic boundary conditions acting at the sides of the model are more effectively transferred into the central areas of the model so that coseismic slip is increased. Besides, the higher shear modulus contributes to increased seismic moment. In the upper part of the rupture however, the MAT_grad rock property distribution is less stiff than the homogeneous rock property distribution so that for testing earthquake iii, where the basement-topography is deep, total seismic moment becomes lower due to the reduced shear modulus.

Higher slip compared to the homogeneous reference model even in the sediments case can be explained by the reduced fault normal stress due to the lower density of the sediments so that at a given coefficient of friction slip is higher. However, since shear modulus was assumed one order of magnitude lower in the sediments (μ = 3.7 GPa) than in the basement (μ = 28 GPa) (Tab. 3.1), the contribution of slip within the sediments to total seismic moment is negligible and therefore total seismic moment is reduced. On the Central Segment, the reduction in seismic moment by 10 % due to sediments is moderate, whereas it is 19 % on the western segment between Central Basin and Ganos Bend due to the thick sediments and cannot be neglected there in estimations of the seismic moment.

Tab. 5.5: Influence of rock properties on seismic moments for testing earthquakes ii and iii (Fig. 5.12). The second column refers to the applied rock property distribution in Tab. 3.1 and "rsw" denotes the option of a reduced seismogenic width restricted to the basement (see text). Left columns of the source parameters for MAT_sedi refer to the values within the basement and right columns to the sediments. The reference model "ref" here is the homogeneous (MAT_hom) model from Tab. 5.2.

Scen	**Material**	**area [km²]**		**max. slip [m]**		**mean slip [m]**		**M_0 [10^{20} Nm]**		**M_w**	**($M_{0,inhom}$ - $M_{0,ref}$)/ $M_{0,ref}$**
ii	MAT_sedi	1005	212	3.56	3.43	2.78	2.70	0.78	0.02	7.27	- 10.3 %
ii	MAT_grad	1216		3.74		2.89		0.93		7.31	+ 4.5 %
ii	rsw	1229		3.49		2.67		0.91		7.31	+ 1.9 %
ii	ref	1216		3.42		2.62		0.89		7.30	
iii	MAT_sedi	630	198	3.43	3.30	2.37	2.59	0.42	0.02	7.09	- 18.8 %
iii	MAT_grad	828		3.56		2.52		0.50		7.14	- 6.4 %
iii	rsw										
iii	ref	828		3.33		2.32		0.54		7.15	

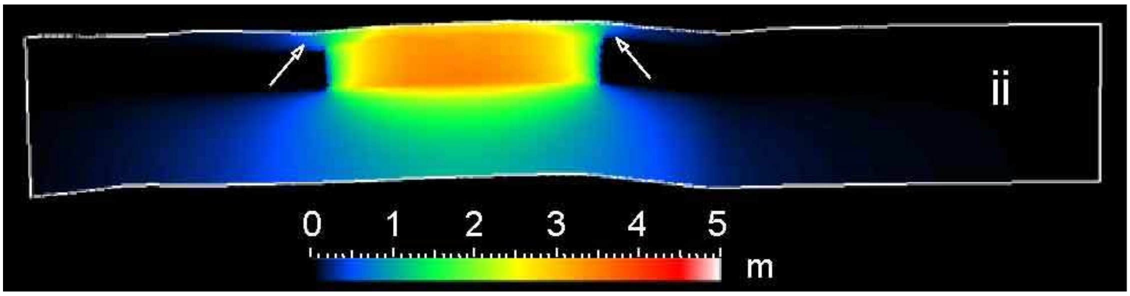

Fig. 5.16: Testing earthquake ii (Fig. 5.12; 5.13) with reduced seismogenic width (rsw) restricted to the basement. White arrows mark slip within the sediments beyond the released fault section in the basement. This is permitted by the permanently unlocked fault in the sediments.

Within the framework of 5.6 the reduced seismic moments accounting for the sediments would imply a delay of earthquake occurrence times of several decades – or that the ratios of modelled to empirical seismic moments after Wells and Coppesmith (1994) and Wesnousky (2008) drop to about 100 % at present for some of the scenario earthquakes (Tab. 5.3). In this case, a large earthquake should occur in the near future and these scaling relations would also be applicable to the Marmara Sea. In case of of the scaling relation (5.1) there should be no important consequence for changes in occurrence time due to the sediments since this relation considers shear modulus.

At this point, the approach of using scaling relations for assessing probabilities or occurrence times is devoid of a physical criterion for failure. Since rupture generally initiates when a critical shear stress level is reached and since the stress in the basement is largely unaffected by the sediments above, the sediments should not markedly alter the occurrence time of an earthquake but rather reduce its magnitude.

The alternative approach of modelling the effect of the sediments on seismic moment by locking the fault only within the basement, hardly brought about a difference to the reference model. Although slip during the interseismic period within the sediments is possible, there is no appreciable reduction in coseismic slip. Instead, slip is even slightly increased since coseismic slip doesn't stop at where the fault was released in the basement but prolongs several kilometres within the sediments (Fig. 5.16). Because of this. also the rupture area is increased compared to the reference model so that the resulting seismic moment is even little higher.

5.8 Rupture propagation at Istanbul Bend

The impact of an earthquake in the Marmara Sea on the city of Istanbul depends to some degree on the question whether an earthquake on the MMF propagates around the bend near Istanbul or terminates there. The modelled changes in fault normal stress during testing earthquakes i and ii on the Prince's Islands and Central Segment, respectively, may help unravel what is expectable.

Fig. 5.17 shows the coseismic changes in normal stress on the MMF due to testing earthquakes i and ii. An earthquake on the Prince's Islands Segment (i) slightly increases σ_n towards Istanbul Bend and more pronounced on the adjacent Izmit segment. In turn, an earthquake on the Central Segment (ii) reduces σ_n on the Prince's Islands Segment by up to 1.9 MPa, which is quite a lot.

From these results it can be concluded that a rupture starting on the Prince's Islands Segment is impeded to propagate round its two limiting fault bends by the coseismic increase of σ_n on the Central and Izmit segments. Contrarily, an earthquake on the Central Segment is favoured to prolong on the Prince's Islands Segment since it is unclamped by slip on the Central Segment. From this perspective, testing earthquakes iv and vi are more likely if rupture initiates west of the Istanbul Bend than if the rupture starts on the Prince's Islands Segment.

The current state of stress on the Prince's Islands and Central Segments however weakens this conclusion. A small shear stress increase on the almost critically stressed Central Segment may be sufficient for a continuation of a rupture starting on the Prince's Islands Segment. On the other hand, though a rupture on the Central Segment may pass the Istanbul Bend because of coseismically increased shear stress, it may eventually die out not far after due to the stress shadow on the Prince's Islands Segment from the 1894 event (Fig. 5.2).

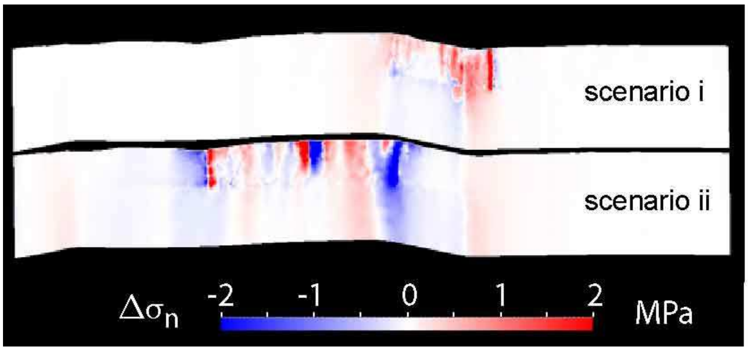

Fig. 5.17: Coseismic changes in normal stress on the MMF due to testing earthquakes i and ii (Fig. 5.12).

5.9 Contribution to dynamic rupture propagation

Though the quasi-static modelling of earthquakes performed here represents a major simplification of a spontaneous dynamic rupture propagation that considers the temporal derivatives of stress and velocity, the resulting slip is well described.

However, for the conditions under which a rupture can propagate, how far it extends and were it arrests the dynamics of rupture propagation is relevant (of course also for the radiation of seismic energy which however was not addressed in this work). Here, the spatial terminations of the testing earthquakes were predefined. Using this method it is possible to make rough estimates on probable rupture lengths for if a testing earthquake of a given length yields much greater seismic moments than expectable from empirical relations it can be concluded that an earthquake should have a greater length if it occurred to that time. In turn, if a testing earthquake of a given length and to a given time yields a smaller seismic moment than expectable for this rupture length then an earthquake should have a smaller rupture length if it occurs at that time or more loading time is required for the assumed length so that it will occur later in the future.

Nevertheless, the final goal must be that earthquakes commence spontaneously and that rupture propagates dynamically in dependence on the state of stress on the fault and its frictional properties. Just recently, Oglesby et al. (2008) presented a model for dynamic rupture propagation on the MMF. Their principle result is that rupture initiating on the Prince’s Islands Segment would probably not extend to the adjacent Izmit and Central Segments, whereas ruptures starting on the latter segments are likely to pass the Tuzla and Istanbul Bends. This result confirms the conclusions drawn in 5.8. The model presented in this thesis could either help improve such spontaneous rupture propagation models or be further developed to accomplish this goal. The most important contribution this model could make to typical spontaneous rupture models is the initial stress on the fault before rupture.

Generally, rupture propagation is controlled by two different quantities, the initial stress right before the rupture and the rupture resistance by friction (Peyrat et al., 2001; Oglesby et al., 2008). Commonly, for the initial stress either very simple assumptions are made or the slip distribution of a recent earthquake on another fault is used to deduce the stress before the earthquake and this stress is then applied as initial stress on the fault of interest (e.g. Olsen et al., 2008) though the pattern of stress on one fault does not need to have much in common with the stress on another fault. As an initial stress for modelling rupture propagation on the MMF, Oglesby et al. (2008) resolved a uniform regional stress field on the fault consisting of piecewise planar segments. The state of stress on the MMF in the model presented here considers three additional contributions beside the fault geometry and a regional stress field. These are: (1) Stresses due to gravitational potential energy arising from density variations and topography. (2) The interaction between plate motion and the fault system leading to local deviations from the regional stress field. E.g. on the Central Segment maximum horizontal stress was found at high angles to fault strike whereas in the western Marmara Sea nearly EW orientations of σ_H were modelled. Oglesby et al. (2008) found that rotating their assumed regional stress field by only 10° makes the difference whether a rupture propagates or not. Therefore, the interplay between fault geometry and driving stresses can be quite important. (3) The seismic cycle is considered, as historical earthquakes are included and the meanwhile accrued shear stress. By that, also the temporal changes in stress due to the secular loading are included. Therefore, in view of the fact that rupture propagation is “extremely sensitive to small changes in the distribution of prestress” (Peyrat et al., 2001) there is room for improvements in the initial stress that can be provided by this model.

It was found that seismic data cannot distinguish between barriers and asperities (Peyrat et al. 2001). This means that recorded seismic data of an earthquake can equally well be explained by variations in initial stress on a fault with uniform frictional properties or in contrast by uniform initial stress with spatially variable friction or by different heterogeneous distributions of initial stress and frictional properties between these two extremes (Peyrat et al., 2001). Therefore, the state of stress modelled here helps to constrain one of these two unknowns.

It was not tested whether it is technically possible to develop the presented model proceeding from its current status, that dynamic rupture propagation can be simulated. An important step would be to establish a more realistic frictional behaviour on the fault. Instead of assigning infinite friction in the locked fault case and $\mu'=0.05$ during the rupture and beneath the seismogenic zone, a slip weakening law has to be applied. As soon as somewhere on the fault a critical stress level is reached it has to be switched over from the quasi-static modelling of secular loading to explicit dynamic rupture propagation.

Chapter 6

Conclusions and Outlook

The key goal of this thesis was to develop a 4D (space and time) geomechanical numerical model that describes the absolute stress and strain field in order to contribute to seismic hazard assessment in the Sea of Marmara. The absolute stress state and velocity field determination permits quantification of fault slip rates and provides insight into the interconnections of motion and stress within the submarine fault system of the Marmara Sea. In particular, the interseismic velocity field and associated stress accumulation was modelled and for the first time, the coseismic slip of the well-documented 1999 Izmit earthquake could be simulated as release of shear stress that had accrued due to tectonic loading. The difference in amount of slip close to the fault is only 6 % between modelled and observed displacements. No assumptions on heterogeneous asperities or barriers were necessary to obtain this result. Potential slip on the fault segments of the NAF below the Marmara Sea were quantified in the same way by releasing the accumulated stress on the fault. Three fault segments were anticipated as likely locations of future earthquakes and it turned out that two of them would yield a M>7 earthquake at present and these segments were found late in their seismic cycle. A worst case scenario filling the whole seismic gap in the Marmara Sea would yield a M=7.6 earthquake at present.

A number of further results are briefly summarised in the following.

- The slip rate on the main branch of the NAF is 12.5-18 mm/yr and is hence variable along strike and lower than commonly reported (typically ~20 mm/yr or more). Rock properties, the coefficient of friction on the faults and the regional velocity field could account for additional 2-4 mm/yr. Mainly slip partitioning on several strands of the fault system and internal deformation involving also rotations are responsible for the lower rates.
- Besides the horizontal, also the vertical velocity field could be well reproduced with high subsidence rates in the basins of the North Marmara Trough, thereby confirming that the adopted geometry of the fault system is meaningful. The pattern of subsiding and stable or uplifting areas reflects the evolution of stress in response to plate motion and the given fault geometry.
- There is a strike-slip tectonic stress regime in the Marmara region that is close to extension. Local variations in the stress field are mostly fault related.
- σ_1 is oriented NWSE or vertical, σ_2 vertical or NWSE and σ_3 NESW.
- Microseismicity in the Marmara Sea can be explained in terms of differential stresses that evolve during the interaction between plate motion and geometry of the fault system.
- Very high changes along strike in normal stress in the order of several hundreds of MPa were modelled along the MMF with minimum values on the Prince’s Islands Segment and below the Tekirdag Basin and high fault normal stresses on the Central Segment.
- The high variability of fault slip-rate and fault normal stress along strike of the MMF should have consequences for recurrence rates of earthquakes on the respective fault segments. Furthermore, this gives reason to expect several smaller events instead of one large earthquake due to the different loading conditions and the probably different amount of shear stress required for failure.

- Depending on the anticipated location of historical earthquakes (Fig. 5.2) the most likely locations for the next earthquake are the western segment of the Marmara Sea between Ganos Bend and Central Basin and the Central Segment between Central Basin and Istanbul Bend. These segments have the potential of M_w=7.1 and 7.3 earthquakes, respectively, at present. A worst case scenario rupturing the whole MMF from Tuzla to Ganos Bend would yield a M_w=7.6 event at present. The next M_w>7 earthquake in the Marmara Sea has to be expected within a few decades.
- The sediments in the Sea of Marmara reduce seismic moments by 10-20 % depending on the fault segment.
- A rupture comprising both the Central and Prince's Islands Segments is more likely if the rupture starts on the former one.

As an outlook for future research, several goals are compiled in the following that can be addressed with the model, either as it is now or with some further development:

- Develop and apply more advanced methods describing the yield criterion on a fault. The approach employed here using scaling relations can provide only very rough estimates on earthquake occurrence times. Preferably, criterions based on the stress state should be used that directly reflect the pattern of stress on the faults. Different failure criterions and frictional rock strength data from laboratory measurements should be tested.
- Extending the model to more complex rheologies. These can be temperature dependent viscoelasticity as well as plasticity. The former could yield a more realistic deformation pattern at greater depth and would account for postseismic viscoelastic stress relaxation. Plasticity would ensure that stresses around fault tips or in between neighbouring faults will not in- or decrease to unrealistic values.
- A strain analysis can be performed based on the modelled velocity field and a decomposition of the velocity gradient tensor in its various components can be undertaken. The strain field can be compared to strain derived by geodetic or seismological analyses. The advantage of the model compared to geodetic strain analyses is that it provides the strain field also in the Sea were no measurements are possible and allows a higher spatial resolution compared to GPS observations.
- Joint investigation of seismotectonics by means of fault plane solutions of microseismicity and stress field modelling. Given a special subvolume of interest, a refined model can be established that is enclosed and driven by the Marmara model. Different hypotheses concerning the geometry of structures of weakness can be investigated that can best explain observed T and P axes by comparing the modelled maximum and minimum principle strain axes to them.
- Implementation of more realistic friction laws as e.g. a velocity dependent slip weakening law instead of either a coefficient of friction of infinity in the locked fault case or μ' = 0.05 in the unlocked case. In particular, using a refined distribution of frictional properties a transition zone at the base of the seismogenic layer could be established that would prohibit the overestimated slip in the lower crust and upper mantle.
- Within the framework of an advanced friction law a spontaneous elastodynamic rupture propagation can be attempted. The great advantage of this model is that it provides a meaningful stress state prior to an earthquake since various influences on the state of stress at any point on the fault are considered. These are the accumulated shear stress since the previous earthquake, stresses due to the weight of the rock column and lateral density variations, lateral changes in fault normal stress due to interaction between plate motion and fault geometry and coseismic stress changes due to earthquakes on other fault segments.

Such a model may help to better constrain what scenarios are expectable and to better frame their temporal occurrence.

- For a reliable seismic hazard assessment in the Marmara region relocation of large historical earthquakes in the Marmara region is an important task (5.2.1). The basis of such an analysis would be an extended data set of seismic intensity data. Expectable ground motions at the sites of available intensity data can be estimated by means of wave propagation modelling considering the 3D velocity and density structure as well as site effects. Within this task this model can help to exclude unlikely scenarios, to provide sets of possible scenarios as well as their source parameters.

Modelling the kinematics and the absolute state of stress simultaneously, allows fundamentally new concepts of time-dependent seismic hazard assessment. The presented or similar approaches will be of importance in the future. An example attesting this is the proposal for the third phase of the Southern California Earthquake Center (SCEC3)[4], an outstanding consortium of more than 50 universities and institutions in the field of earthquake research, that was submitted to the National Science Foundation of the United States addressing the science plan for 2007 through 2012. Herein, one key issue on the way to the “ultimate goal of physics-based seismic hazard assessment” is stated as “to develop representations of the … evolution of stress and strain that can predict fault system behaviours”. The work presented here provides a technical concept for this purpose and could be transferred to the San Andreas Fault system.

This work demonstrated the usefulness of various kinds of geophysical data for validation of the kinematic and dynamic performance of the model. In this respect, also data that are not directly linked to seismic hazard assessment proof to be valuable in this context. Highly appreciated are stress magnitude data at greater depths in the Marmara Sea region, preferably in the basement, to better constrain the stress field. In this respect the planned scientific drill hole on one of the Prince Islands (Dresen et al., 2008) represents an outstanding opportunity to predict stress magnitudes from the model, to validate the model by stress measurement data and to interpret these within the modelled overall stress field. Deeper knowledge on the deep structures of the fault system in the Marmara Sea would be also important. Though most of the observations can be explained with the assumed fault geometry, it can be not excluded that the fault system in the NAF may represent a large scale negative flower structure.

The standard approach for probabilistic seismic hazard assessment (1.3.2) allows quick solutions for large areas and is therefore advantageous if its prerequirements are satisfied, i.e. knowledge of fault slip rates and/or availability of an ample seismic record and information on historical earthquakes that allows determination of mean earthquake recurrence rates. However, in complex tectonic settings often precise fault slip rates are not known and recurrence rates are not inferable reliably. If a particular region is to be investigated in detail, that was surveyed by various geophysical methods already, the presented approach provides the possibility to elucidate the ongoing tectonic processes, how movements and seismicity can be related to characteristics in the stress field and how the spatial and temporal occurrence of large earthquakes can be understood. It finally permits a time-dependent assessment of potential coseismic slip and seismic moment for particular fault segments, rewarding the most basic physical background of earthquakes as well as rough estimates on earthquake occurrence times.

---

[4] http://www.scec.org/aboutscec/documents/SCEC3proposal.pdf;

Acknowledgements

Diese Arbeit wurde unterstützt von und durchgeführt im Rahmen des CEDIM (Center for Disaster Management and Risk Reduction Technology) Projekts, getragen vom Helmholtz-Zentrum Potsdam Deutsches GeoForschungsZentrum – GFZ und der Universiät Karlsruhe (TH), sowie des World Stress Map (WSM) Projekts, angesiedelt bei der Heidelberger Akademie der Wissenschaften.

Herrn Prof. Dr. Friedemann Wenzel danke ich für die Übernahme des Referats sowie für Anmerkungen im Zusammenhang mit der seismischen Gefährdung, die eine klarere Darstellung erlaubten. Herrn Prof. em. Dr. Karl Fuchs danke ich für die Übernahme des Korreferats sowie für die detaillierten Verbesserungsvorschläge des Textes.

Dr. Oliver Heidbach danke ich besonders für die Betreuung meiner Arbeit sowie für sein großes Interesse und Engagement, für richtungsweisende Diskussionen und die Erledigung diverser organisatorischer Dinge.

I thank Prof. Dr. Alfred Hirn and Dr. Anne Bécel for discussions that helped me to get the picture of how various structures can be interpreted kinematically and for providing me the data for the basement-topography which made an estimation of the influence of the sediments on slip rate, stress and seismic moments possible.

Den verbliebenen und ehemaligen Mitgliedern der stress group am Geophysikalischen Institut Andreas Barth, Birgit Müller, Daniel Kurfess, Johannes Altmann, Gwendolyn Peters, Paola Ledermann, Alik Ismail-Zadeh, Mark Tingay, Peter Connolly, José Dirkzwager danke ich für eine gute Arbeitsatmosphäre, hilfreiche Diskussionen und Tips. Besonders danke ich hierbei Andreas Eckert und Thies Buchmann, die mir in der Anfangsphase bei der Modellerstellung und bei modelliertechnischen Dingen geholfen haben.

Meinen Eltern und Freunden danke ich für Gebetsunterstützung und ihr Verständnis, wenn ich mal wieder keine Zeit hatte.

Appendix

Virtual work principle and finite element method

Here, the equations to be solved are rewritten as virtual work statement, that allows application of the finite element method. In order to obtain an approximation for the equilibrium equations (2.4), they are multiplied by a vector $\delta\vec{u}$, which is the virtual displacement field, and integrated.

$$\int_V \left[\mathrm{div}\underline{\underline{\sigma}} + \vec{f}\right] \cdot \delta\vec{u}\,\mathrm{d}V = 0 \tag{App.1}$$

Thus, the three equations (2.4) are replaced by one equation, which is the virtual work. It states, that forces applied to a static system do no virtual work. $\delta\vec{u}$ is arbitrary, except that it is continuous over the entire volume and consistent, i.e. the forces do no work in directions perpendicular to $\delta\vec{u}$.

Using the chain rule, the first term in eq. (App.1) gives

$$\int_V \mathrm{div}\underline{\underline{\sigma}} \cdot \delta\vec{u}\,\mathrm{d}V = \int_V \mathrm{div}\left(\underline{\underline{\sigma}} \cdot \delta\vec{u}\right)\mathrm{d}V - \int_V \underline{\underline{\sigma}} \bullet \mathrm{div}\delta\vec{u}\,\mathrm{d}V$$

Application of Gauss's theorem and the definition of Cauchy stress (eq. 2.2) with the first term on the right-hand side and inserting eq. (2.4) on the left-hand side and regrouping yields the virtual work equation:

$$\int_V \vec{f} \cdot \delta\vec{u}\,\mathrm{d}V + \int_S \vec{t} \cdot \delta\vec{u}\,\mathrm{d}S = \int_V \underline{\underline{\sigma}} \bullet \mathrm{div}\delta\vec{u}\,\mathrm{d}V \;, \tag{App.2}$$

where $\mathrm{div}\delta\vec{u}$ is the symmetrical part of the virtual displacement gradient field (i.e.virtual strain)

$$\delta\underline{\underline{\varepsilon}} = \frac{1}{2}\left(\mathrm{div}\delta\vec{u} + \mathrm{div}\delta\vec{u}^{\,\mathrm{T}}\right) , \tag{App.3}$$

so that

$$\int_V \vec{f} \cdot \delta\vec{u}\,\mathrm{d}V + \int_S \vec{t} \cdot \delta\vec{u}\,\mathrm{d}S = \int_V \underline{\underline{\sigma}} \bullet \delta\underline{\underline{\varepsilon}}\,\mathrm{d}V \tag{App.4}$$

Equation (App.4) states, that for every virtual displacement field the work done by external forces (external virtual work; left-hand side) is equal to the work done by the equilibrating stresses on deformation by the virtual displacement field (internal virtual work; right-hand side).

Now an approximation is performed, that weakens equation (App.4). Instead of demanding that external and internal virtual work are in equilibrium for any virtual displacement field, equilibrium will be maintained only for a subset of virtual velocity fields. This allows an approximate solution of the displacement field. For this purpose, the volume under consideration is divided into discrete portions, the so-called finite elements, that are interconnected by shared nodes. The nodal displacements are the fundamental variables that are calculated. Due to the discretisation the terms of equation (App.4) become sums over the contributions of each element. In order to evaluate this equation, at first the displacement field is interpolated within the elements by expressing it in terms of linear combinations of the element's nodal displacements $\vec{q}$

$$\vec{u} = \underline{\underline{N}}\vec{q} \quad , \qquad \text{(App.5)}$$

where N is a matrix of shape functions, that are continuous within an element and describe the interpolation. The same is done for the virtual displacements

$$\delta\vec{u} = \underline{\underline{N}}\delta\vec{q} \quad . \qquad \text{(App.6)}$$

In this work, linear tetrahedral elements are used, so that the displacement field varies linear between neighbouring nodes. Then the strains in the elements are computed from the nodal displacements by

$$\underline{\underline{\varepsilon}} = \underline{\underline{D}}\vec{u} = \underline{\underline{D}}\,\underline{\underline{N}}\vec{q} =: \underline{\underline{B}}\vec{q} \quad , \qquad \text{(App.7)}$$

where $\underline{\underline{D}}$ is a matrix of differential operators that transform displacements to strain. Accordingly, the virtual strains are expressed by the virtual nodal displacements.

$$\delta\underline{\underline{\varepsilon}} = \underline{\underline{B}}\delta\vec{q} \qquad \text{(App.8)}$$

Then the stresses can be expressed in terms of nodal displacements by using a constitutive law, as Hooke's law in the linear elastic case:

$$\underline{\underline{\sigma}} = \underline{\underline{\underline{\underline{C}}}}\,\underline{\underline{\varepsilon}} \qquad \text{(App.9)}$$

where $\underline{\underline{\underline{\underline{C}}}}$ is the stiffness tensor relating strain to stress. In the isotropic case, two independent parameters, e.g. Young's modulus and Poisson's ratio, fully define the stiffness tensor. These properties are constant within one element (anisotropy is possible), but can be different in other elements. This implies, that the Lagrangian view is considered, i.e. material belongs to certain elements, that deform, in opposite to the Eulerian view of material flowing through a spatially fixed mesh. Inserting equations (App.5)-(App.9) into (App.4), gives

$$\delta\vec{q}^{\,T}\sum_k \vec{p}_k + \delta\vec{q}^{\,T}\sum_e \int_{V_e} \underline{\underline{N}}^T \vec{f}_e\, dV_e + \delta\vec{q}^{\,T}\sum_e \int_{S_e} \underline{\underline{N}}^T \vec{t}_e\, dS_e = \delta\vec{q}^{\,T}\left[\sum_e \int_{V_e} \underline{\underline{B}}^T \underline{\underline{\underline{\underline{C}}}}\,\underline{\underline{B}}\, dV_e\right]\vec{q} \qquad \text{(App.10)}$$

As a consequence of discretisation, on the left-hand side, which represents the external loads, the term accounting for point loads $\vec{p}$ at nodes was added, since this kind of force is not contained in the surface tractions. k denotes the number of point loads. In practice this term is relevant, when prescribing displacement boundary conditions, that are internally handled as forces acting on nodes. Since the virtual displacements $\delta\vec{q}^{\,T}$ are arbitrary, they can be cancelled. The respective integrals in eq. (App.10) are evaluated by numerical integration for each element, and then it is summed over all elements. This gives the formulation for assembling the system matrix of a finite element model. In a more concise form

$$\vec{F} = \underline{\underline{K}}\,\vec{q}\,, \tag{App.11}$$

where $\underline{\underline{K}}$ is the systems' stiffness matrix, that assembles the contributions $\underline{\underline{k}}_e$ from all elements

$$\underline{\underline{K}} = \sum_e \underline{\underline{k}}_e = \sum_e \int_{V_e} \underline{\underline{B}}^T \underline{\underline{\underline{C}}}\,\underline{\underline{B}}\,dV_e$$

and $\vec{F}$ is the global load column, that sums the contributions of the body force and traction from all elements.

$$\vec{F} = \sum_k \vec{p}_k + \sum_e \int_{V_e} \underline{\underline{N}}^T \vec{f}_e\,dV_e + \sum_e \int_{S_e} \underline{\underline{N}}^T \vec{t}_e\,dS_e \tag{App.12}$$

The nodal displacements are found by solving the system of linear equations (App.11). Once, the nodal displacements are known, they are used to calculate the strains (eq. App.7) and stresses (eq. App.9).

If there is an initial stress $\underline{\underline{\sigma}}^0$ in an element, eq. (App.9) may be written as

$$\underline{\underline{\sigma}} = \underline{\underline{\underline{C}}}\left(\underline{\underline{\varepsilon}} - \underline{\underline{\varepsilon}}^0\right) + \underline{\underline{\sigma}}^0 = \underline{\underline{\underline{C}}}\left(\underline{\underline{B}}\,\vec{q} - \underline{\underline{\varepsilon}}^0\right) + \underline{\underline{\sigma}}^0 \tag{App.13}$$

where $\underline{\underline{\varepsilon}}^0$ is the initial strain in the element. Inserting (App.13) into eq. (App.4) leads to an additional load term in eq. (App.12).

Deviations between real displacements and stresses and the model results come mainly from three sides. First, representation of the actual displacement-strain and stress-strain relations by assumption of a constitutive law and prescription of the spatial variations of material properties and properties and geometry of contact (chapter 3). Second, the discretisation influences accuracy. High element density is required, where stress gradients are expected to be high, since otherwise the true solution cannot be properly approximated by linear interpolation. Third, the numerical error due to numerical integration. For more details on the finite element method, the reader is referred to Zienkiewicz and Taylor (1994a;b).

Regime-Stress-Ratio (RSR)

Different types of quantities have been proposed to ascribe a certain stress state to a stress regime. Here, the RSR parameter is used to visualise the stress regime. RSR stands for regime stress ratio and was introduced by Simpson (1997). It is basically a combination of the Andersonian stress regime r (Anderson, 1905)

$$\mathrm{r} = \begin{cases} 0 & \sigma_h < \sigma_H < \sigma_V \\ 1 & \sigma_h < \sigma_V < \sigma_H \\ 2 & \sigma_V < \sigma_h < \sigma_H \end{cases}$$

and the ratio of the smaller and greater differential stress (Bott, 1959)

$$\mathrm{R} = \frac{\sigma_2 - \sigma_3}{\sigma_1 - \sigma_3}.$$

RSR is then defined as

$$\mathrm{RSR} = (\mathrm{r} + 0.5)(-1)^{\mathrm{r}}(\mathrm{R} - 0.5).$$

An advantageous property of the RSR parameter is that it provides a continuous scale from radial extension over extension, strike-slip and compression to constriction, including the transitional regimes of transtension and transpression (Fig. 4.14).

Fracture potential

The Fracture Potential (FP) expresses differential stress in a rock with respect to an empirical failure criterion and by that quantifies the likelihood for the generation of fractures in a rock mass subjected to stress.

The concept of FP was described by Connolly and Cosgrove (1999). FP is defined as the ratio of the differential stress in the rock and the critical differential stress at failure (Fig. App.3). This definition holds only for shear failure which is considered here since the crust is generally in a compressional state of stress. The critical differential stress is based on the Navier-Coulomb criterion and hence dependent on the internal coefficient of friction μ_i of the rock and on its cohesion C_0. These two parameters have to be provided to calculate the FP at a given stress state.

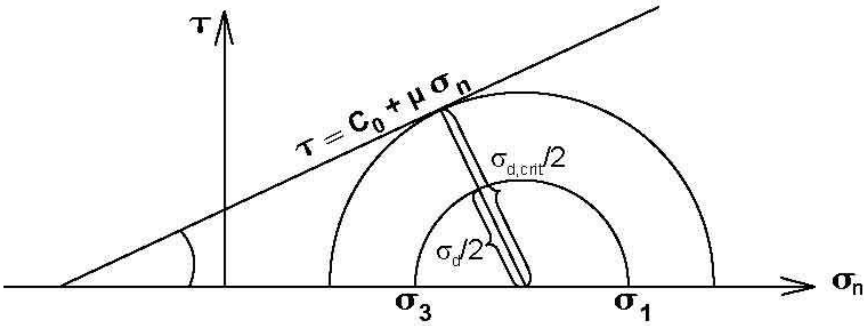

Fig. App.3: Sketch explaining fracture potential.

References

Akinci, A., Malagnini, L., Herrmann, R.B., Gok, R., Sorensen, M., 2006. Ground motion scaling in the Marmara region, Turkey. Geophys. J. Int, 166 635-651.

Akman, A.Ü., Tüfekçi, K., 2004. Determination and Characterisation of Fault Systems ans Geomorphological Features by RS and GIS Techniques in the WSW Part of Turkey, XXth ISPRS congress, commission VII, Istanbul, pp. 899-905.

Aksoy, M.E., Meghraoui, M., Ferry, M., Çakir, Z., Akyüz, S., Karabacak, V., Altunel, E., 2006. Fault characteristics, segmentation and paleoseismology along the 9 August 1912 Ganos earthquake-rupture (North Anatolian Fault, Turkey). Geoph. Res. Abs., 8 (10002), SRef-ID: 1607-7962/gra/EGU06-10002.

Aksu, A.E., T.J., C., Hiscott, R.N., 2000. Anatomy of the North Anatolian Fault Zone in the Marmara Sea, Western Turkey: Extensional Basins Above a Continental Transform. GSA Today, 10 (6).

Aktar, M., Özalaybey, S., Ergin, M., Karabulut, H., Bouin, M.-P., Tapırdamaz, C., Biçmen, F., Yörük, A., Bouchon, M., 2004. Spatial variation of aftershock activity across the rupture zone of the 17 August 1999 Izmit earthquake, Turkey. Tectonophysics, 391 325– 334 doi:10.1016/j.tecto.2004.07.020.

Allen, M., Jackson, J., Walker, R., 2004. Late Cenozoic reorganization of Arabia-Eurasia collision and comparison of short-term deformation rates. Tectonics, 23 (TC2008), doi:10.1029/2003TC001530.

Allmendinger, R.W., Reilinger, R., Loveless, J., 2007. Strain and rotation rate from GPS in Tibet, Anatolia, and the Altiplano. Tectonics, 26 (TC3013), doi:10.1029/2006TC002030.

Alpar, B., Yaltırak, C., 2002. Characteristic features of the North Anatolian Fault in the eastern Marmara region and its tectonic evolution. Marine Geol., 190 329-350 PII:S0025-3227(02)00353-5.

Altınok, Y., Alpar, B., Yaltırak, C., 2003. Şarköy-Mürefte 1912 Eathquake´s Tsunami, extension of the associated faulting in the Marmara Sea, Turkey. Journal of Seismology, 7 329-346.

Altınok, Y., Tinti, S., Alpar, B., Yalçıner, A.C., Ersoy, S., Bortoluzzi, G., Armigliato, A., 2001. The Tsunami of August 17, 1999 in Izmit Bay, Turkey. Natural. Hazards, 24 133-146.

Altunel, E., Meghraoui, M., Akyüz, H.S., Dikbas, A., 2004. Characteristics of the 1912 co-seismic rupture along the North Anatolian Fault Zone (Turkey): implications for the expected Marmara earthquake. Terra Nova, 16 198-104 doi:10.1111/j.1365-3121.2004.00552.x.

Ambraseys, N., 2001a. The earthquake of 10 July 1894 in the Gulf of Izmit (Turkey) and its relation to the earthquake of 17 August 1999. J. of Seismol., 5 117-128.

Ambraseys, N., 2002. The Seismic Activity of the Marmara Sea Region over the Last 2000 Years. Bull. Seism. Soc. Am., 92 (1), 1-18.

Ambraseys, N., 2006. Comparison of frequency of occurrence of earthqaukes with slip rates from long-term seismicity data: the cases of Gulf of Corinth, Sea of Marmara and Dead Sea Fault Zone. Geophys. J. Int, 165 516-526.

Ambraseys, N., Finkel, C.F., 1991. Long-term seismicity of Istanbul and of the Marmara Sea region. Terra Nova, 3 527-539.

Ambraseys, N.N., 2001b. The Earthquake of 1509 in the Sea of Marmara, Turkey, Revisited. Bull. Seism. Soc. Am., 91 (6), 1397–1416.

Ambraseys, N.N., Jackson, J.A., 1998. Faulting associated with historical and recent earthquakes in the Eastern Mediterranean region. Geophys. J. Int, 133 390-406.

Ambraseys, N.N., Jackson, J.A., 2000. Seismicity of the Sea of Marmara (Turkey) since 1500. Geophys. J. Int., 141 F1-F6.

Anderson, E.M., 1905. The dynamics of faulting. Trans. Edin. Geol. Soc., 8 387-402.

Angevine, C.L., Turcotte, D.L., Furnish, M.D., 1982. Pressure Solution Lithification as a Mechanism for the Stick-slip Behavior of Faults. Tectonics151-160.

Armijo, R., Flerit, F., King, G., Meyer, B., 2003. Linear elastic fracture mechanics explains the past and present evolution of the Aegean. Earth and Planet. Sci. Lett., 217 85-95.

Armijo, R., Meyer, B., Hubert, A., Barka, A., 1999. Westward propagation of the North Anatolian fault into the nothern Aegean: Timing and kinematics. Geology, 27 (3), 267-270.

Armijo, R., Meyer, B., Navarro, S., King, G., Barka, A., 2002. Asymmetric slip partitioning in the Sea of Marmara pull-apart: a clue to propagation processes of the North Anatolian Fault? Terra Nova, 13 (6), 80-86.

Armijo, R., Pondard, N., Meyer, B., Ucarkus, G., Mercie de Lepinay, B., Malavieille, J., Dominguez, S., Gustcher, M.A., Schmidt, S., Beck, C., Çagatay, N., Çakir, Z., Imren, C., Eris, K., Natalin, B., Özalaybey, S., Tolun, L., Lefévre, I., Seeber, L., Gasperini, L., Rangin, C., Emre, O., Sarikavak, K., 2005. Submarine fault scarps in the Sea of Marmara pull-apart (North Anatolian Fault): Implications for seismic hazard in Istambul. G3, 6 (6), Q06009, doi:10.1029/2004GC000896.

Atakan, K., Ojeda, A., Meghraoui, M., Barka, A.A., Erdik, M., Bodare, A., 2002. Seismic Hazard in Istanbul following the 17 August 1999 İzmit and 12 November 1999 Düzce Earthquakes. Bull. Seism. Soc. Am., 92 (1), 466–482.

Aydin, A., Kalafat, D., 2002. Surface Ruptures of the 17 August and 12 November 1999 Izmit and Düzce Earthquakes in Northwestern Anatolia, Turkey: Their Tectonic and Kinematic Significance and the Associated Damage. Bull. Seism. Soc. Am., 92 (1), 95-106.

Aydın, İ., Karat, H.İ., Koçak, A., 2005. Curie-point depth map of Turkey. Geophys. J. Int, 162 633-640 doi:10.1111/j.1365-246X.2005.02617.x.

Ayhan, M.E., Demir, C., Lenk, O., Kiliçogul, A., Altiner, Y., Barka, A.A., Ergintav, S., Özener, H., 2002. Interseismic Strain Accumulation in the Marmara Sea Region. Bull. Seism. Soc. Am., 92 (1), 216-229.

Barış, Ş., Ito, A., Üçer, S.B., Honkura, Y., Kafadar, N., Pektaş, R., Komut, T., Isıkara, A.M., 2002. Microearthquake Activity before the Izmit Earthquake in the Eastern Marmara Region, Turkey (1 January 1993–17 August 1999). Bull. Seism. Soc. Am., 92 (1), 394–405.

Barka, A., 1992. The North Anatolian fault zone. Annales Tectonicae, VI suppl 164-195.

Barka, A., 1996. Slip distribution along the North Anatolian Fault associated with the large earthquakes of the period 1939 to 1967. Bull. Seism. Soc. Am., 86 (5), 1238-1254.

Barka, A., 1997. Neotectonics of the Marmara region. In: C. Schindler,M. Pfister (Editors), Active tectonics of northwestern Anatolia-The MARMARA Poly-Project. vdf Hochschulverlag AG ETH Zürich, pp. 55-87.

Barka, A., Akyüz, H.S., Altunel, E., Sunal, G., Çakir, Z., Dikbas, A., Yerli, B., Armijo, R., Meyer, B., de Chabalier, J.B., Rockwell, T., Dolan, J.R., Hartleb, R., Dawson, T., Christofferson, S., Tucker, A., Fumal, T., Langridge, R., Stenner, H., Lettis, W., Bachhuber, J., Page, W., 2002. The Surface Rupture and Slip Distribution of the 17 August 1999 I˙zmit Earthquake (M 7.4), North Anatolian Fault. Bull. Seism. Soc. Am., 92 (1).

Barka, A.A., Kadinsky-Cade, C., 1988. Strike-slip fault geometry in Turkey and its influence on earthquake activity. Tectonics, 7 663-684.

Bayrak, M., Gürer, A., Gürer, Ö.F., 2004. Electromagnetic Imaging of the Thrace Basin and Intra-Pontide Subduction Zone, Northwestern Turkey. Int. J. Earth Sci (Geol Rundschau), 46 (1), 64-74(11).

Bécel, A., Laigle, M., de Voogd, B., Hirn, A., Taymaz, T., Galvé, A., Shimamura, H., Murai, Y., Lépine, J.-C., Sapin, M., Özalaybey, S., 2009. Moho, crustal architecture and deep deformation under the North Marmara Trough, from the SEISMARMARA Leg1 offshore-onshore reflection-refraction survey. Tectonophysics, 467, 1-21.

Bekler, T., Gurbüz, C., Toksöz, M.N., 2005. Seismic Refraction Experiments and Crustal Structure in Turkey. Geophys. Res. Abs., 7 (00753), SRef-ID: 1607-7962/gra/EGU05-A-00753.

Bendimerad, F., 2001. Modeling and quantification of earthquake risk: Application to emerging economies. In: P.R. Kleindorfer,M.R. Sertel (Editors), Mitigation and financing of seismic risks: Turkish and international perspectives. IV. Earth and Environmental Sciences - vol. 3. NATO Science series.

Bendimerad, F., Coburn, A., Morrow, G., Johnsson, L., Rahnama, M., 2000. Event report. Kocaeli, Turkey earthquake, Risk Management Solutions Inc., Menlo Park, CA, USA.

Beresnev, I.A., 2003. Uncertainties in finite-fault slip inversions: To what extent to believe? (A critical review). Bull. Seism. Soc. Am., 93 (6), 2445-2458.

Bindi, D., Parolai, S., Grosser, H., Milkereit, C., Durukal, E., 2007. Empirical ground-motion prediction equations for northwerstern Turkey using the aftershocks of the 1999 Kocaeli earthquake. Geophys. Res. Lett., 34 L08305 doi:10.1029/2007GL029222.

Bindi, D., Parolai, S., Grosser, H., Milkereit, C., Zünbül, S., 2006. Cumulative attenuation along Source-to-receiver paths in northwestern Turkey. Bull. Seism. Soc. Am., 96 (1), 188-198 doi:10.1785/0120050037.

Bird, P., 1996. Computer simulations of Alaskan neotectonics. Tectonics, 15 225-236.

Bird, P., 1998. Testing hypotheses on plate-driving mechanisms with global lithosphere models including topography, thermal structure, and faults. J. Geophys. Res., 103 (B5), 10115-10129.

Bird, P., Kong, X., 1994. Computer simulations of California tectonics confirm very low strength of major faults. Geol. Soc. Am. Bull., 106 159-174 doi:10.1130/0016-7606(1994)106<0159:CSOCTC>2.3.CO;2.

Biryol, C.B., Zandt, G. Beck, S.L., Garıs, C., Ozacar, A.A, Tok, H.E., Koçyığıt, A., Bozkurt, E., Taymaz, T., 2008. NAF Experiment: Seismic anisotropy beneath northern Anatolia from shear-wave splitting. Eos. Trans. AGU, 89(53), Fall Meet. Suppl., xxxxx-xx.

Blanpied, M.L., Lockner, D.A., Byerlee, J.D., 1992. An earthquake mechanism based on rapid sealing of faults. Nature, 358 574 - 576 doi:10.1038/358574a0.

Blanpied, M.L., Lockner, D.A., Byerlee, J.D., 1995. Frictional slip of granite at hydrothermal conditions. J. Geophys. Res, 100 (B7), 13,045-13,064.

Bohnhoff, M., Grosser, H., Dresen, G., 2006. Strain partitioning and stress rotation at the North Anatolian fault zone from aftershock focal mechanisms of the 1999 Izmit Mw=7.4 earthquake. Geophys. J. Int., 166 373-385 doi:10.1111/j.1365-246X.2006.03027.x.

Bos, A.G., Spakman, W., 2003. The resolving power of coseismic surface displacement data for a fault slip distribution at depth. Geophys. Res. Letts., 30 (21), 2110, doi:10.1029/2003GL017946.

Bos, A.G., Usai, S., Spakman, W., 2004. A joint analysis of GPS motions and InSAR to infer the coseismic surface deformation of the Izmit, Turkey earthquake. Geophys. J. Int, 158 849-863.

Bouchon, M., Toksöz, M.N., Karabulut, H., Bouin, M.-P., Dietrich, M., Aktar, M., Edie, M., 2002. Space and Time Evolution of Rupture and Faulting during the 1999 Izmit (Turkey) Earthquake. Bull. Seism. Soc. Am., 92 (1), 256–266.

Boykova, A., 1999. Moho discontinuity in Central Balkan Peninsula in the light of geostatistical structural analysis. Physics of the Earth's Interiors, 114 49-58.

Bozkurt, E., Mittwede, S.K., 2001. Introduction to the geology of Turkey - a synthesis. Int. J. Earth Sci (Geol Rundschau), 43 578-594.

Bozkurt, E., Sözbılır, H., 2004. Tectonic evolution of the Gediz Graben: field evidence for an episodic, two-stage extension in western Turkey. Geol. Mag., 141 (1), 63-79 doi:10.1017/S0016756803008379.

Brocher, T.M., 2005. Empirical Relations between Elastic Wavespeeds and Density in the Earth’s Crust. Bull. Seism. Soc. Am., 95 (6), doi: 10.1785/0120050077.

Brown, K.M., Kopf, A., Underwood, M.B., Weinberger, J.L., 2003. Compositional and fuid pressure controls on the state of stress on the Nankai subduction thrust: A weak plate boundary. Earth Planet. Sci. Lett., 214 589-603 doi:10.1016/S0012-821X(03)00388-1.

Brudy, M., Zoback, M.D., Fuchs, F., Rummel, F., Baumgärtner, J., 1997. Estimation of the complete stress tensor to 8 km depth in the KTB scientific drill holes: Implications for crustal strength. J. Geophys. Res., 102 18453-18457.

Bulut, F., Aktar, M., 2007. Accurate relocation of Izmit Earthquake (Mw=7.4, 1999) aftershocks in Çinarcik Basin using Double Difference Method. Geophys. Res. Lett., 34 L10307, doi:10.1029/2007GL029611.

Bulut, F., Bohnhoff, M., Aktar, M., Dresen, G., 2007. Characterization of aftershock-fault plane orientations of 1999 Izmit (Turkey) earthquake using high-resolution aftershock locations. Geophys. Res. Lett., 34 L20306, doi:10.1029/2007GL031154.

Bürgmann, R., Ergintav, S., Segall, P., Hearn, E.H., McClusky, S., Reilinger, R., Woith, H., Zschau, J., 2002. Time-Dependent Distributed Afterslip on and Deep below the İzmit Earthquake Rupture. Bull. Seismol. Soc. Am., 92 (1), 126-137.

Byerlee, J.D., 1978. Friction of rocks. Pure Appl. Geophys., 116 615-626.

Byerlee, J.D., 1990. Friction, overpressure and fault normal compression. Geophys. Res. Lett., 17 (12), 2109-2112.

Çağatay, N., Görür, N., Polonia, A., Demirbağ, E., Sakınç, M., Cormier, M.-H., Capotondi, L., McHugh, C.M.G., Emre, Ö., Eriş, K., 2003. Sea-level changes and depositional environments in the Izmit Gulf, eastern Marmara Sea, during the late glacial- Holocene period. Marine Geol., 202 159-173.

Cai, J., Grafarend, E.W., 2007. Statistical analysis of geodetic deformation (strain rate) derived from the space geodetic measurements of BIFROST Project in Fennoscandia. J. Geodymamics, 43 214-238.

Çakir, Z., Barka, A., Evren, E., 2003a. Coulomb Stress Interactions and the 1999 Marmara Earthquakes. Turkisch J. of Earth Sciences, 12 91-103.

Çakir, Z., de Chabalier, J.B., Armijo, R., Meyer, B., Barka, A., Peltzer, G., 2003b. Coseismic and early post-seismic slip associated with the 1999 Izmit earthquake (Turkey), from SAR interferometry and tectonic field observations. Geophys. J. Int., 155 93-110.

Çakir, Z., Akoglu, A.M., Belabbes, S., Ergintav, S., Meghraoui, M., 2005. Creeping along the Ismetpasa section of the North Anatolian fault (Western Turkey): Rate and extent from InSAR. Earth Planet. Sci. Lett., 238 225-234.

Carton, H., Singh, S.C., Hirn, A., Bazin, S., Voogd, B.d., Vigner, A., Ricolleau, A., Cetin, S., Oçakoğlu, N., Karakoç, F., Sevilgen, V., 2007. Seismic imaging of the tree-dimensional architecture of the Çınarık Basin along the North. J. Geophys. Res., 112 (B06101), doi:10.1029/2006JB004548.

Célérier, B., 1995. Tectonic regime and slip orientation of reactivated faults. Geophys. J. Int, 121 143-161.

Cianetti, S., Giunchi, C., Cocco, M., 2005. Three-dimensional finite element modeling of stress interaction: An application to Landers and Hector Mine fault systems. Journal of Geophysical Reasearch, 110 (B05S17), doi:10.1029/2004JB003384.

Ciccotti, M., Mulargia, F., 2004. Differences between static and dynamic elastic moduli of a typical seismogenic rock. Geophys. J. Int, 157 474-477.

Cisternas, A., Polat, O., Rivera, L., 2004. The Marmara Sea region:Seismic behaviour in time and the likelihood of another large earthquake near Istanbul (Turkey). Journal of Seismology, 8 427-437.

Clévédé, E., Bouin, M.-P., Bukchin, B., Mostinkiy, A., Patau, G., 2004. New contraints on the rupture progress of the 1999 August 17 Izmit earthquake deduced from estimates of stress glut rate moments. Geophys. J. Int, 159 931-942 doi:10.1111/j.1365-246X.2004.02304.x.

Cormier, M.-H., Seeber, L., McHugh, C.M.G., Polonia, A., Çagatay, N., Emre, Ö., Gasperini, L., Görür, N., Bortoluzzi, G., Bonatti, E., Ryan, W.B.F., Newman, K.R., 2006. North Anatolian Fault in the Gulf of Izmit (Turkey): Rapid vertical motion in response to minor bends of a nonvertical continental transform. J. Geophys. Res, 111 (B04102), doi:10.1029/2005JB003633.

Cornell, C.A., 1968. Engineering seismic risk analysis. Bull. Seism. Soc. Am., 58 (5), 1583-1606.

d'Alessio, M.A., Williams, C.F., Bürgmann, R., 2006. Frictional strength heterogeneity and surface heat flow: Implications for the strength of the creeping San Andreas fault. J. Geophys. Res, 111 (B05410), doi:10.1029/2005JB003780.

Delouis, B., Giardini, D., Lundgren, P., Salichon, J., 2002. Joint inversion of InSAR, GPS, teleseismic, and strong-motion data for the spatial and temporal distribution of earthquake slip: application to the 1999 Izmit mainshock. Bull. Seism. Soc. Am., 92 (1), 278-299.

Demirbağ, E., Rangin, C., Pichon, X.L., Şengör, A.M.C., 2003. Investigation of the tectonics of the Main Marmara Fault by means of deep-towed seismic data. Tectonophysics, 361 1-19 PII: S0040-1951(02)00535-8.

Deniz, R., Aksoy, A., Yalin, D., Seeger, H., Franke, P., Hirsch, O., Bautsch, P., 1993. Determination of crustal movements in Turkey by terrestrial geodetic methods. J. Geodymamics, 18 (1-4), 13-22.

Dhont, D., Chorowicz, J., Luxey, P., 2006. Anatolian escape tectonics driven by Eocene crustal thickening and Neogene–Quaternary extensional collapse in the eastern Mediterranean region. GSA Today, Special Paper 409 441–462 DOI: 10.1130/2006.2409(21).

Dietrich, M., Gürbüz, C., Brenguier, F., Karabulut, H., Bouchon, M., Aktar, M., 2004. A vibroseis seismic reflection campaign along the North Anatolian Fault. Geophys. Res. Abstr., 6 04520, SRef-ID: 1607-7962/gra/EGU04-A-04520.

Dilek, Y., Pavlides, S., 2006. Post-collisional tectonics and magmatism in the Mediterranean and Asia. Geol. Soc. of America, 409.

Doglioni, C., Agostini, S., Crespi, M., Innocenti, F., Manetti, P., Riguzzi, F., Savasçin, Y., 2002. On the extension in western Anatolia and the Aegean sea. J. of the Virtual Explorer, 7 167-181.

Dolu, E., Gökaşan, E., Meriç, E., Ergin, M., Görüm, T., Tur, H., Ecevitoğlu, B., Avşar, N., Görmüş, M., Batuk, F., Tok, B., Çetin, O., 2007. Quaternary evolution of the Gulf of İzmit (NW Turkey): a sedimentary basin under control of the North Anatolian Fault Zone. Geo. Mar. Lett., 27 (8), 355-381 doi:10.1007/s00367-007-0057-3.

Dresen, G., Bohnhoff, M., Aktar, M. Eyidogan, H., 2008. Drilling the North Anatolian Fault. Scientific Drilling, 6 58-59 doi:10.2204/iodp.sd.6.10.2008.

Eckert, A., Heidbach, O., Hergert, T., Buchmann, T., Peters, G., Müller, B. 2007. Karlsruhe recipe for an appropriate initial stress state in numerical geomecanical models – Part One: Theory. 2nd International Geoscientific Abaqus Workshop, Oct. 10-12, Potsdam.

Elmas, A., 2003. Late Cenozoic tectonics and stratigraphy of northwestern Anatolia: the effects of the North Anatolian Fault to the region. Int. J. Earth Sci (Geol Rundschau), 92 380–396 doi:10.1007/s00531-003-0322-2.

Elmas, A., Yiğitbaş, E., 2001. Ophiolite emplacement by strike-slip tectonics between the Pontide Zone and the Sakarya Zone in northwestern Anatolia, Turkey. Int. J. Earth Sci (Geol Rundschau), 90 257-269 doi:10.1007/s005310000129.

Emre, Ö., Erkal, T., Tchepalyga, A., Kazancı, N., Keçer, M., Ünay, E., 1998. Neogene-Quaternary evolution of the eastern Marmara region, northwest Turkey. Mineral. Res. Expl. Bull., 120 119-145.

Engdahl, E.R., Villasenor, A., 2002. Global Seismicity: 1900-1999. In: W.H.K. Lee, H. Kanamori, P.C. Jennings,C. Kisslinger (Editors), International Handbook of Earthquake and Engineering Seismology. Academic Press, pp. 665-690.

Engelder, T., Fischer, M.P., 1994. Influence of poroelastiv behavior on the magnitude of minimum horizontal stress, Sh, in overpressured parts of sedimentary basins. Geology, 22 949-952.

Erdik, M., 2000. Report on 1999 Kocaeli and Düzce (Turkey) earthquakes. http://www.koeri.boun.edu.tr/depremmuh/eqspecials/kocaeli/Kocaelireport.pdf.

Erdik, M., Biro, Y.A., Onur, T., Sesetyan, K., Birgoren, G., 1999. Assessment of earthquake hazard in Turkey and neighboring regions. Annali di Geofisica, 42 (6), 1125-1138.

Erdik, M., Demircioglu, M., Sesetyan, K., Durukal, E., Siyahi, B., 2004. Earthquake hazard in Marmara Region, Turkey. Soil Dynamics and Earthquake Engineering, 24 605-631.

Erdik, M., Doyuran, V., Akkaş, N., Gülkan, P., 1985. A probabilistic assessment of the seismic hazard in Turkey. Tectonophysics, 117 295-344.

Ergin, M., Kazanci, N., Varol, B., Ileri, Ö., Karadenzili, L., 1997. Sea-level changes and related depositional enviroments on the southern Marmara shelf. Marine Geol., 140 391-403 PII:S0025-3227(97)00029-7.

Ergintav, S., Doğan, U., Gerstenecker, C., Çakmak, R., Belgen, A., Demirel, H., Aydın, C., Reilinger, R., 2007. A snapshot (2003-2005) of the 3D postseismic deformation for the 1999, MW=7.4 İzmit earthquake in the Marmara Region, Turkey, by first results of joint gravity and GPS monitoring. J. Geodymamics.

Ergün, M., Özel, E., 1995. Structural relationship between the Sea of Marmara Basin and the North Anatolian Fault Zone. Terra Nova, 7 278-288.

Eyidoğan, H., 1988. Rates of crustal deformation in western Turkey as deduced from major earthquakes. Tectonophysics, 148 83-92.

Fabricius, I.L., 2006. Modeling Biot's Coefficient for High Porosity Sediments From P Wave Velocity and Density Data, American Geophysical Union, Fall Meeting, pp. abstract #H42B-06.

Faulkner, D.R., Rutter, E.H., 2001. Can the maintenance of overpressured fluids in large strike-slip fault zones explain their apparent weakness? Geology, 29 (6), 503-506 DOI: 10.1130/0091-7613(2001)029<0503:CTMOOF>2.0.CO;2.

Feigl, K.L., Sarti, F., Vadon, H., McClusky, S., Ergintav, S., Durand, P., Bürgmann, R., Rigo, A., Massonnet, D., Reilinger, R., 2002. Estimating slip distribution for the Izmit mainshock from coseismic GPS, ERS-1, RADARSAT, and SPOT measurements. Bull. Seism. Soc. Am., 92 (1), 138-160.

Flerit, F., Armijo, R., King, G., Meyer, B., 2004. The mechanical interaction between the propagating North Anatolian Fault and the back-arc extension in the Aegean. Earth Planet. Sci. Lett., 224 347-362 doi:10.1016/.epsl.2004.05.028.

Frankel, A., 1995. Mapping seismic hazard in the central and eastern United States. Seismol. Res. Lett., 66 (4), 8-21.

Fuchs, K. 2009. The Great Earthquakes of Lisbon 1755 and Aceh 2004 Shook the World. Seismologists' Societal Responsibility. in *The 1755 Lisbon Earthquake: Revisited.* Mendes-Victor, L. et al. , eds., Springer, pp.597.

Fulton, P.M., Saffer, D.M., Harris, R.N., Bekins, B.A., 2004. Re-evaluation of heat flow data near Parkfield, CA: Evidence for a weak San Andreas Fault. Geophys. Res. Lett., 31 L15S15, doi:10.1029/2003GL019378.

Gahalaut, K., Gahalaut, V.K., 2008. Stress triggering of normal aftershocks due to strike slip earthquakes in compressive regime. J. of Asian Earth Sciences, 33 379-382.

Gasperini, L., Armijo, R., Emre, O., 2003. How far did the surface rupture of the 1999 Izmit earthquake reach in Sea of Marmara? Geoph. Res. Abs., 5 (11367).

Geiss, E., 1987. A new compilation of crustal thickness data for the Mediterranean area. Ann. Geophys., 5B (6), 623-630.

Geist, E.L., Andrews, D.J., 2000. Slip rates on San Francisco Bay area faults from anelastic deformation of the continental lithosphere. J. Geophys. Res, 105 (11), 2 5,543-25,552.

Genç, H.T., Aydin, I., Demirel, S., Aygül, H., Akdogan, N., Kanat, H.I., Tufan, S., Konak, N., 1996. Ege Denizi ve Çevresinin Gravite ve Manyetik Yöntemlerle Arastirilmasi. Ulusal Deniz Jeolojisi ve Jeofizigi Programi (Unpublished Report)55.

Giardini, D., 1999. The Global Seismic Hazard Assessment Program (GSHAP): 1992-1999. Ann. Geofis., 42 957-974.

Gök, R., Pasyanos, M., Zor, E., 2007. Lithospheric structure of the continent-continent collision zone: eastern Turkey. Geophys. J. Int, 169 (3), 1079-1088.

Gökaşan, E., Gazioğlu, C., Alpar, B., Yücel, Z.Y., Ersoy, S., Gündoğdu, O., Yaltırak, C., Tok, B., 2002. Evidence of NW extension of the North Anatolian Fault Zone in the Marmara Sea: a new interpretation of the Marmara Sea (Izmit) earthquake on 17 August 1999. Geo-Mar Lett., 21 183–199 doi:10.1007/s00367-001-0088-0.

Gökaşan, E., Ustaömer, T., Gazioğlu, C., Yücel, Z.Y., Öztürk, K., Tur, H., Ecevitoğlu, B., Tok, B., 2003. Morpho-tectonic evolution of the Marmara Sea inferred from multi-beam bathymetric and seismic data. Geo-Mar Lett., 23 19-23 doi:10.1007/s00367-003-0120-7.

Görür, N., Okay, A.I., 1996. A fore-arc origin for the Thrace Basin, NW Turkey. Geol. Rundsch., 85 662-668.

Goto, H., Sawada, S., Morikawa, H., Kiku, H., Özalaybey, S., 2005. Modeling of 3D subsurface structure and numerical simulation of strong ground motion in the Adapazari Basin during the 1999 Kocaeli earthquake, Turkey. Bull. Seism. Soc. Am., 95 (6), 2197-2215.

Gross, S., Bürgmann, R., 1998. Rate and state of background stress estimated from the aftershocks of the 1989 Loma Prieta, California, earthquake. J. Geophys. Res, 103 (B3), 4915-4927.

Grünthal, G., 1984. Seismische Gefährdung. In: E. Hurtig,H. Stiller (Editors), Erdbeben und Erdbebengefährdung. Akademie-Verlag Berlin, Berlin, pp. 169-238.

Gülen, L., Pınar, A., Kalafat, D., Özel, N., Horasan, G., Yılmazer, M., Isıkara, A.M., 2002. Surface fault breaks, aftershock distribution, and rupture process of the 17 August 1999 Izmit, Turkey, earthquake. Bull. Seism. Soc. Am., 92 (1), 230-244.

Gürbüz, C., Aktar, M., Eyidoğan, H., Cisternas, A., Haessler, H., Barka, A., Ergin, M., Türkelli, N., Polat, O., Üçer, S.B., Kuleli, S., Baris, S., Kaypak, B., Bekler, T., Zor, E., Bicmen, F., Yoruk, A., 2000. The seismotectonics of the Marmara region (Turkey): results from a microseismic experiment. Tectonophysics, 316 1-17 PII: S0040-1951(99)00253-X.

Gürbüz, C., Bekler, T., Toksöz, M.N., Kuleli, H.S., Kalafat, D., Schultz, C.A., 2003. Sesismic refraction studies and crustal structure in Anatolia, Commission on Controlled-Source Seismology, 12th International Workshop, Mountain Lake, Virginia, pp. 74-78.

Gürbüz, C., Puskulcu, S., Ucer, S.B., 1992. A study of crustal structure in the Marmara region using earthquake data. In: A.M. Isıkara,Y. Honkura (Editors), Multidisciplinary research on fault activity in the western part of the NAF. B.U, pp. 29-41.

Haldar, A., Mahadevan, S., 2000. Reliability Assessment Using Stochastic Finite Element Analysis. John Wiley & Sons, Inc.

Hamiel, Y., Fialko, Y., 2007. Structure and mechanical properties of faults in the North Anatolian Fault system from InSAR observations of coseismic deformation due to the 1999 Izmit (Turkey) earthquake. J. Geophys. Res, 112 (B07412), doi:10.1029/2006JB004777.

Hanks, T., Kanamori, H., 1979. A moment magnitude scale. J. Geophys. Res, 84 2348-2350.

Hardebeck, J.L., Hauksson, E., 1999. Role of fluids in faulting inferred from stress field signatures. Science, 285 236-239.

Hatzfeld, D., Karagianni, E., Kassaras, I., Kiratzi, A., Louvari, E., Lyon-Caen, H., Makropoulos, K., Papadimitriou, P., Bock, G., Priestley, K., 2001. Shear wave anisotropy in the upper mantle beneath the Aegean related to internal deformation. J. Geophys. Res, 106 (B12), 30,737-30,753.

Hatzfeld, D., Ziazia, M., Kementzetzidou, D., Hatzidimintriou, P., Panagiotopoulos, D., Makropoulos, K., Papadimintriou, P., Deschamps, A., 1999. Microseismicity and focal mechanisms at the western termination of the North Anatolian Fault and their implications dor continental tectonics. Geophys. J. Int, 137 891-908.

Hearn, E.H., Hager, B.H., Reilinger, R.E., 2002. Viscoelastic deformation from North Anatolian Fault Zone earthquakes and the eastern Mediterranean GPS velocity field. Geophys. Res. Lett., 29 (0), 10.1029/2002GL014889.

Heidbach, O., Drewes, H., 2003. 3-D Finite Element model of major tectonic processes in the Eastern Mediterranean, in New insigths in structural interpretation and modelling. In: D. Nieuwland (Editor), Spec. Publs. Geol. Soc., London, pp. 259-272.

Heidbach, O., Reinecker, J., 2004. The World Stress Map Project - Stress Orientations Near Plate Boundaries From Focal Mechanisms, AGU Fall Meeting, San Francisco.

Hergert, T., Heidbach, O., 2006. New insights in the mechanism of postseismic stress relaxation exemplified by the June 23rd 2001 Mw = 8.4 earthquake in southern Peru. Geophys. Res. Lett., 33 (L02307), doi:1029/2005GL024585.

Hergert, T., Heidbach. O., 2007. Karlsruhe recipe for an appropriate initial stress state in numerical geomecanical models – Part Two: Application to the Sea of Marmara. 2nd International Geoscientific Abaqus Workshop, Oct. 10-12, Potsdam.

Hickman, S., Zoback, M.D., 2004. Stress orientations and magnitudes in the SAFOD Pilot Hole. Geophys. Res. Lett., 31 L15S12, doi:10.1029/2004GL020043.

Hillers, G., Wesnousky, S.G., 2008. Scaling relations of strike-slip earthquakes with different slip-rate-dependent properties at depth. Bull. Seism. Soc. Am., 98 (3), 1085-1101.

Holdsworth, R.E., 2004. Weak faults-Rotten cores. Science, 303 181-182.

Horasan, G., Gülen, L., Pınar, A., Kalafat, D., Özel, N., Kuleli, H.S., Işıkara, A.M., 2002. Lithospheric Structure of the Marmara and Aegean Regions, Western Turkey. Bull. Seism. Soc. Am., 92 (1), 322-329.

Horasan, G., Güney, A.B., Küsmezer, A., Bekler, F., Öğütçü, Z., Musaoğlu, N., 2009. Contamination of seismicity catalogs by quarry blasts: An example from _Istanbul and its vicinity, northwestern Turkey. J. of Asian Earth Sciences, 34 90-99.

Hubert-Ferrari, A., Armijo, R., King, G., Meyer, B., Barka, A., 2002. Morphology, displacement, and slip rates along the North Anatolian Fault, Turkey. J. Geophys. Res, 107 (10), 2235, doi:10.1029/2001JB000393.

Hubert-Ferrari, A., Barka, A., Jacques, E., Nalbant, S., Meyer, B., Armijo, R., Tapponier, P., King, G.C.P., 2000. Seismic hazard in the Marmara Sea region following the 17 August 1999 Izmit earthquake. Nature, 404 269-271.

Hubert-Ferrari, A., King, G., Manighetti, I., Armijo, R., Meyer, B., Tapponnier, P., 2003. Long-term elasticity in the continental litosphere; modelling the Aden Ridge propagation and the Anatolian extrusion process. Geophys. J. Int., 153 111-132.

Hurtig, E., Cermák, V., Haenel, R., Zui, V., 1991. Geothermal Atlas of Europe.

IEMP, 2003. Earthquake Masterplan for Istanbul, Metropolitan Municipality of Istanbul, Planning and Construction Directoriat, Geotechnical and Earthquake Investigation Department, Bogazici University, Istanbul Technical University, Middle East Technical University, Yildiz Technical University, Istanbul.

İmren, C., Le Pichon, X., Rangin, C., Demirbağ, E., Ecevitoğlu, B., Görür, N., 2001. The North Anatolian Fault within the Sea of Marmara: a new interpretation based on multi-channel seismic and multi-beam bathymetry data. Earth Planet. Sci. Lett., 186 143-158 PII:S0012-821X(01)00241-2.

Inan, S., Ergintav, S., Saatçılar, R., Tüzel, B., İravul., Y. 2007. Turkey makes major investment in earthquake research. EOS, Transactions, AGU, 88 (34), 21 Aug.

Ito, A., Üçer, B., Barış, S., Nakamura, A., Honkura, Y., Kono, T., Hori, S., Hasegawa, A., R., P., Işıkara, A.M., 2002. Aftershock Activity of the 1999 I˙zmit, Turkey, Earthquake Revealed from Microearthquake Observations. Bull. Seism. Soc. Am., 92 (1), 418–427.

Jackson, J.A., 1994. Active tectonics of the Mediterranean region. Annual Rev. of Earth Planet. Sci.239-271.

Jaeger, J.C., Cook, N.G.W., 1969. Fundamentals of Rock Mechanics. Methuen & Co., London.

Jamison, D.B., Cook, N.G.W., 1980. Note on Measured Values for the State of Stress in the Earth's Crust. J. Geophys. Res, 85 1833-1838.

Jiménez-Munt, I., Sabadini, R., 2002. The block-like behavior of Anatolia envisaged in the modeled and geodetic strain rates. Geophys. Res. Lett., 29 (20), 1978, doi:10.1029/2002GL015995.

Jiménez-Munt, I., Sabadini, R., Gardi, A., Bianco, G., 2003. Active deformation in the Mediterranean from Gibraltar to Anatolia inferres from numerical modeling and geodetic and seismological data. Journal of Geophysical Reasearch, 108 (B1), 2006, doi:10.1029/2001JB001544.

Jónsson, S., Segall, P., Pedersen, R., Björnsson, G., 2003. Post-earthquake ground movements correlated to pore-pressure transients. Nature, 424 170-183.

Kagan, Y.Y., Jackson, D.D., 1994. Long-term probabilistic forecasting of earthquakes. J. Geophys. Res, 99 (B7), 13,685-13,700.

Kahle, H.-G., Cocard, M., Peter, Y., Geiger, A., Reilinger, R., Barka, A., Veis, G., 2000. GPS-derived strain rate field within the boundary zones of the Eurasian, African, and Arabian Plates. J. Geophys. Res., 105 (B10), 23,353-23,370.

Kalkan, E., Gülkan, P., Yılmaz Öztürk, N., Çelebi, M., 2008. Seismic hazard in the Istanbul metropolitan area: a preliminary re-evaluation. J. Earthquake Engineering, 12 (S2), 151-164.

Kalkan, E., Gülkan, P., Yılmaz Öztürk, N., Çelebi, M., in press. Re-Examination of probabilistic seismic hazard in the Marmara region. Bull. Seism. Soc. Am.,

Kanbur, Z., Alptekin, Ö., Utkucu, M., Kanbur, S., 2007. Imaging the basin and fault geometry from the multichannel seismic reflection data in the Tekirdağ Basin, Marmara Sea, Turkey. Geophys. J. Int, 169 659-666 doi:10.1111/j.1365-246X.2007.03356.x.

Karabulut, H., Bouin, M.-P., Bouchon, M., Dietrich, M., Cornou, C., Aktar, M., 2002. The Seismicity in the Eastern Marmara Sea after the 17 August 1999 İzmit Earthquake. Bull. Seism. Soc. Am., 92 (1), 387-393.

Karabulut, H., Özalaybey, S., Taymaz, T., Aktar, M., Selvi, O., Kocaoğlu, A., 2003. A tomographic image of the shallow crustal structure in the Eastern Marmara. Geophys. Res. Lett., 30 (24), doi:10.1029/2003GL018074.

Karagianni, E.E., Papazachos, C.B., Panagiotopoulos, D.G., Suhadolc, P., Yuan, A., Panza, G.F., 2005. Shear velocity structure in the Aegean area obtained by inversion of Rayleigh waves. Geophys. J. Int, 160 127-143.

Karakaisis, G.F., Papazachos, C.B., Scordilis, E.M., Papazachos, B.C., 2004. Current accelerating seismic excitation along the northern boundary of the Aegean microplate. Tectonophysics, 383 81-89 doi:10.1016/j.tecto.2004.03.005.

King, G., Hubert-Ferrari, A., Nalbant, S.S., Meyer, B., Armijo, R., Bowman, D., 2001. Coulomb interactions and the 17 August 1999 Izmit, Turkey earthquake. Earth Planet. Sci. Lett., 333 557-569.

King, G.C.P., Stein, R.S., Lin, J., 1994. Static Stress Changes and the Triggering of Earthquakes. Bull. Seism. Soc. Am., 84 935-953.

King, G.C.P., Wesnousky, S.G., 2007. Scaling of fault parameters for continental strike-slip earthquakes. Bull. Seism. Soc. Am., 97 (6), 1833-1840.

Kiratzi, A., 1993. A study on the active crustal deformation of the North and East Anatolian Fault Zones. Tectonophysics, 225 191-203.

Kiratzi, A.A., 2002. Stress tensor inversions along the westernmost North Anatolian Fault Zone and its continuation into the North Aegean Sea. Geophys. J. Int., 151 360-376.

Kiratzi, A.A., Papazachos, C.B., 1995. Active crustal deformation from the Azores triple junction to the Middle East. Tectonophysics, 243 1-24 SSDI 0040-1951(94)00188-X.

Klingele, E., Medici, F., 1997. Gravimetric Studies of the Marmara Sea Region, Active Tectonics of Northwestern Anatolia. In: C. Schindler,M. Pfister (Editors), The Marmara Poly -Project, pp. 487-501.

Klinger, Y., Sieh, K., Altunel, E., Akoglu, A., Barka, A., Dawson, T., Gonzalez, T., Meltzner, A., Rockwell, T., 2003. Paleoseismic evidence of characteristic slip on the western segment of the North Anatolian Fault, Turkey. Bull. Seism. Soc. Am., 93 (6), 2317-2332.

Knopoff, L. 1999. Earthquake prediction is difficult but not impossible. Nature Debates, 11 March.

Koçyığıt, A., Özacar, A.A., 2003. Extensional Neotectonic Regime through the NE Edge ofthe Outer Isparta Angle, SW Turkey: New Field and Seismic Data. Turkish J. Earth Sci., 12 67-90.

Koral, H., 2007. Modes, rates and geomorphological consequences of active tectonics in the Marmara Region, NW Turkey - A critical overview based on seismotectonic field observations. Quaternary International, 167-168 149–161 doi:10.1016/j.quaint.2007.02.023.

Koravos, G.C., Main, I.G., Tsapanos, T.M., Musson, R.M.W., 2003. Perceptible earthquakes in the broad Aegean area. Tectonophysics, 371 175– 186 doi:10.1016/S0040-1951(03)00216-6.

Kozacı, Ö., Dolan, J.F., Finkel, R., Hartleb, R., 2007. Late Holocene slip rate for the North Anatolian fault, Turkey, from cosmogenic ^{36}Cl geochronology: Implications for the constancy of fault loading and strain release rates. Geology, 35 (10), 867-870 DOI: 10.1130/G23187A.1.

Kozacı, Ö., Dolan, J.F., Finkel, R.C., in press. A Late Holocene slip rate for the central North Anatolian fault, at Tahtaköprü, Turkey, from cosmogenic ^{10}Be geochronology: Implications for fault loading and strain release rates. J. Geophys. Res.

Kreemer, C., Chamot-Rooke, N., 2004. Contemporary kinematics of the southern Aegean and the Mediterranean Ridge. Geophys. J. Int., 157 1377-1392 doi:10.1111/j.1365-246X.2004.02270.x.

Kudo, K., Kanno, T., Okada, H., Özel, O., Erdik, M., Sasatani, T., Higashi, S., Takahashi, M., Yoshida, K., 2002. Site-specific issues for strong ground motions during the Kocaeli, Turkey, earthquake of 17 August 1999, as inferred from array observations of microtremors and aftershocks. Bull. Seism. Soc. Am., 92 (1), 448–465.

Kürçer, A., Chatzipetros, A., Tutkun, S.Z., Pavlides, S., Ate, Ö., Valkaniotis, S., 2008. The Yenice – Gönen active fault (NW Turkey): active tectonics and palaeoseismology. Tectonophysicsdoi:10.1016/j.tecto.2007.07.010.

Kurtuluş, C., Canbay, M.M., 2007. Tracing the middle strand of the North Anatolian Fault Zone through the southern Sea of Marmara based on seismic reflection studies. Geo-Mar Lett., 27 27-40 doi:10.1007/s00367-006-0050-2.

Lachenbruch, A.H., Sass, J.H., 1980. Heat flow and energetics of the San Andreas fault zone. J. Geophys. Res, 85 6185-6222.

Laigle, M., Becél, A., de Voogd, B., Hirn, A., Taymaz, T., Özalaybey, S., Team, S.L., 2008. A first deep seismic survey in the Sea of Marmara: Deep basins and whole crust architecture and evolution. Earth Planet. Sci. Lett., 270 168-179.

Lamb, S., 2006. Shear stresses on megathrusts: Implications for mountain building behind subduction zones. J. Geophys. Res., 111 (B07401), doi:10.1029/2005JB003916.

Larsen, C.F., Motyka, R.J., Freymueller, J.T., Echelmeyer, K.A., Ivins, E.R., 2005. Rapid viscoelastic uplift in southeast Alaska caused by post-Little Ice Age glacial retreat. Earth Planet. Sci. Lett., 237 548-560.

Le Pichon, X., Chamot-Rooke, N., Lallemant, S., Noomen, R., Veis, G., 1995. Geodetic determination of kinematics of Central Greece with respect to Europe: Implications for Eastern Mediterranean. J. Geophys. Res, 100 12675-12690.

Le Pichon, X.L., Chamot-Rooke, A., Rangin, C., Şengör, A.M.C., 2003. The North Anatolian fault in the Sea of Marmara. J. Geophys. Res., 108 (B4), 2179, doi:10.1029/2002JB001862.

Le Pichon, X.L., Kreemer, C., 2005. Asymmertry in elastic properties and evolution of large continental strike-slip faults. Journal of Geophysical Reasearch, 110 (B03405), doi:10.1029/2004JB003343.

Le Pichon, X.L., Şengör, A.M.C., Demirbağ, E., Rangin, C., İmren, C., Armijo, R., Görür, N., Çağatay, N., Lepinay, B.M.d., Meyer, B., Saatçılar, R., Tok, B., 2001. The active Main Marmara Fault. Earth Planet. Sci. Lett., 192 595-616 PII:S0012-821X(01)00449-6.

Lenk, O., Türkezer, A., Ergintav, S., Kurt, A.I., Belgen, A., 2003. Monitoring the kinematics of Anatolia using permanent GPS network stations. Turkish J. Earth Sci., 12 55-65.

Li, X., Bock, G., Vafidis, A., Kind, R., Harjes, H.-P., Hanka, W., Wylegalla, K., Van der Meijde, M., Yuan, X., 2003. Receiver function study of the Hellenic subduction zone: imaging crustal thickness variations and the oceanic Moho of the descending African lithosphere. Geophys. J. Int, 155 733-748.

Liu, Z., Bird, P., 2002. Finite element modeling of neotectonics in New Zealand. J. Geophys. Res, 107 (12), 2328, doi:10.1029/2001JB001075.

Lorenzo-Martin, F., Roth, F., Wang, R., 2006. Elastic and inelastic triggering of earthquakes in the North Anatolian Fault zone. Tectonophysics, 424 271-289 doi:10.1016/j.tecto.2006.03.046.

Ludwig, W.J., Nafe, J.E., Drake, C.L., 1970. Seismic refraction. In: A.E. Maxwell (Editor), The Sea. Wiley-Interscience, New York, pp. 53-84.

Lund, B., Townend, J., 2007. Calculating horizontal stress orientations with full or partial knowledge of the tectonic stress tensor. Geophys. J. Int, 170 1328-1335 doi:10.1111/j.1365X.2007.03468.x.

Makris, J., 1978. Some geophysical considerations in the ggeodynamic situation in Greece. Tectonophysics, 46 251-268.

Makris, J., 1985. Geophysics and geodynamic implications for the evolution of the Hellenides. In: D. Stanley,F. Wezel (Editors), Geological Evolution of the Mediterranean Basin, Berlin, pp. 231-248.

Manighetti, I., Campillo, M., Bouley, S., Cotton, F., 2007. Earthquake scaling, fault segmentation, and structural maturity. Earth Planet. Sci. Lett., 253 429–438 doi:10.1016/j.epsl.2006.11.004.

Masterlark, T., Wang, H.F., 2002. Transient stress-coupling between the 1992 Landers and 1999 Hector Mine earthquakes. Bull. Seism. Soc. Am., 92 1470-1486.

Matthews, M.V., Ellsworth, W.L., Raesenberg, P.A., 2002. A Brownian model for recurrent earthquakes. Bull. Seism. Soc. Am., 92 (6), 2233-2250.

McClusky, S., Balassananian, S., Barka, A., Demir, C., Ergintav, S., Georgiev, I., Gurkan, O., Hamburger, M., Hurst, K., Kahle, H.G., Kastens, K., Kekelidze, G., King, R., Kotzev, V., Lenk, O., Mahmoud, S., Mishin, A., Nadariya, M., Ouzounis, A., Paradissis, D., Peter, Y., Prilepin, M., Reilinger, R., Sanli, I., Seeger, H., Tealeb, A., Toksöz, M.N., Veis, G., 2000. Global Positioning System constraints on plate kinematics and dynamics in the eastern Mediterranean and Caucasus. J. Geophys. Res, 105 (B3), 5695-5719.

McClusky, S., Reilinger, R., Mahmoud, S., Ben Sari, D., Tealeb, A., 2003. GPS constraints on Africa (Nubia) and Arabia plate motions. Geophys. J. Int, 155 (1), 126-138(13).

McGarr, A., 1988. On the state of lithospheric stress in the absence of apllied tectonic forces. J. Geophys. Res, 93 (B11), 13,609-13,617.

McGuire, R., 1993. Computations of seismic hazard. Ann. Geofis., 36 (3-4), 181-200.

McHugh, C.M.G., Seeber, L., Cormier, M.-H., Dutton, J., Cagatay, N., Polonia, A., Ryan, W.B.F., Gorur, N., 2006. Submarine earthquake geology along the North Anatolia Fault in the Marmara Sea, Turkey: A model for transform basin sedimentation. Earth Planet. Sci. Lett., 248 661-684 doi:10.1016/j.epsl.2006.05.038.

McKenzie, D.P., 1972. Active tectonics of the Mediterranean region. Geophys. J. R. astr. Soc., 30 109-185.

Meade, B.J., Hager, B.H., McClusky, S.C., Reilinger, R., Ergintav, S., Lenk, O., Barka, A., Özener, H., 2002. Estimates of Seismic Potential in the Marmara Sea Region from Block Models of Secular Deformation Constrained by GPS Measurements. Bull. Seism. Soc. Am., 92 208-215.

Meghraoui, M., Akyüz, S., Ferry, M., Altunel, E., Dikbas, A., Uçarkus, G., Çakır, Z., Sorensen, M., Pantosti, D., Pucci, S., Yalciner, C., Zabci, G., 2004. Faulting behaviour along the 1912 Ganos Fault segment west of the Marmara Sea: Results from paleoseismic investigations. Geoph. Res. Abs.EGU04-A-06211-1.

Meissner, R., Wever, T., E, F., 1987. The Moho in Europe – Implications for crustal development. Geophysicae, 5B 357-364.

Motagh, M., Hoffmann, J., Kampes, B., Baes, M., Zschau, J., 2007. Strain accumulation across the Gazikoy–Saros segment of the North Anatolian Fault inferred from Persistent Scatterer Interferometry and GPS measurements. Earth Planet. Sci. Lett., 255 432-444.

Muller, J.R., Aydin, A., 2004. Rupture progression along discontinuous oblique fault sets: implications for the Karadere rupture segment of the 1999 Izmit earthquake, and future rupture in the Sea of Marmara. Tectonophysics, 391 283-302 doi:10.1016/j.tecto.2004.07.017.

Muller, J.R., Aydin, A., 2005. Using mechanical modeling to constrain fault geometries proposed for the northern Marmara Sea. J. Geophys. Res, 110 (B03407), doi:10.1029/2004JB003226.

Muller, J.R., Aydin, A., Maerten, F., 2003. Investigating the transition between the 1967 Mudurnu Valley and 1999 Izmit earthquakes along the North Anatolian fault with static stress changes. Geophys. J. Int., 154 471-482.

Muller, J.R., Aydin, A., Wright, T.J., 2006. Using an elastic dislocation model to investigate static Coulomb stress change scenarios for earthquake ruptures in the eastern Marmara Sea region, Turkey. In: S.J.H. Buiter,G. Schreuers (Editors), Analogue and Numerical Modelling of Crustal-Scale Processes. Special Publication. Geological Society, Londong, pp. 397-414.

Nalbant, S.S., Hubert, A., King, G.C.P., 1998. Stress Coupling Between Earthquakes in Northwest Turkey and the North Aegean Sea. J. Geophys. Res., 103 24469-24486.

Necioglu, A., Maddison, B., Türkelli, N., 1981. A study of crustal and upper mantle structure of northwestern Turkey. Geophys. Res. Lett., 8 33-35.

Nishenko, S.P., Buland, R., 1987. A generic recurrence interval distribution for earthquake forecasting. Bull. Seism. Soc. Am., 77 (4), 1382-1399.

Noomen, R., Springer, T.A., Ambrosius, B.A.C., Herzberger, K., Kuijper, D.C., Mets, G.-J., Overgaauw, B., Wakker, K.F., 1996. Crustal deformations in the Mediterranean area computed from SLR and GPS observations. J. Geodymamics, 21 (1), 73-96.

Nyst, M., Thatcher, W., 2004. New constraints on the active tectonic deformation of the Aegean. J. Geophys. Res, 109 (B11406), doi:10.1029/2003JB002830.

Ocakoğlu, F., 2007. A re-evaluation of the Eskişehir Fault Zone as a recent extensional structure in NW Turkey. J. of Asian Earth Sciences, 31 91–103 doi:10.1016/j.jseaes.2007.05.002.

Oglesby, D.D., Mai, P.M., Atakan, K., Pucci, S., 2008. Dynamic models of earthquakes on the North Anatolian fault zone under the Sea of Marmara: Effect of hypocenter location. Geophys. Res. Lett., 35 (L18302), doi:10.1029/2008GL035037.

Okay, A.I., Demirbağ, E., Kurt, H., Okay, N., Kuşçu, İ., 1999. An active deep marine strike-slip basin along the North Anatolian fault in Turkey. Tectonics, 18 (1), 129-147.

Okay, A.I., Kaşlılar-Özcan, A., İmren, C., Boztepe-Güney, A., Demirbağ, E., Kuşçu, İ., 2000. Active faults and evolving strike-slip basins in the Marmara Sea, northwest Turkey: a multichannel seismic reflection study. Tectonophysics, 321 189-218 PII:S0040-1951(00)00046-9.

Okay, A.I., M., S., M., Z., W., C., G., T., 2008. An Oligocene ductile strike-slip shear zone: The Uludağ Massif, northwest Turkey—Implications for the westward translation of Anatolia. GSA Bulletindoi: 10.1130/B26229.1.

Okay, A.I., Satır, M., Tüysüz, O., Akyüz, H.S., Chen, F., 2001a. The tectonics of the Strandja Massif: late-Variscan and mid-Mesozoic deformation and metamorphismin the northern Aegean. Int. J. Earth Sci (Geol Rundschau), 90 217-233 doi: 10.1007/s005310000104.

Okay, A.I., Tansel, Z., Tüysüz, O., 2001b. Obduction, subduction and collision as reflected in the Upper Cretaceous–Lower Eocene sedimentary record of western Turkey. Geol. Mag., 138 (2), 117–142.

Okay, A.I., Tüysüz, O., 1999. Tethyan sutures of northern Turkey. Geol. Soc., London, Spec. Publ., 156 (DOI: 10.1144/GSL.SP.1999.156.01.22), 475-515.

Okay, N., Ergün, B., 2005. Source of the basinal sediments in the Marmara Sea investigated using heavy minerals in the modern beach sands. Marine Geol., 216 (1-2), 1-15.

Okay, N., Okay, A.I., 2002. Tectonically induced Quaternary drainage diversion in the northeastern Aegean. J. Geol. Soc.Lond, 159 393-399.

Oktay, F.Y., Gökaşan, E., Sakınç, M., Yaltırak, C., C., I., Demirbağ, E., 2002. The e¡ects of the North Anatolian Fault Zone on the latest connection between Black Sea and Sea of Marmara. Marine Geol., 190 367-382.

Olsen, K.B., Day, S.M., Minster, J.B., Cui, Y., Chourasia, A., Okaya, D., Maechling, P., Jordan, T., 2008. TeraShake2: Spontaneous rupture simulations of M_w 7.7 earthquakes on the southern San Andreas Fault. Bull. Seism. Soc. Am., 98 (3), 1162-1185.

Öncel, A.O., Wilson, T., 2004. Correlation of seismotectonic variables and GPS strain measurements in western Turkey. J. Geophys. Res, 109 (B11306), doi:10.1029/2004JB003101.

Öncel, A.O., Wilson, T., 2006. Evaluation of earthquake potential along the Northern Anatolian Fault Zone in the Marmara Sea using comparisons of GPS strain and seismotectonic parameters. Tectonophysics, 418 205-218 doi:10.1016/j.tecto.2006.02.006.

Oral, M.B., Reilinger, R., Toksöz, M.N., King, R.W., Barka, A., al., e., 1995. Global Positioning System offers evidence of plate motions in the eastern Mediterranean. Eos, Trans. Am. Geophys. Union, 76 (2), 9-11.

Örgülü, G., Aktar, M., 2001. Regional Moment Tensor Inversion for Strong Aftershocks of the August 17, 1999 İzmit Earthquake (MW=7.4). Geophys. Res. Lett., 28 (2), 371-374.

Özaksoy, V., Emre, Ö., Doğan, B., Yıldırım, C., Özalp, S., Tokay, F., 2006. Late Holocene uplift of the Hersek Ridge on the restraining bend of NAFS, International Workshop in Comparative Studies of the North Anatolian Fault and the San Andreas Fault, Istanbul, pp. 77.

Özalaybey, S., Ergin, M., Aktar, M., Tapırdamaz, C., Biçmen, F., Yörük, A., 2002. The 1999 İzmit Earthquake Sequence in Turkey: Seismological and Tectonic Aspects. Bull. Seism. Soc. Am., 92 (1), 376-386.

Öztürk, K., Yaltırak, C., Alpar, B., in press. Relationship Between The Tectonic Setting of Lake İznik Basin and North Anatolian Fault Middle Strand. Turkish J. Earth Sci.

Papadimitriou, E.E., Karakostas, V.G., Papazachos, B.C., 2001. Rupture zones in the area of the 17.08.99 Izmit (NW Turkey) large earthquake (M_w 7.4) and stress changes caused by its generation. J. of Seismol., 5 269-276.

Papazachos, B.C., Karakostas, V.G., Papazachos, C.B., Scordilis, E.M., 2000. The geometry of the Wadati-Benioff zone and lithospheric kinematics in the Hellenic arc. Tectonophysics, 319 275-300.

Papazachos, B.C., Kiratzi, A.A., 1996. A detailed study of the active crustal deformation in the Aegean and surrounding area. Tectonophysics, 253 129-153.

Papazachos, C.B., 1999. Seismological and GPS evidence for the Aegean-Anatollia interaction. Geophys. Res. Lett., 26 (17), 2653-2656.

Papazachos, C.B., Hatzidimitriou, P.M., Panagiotopoulos, D.G., Tsokas, G.N., 1995. Tomography of the crust and upper mantle in southeast Europe. J. Geophys. Res, 100 12,405–12,422.

Parke, J.R., White, R.S., McKenzie, D., Minshull, T.A., Bull, J.M., Kuşçu, I., Görür, N., Şengör, C., 2002. Interaction between faulting and sedimentation in the Sea of Marmara, western Turkey. Journal of Geophysical Reasearch, 107 (B11), doi:10.1029/2001JB000450.

Parsons, T., 2002. Nearly frictionless faulting by unclamping in long-term interaction models. Geology, 30 (12), 1063-1066.

Parsons, T., 2004. Recalculated probability of M>=7 earthquakes beneath the Sea of Marmara, Turkey. J. Geophys. Res., 109 (B05304), doi:10.1029/2003JB002667.

Parsons, T., 2005. Signifcance of stress transfer in time-dependent earthquake probability calculations. Journal of Geophysical Reasearch, 110 (B05S02), doi:10.1029/2004JB003190.

Parsons, T., Toda, S., Stein, R.S., Barka, A., Dieterich, J.H., 2000. Heightened odds of large Earthquakes near Istanbul: An interaction-based Probability calculatin. Science, 288 661-664.

Pavlides, S.B., Chatzipetros, A., Tutkun, Z.S., Özaksoy, V., Doğan, B., 2006. Evidence for late Holocene activity along the seismogenic fault of the 1999 Izmit earthquake, NW Turkey. Geol. Soc., London, Spec. Publ., 260, 635-647.

Peyrat, S., Olsen, K., Madariaga, R., 2001. Dynamic modeling of the 1992 Landers earthquake. J. Geophys. Res, 106 (B11), 26,467-26,482.

Pfister, M., Rybach, L., Simsek, S., 1998. Geothermal reconnaissance of the Marmara Sea region (NW Turkey): surface heat flow density in an area of active continental extension. Tectonophysics, 291 77-89 PII S0040-1951(98)00032-8.

Pınar, A., Honkura, Y., Kikuchi, M., 1996. A rupture model for the 1967 Mudurnu Valley, Turkey earthquake and its implication for seismotectonics in the western part of the North Anatolian Fault Zone. Geophys. Res. Lett., 23 (1), 29-32.

Pınar, A., Kuge, K., Honkura, Y., 2003. Moment tensor inversion of recent small to moderate sized earthquakes: implications for seismic hazard and active tectonics beneath the Sea of Marmara. Geophys. J. Int, 153 133-145.

Polat, O., Eyidogan, H., Haessler, H., Cisternas, A., Philip, H., 2002a. Analysis and interpretation of the aftershock sequence of the August 17, 1999, Izmit (Turkey) earthquake. J. of Seismol., 6 287–306.

Polat, O., Haessler, H., Cisternas, A., Philip, H., Eyidoğan, H., Aktar, M., Frogneux, M., Comte, D., Gürbüz, C., 2002b. The Izmit (Kocaeli), Turkey Earthquake of 17 August 1999: Previous Seismicity, Aftershocks, and Seismotectonics. Bull. Seism. Soc. Am., 92 (1), 361-375.

Pollitz, F.F., 2003. Transient Rheology of the Uppermost Mantle Beneath the Mojave Desert. Earth Planet. Sci. Lett., 215 89-104.

Pollitz, F.F., Wicks, C., Thatcher, W., 2001. Mantle Flow Beneath a Continental Strike-Slip Fault: Postseismic Deformation After the 1999 Hector Mine Earthquake. Science, 293 1814-1817.

Polonia, A., Gasperini, L., Amorosi, A., Bonatti, E., Bortoluzzi, G., Çağatay, M.N., Capotondi, L., Cormier, M.-H., Görür, N., McHugh, C.M.G., Seeber, L., 2004. Holocene slip rate of the North Anatolian Fault beneath the Sea of Marmara. Earth Planet. Sci. Lett., 227 411-426.

Pondard, N., Armijo, R., King, G.C.P., Meyer, B., Flerit, F., 2007. Fault interactions in the Sea of Marmara pull.apart (North Anatolian Fault): earthquake clustering and propagating earthquake sequences. Geophys. J. Intdoi:10.1111/j.1365-246X.2007.03580.x.

Pondrelli, S., Morelli, A., Ekström, G., 2004. European-Mediterranean regional centroid-moment tensor catalog: solutions for years 2001 and 2002. Physics of the Earth's Interiors, 145 127-147.

Pondrelli, S., Salimbeni, S., Morelli, A., Ekström, G., Boschi, E., 2007. European–Mediterranean Regional Centroid Moment Tensor catalog: Solutions for years 2003 and 2004. Physics of the Earth's Interiors, 164 90-112.

Provost, A.-S., Chéry, J., Hassani, R., 2003. 3D mechanical modeling of the GPS velocity field along the North Anatolian fault. Earth Planet. Sci. Lett., 209 361-377 doi:10.1016/S0012-821X(03)00099-2.

Pulido, N., Ojeda, A., Atakan, K., Kubo, T., 2004. Strong ground motion estimation in the Sea of Marmara region (Turkey) based on a scenario earthquake. Tectonophysics, 391 357-374.

Raesenberg, P.A., Simpson, R.W., 1992. Response of regional seismicity to the static stress change produced by the Loma Prieta earthquake. Science, 255 1687-1690.

Ramberg, H., 1981. Gravity, deformation and the Earth’s crust. Academic Press.

Rangin, C., Pichon, X.L., Demirbag, E., Imren, C., 2004. Strain localization in the Sea of Marmara: Propagation of the North Anatolian Fault in a now inactive pull-apart. Tectonics, 23 TC2014, doi:10.029/2002TC001437.

Reid, H.F., 1910. The Mechanics of the Earthquake, The California Earthquake of April 18, 1906. vol. 2, Carnegie Institution of Washington, Washington.

Reilinger, R., McClusky, S., Oral, M.B., King, R.W., Toksöz, M.N., Barka, A., Kinik, I., Lenk, O., Sanli, I., 1997. Global Positioning System measurements of present-day crustal movements in the Arabia-Africa-Eurasia plate collision zone. J. Geophys. Res, 102 (B5), 9983-9999.

Reilinger, R., McClusky, S., Vernant, P., Lawrence, S., Ergintav, S., Cakmak, R., Ozener, H., Kadirov, F., Guliev, I., Stepanyan, R., Nadariya, M., Hahubia, G., Mahmoud, S., Sakr, K., ArRajehi, A., Paradissis, D., Al-Aydrus, A., Prilepin, M., Guseva, T., Evren, E., Dmitrosta, A., Filikov, S.V., Gomez, F., Al-Ghazzi, R., Karam, G., 2006. GPS constraints on continental deformation in the Africa-Arabia-Eurasia continental collision zone and implications for the dynamics of plate interaction. J. Geophys. Res., 111 (B05411), doi:10.1029/2005JB004051.

Reilinger, R.E., Ergintav, S., Bürgmann, R., McClusky, S., Lenk, O., Barka, A., Gurkan, O., Hearn, L., Feigl, K.L., Cakmak, R., Aktug, B., Ozener, H., Töksoz, M.N., 2000. Coseismic and Postseismic Fault Slip for the 17 August 1999, M=7.5, Izmit, Turkey Earthquake. Science, 289 1519-1524 doi:10.1126/science.289.5484.1519.

Reinecker, J., Heidbach, O., Tingay, M., Sperner, B., Müller, B., 2005. The 2005 release of the World Stress Map. http://www.world-stress-map.org.

Rice, J.R., 1992. Fault stress states, pore pressure distributions, and the weakness of the San Andreas fault. In: B. Evans,T.F. Wong (Editors), Earthquake Mechanics and Transport Properties of Rocks. Academic Press, London, pp. 475-503.

Richter, C.F., 1958. New Dimensions in Seismology: Earthquakes are characterized by geographical position, instant of occurrence, depth, and magnitude. Science, 128 175-182 doi:10.1126/science.128.3317.175.

Robertson, A.H., Mountrakis, D., 2006. Tectonic development of the eastern Mediterranean region. Special Publications, 260. Geol. Soc., London.

Robertson, A.H., Ustaömer, T., 2004. Tectonic evolution of the Intra-Pontide suture zone in the Armutlu Peninsula, NW Turkey. Tectonophysics, 381 175-209.

Rockwell, T., Barka, A., Dawson, T., Akyuz, S., Thorup, K., 2001. Paleoseismology of the Gazikoy-Saros segement of the North Anatolia fault, northwestern Turkey: Comparison of the historical and paleoseismic records, implications of regional seismic hazard, and models of earthquake recurrence. Journal of Seismology, 5 433-448.

Rockwell, T.K., Okumura, K., Duman, T., Rogona, D., Seitz, G., Awata, Y., Uçarkus, G., Aksoy, M.E., Ferry, M., Meghraoui, M., 2006. Paleoseismology of the 1912, 1944 and 1999 ruptures on the North Anatolian fault: Implications for late Holocene patterns of strain release, International Workshop in Comparative Studies of the North Anatolian Fault and the San Andreas Fault, Istanbul, pp. 11-12.

Romanowicz, B., Ruff, L.J., 2002. On moment-length scaling of large strike slip earthquakes and the strength of faults. Geophys. Res. Lett., 29 (12), 10.1029/2001GL014479.

Sadigh, K., Chang, C.Y., Egan, J.A., Makdisi, F., Youngs, R.R., 1997. Attenuation relationships for shallow crustal earthquakes based on Californian strong motion data. Seismol. Res. Lett., 68 180-189.

Sato, T., Kasahara, J., Taymaz, T., Ito, M., Kamimura, A., Hayakawa, T., Tan, O., 2004. A study of microearthquake seismicity and focal mechanisms within the Sea of Marmara (NW Turkey) using ocean bottom seismometers (OBSs). Tectonophysics, 391 303– 314 doi:10.1016/j.tecto.2004.07.018.

Saunders, P., Priestley, K., Taymaz, T., 1998. Variations in the crustal structure beneath western Turkey. Geophys. J. Int, 134 373-389.

Sayers, C.M., Schutjens, P.M.T.M., 2007. An introduction to reservoir geomechanics. The Leading Edge, 26 (5), 597-601.

Sayil, N., Osmansahin, I., 2008. An investigation of seismicity for western Anatolia. Natural. Hazards, 44 (1), 51-64 doi:10.1007/s11069-007-9141-2.

Schindler, C., 1997. Geology of northwestern Turkey: Results of the MARMARA Poly-Project. In: C. Schindler,M. Pfister (Editors), Active tectonics of northwestern Anatolia-The MARMARA Poly-Project. vdf Hochschulverlag AG ETH Zürich, pp. 329-374.

Scholz, C., 2000. Evidence for a strong San Andreas fault. Geology, 28 (2), 163-166.

Scholz, C.H., 1982. Scaling laws for large earthquakes: consequences for physical models. Bull. Seism. Soc. Am., 72 (1), 1-14.

Scholz, C.H., Aviles, C.A., Wesnousky, S.G., 1986. Scaling differences between large interplate and intraplate earthquakes. Bull. Seism. Soc. Am., 76 (1), 65-70.

Scholz, C.H., Sykes, L.R., Aggarwal, Y.P., 1973. Earthquake prediction: a physical basis. Science, 181, 4102, 803-810.

Schwartz, D.P., Coppersmith, K.J., 1984. Fault behavior and characteristic earthquakes: examples from the Wasatch and San Andreas Faults. J. Geophys. Res, 89 5681-5698.

Seeber, L., Cormier, M.-H., McHugh, C., Emre, O., Polonia, A., Sorlien, C., 2006. Rapid subsidence and sedimentation from oblique slip near a bend on the North Anatolian transform fault in the Marmara Sea, Turkey. Geology, 34 (11), 933-936 doi:10.1130/G22520A.1.

Seeber, L., Embre, O., Cormier, M.-H., Sorlien, C.C., McHugh, C.M.G., Polonia, A., Ozer, N., Cagatay, N., 2004. Uplift and subsidence from oblique slip: the Ganos-Marmara bend of the North Anatolian Transform, Western Turkey. Tectonophysics, 391 239-258 doi:10.1016/j.tecto.2004.07.015.

Sekiguchi, H., Iwata, T., 2002. Rupture process of the 1999 Kocaeli, Turkey, earthquake estimated from strong-motion waveforms. Bull. Seism. Soc. Am., 92 (1), 300–311.

Şengör, A.M.C., Tüysüz, O., Sakınç, M., Eyidoğan, H., Görür, N., Pichon, X.L., Rangin, C., 2005. The North Anatolian Fault: a new Look. Annual Rev. of Earth Planetary Sciences, 33 doi:10.1146/annurev.earth.32.101802.120415.

Şengör, A.M.C., Yılmaz, Y., 1981. Tethyan evolution of Turkey: a plate tectonic approach. Tectonophysics, 75 181-241.

Seyitoglu, G., Scott, B., 1996. The age of the Büyük Menderes graben (west Turkey) and its tectonic implications. Geol. Mag., 129 239-242.

Shaw, B.E., Wesnousky, S.G., 2008. Slip-length scaling in large earthquakes: the role of deep-penetrating slip below the seismogenic layer. Bull. Seism. Soc. Am., 98 (4), 1633-1641 doi: 10.1785/0120070191.

Sheorey, P.R., 1994. A theory for in situ stresses in isotropic and transversely isotropic rock. Int. J. Rock. Mech. Min. Sci & Geomech. Abtsr., 31 (1), 23-34.

Sibson, R.H., 1994. An Assessement of Field Evidence for `Beyerlee` Friction. Pageoph, 142 (3/4), 645-662.

Siyako, M., Huvaz, O., 2007. Eocene stratigraphic evolution of the Thrace Basin, Turkey. Sedimentary Geology, 198 75–91 doi:10.1016/j.sedgeo.2006.11.008.

Sodoudi, F., Kind, R., Hatzfeld, D., Priestley, K., Hanka, W., Wylegalla, K., Stavrakakis, G., Vafidis, A., Harjes, H.-P., Bohnhoff, M., 2006. Lithospheric structure of the Aegean obtained from P and S receiver functions. J. Geophys. Res, 111 (B12307), doi:10.1029/2005JB003932.

Sorensen, M.B., Oprasal, I., Bonnefoy-Claudet, S., Atakan, K., Mai, P.M., Pulido, N., Yalciner, C., 2006. Local site effects in Ataköy, Istanbul, Turkey, due to a future large earthquake in the Marmara Sea. Geophys. J. Int, 167 1413-1424 doi: 10.1111/j.1365-246X.2006.03204.x.

Sornette, D., Knopoff, L. 1997. The paradox of the expected time until the next earthquake. Bull. Seism. Soc. Am., 87(4), 789-798.

Starostenko, V., Buryanov, V., Makarenko, I., Rusakov, O., Stephenson, R., Nikishin, A., Georgiev, G., Gerasimov, M., Dimitriu, R., Legostaeva, O., Pchelarov, V., Sava, C., 2004. Topography of the crust–mantle boundary beneath the Black Sea Basin. Tectonophysics, 381 211-233.

Stein, R.S., Barka, A.A., Dietrich, J.H., 1997. Progressive failure on the North Anatolian fault since 1939 by earthquake stress triggering. Geophys. J. Int., 128 594-604.

Straub, C., Kahle, H.G., Schindler, C., 1997. GPS and geologic estimates of the tectonic activity in the Marmara Sea region, NW Anatolia. Journal of Geophysical Reasearch, 102 (B12), 27,587-27,601.

Taymaz, T., Jackson, J., McKenzie, D., 1991. Active tectonics of the north and central Aegean Sea. Geophys. J. Int., 106 433-490.

Taymaz, T., Westaway, R., Reilinger, R., 2004. Active faulting and crustal deformation in the eastern Mediterranean region. Tectonophysics, 391 1-374.

Tezcan, A.K., Turgay, M.I., 1991. Catalogue of Heat Flow Density Data: Turkey. In: E. Hurtig, V. Cermák, R. Haenel,V. Zui (Editors), Geothermal Atlas of Europe, pp. 84-85.

Tibi, R., Bock, G., Xia, Y., Baumbach, M., Grosser, H., Milkereit, C., Karakisa, S., Zünbül, S., Kind, R., Zschau, J. 2001. Rupture process of the 1999 August 17 Izmit and November 12 Düzce (Turkey) earthquakes. Geophys. J. Int., 144, F1-F7.

Tingay, M., Müller, B., Reinecker, J., Heidbach, O. Wenzel, F., Fleckenstein, P., 2005. Understanding tectonic stress in the oil patch: The World Stress Map Project. The Leading Edge, 1276-1282.

Tinti, S., Armigliato, A., Manucci, A., Pagnoni, G., Zaniboni, F., Yalçıner, A.C., Altinok, Y., 2006. The generating mechanisms of the August 17, 1999 Izmit bay (Turkey) tsunami: Regional (tectonic) and local (mass instabilities) causes. Marine Geol., 225 311-330.

Tirel, C., Gueydan, F., Tiberi, C., Brun, J.-B., 2004. Aegean crustal thickness inferred from gravity inversion. Geodynamical implications. Earth Planet. Sci. Lett., 228 267– 280 doi:10.1016/j.epsl.2004.10.023.

Tokay, F., Altunel, E., 2005. Neotectonic Activity of Eskışehır Fault Zone in Vicinity of İnönü - Dodurga Area. Mineral Res. Exp., 130 1-15.

Toksöz, M.N., Kuleli, H.S., Gürbüz, C., Kalafat, D., Bekler, T., Zor, E., Yilmazer, M., Ogutcu, Z., Schultz, C.A., Harris, D.B., 2003. Calibration of regional seismic stations in the Middle East with shots in Turkey, 25th Seismic Research Review - Nuclear Explosion Monitoring: Building the Knowledge Base, Tucson, Arizona.

Toksöz, M.N., Kuleli, S., Schultz, C.A., Harris, D.B., Gurbüz, C., Kalafat, D., Bekler, T., Isikara, A.M., 2002. Calibration of regional seismic stations in the Middle East with shots in Turkey, 24th Seismic Research Review - Nuclear Explosion Monitoring: Innovation and Integration, Ponte Vedra Beach, Florida, pp. 17-19.

Townend, J., 2007. What do faults feel? Observational constraints on the stresses acting on seismogenic faults. In: R. Abercrombie, A. McGarr, H. Kanamori,G. Di Toro (Editors), Earthquakes: Radiated Energy and the Physics of Faulting. American Geophysical Union Geophysical Monograph Series, pp. 313-327.

Townend, J., Zoback, M.D., 2000. How faulting keeps the crust strong. Geology, 28 399-402.

Townend, J., Zoback, M.D., 2004. Regional Tectonic Stress Near the San Andreas Fault in Central and Southern California. Geophys. Res. Lett., 31 (L15S11), doi:10.1029/2003GL018918.

Tsenn, M.C., Carter, N.J., 1987. Upper limits of power law creep of rocks. Tectonophysics, 136 1-26.

Tsokas, G., Hansen, R., 1997. Study of the crustal thickness and subducting lithosphere in Greece from gravity data. J. Geophys. Res, 102 20,585–20,597.

Tuncay, E., Ulusay, R., Watanabe, H., Tano, H., Aydan, Ö., Yüzer, E., 2002. Akusitik Emisyon (AE) tekniği: 2-AE tekniğiyle Türkiye´de arazi gerilmelerinin belirlenmesi konusunda bir ön inceleme - Acoustic Wmission (AE): 2-A preleminary investigation on the determination of in-situ stresses by AE technique in Turkey. Hacattepe Üniversitesi Yerbilimleri Uygulama ve Araştirma Merkezi Bülteni, 25 83-98.

Turcotte, D.L., Schubert, G., 2002. Geodynamics. Cambridge University Press, 456 pp.

Türkelli, N., Sandvol, E., Zor, E., Gök, R., Bekler, T., Al-Lazki, A., Karabulut, H., Kuleli, H.S., Eken, T., Gürbüz, C., Bayraktutan, S., Seber, D., Barazangi, M., 2003. Seismogenic zones in Eastern Turkey. Geophys. Res. Lett., 30 (24).

Uçarkuş, G., Armijo, R., Pondard, N., Meyer, B., Çakır, Z., 2006. The Eastern Marmara pull-apart junction (North Anatolian Fault) and its relation to the submarine end of the 1999 Izmit earthquake rupture, International Workshop in Comparative Studies of the North Anatolian Fault and the San Andreas Fault, Istanbul, pp. 90.

Uribe-Carvajal, A., Nyland, E., 1985. Stochastic Finite Element Calculation of Seismic Risk. Tectonophysics, 117 193-203.

van der Meijde, M., van der Lee, S., Giardini, D., 2003. Crustal structure beneath broad-band seismic stations in the Mediterranean region. Geophys. J. Int, 152 729–739.

Vernant, P., Chéry, J., 2006. Low fault friction in Iran implies localized deformation for the Arabia–Eurasia collision zone. Earth Planet. Sci. Lett., 246 197–206 doi:10.1016/j.epsl.2006.04.021.

Wang, K., He, J., 1999. Mechanics of low-stress forearcs: Nankai and Cascadia. J. Geophys. Res, 104 15191-15205.

Wells, D.L., Coppersmith, K.J., 1994. New Empirical Relationship among Magnitude, Rupture Length, Rupture Width, Rupture Area, and Surface Displacement. Bull. Seismol. Soc. Am., 84 (4), 974-1002.

Wesnousky, S.G., 2008. Displacement and geometrical characteristics of earthquake surface ruptures: issues and implications for seismic-hazard analysis and the process of earthquake rupture. Bull. Seism. Soc. Am., 98 (4), 1609-1632.

Westaway, R., 1994. Present-day kinematics of the Middle East and eastern Mediterranean. J. Geophys. Res, 99 12071-12090.

Wong, H.K., Liidmann, T., Ulug, A., Görür, N., 1995. The Sea of Marmara: a plate boundary sea in an escape tectonic. Tectonophysics, 244 231-250.

Wright, T.J., Fielding, E.J., Parsons, B.E., England, P.C., 2001. Triggered slip: observations of the 17 August 1999 I˙zmit (Turkey) earthquake using radar interferometry. Geophys. Res. Lett., 28 1079-1082.

Yagi, Y., Kikuchi, M., 2000. Source rupture process of the Kocaeli, Turkey, earthquake of August17, 1999, obtained by joint inversion of near-field data and teleseismic data. Geophys. Res. Lett.

Yalçıner, A.C., Alpar, B., Altınok, Y., Özbay, I., Imamura, F., 2002. Tsunamis in the Sea of Marmara Historical documents for the past, models for the future. Marine Geol., 190 445-463.

Yaltırak, C., Alpar, B., 2002. Evolution of the middle strand of North Anatolian Fault and shallow seismic investigation of the southeastern Marmara Sea (Gemlik Bay). Marine Geol.(190), 307-327 PII:S0025-3227(02)00352-3.

Yaltırak, C., Alpar, B., Yüce, H., 1998. Tectonic elements controlling the evolution of the Gulf of Saros (northeastern Aegean Sea, Turkey). Tectonophysics, 300 227–248 PII:S0040-1951(9 8)00242-X.

Yaltırak, C., Sakinc, M., Aksu, A.E., Hiscott, R.N., Galleb, B., Ulgen, U.B., 2002. Late Pleistocene uplift history along the southwestern Marmara Sea determined from raised coastal deposits and global sea-level variations. Marine Geol., 190 283-305 PII:S0025-3227(02)00351-1.

Yaltırak, C., Sakınç, M., Oktay, F.Y., 2000. Westward propagation of North Anatolian fault into northern Aegean: Timing and kinematics, Comment. Geology, 28 187-188.

Yaltırak, C., Yalçın, T., Yüce, G., Bozkurtoglu, E., 2005. Water-level changes in shallow wells before and after the 1999 Izmit and Düzce earthquakes and comparison with long-term water-level observations (1999-2004), NW Turkey. Turkish J. Earth Sci., 14 281-309.

Youngs, R.R., Coppersmith, K.J., 1985. Implications of fault slip rates and earthquake recurrence models to probabilistic seismic hazard estimates. Bull. Seism. Soc. Am., 75 (4), 939-964.

Zanchi, A., Angelier, J., 1993. Seimotectonics of western Anatolia: regional stress orientation from geophysical and geological data. Tectonophysics, 222 259-274.

Zhu, L., Mitchell, B.J., Akyol, N., Cemen, I., Kekovali, K., 2006. Crustal thickness variations in the Aegean region and implications for extension of continental crust. J. Geophys. Res, 111 (B01301), doi:1029/2005JB003770.

Zienkiewicz, O.C., Taylor, R.L. (1994). The Finite Element Method. Vol. 1&2, McGraw Hill Book Company, London.

Zoback, M.D., 2000. Strength of the San Andreas. Nature, 405 31-32.

Zoback, M.D., Zoback, M.L., Mount, V.S., Suppe, J., Eaton, J.P., Healy, J.H., Oppenheimer, D.H., Reasenberg, P.A., Jones, L., Raleigh, C.B., I.G., W., Scotti, O., Wentworth, C., 1987. New Evidence on the State of Stress of the San Andreas Fault System. Science, 238 1105-1111.

Zoback, M.L., 1992. First and second order patterns of stress in the lithosphere: the World Stress Map project. J. Geophys. Res, 97 11703-11728.

Zor, E., Özalaybey, S., Gürbüz, C., 2006. The crustal structure of the eastern Marmara region, Turkey by teleseismic receiver functions. Geophys. J. Int, 167 213-222 doi:10.1111/j.1365-246X.2006.03042.x.

Zor, E., Sandvol, E., Gürbüz, C., Türkelli, N., Seber, D., Barazangi, M., 2003. The crustal structure of the East Anatolian plateau (Turkey) from receiver functions. Geophys. Res. Lett., 30 (24), 8044 doi:10.1029/2003GL018192.